Национальный исследовательский университет ИТМО

(Университет ИТМО)

На правах рукописи

Зограф Георгий Петрович

Спектроскопия усиленного и термочувствительного комбинационного рассеяния оптически резонансных полупроводниковых наночастиц

Диссертация на соискание учёной степени

кандидата физико-математических наук

Санкт-Петербург 2020

Национальный исследовательский университет ИТМО

(Университет ИТМО)

На правах рукописи

Зограф Георгий Петрович

Спектроскопия усиленного и термочувствительного комбинационного рассеяния оптически резонансных полупроводниковых наночастиц

Специальность 01.04.05

«Оптика (физико-математические науки)»

Диссертация на соискание учёной степени

кандидата физико-математических наук

Научный руководитель:
доктор физико-математических наук, профессор
Макаров Сергей Владимирович

Санкт-Петербург 2020

Диссертация подготовлена в: федеральное государственное автономное образовательное учреждение высшего образования «Национальный исследовательский университет ИТМО».

Научный руководитель:	доктор физико-математических наук, профессор Макаров Сергей Владимирович
Официальные оппоненты:	Бонод Николас, доктор философии, Университет Экс-Марсель, Главный научный сотрудник, Институт Френеля
	Харинцев Сергей Сергеевич, доктор физико-математических наук, доцент, Казанский федеральный университет, Профессор, Институт Физики

Защита состоится 17.12.2020 г. в 15:00 часов на заседании диссертационного совета 05.19.30 Университета ИТМО. Санкт-Петербург, Кронверкский пр., д. 49, лит. А, ауд. 422.

С диссертацией можно ознакомиться в библиотеке Университета ИТМО по адресу: 197101, Санкт-Петербург, Кронверкский пр., д.49 и на сайте https://dissovet.itmo.ru.

Ученый секретарь диссертационного совета 05.19.00 Университета ИТМО, кандидат физико-математических наук, Старовойтов Антон Андреевич.

ITMO University

As a manuscript

Zograf Georgii Petrovich

Enhanced and heat-sensitive Raman scattering spectroscopy of optically resonant semiconductor nanoparticles

Speciality 01.04.05
Optics (Physics and Mathematics)

Academic dissertation candidate of physics and mathematics

Supervisor:
doctor of science
Makarov Sergey Vladimirovich

Saint-Petersburg 2020

The research was carried out at: ITMO University.

Supervisor:	doctor of science Makarov Sergey Vladimirovich
Official opponents:	Bonod Nicolas, PhD, CNRS/Aix-Marseille Universite, Principle researcher, Institut Fresnel
	Kharintsev Sergey Sergeevich, Doctor of science, Kazan Federal University, Professor, Institute of Physics

The defense will be held on 17.12.2020 at 15:00 at the meeting of the ITMO University Dissertation Council 05.19.30, 49 Kronversky pr., Saint-Petersburg, Russia.

The thesis is available in the Library of ITMO University, 49 Kronversky pr., Saint-Petersburg, Russia and on https://dissovet.itmo.ru website.

Science Secretary of the ITMO University Dissertation Council 05.19.00, Candidate of Physics and Mathematics, Starovoytov Anton A.

CONTENTS

Реферат

Общая характеристика работы

Введение и мотивация. Возможность удаленного и неинвазивного изучения свойств, присущих объектам и структурам, на микро- и наномасштабах вызывала большой интерес исследователей в последние полвека. Идея создания датчиков (сенсоров), которые давали бы точную и исчерпывающую информацию об объектах, к которым они прикреплены, была, своего рода, путеводной звездой в течение многих лет.

Одно из возможных решений было предложено в 1973 году Мартином Флейшманном, Патриком Дж. Хендрой и А. Джеймсом МакКвилланом. Авторы наблюдали значительное усиление сигнала комбинационного рассеяния света, помещая пиридин на шероховатую серебряную подложку - этот эффект позже был назван SERS (поверхностно-усиленная рамановская спектроскопия) [1]. Комбинационное рассеяние представляет собой очень слабый оптический эффект, возникающий в полупроводниках или молекулах из-за неупругого рассеяния либо на колебаниях решетки, либо на колебаниях химических связей, обеспечивая уникальный спектр для любой молекулы или состава. Данный эффект может быть усилен на несколько порядков за счет локализации электромагнитного поля в ближней зоне [2, 3], позволяющей обнаруживать "следы"одиночных молекул. В связи с этим, особый интерес для задач SERS-сенсоров вызвали именно плазмонные наночастицы и наноструктуры [4]. Стоит отметить, что не только факт наличия или отсутствия химического соединения или вещества был целью исследований приложений сенсинга, но также и возможность определять температуру. Благодаря этому, исследования в области локального управления и контроля температуры с одновременной возможностью различать химические соединения и составы с помощью комбинационного рассеяния света были особенно актуальны [5].

Так, недавно было продемонстрировано, что одиночные плазмонные наночастицы могут поддерживать нанотермометрию и эффективный оптический нагрев с одновременной возможностью служить SERS-зондом [6].

Однако группа профессора Мишеля Оррита столкнулась с серьезным недостатком из-за очень длительного времени сбора сигнала, составляющего несколько минут, что ограничивало применимость плазмонных наностержней. Другим фактором, ограничивающим применимость плазмонных наноструктур в качестве теплового датчика, является отсутствие собственного рамановского сигнала (комбинационного рассеяния). Отсутствие такого сигнала комбинационного рассеяния требует дополнительных манипуляций для получения данных о температуре.

С другой стороны, в последние годы диэлектрическая нанофотоника вызвала большой интерес из-за способности локализовывать свет внутри наноразмерных резонаторов посредством резонансов Ми или других состояний с высокой добротностью, в отличие от плазмонных наноантенн. Такие наноструктуры позволили получить субволновые нанолазеры [7,8], усиленную нелинейную генерацию света [9–11], усиленную фотолюминесценцию [12,13], ближнепольное усиление [14,15] и добиться значительного усиления ряда других фотонных эффектов [16]. При возбуждении различных оптических резонансных мод внутри полупроводниковых наноструктур лазерным источником может наблюдаться значительное усиление поля. Кроме того, эти структуры оказались очень эффективными для оптического нагрева и термометрии при умеренных интенсивностях. Основываясь на собственном комбинационном рассеянии полупроводников и диэлектрических наноструктур, интенсивность которого может быть значительно улучшена путем согласования резонансных условий [17,18], можно добиться эффективного оптического нагрева, нанотермометрии и усиления ближнего поля, что позволяет обнаружение молекулярных событий на наноуровне.

Диссертация посвящена созданию и исследованию альтернативного к плазмонному подходу для сенсинга, эффективного оптического нагрева, термометрии и усиления комбинационного рассеяния света. В работе предлагается подход на основе диэлектрических и полупроводниковых резонансных наноструктур. Диссертация охватывает анализ различных форм и геометрий наноструктур; ряда устойчивых к оптическому нагреву и термометрии материалов; различных материалов для подложек и различных

внешних условий; усиления комбинационного рассеяния света наночастицами, за счет либо оптических резонансов, либо с помощью вынужденного излучения; и, наконец, возможности зондирования оптических состояний и распределения ближнего электромагнитного поля за счет комбинационнного рассеяния света. **Основные цели данной работы:**

- Разработка подхода для одновременного оптического нагрева и термометрии на основе резонансно-усиленного комбинационного рассеяния света на диэлектрических и полупроводниковых наноструктурах.
- Демонстрация оптически индуцированного фазового перехода из аморфного в поликристаллическое состояние в полупроводниковых наноструктурах с возможностью детектирования такого фазового перехода посредством комбинационного рассеяния света.
- Зондирование оптических состояний наноструктур с помощью резонансно-усиленного комбинационного рассеяния света из дальней зоны электромагнитного поля.
- Демонстрация и реализация перехода от режима спонтанного к вынужденному комбинационному рассеянию света изолированной одиночной полностью субволновой наночастицы.

Положения, выносимые на защиту:

- Резонансное оптическое возбуждение Ми-моды в полупроводниковой наночастице со сбалансированными радиационными и нерадиационными потерями обеспечивает наиболее эффективный оптический нагрев среди прочих соотношений потерь для данной оптической моды.
- Оптический нагрев непрерывным лазерным источником полупроводниковой Ми-резонансной наноструктуры позволяет индуцировать фазовый переход из аморфного в поликристаллическое состояние и в то же время позволяет детектировать такой переход при помощи комбинационного рассеяния света.
- Двумерное картирование распределения интенсивности комбинационного рассеяния света резонансной полупроводниковой наноструктуры позволяет исследовать возбужденные оптические моды в ней из

дальней зоны электромагнитного поля и предоставляет информацию о структуре ближнего поля собственных мод на длине волны накачки.

- Переход от режима спонтанного комбинационного рассеяния света к вынужденному происходит при возбуждении высокодобротных оптических резонансных мод, как на длине волны накачки, так и на длине волны стоксовой компоненты комбинационного рассеяния света, с оптимизированными эффективностями возбуждения мод и пространственным их перекрытием на длинах волн накачки и излучения в одиночном наноцилиндре из кристаллического кремния с оптимизированным теплоотводом в материал подложки.

Научная новизна этой работы включает, но не ограничивается следующими пунктами:

1. Первая экспериментальная демонстрация одновременного оптического нагрева непрерывным лазерным источником и наноразмерной термометрии с помощью резонансных полупроводниковых наноструктур, поддерживающих комбинационное рассеяние света.
2. Первая демонстрация использования Ми-резонансных полупроводниковых наночастиц, поддерживающих оптический нагрев и нанотермометрию посредством комбинационного рассеяния света для приложений адресной доставки лекарственных средств. Наночастицы α-Fe_2O_3 использовались в качестве мишени для лазерного возбуждения в ближнем ИК-диапазоне для эффективного преобразования света в тепло в стенках полимерных носителей лекарств и в качестве прямого оптического датчика температуры за счет термочувствительного Рамановского рассеяния. В качестве доказательства была продемонстрирована *in vitro* успешная доставка и оптически-индуцированный разрыв полимерного носителя посредством лазерного нагрева наночастиц α-Fe_2O_3 с последующим высвобождением противоопухолевого лекарственного средства винкристина. Предложенная система работала при умеренном значении лазерной интенсивности всего 4.0×10^4Вт см $^{-2}$.

3. Первая демонстрация контролируемого, оптически-индуцированного фазового перехода из аморфной в поликристаллическую фазу для кремниевых нанодисков на стеклянной подложке с оптическим зондированием температуры и кристаллической фазы нанодиска посредством комбинационного рассеяния света.
4. Первая демонстрация получения качественного распределения «горячих точек» ближнего электромагнитного поля оптических мод резонансных полупроводниковых наноструктур из дальнего поля с помощью пространственного и спектрального картирования интенсивности комбинационного рассеяния света.
5. Первая экспериментальная демонстрация перехода от спонтанного комбинационного рассеяния света к вынужденному режиму комбинационного рассеяния для одиночного изолированного кристаллического кремниевого наноцилиндра.

Практическая значимость работы заключается в том, что автор предложил новый подход к оптическому нагреву и термометрии с наноразмерным пространственным разрешением с помощью одиночных резонансных полупроводниковых наночастиц, поддерживающих комбинационное рассеяние света. Предлагаемый подход на основе наночастиц, которые служат как датчиком температуры, так и преобразователем света в тепло, не требует каких-либо дополнительных этапов изготовления. Более того, данных подход использует один источник излучения как для оптического нагрева, так и для возбуждения комбинационного рассеяния света, устойчив и поддерживает многократные циклы повторения оптического нагрева. Такой подход продемонстрировал свою применимость в передовых биомедицинских приложениях для систем доставки лекарств для лечения рака с дистанционным полностью оптическим механизмом высвобождения лекарственного препарата. Данный способ оптической термометрии, основанный на спектральном сдвиге сигнала комбинационного рассеяния света наноструктур при интенсивном лазерном облучении с последующим оптическим нагревом, нашел очень многообещающее применение для *in situ* модификации кристаллического состояния наноструктур. Рамановское рассеяние служит

как температурным зондом, так и зондом состояния степени кристалличности, поэтому существенный оптический нагрев нанодиска из аморфного кремния на стеклянной подложке может привести к фазовому переходу из аморфного состояния в поликристаллическое. Изготовление кристаллических наноструктур на стекле SiO_2 остается довольно сложной технологической задачей, поэтому метод контролируемого оптического нагрева нанодисков из аморфного кремния на стеклянной подложке с *in situ* температурным откликом и возможностью отслеживать кристаллическое состояние может решить технологические трудности для некоторых задач и приложений. Как было упомянуто выше, комбинационное рассеяние является эффективным методом зондирования для измерения температуры и оценки состояния кристалличности, однако интенсивность комбинационного рассеяния может служить зондом для качественной сравнительной оценки плотности электромагнитной мощности, запасенной в наноструктурах. Пространственное картирование интенсивности комбинационного рассеяния света зигзагообразного олигомера, состоящего из трех нанодисков одинакового размера, показывает переключение распределения «горячих точек» ближнего электромагнитного поля при изменении поляризации падающего возбуждения. Существенным преимуществом этого подхода является то, что он не требует каких-либо вспомогательных методов и использует только один источник для возбуждения оптических мод, комбинационного рассеяния света и детектирует сигнал в дальней зоне. Быстрое получение такой качественной информации о распределении электромагнитных «горячих точек» ближнего поля у наноструктуры может быть полезно для экспресс-анализа оптических состояний наноструктуры, а так же может стать платформой для селективного возбуждения биологических красителей или полимеров в зазорах зигзагообразного олигомера. Наконец, комбинационное рассеяние света – довольно слабый и маловеоятный оптический процесс. Однако его можно значительно усилить, за счет возбуждения оптических резонансов в наноструктурах. Более того, интенсивность комбинационного рассеяния света может быть дополнительно увеличена за счет перехода от режима спонтанного излучения к режиму вынужденного излучения. Такой переход, наблю-

даемый в полностью субмикронном наноцилиндре, может послужить шагом на пути создания высокоэффективных наносенсоров на основе комбинационного рассеяния света, а также эффективных источников излучения.

Достоверность полученных результатов обеспечивается применением современных методов исследования, основана на воспроизводимости результатов измерений, а также подтверждается хорошим согласием экспериментальных данных с результатами численного моделирования и аналитическим описанием эффектов.

Применимость полученных результатов. Автору диссертации принадлежит патент РФ № 177658 на полезную модель «Нелинейная диэлектрическая наноантенна», зарегистрированный 05.03.2018, концепция которой основана на принципах и результатах, полученных в рамках диссертации. Более того, концепция оптического нагрева и термометрии на основе полупроводников продемонстрировала свою применимость для реальных систем доставки лекарств.

Апробация. Основные результаты работы были представлены и обсуждались на всероссийских и международных конференциях, таких как: Международная зимняя школа по физике полупроводников 2016, Зеленогорск, Санкт-Петербург, Россия (постер); Международная школа и конференция «Saint-Petersburg Open» 2016, 2017, 2019, Санкт-Петербург, Россия (постер); Международная конференция «Дни дифракции» 2016 (постер), 2017 (устный), 2018 (устный), Санкт-Петербург, Россия; Международная конференция МЕТАНАНО 2016, Анапа, Россия (постер); Всероссийский конгресс «Наука будущего - наука молодых» 2016, Казань, Россия (постер); Международная конференция МЕТАНАНО 2017, Владивосток, Россия (устный); Международная конференция NANOP 2017, Барселона, Испания (устный); Международная конференция МЕТАНАНО 2018, Сочи, Россия (устный); Международная летняя школа Николя Кабрера о «продвинутой манипуляции со светом в наномасштабе» 2018, Мирафлорес-де-ла-

Сьерра, Мадрид, Испания (постер); Международная конференция ICMAT 2019, Сингапур (постер); Международная конференция МЕТАНАНО 2019, Санкт-Петербург, Россия (устный); Международная конференция МЕТАНАНО 2020 (онлайн, устный); OSA Advanced Photonics Congress 2020 (онлайн, устный); а также на научных семинарах в Университете ИТМО, Северо-Осетинском государственном университете, Чжэцзянском университете (Китай) и Технологическом университете Квинсленда (Австралия).

Публикации. Основные результаты диссертационной работы отражены в 10 научных статьях, включенных в список ВАК, в том числе 7 статьях в научных журналах, индексируемых научными базами данных Scopus и Web of Science, и 3 конференционных рецензируемых материалах, которые индексируются научными базами данных Scopus и Web of Science.

Личный вклад автора. Личный вклад автора заключается в измерениях и обработке экспериментальных результатов (спектры темнопольного рассеяния, спектры комбинационного рассеяния света), существенной части численного моделирования оптических свойств исследуемых наноструктур, реализации численной модели оптического нагрева полупроводниковых наноструктур, участии в постановке исследовательских задач и написании научных статей.

Объем и структура работы. Диссертация состоит из введения, пяти глав, заключения и списка использованной литературы. Общий объем диссертации 112 страниц, в том числе список литературы, включающий в себя 158 наименований. Работа содержит 36 рисунков и 1 таблицу, размещенных внутри глав.

ОСНОВНОЕ СОДЕРЖАНИЕ РАБОТЫ

В первой главе представлен краткий обзор предложенных и используемых в исследовании экспериментальных и теоретических подходов;

описывается необходимость каждого конкретного метода и описывается его применимость в конкретных случаях; доказывается актуальность метода для проводимых исследований.

Во второй главе диссертации обсуждаются оптимальные условия для оптического нагрева резонансных полупроводниковых наночастиц сферической формы. Оптимизация резонансов Ми и параметров материала может привести к сильному и эффективному лазерному нагреву даже полупроводниковых частиц с малыми потерями. Основной принцип нагрева и поглощения света для одиночной сферической наночастицы в однородной среде был разработан и исследован ранее [19, 20]. Диэлектрические и полупроводниковые наночастицы могут поддерживать сильные резонансные отклики в видимом диапазоне, поэтому поглощение света может сильно варьироваться от размера и длины волны. В связи с этим аналитическое решение для оптического нагрева одиночных сферических наночастиц должно учитывать из резонансный характер. В результате получается точное решение для повышения температуры сферической наночастицы диаметром D в стационарном уравнении теплопередачи с бесконечными внешними граничными условиями и с заранее заданным источником с интенсивностью (I), рассчитанным сечением поглощения наночастицы (C_{abs}), определенным теорией Ми, заранее известной теплопроводностью окружающей среды κ_2, в случае, если теплопроводность наночастицы намного больше, чем теплопроводность окружающей среды. Тогда точное значение температуры наночастицы можно найти следующим образом:

$$\delta T_{NP} = \frac{IC_{abs}}{2\pi\kappa_2 D}. \tag{1}$$

Результаты расчетов оптического нагрева можно увидеть на двумерных цветовых картах, показанных на Рис. 1 (b, c). Температуры оптического нагрева сферической наночастицы в воздушной среде с различными действительными ($\mathrm{Re}(\varepsilon)$ от -10 до 30) и мнимыми ($\mathrm{Im}(\varepsilon)$ от 0 до 5) частями диэлектрической проницаемости в случае малых наносфер (отношение длины волны к диаметру $\lambda/D = 10$) показаны на Рис. 1(b); те же вычисления, но для более крупных наночастиц, где отношение длины волны к диаметру составляет 2.8, показаны на Рис. 1(c). Когда размер наночастиц мал для

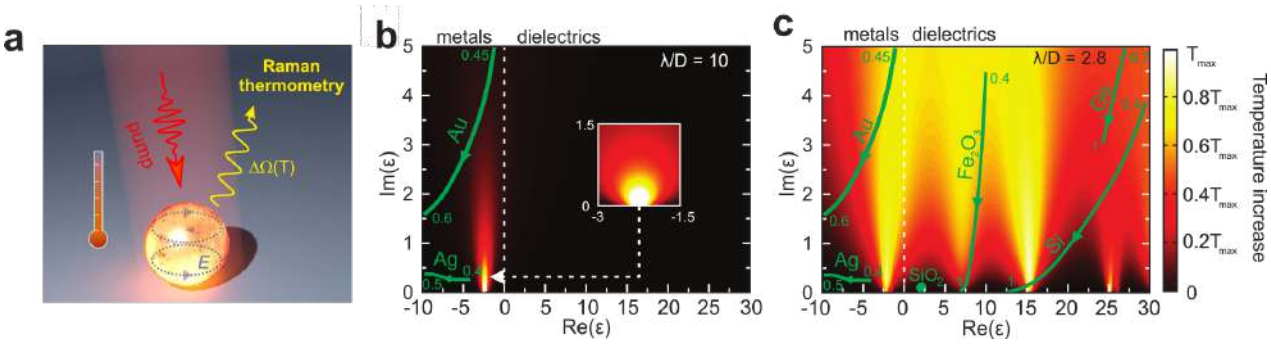

Рисунок 1 — **Оптический нагрев сферических наночастиц.** (a) Концепция оптического нагрева и термометрии. Результаты расчета теоретического оптического нагрева в однородной воздушной среде для одиночных сферических наночастиц с фиксированным соотношением длины волны к диаметру λ/D в зависимости от различных действительных и мнимых частей диэлектрической проницаемости: (b) $\lambda/D = 10$; (c) $\lambda/D = 2.8$. Линии с зелеными стрелками в b) и c) соответствуют значениям Re (ε) и Im (ε) для конкретных реальных материальных дисперсий. Направление стрелок соответствует увеличению длины волны. Цифры указывают диапазон длин волн в микронах. Взято из [21].

поддержания резонансов Ми в видимой области, только наносферы с отрицательной действительной частью диэлектрической проницаемости (металлы) поддерживают оптический нагрев, что ясно видно из Рис. 1(b). Однако при увеличении диаметра наночастицы, а значит уменьшении отношения длины волны к диаметру до значения $\lambda/D = 2.8$ (Рис. 1(c)), можно заметить эффективный оптический нагрев в области положительной действительной части диэлектрической проницаемости, что соответствует диэлектрическим и полупроводниковым материалам. Это происходит из-за возбуждения различных мод Ми в наносфере и, как следствие, резонансного оптического поглощения света. Более интересным в этих результатах является то, что увеличение мнимой части диэлектрической проницаемости не обязательно приводит к увеличению температуры оптического нагрева. Для более глубокого понимания лежащих в основе принципов и исследования причин эффективного оптического нагрева полупроводников с низким уровнем потерь, при резонансном лазерном возбуждении мод Ми, следует начать рассмотрение с классического общего выражения для поглощенной

электромагнитной мощности P:

$$P = \frac{1}{2}\mathrm{Re}\int_V \mathbf{J}^*(\mathbf{r})\mathbf{E}(\mathbf{r})dV \tag{2}$$

где $\mathbf{J}(\mathbf{r})$ - плотность тока, $\mathbf{E}(\mathbf{r})$ - электрическое поле внутри объекта, а интегрирование выполняется по объему рассматриваемой наночастицы V. Выражение в уравнении 2 дает понимание, что чем выше электромагнитное поле внутри наночастицы и чем выше плотность тока, генерируемая падающей электромагнитной волной, тем больше общая поглощенная мощность. Кроме того, можно заметить, что $\mathbf{J} = \sigma\mathbf{E}$ и $\sigma = \varepsilon_0\omega\mathrm{Im}(\varepsilon)$, где ε_0 - диэлектрическая проницаемость вакуума, ω - частота падающего света, σ - электрическая проводимость. Интегрирование уравнения 2 по объему наночастицы, поддерживающей оптические Ми-моды, позволяет модифицировать уравнение 2 в терминах эффективного объема моды V_{eff} и пространственно усредненного коэффициента усиления поля $F = < |E|^2 > /|E_0|^2$, который дает информацию о запасенной плотности мощности внутри наночастицы, и где $|E_0|$ - это величина напряженности падающего электрического поля. Следовательно, можно модифицировать уравнение 2 для полной поглощенной мощности следующим образом:

$$P \sim \sigma F^2 \, V_{\text{eff}}. \tag{3}$$

Общая поглощенная мощность теперь имеет 3 различных независимых вклада: σ, F^2 и V_{eff}, которые оказывают значительное влияние на общую температуру оптического нагрева δT_{NP}. В следующих подразделах все вклады будут рассмотрены отдельно.

Влияние безызлучательных потерь. Как было показано в выражении 3, повышение омических потерь не обязательно увеличивают полное поглощение света наночастицей, следовательно, и общий оптический нагрев. Увеличения мнимой части диэлектрической проницаемости приводит к увеличению электрической проводимости, однако, в то же время, это также значительно влияет на добротность резонанса, уменьшая ее. В связи с этим, вклад σF^2 следует рассмотреть подробнее.

Оптические резонансы можно описать моделью осциллятора с вязким трением с некоторыми допущениями. Следовательно, вблизи оптиче-

ского резонанса ω_0 фактор усиления поля F может быть выражен как $F \sim 1/\left(\omega_0^2 - \omega^2 - i\omega\gamma\right)$, где γ - полные оптические потери системы. При более детальном рассмотрении, полные оптические потери имеют два вклада: $\gamma = \gamma_{\text{rad}} + \gamma_{\text{ohmic}}$, а именно – *радиационные* и *безызлучательные* (или *омические*) потери. Безызлучательная часть пропорциональна $\text{Im}(\varepsilon)$, поэтому вклад σF^2 на резонансной частоте ω_0 пропорционален $\sim \gamma_{\text{Ohmic}}/(\gamma_{\text{Ohmic}} + \gamma_{\text{rad}})^2$, из чего следует, что при экстремально высоких омических потерях, полная поглощаемая мощность стремится к нулю.

Дальнейшее рассмотрение приводит к тому, что при определенном фиксированном значении радиационных потерь γ_{rad} максимальное значение поглощенной мощности будет достигаться при $(\sigma F^2)_{\max} \sim 1/(4\gamma_{\text{rad}})$. Данное максимальное значение достигается при равенстве радиационных и нерадиационных потерь $\gamma_{\text{Ohmic}} \approx \gamma_{\text{rad}}$. Радиационный вклад потерь γ_{rad} можно минимизировать, взяв резонансную наночастицу, размер которой много меньше длины волны λ. Этого можно достичь для случая плазмонной наночастицы, поддерживающей локализованный поверхностный плазмонный резонанс (ЛППР) с заданной плазменной частотой ω_p, где $\gamma_{\text{rad}} \ll \gamma_{\text{Ohmic}}$. При ЛППР радиационные потери γ_{rad} приблизительно равны $\approx \omega_0^3/\omega_p^2(\pi D/\lambda)^3$. Этот анализ приводит к тому, что радиационные потери γ_{rad} относительно невелики по сравнению с ω_0 из-за соотношения $(D/\lambda)^3$.

Действительно, эти теоретические предсказания и оценки подтверждены аналитически, и их можно увидеть на Рис. 1(b), где в случае относительно небольших наночастиц ($\lambda/D = 10$) резонансный оптический нагрев наблюдается только в области с отрицательной действительной частью диэлектрической проницаемости $\text{Re}(\varepsilon)$, а максимальное значение температуры достигается при относительно небольших значениях мнимой части диэлектрической проницаемости $\text{Im}(\varepsilon)$, где как раз выполняется соотношение баланса излучательных и омических потерь $\gamma_{\text{Ohmic}} \approx \gamma_{\text{rad}}$. Обратная картина наблюдается для более крупных наночастиц, что можно увидеть на Рис. 1(c). Наличие горячих точек для оптического нагрева в положительном диапазоне действительной части диэлектрической проницаемости означает, что полупроводниковые наночастицы могут очень эффективно опти-

чески нагреваться. Например, γ_{rad} для дипольных мод довольно высока, а максимальная температура достигается при больших омических потерях. С другой стороны, если рассматривать резонансы более высокого порядка, например магнитный квадрупольный, то следует ожидать меньшего значения γ_{rad}, и, следовательно, оптимальным лазерным нагревом окажутся более низкие значения γ_{Ohmic}. Последнее можно увидеть для более высоких $\text{Re}(\varepsilon)$ на Рис. 1(c).

Влияние эффективного объема моды. Другой фактор, который вносит большой вклад в общее поглощение света наночастицей и, следовательно, способствует нагреву, - это эффективный объем резонансной оптической моды нанорезонатора V_{eff}. В общем случае, чем больше размер наночастицы, тем больше оптический нагрев. Однако следует отметить, что V_{eff} может существенно изменить такое предположение. Если рассматривать плазмонную наночастицу, где действительная часть диэлектрической проницаемости отрицательна ($\text{Re}(\varepsilon)< 0$), глубина скин-слоя начинает определять эффективный объем моды. А именно, типичная толщина скин-слоя, расстояние, на котором свет распространяется внутри материала при уменьшении величины поля в e раз, для плазмонных материалов едва ли превышает $\delta \approx 20$ нм в видимом диапазоне. Следовательно, V_{eff} для плазмонной наночастицы определяется глубиной скин-слоя следующим образом: $V_{\text{eff}} \approx \pi D^2 \delta$. В отличие от плазмонных материалов и наночастиц, диэлектрические и полупроводниковые материалы в основном прозрачны для света в видимой области спектра, поэтому эффективный объем моды обычно порядка физического объема наночастицы. Чтобы быть более точным, для резонанса типа Ми эффективный объем мод можно определить, как $V_{\text{eff}} \approx \pi D^3/6$.

Непосредственный вывод, который следует из анализа эффективного объема моды, заключается в том, что для диэлектрических и полупроводниковых нанорезонаторов – увеличение размера нанорезонатора увеличивает температуру оптического нагрева. Тот же подход для плазмонных гораздо менее эффективен.

Общий вывод для анализа такого оптического нагрева полупроводниковых и диэлектрических наноструктур можно описать следующим обра-

зом: эффективный оптический нагрев в резонансных полупроводниковых и диэлектрических наночастицах может быть достигнут при соблюдении баланса потерь – радиационных и омических. Поскольку по своей сути омические потери в диэлектриках низкие, следует рассматривать более крупные частицы, которые поддерживают узкие оптические моды высокого порядка с высокой добротностью, которые также обладают низким радиационным каналом потерь. Напротив, плазмонные частицы демонстрируют лучшую эффективность, когда размеры наночастиц довольно малы [19].

Оптический нагрев с температурной обратной связью. Основным преимуществом кристаллических полупроводников перед плазмонными материалами является наличие собственного комбинационного рассеяния, которое можно эффективно использовать в качестве теплового зонда. Более того, резонансные кристаллические наночастицы, поддерживающие моды Ми, могут остро усиливать интенсивность комбинационного рассеяния на два порядка [17], что впоследствии может обеспечить прямую термометрию на основе рамановского сдвига. В самом деле, оптический нагрев одиночного нанорезонатора можно увидеть из спектров комбинационного рассеяния в виде синего сдвига спектра при более высоких температурах, как показано на Рис. 2а. Более того, как теоретически, так и экспериментально было хорошо изучено М. Балакнским *и др.* [22], что из-за ангармонических эффектов в колебаниях решетки положение спектральной линии комбинационного рассеяния является термочувствительным. Действительно, частота линии оптического фонона, ответственной за комбинационное рассеяние света (Ω), определяется температурой следующим образом:

$$\Omega(T) = \Omega_0 + A\left(1 + \frac{2}{e^x - 1}\right) + B\left(1 + \frac{3}{e^y - 1} + \frac{3}{(e^y - 1)^2}\right), \qquad (4)$$

где Ω_0 = 528 см$^{-1}$, A = -2.96 см$^{-1}$, B = -0.174 см$^{-1}$, $x = \hbar\Omega_0/2kT, y = \hbar\Omega_0/3kT$ для кристаллического кремния [22].

Прямое соответствие между спектральным положением комбинационного рассеяния света и температурой открывает прекрасные возможности для рамановской нанотермометрии [23].

Рис. 2а изображает спектральный сдвиг спектров комбинационно-

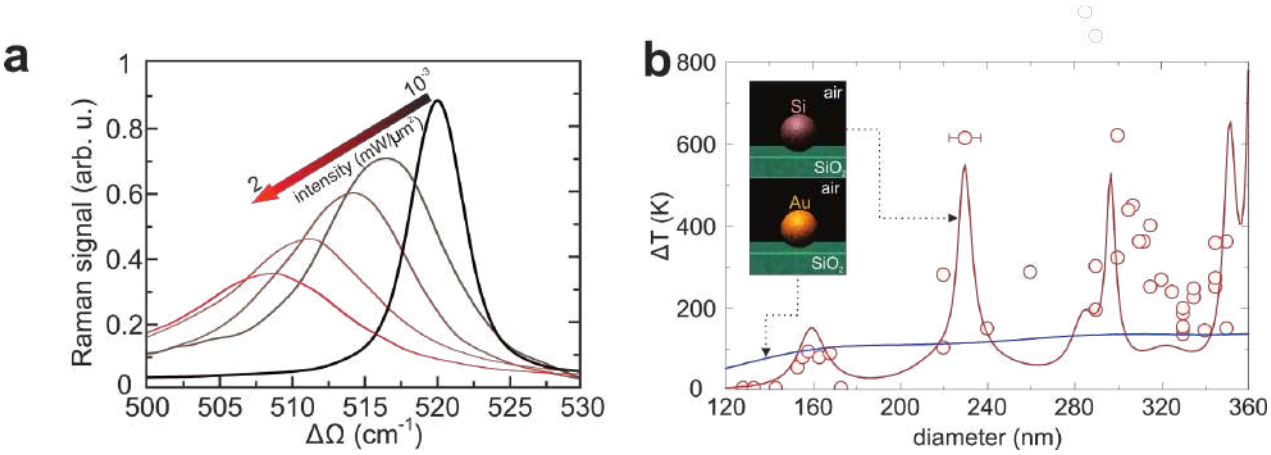

Рисунок 2 — **Оптический нагрев и Рамановская термометрия кристаллических кремниевых наночастиц.** a) Экспериментальные спектры комбинационного рассеяния света для сферических наночастиц c-Si диаметром 350 нм на стеклянной подложке. b) Экспериментальный (красные кружки) и численно рассчитанный (красные сплошные линии) оптический нагрев сферических наночастиц c-Si. Синие линии соответствуют оптическому нагреву сферических наночастиц золота. Рассматриваемая длина волны $\lambda = 633$ нм и интенсивность света $I_0 = 2$ мВт/мкм^2. Взято из [21]

го рассеяния при увеличении интенсивности падающего лазера. Из уравнения 8 можно определить, что спектральный сдвиг от начальных условий до 509 см $^{-1}$ соответствует оптическому нагреву $\Delta T \approx 600$ K. Более того, метод, основанный на рамановской нанотермометрии и оптическом нагреве, позволяет с точностью до субмикронного разрешения картографировать распределение температуры нанообъектов с помощью точного позиционирования пьезо-приводом. Стоит отметить, что в ходе экспериментальных исследований не было обнаружено необратимых изменений фазы, формы или размера наночастиц.

Описанный в этом разделе метод, основанный на термочувствительном комбинационном рассеянии света, позволяет исследовать температуру наночастиц, сделанных из различных полупроводниковых материалов, при произвольном лазерном возбуждении, при различных других свойствах и, что более важно, в очень широком диапазоне температур до 1000 K, как показано на Рис. 2(b). Оптический нагрев и нанотермометрия комбинационного рассеяния хорошо согласуются с теоретическими расчетами, и результаты воспроизводимы. Стоит отметить, что экспериментальные данные

были хорошо описаны без учета термооптических нелинейных эффектов в материалах нанорезонатора, которые на самом деле могут существенно изменить показатель преломления, теплопроводность нагретых материалов, следовательно, оптические резонансы и характеристики оптического нагрева [24].

Теоретически и экспериментально доказано, что оптический нагрев наночастиц кристаллического кремния очень чувствителен к условиям резонанса, поэтому оптический нагрев сильно зависит от диаметра наносферы, как видно из Рис. 2(b). Общая концепция заключается в том, что чем точнее можно настроить размер наночастицы под резонансные условия, тем более явно будет наблюдаться спектральный сдвиг комбинационного рассеяния света, и, следовательно, тем сильнее будет достигнутый оптический нагрев. Рис. 2(b) демонстрирует ярко выраженное резонансное поведение, из которого можно сделать вывод, что оптические моды низкого порядка (ЭД) не поддерживают высокоэффективный оптический нагрев (примерный диаметр 160 нм), однако при диаметре 230 нм наночастица кристаллического кремния обладает МК оптическим резонансом. Моды более высокого порядка, появляющиеся в наночастицах большего размера, недостаточно улучшают характеристики оптического нагрева. Таким образом, можно сделать вывод, что для случая оптического нагрева наносферы монокристаллического кремния непрерывным HeNe 632,8 нм лазером наиболее оптимальным условием является возбуждение магнитной квадрупольной моды.

Применение оптического нагрева для систем доставки лекарств. Как уже упоминалось ранее, тесный «союз» между нанофотоникой и биомедициной привел к широкому спектру беспрецедентных применений оптических концепций в реальных приложениях. В последние десятилетия нанофотоника и биофотоника в основном ассоциировались с плазмонными структурами и наночастицами – как за их яркие свойства преобразования света в тепло [26], так и за высокую локализацию электромагнитного поля [27]. Однако в последние несколько лет все больше и больше био-приложений нанофотоники реализуются на основе диэлектрических материалов и оптических откликов полупроводниковых структур [28–30]. Подход к исполь-

зованию полупроводниковой нанофотоники для биомедицинских приложений в основном основан на возбуждении одиночных оптических мод типа Ми или их комбинаций и коллективных резонансов. Одним из возможных преимуществ диэлектрических структур для биомедицинских приложений является возможность измерения температуры с помощью комбинационного рассеяния света или сигнала фотолюминесценции. В этом разделе мы предлагаем использовать полупроводниковые наночастицы для оптически-индуцированного высвобождения лекарств в системах микроносителей для адресной доставки лекарств.

Применение α-Fe_2O_3 привело к прямому измерению температуры высвобождения лекарства из капсулы. Измерение с помощью рамановской термометрии показывает, что среднее значение температуры разрыва капсулы составляет примерно 170^o (Рис. 3 (c)). Стоит отметить, что на расстоянии 5 мкм от наночастицы температура снижается на порядок (в 10 раз).

В качестве доказательства концепции были продемонстрированы доставка и оптический разрыв полимерного носителя-капсулы и последующее высвобождение противоопухолевого лекарственного препарата винкристин (VCR) с помощью лазера ближнего ИК-диапазона с интенсивностью 4,0 $\times 10^4$ Вт/см^2, действующего в окне прозрачности биологических тканей, с помощью эффективного оптического нагрева и нанотермометрии наночастиц α-Fe_2O_3. Биологические тесты проводились на двух основных типах клеток: (i) клетки карциномы, как пример злокачественной опухоли, и (ii) стволовые клетки человека, как модель здоровых клеток (Рис. 3(e, f)).

Далее эта концепция была экспериментально доказана на клетках карциномы. Капсула, заполненная противоопухолевым лекарственным средством VCR, успешно высвободила лекарственное средство после лазерного облучения и последующего термического разрыва капсулы (Рис. 3(e, f)). Более того, интенсивность лазерного излучения была довольно умеренной, так что контрольные (стволовые) клетки не пострадали. Биологическая часть работы была проделана н.с. Михаилом Зюзиным и н.с. Александром Тиминым, и ее можно найти в [31].

В заключение главы, было показано, что отдельная полупроводнико-

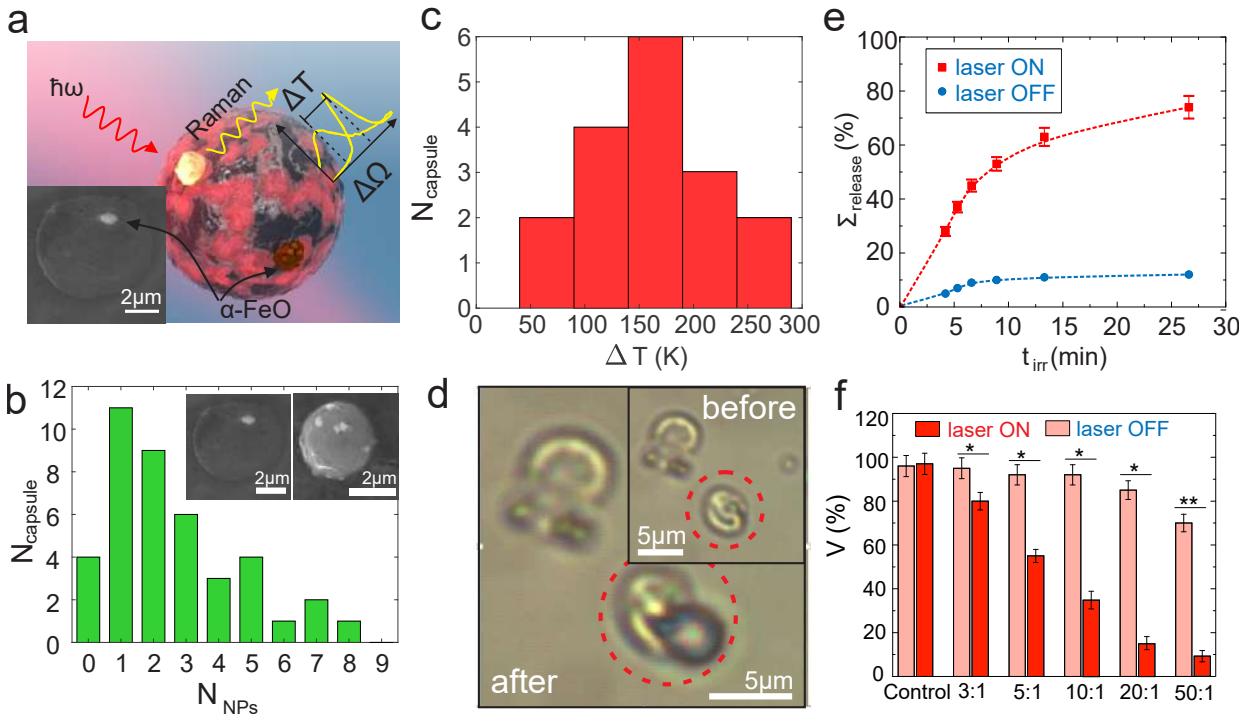

Рисунок 3 — **Полимерные носители лекарств со встроенными наночастицами α-Fe_2O_3.** (a) Схема концепции систем доставки лекарств на основе микрокапсул с наночастицами α-Fe_2O_3, встроенными в стенку для фототермической активации процесса высвобождения лекарства. (b) Гистограмма количества наночастиц α-Fe_2O_3, успешно захваченных в полимерной несущей стенке. Вставка: СЭМ изображения типичных изготовленных капсул. Масштабная шкала - 2 мкм. (c) Гистограмма наблюдаемого разрыва капсулы под действием лазерного излучения. Значения температуры были получены с помощью рамановской термометрии. (d) Светлопольные микроскопические изображения капсулы до и после лазерного облучения. (e) Высвобожденная концентрация винкристина (VCR) как функция времени с лазерным облучением (красный) и без (синий). (f) Жизнеспособность клеток карциномы (CC) после экспериментов по доставке с лазерно-индуцированной активацией высвобождения лекарства. Красные столбцы соответствуют CC, розовые столбцы соответствуют стволовым клеткам (контроль). Разные столбцы соответствуют разной исходной концентрации полимерных капсул. Взято из [31].

вая наночастица, поддерживающая резонансы Ми, может служить простой и универсальной наноплатформой (нагреватель-термометр), которая поддерживает эффективное преобразование света в тепловую энергию и широкий диапазон измерения температуры. В частности, такая наносистема продемонстрировала свою эффективность для биомедицинских приложе-

ний, требующих фототермического воздействия.

В третьей главе описывается реализация комбинационного рассеяния света для исследования и стимулирования фототермического фазового перехода в одиночных нанорезонаторах. Было показано, что одновременный оптический нагрев и нанотермометрия, реализованная за счет термочувствительного комбинационного рассеяния света от резонансных полупроводниковых наночастиц, могут применяться для ряда приложений нанофотоники, связанных с фототермическими процессами. В данной главе изучался процесс кристаллизации оптически резонансных нанодисков из аморфного кремниевой фазы, вызванный локальным оптическим нагревом. Фазовый переход наблюдался и контроль температуры проводился при помощи спектров комбинационного рассеяния света. Получено, что температура начала фазового перехода из аморфного в поликристаллическое состояние для одиночного кремниевого нанодиска составляет около 900°C. Далее, уже поликристаллический нанодиск продемонстрировал возможность к многократному обратимому оптическому нагреву в диапазоне температур 300÷1000 K.

Процесс фазового перехода из аморфной в кристаллическую фазу для кремниевого нанодиска показан на Рис. 4(a). Для обеспечения и контроля фазового перехода в одиночном нанодиске, сперва был получен спектр комбинационного рассеяния в так называемом «холодном» режиме, при интенсивности накачки 0,06 МВт/см^2 такой, что температура диска практически не изменялась. Затем этот диск подвергался более интенсивному облучению гелий-неоновым лазером (0,39 МВт/см^2), что индуцировало фазовый переход. При температурах около 600÷800 °C нанодиск начинал переходить из аморфной в поликристаллическую фазу, как видно из рисунка. Значения температуры кристаллизации совпадают с известными [33], а температура нагрева сопоставима с ранее достигнутыми при аналогичной мощности накачки, но для сферических наночастиц [21].

На Рис. 4(b) показана прямая температурная зависимость спектрального положения комбинационного рассеяния кристаллического кремния при различных температурах. Спектры комбинационного рассеяния по-

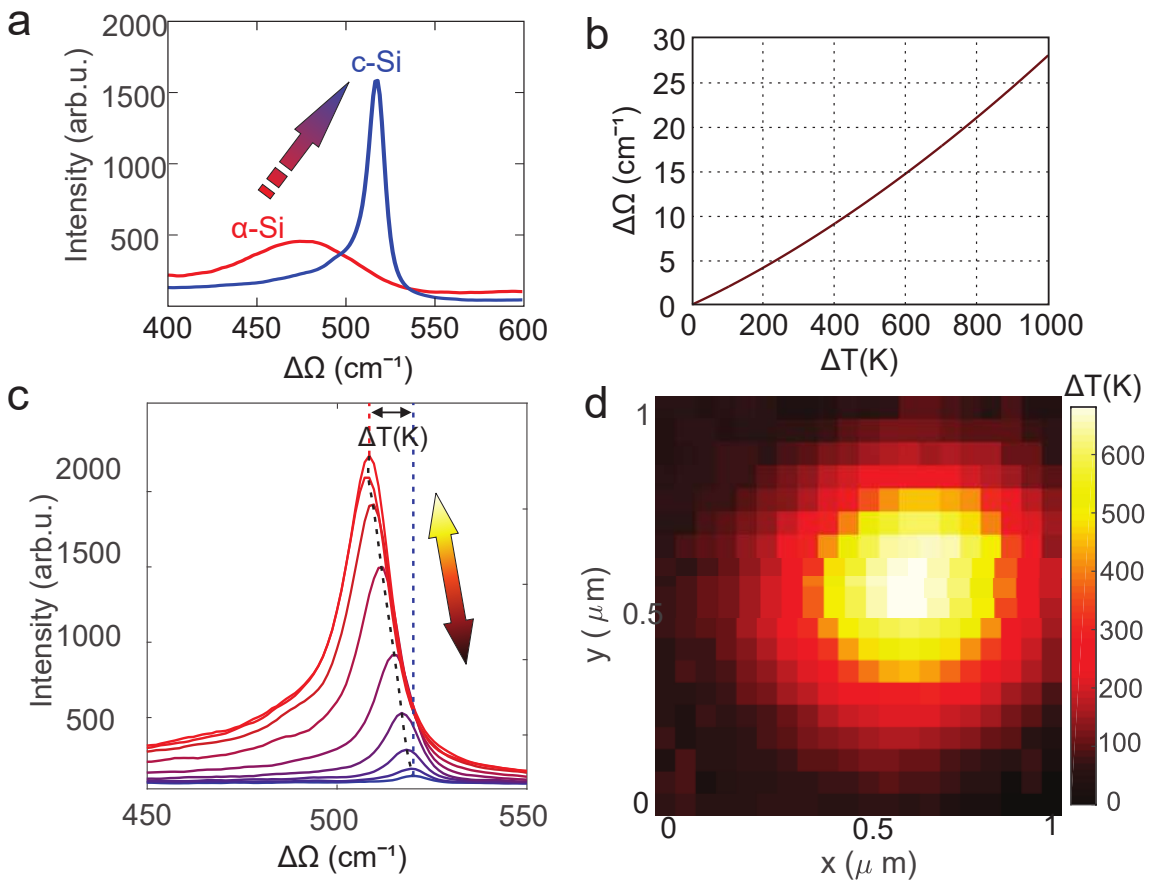

Рисунок 4 — **Фототермический отжиг кремниевого нанодиска.** (a) Спектры комбинационного рассеяния нанодиска до и после лазерного воздействия (b) Теоретическая зависиомсть спектрального сдвига фононной линии кристаллического кремния от температуры (см. уравнение 8). (c) Спектры комбинационного рассеяния одиночного поликристаллического нанодиска при различных значениях интенсивности накачки. (d) Пространственное распределение температуры оптического нагрева в зависимости от положения источника относительно одиночного нанодиска. Взято из [32].

сле отжига соответствуют поликристаллическому кремнию так как [33]: во-первых, обладают асимметрией относительно центрального спектрального положения, которая заметно проявляется при более высоких температурах нагрева диска; во-вторых, характерные спектральные ширины рамановских пиков на полу-высоте превышают 10 см$^{-1}$ даже при малых интенсивностях, в то время как для монокристаллического кремния эта величина не превышает 5 см$^{-1}$.

На Рис. 4(d) представлен пример двумерного картирования распределения оптического нагрева одиночного нанообъекта в зависимости от по-

ложения источника и области сбора.

Данный метод позволяет быстро и удаленно локально индуцировать фазовые переходы в аморфных полупроводниках при помощи оптического нагрева и контроля степени кристалличности и температуры за счет комбинационного рассеяния света. Такой подход особо полезен для генерации второй гармоники [10] и широкополосной фотолюминесценции [34].

В заключение, в этой главе было показано, что комбинационное рассеяние света может быть эффективным как для термометрии, так и для исследования степени кристалличности одиночной наночастицы. В качестве подтверждения концепции было показано, что метаповерхность, состоящая из отдельных кремниевых наностолбиков, может быть модифицирована путем эффективного оптического нагрева. Из-за температурной локализации в вершине наностолбика, которая доказана теоретически, плавление может происходить с большой пространственной точностью без модификации ближайших соседей.

В четвертой главе рассказывается о способности комбинационного рассеяния света представлять структуру распределения ближнего электромагнитного поля оптических состояний полупроводниковых наноструктур.

Под структурой распределения ближнего электромагнитного поля будет подразумеваться обнаружение общих особенностей оптических мод наноструктуры без каких-либо количественных оценок. Как уже было показано ранее, резонансные диэлектрические и полупроводниковые наноструктуры являются мощным инструментом для локализации ближнего поля снаружи и внутри нанорезонаторов, а также для усиления излучения из них. Недавно были предложены различные конструкции светоизлучающих наноантенн и метаповерхностей с перестраиваемыми диаграммами направленности в дальней зоне. Здесь демонстрируется переключение распределения ближнего поля в кремниевом олигомере путем изменения поляризации падающего света, которое детектируется за счет двумерного картирования распределения интенсивности комбинационного рассеяния света полупроводниковой наноструктуры. Кремниевые нанодиски в предлагаемых структурах поддерживают дипольные моды типа Ми, связанные по-разному в

зависимости от поляризации падающего излучения. Поскольку падающая поляризация позволяет контролировать связь между различными парами нанодисков, пространственное распределение комбинационного рассеяния света сильно зависит от фактора усиления локального поля. Предполагается, что такой подход откроет путь к упрощению как возбуждения, так и детектированию различных оптических состояний.

В настоящей работе предлагается метод оптического зондирования «горячих точек» распределения ближнего электромагнитного поля оптических состояний их дальней зоны, основанный на спектроскопии комбинационного рассеяния света. Ранее было показано, что комбинационное рассеяние света может быть использовано для обнаружения оптических состояний, как неизлучающих [35,36], так и "светлых"(излучающих) мод разного порядка [17,21]. Здесь показано теоретически и экспериментально, что киральные фотонные структуры [37,38], способные поддерживать топологические краевые состояния [39], могут быть исследованы с помощью линейного неупругого рассеяния на оптических фононах - комбинационного рассеяния света. Предполагается, что данный подход может быть в дальнейшем расширен на другие топологические тривиальные и нетривиальные структуры с использованием метода картирования комбинационного рассеяния света, который позволяет одновременно оптически нагревать и измерять температуру в реальном времени по спектральному сдвигу стоксовой компоненты комбинационного рассеяния света [22], таким образом, может иметь место термически нелинейное переключение оптического состояния [40].

Экспериментальное исследование предсказанной поляризационно-зависимой локализации интенсивности комбинационного рассеяния на зигзагообразной олигомерной цепи из 3 дисков показано на Рис. 5. Результаты расчета в поляризациях x и y такие же, как и в эксперименте на Рис. 5. Цветовая шкала подобрана так, чтобы оптическое переключение было нагляднее. Локализация рамановского отклика смещена либо в ту, либо в другую сторону, аналогично расчету и измеренному экспериментальному распределению ближнего поля с помощью сканирующей ближнепольной оптической микроскопии (СБОМ). Таким образом, впервые показано зондирование из

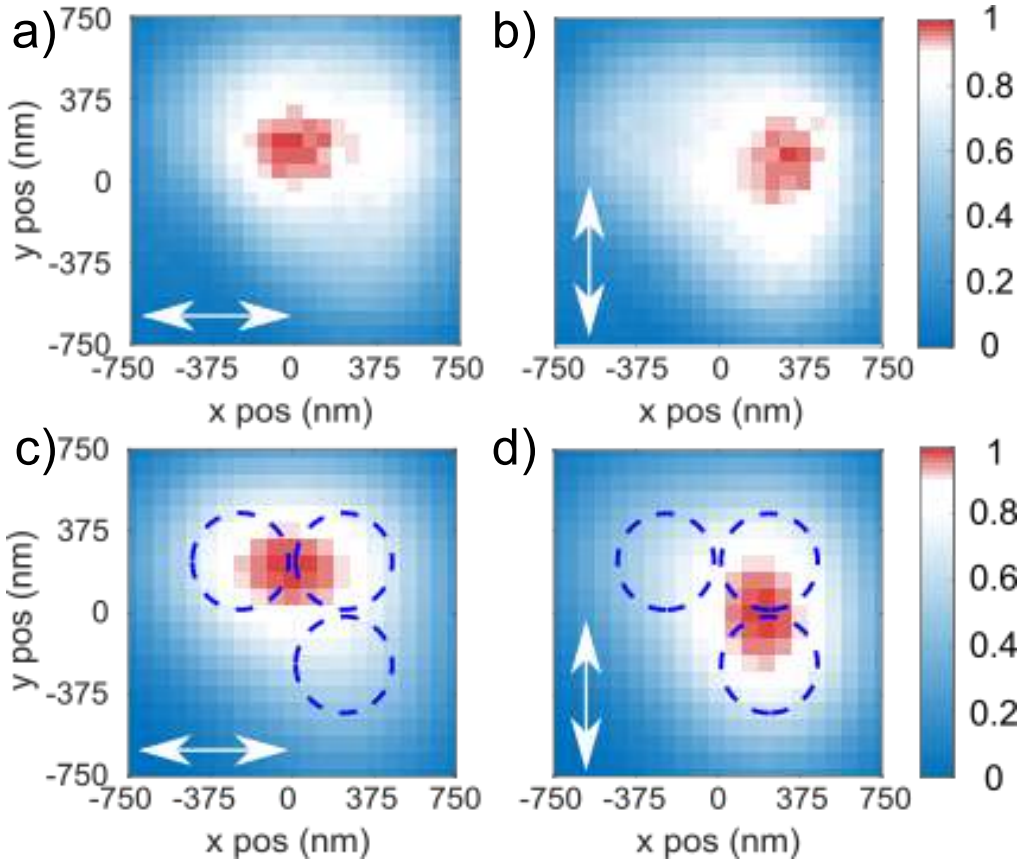

Рисунок 5 — **Вызванное поляризацией переключение «горячих точек» распределения ближнего поля, исследованного с помощью картирования комбинационным рассеянием.** (a, b) Экспериментальное и (c, d) теоретическое распределение комбинационного рассеяния света от олигомера для горизонтальной (a, c) и вертикальной (b, d) поляризаций вдоль поверхности образца. Пунктирная линия соответствует положению олигомера, состоящего из отдельных нанодисков.

дальней зоны распределения ближнего электромагнитного поля оптических состояний посредством комбинационного рассеяния света.

В заключение, в главе было показано, что комбинационное рассеяние света может служить инструментом зондирования оптических состояний резонансных наноструктур. Предлагаемый метод может предоставить информацию о плотности мощности света, поглощенной наноструктурой, а также дать качественную информацию о пространственном распределении ближнего электромагнитного поля в наноструктуре.

Пятая глава посвящается демонстрации впервые достигнутого на одиночном субмикронном наноцилиндре перехода от спонтанного комбинационного рассеяния света к режиму вынужденного излучения. Резонансные диэлектрические структуры появились недавно как новая платформа

для субволновой неплазмонной фотоники. Было высказано предположение и продемонстрировано, что магнитный и электрический резонансы Ми могут существенно усилить многие эффекты на наномасштабе, включая спонтанное комбинационное рассеяние света. Здесь демонстрируется вынужденное комбинационное рассеяние света (ВКР) для изолированных наночастиц кристаллического кремния (c-Si) и экспериментально наблюдается переход от спонтанного к вынужденному рассеянию, проявляющийся в нелинейном росте интенсивности сигнала выше определенного порога накачки. В резонансе Ми свет ограничивается малым объемом резонансной моды с усиленными электромагнитными полями внутри наночастицы c-Si из-за ее высокого показателя преломления, что приводит к общему сильному сигналу ВКР при низких интенсивностях накачки. Данное открытие позволяеь сделать шаг к разработке эффективных рамановских нанолазеров для многофункциональных фотонных метаустройств.

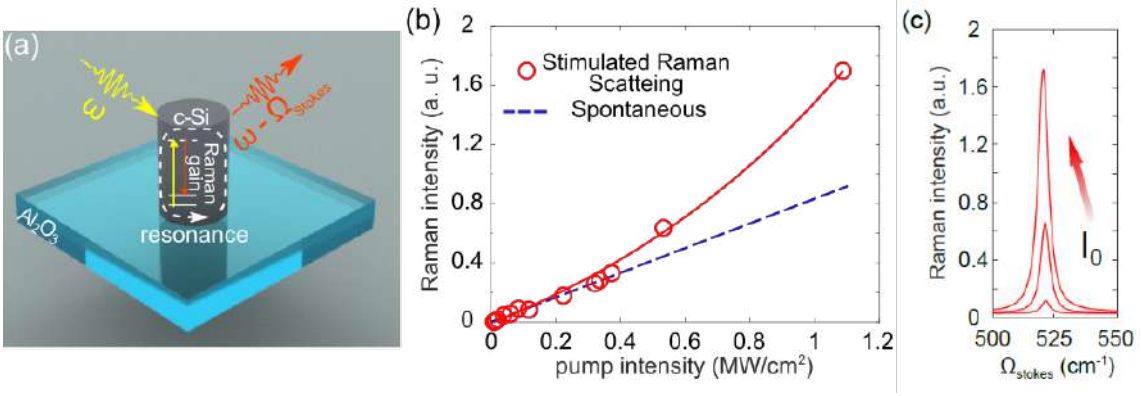

Рисунок 6 — **Экспериментальное вынужденное комбинационное рассеяние света на наночастицах c-Si.** (a) Схематическое изображение наночастицы кремния, возбуждаемой лазерным светом. (b) Экспериментальные интенсивности комбинационного рассеяния света при различных накачках для резонансной наночастицы 475 нм (красные кружки) и нерезонансной наночастицы 445 нм (синие квадраты). Красная линия соответствует экспоненциальной зависимости. (c) Экспериментальные спектры комбинационного рассеяния света. Стрелка показывает более высокое значение интенсивности от спектра к спектру. Взято из [41].

На Рис. 6(b) показаны типичные экспериментальные зависимости сигнала комбинационного рассеяния от интенсивности накачки. При низких интенсивностях доминирует спонтанное комбинационное рассеяние света,

которое характеризуется линейной зависимостью от падающей мощности, как было продемонстрировано ранее с наночастицами c-Si [17, 21]. Однако при более высоких интенсивностях (более 0,3 МВт/см^2) наблюдается нелинейный рост сигнала комбинационного рассеяния света для наноцилиндра диаметром 475 нм, который не наблюдается для других наноцилиндров диаметром 250÷800 нм, см. пунктирную синюю линию на Рис. 6 (b). Это резкое отличие характеризует режим переход к режиму ВКР.

В заключение, в этой главе сообщается о первом наблюдении вынужденного комбинационного рассеяния света на субволновой наночастице кристаллического кремния, достигнутого за счет возбуждения резонансов типа Ми. Выявлена важность критической оптимизации добротностей возбуждаемых оптических мод в наночастице и теплопроводности подложки для достижения сильного оптического отклика и предотвращения перегрева при более высоких интенсивностях накачки. Представленные результаты будут полезны для перспективных приложений резонансной диэлектрической нанофотоники для наноразмерной термометрии и биосенсинга, а также предполагается дальнейшее исследование вынужденного комбинационного рассеяния света в различных нанофотонных структурах [7, 11, 42].

Диссертация посвящена созданию и исследованию альтернативного к плазмонному подходу для эффективного оптического нагрева, термометрии и усиления комбинационного рассеяния света на основе диэлектрических и полупроводниковых резонансных наноструктур. Диссертация охватывает анализ различных форм и геометрий наноструктур. Был рассмотрен ряд устойчивых к оптическому нагреву и термометрии материалов, различные материалы для подложек и различные окружающие среды. Демонстрируется усиление интенсивности сигнала комбинационного рассеяния света от наноструктур за счет оптических резонансов, либо за счет перехода к режиму вынужденного излучения. Также исследуется возможность зондирования оптических состояний и распределения ближнего электромагнитного поля собственных мод наноструктур за счет комбинационного рассеяния света.

Выводы по основным результатам диссертации:

1. Показано, что сферические наночастицы из кристаллического крем-

ния диаметром от 100 до 400 нм, обладающие Ми-резонансами в видимой области спектра, способны поддерживать эффективный оптический нагрев на длине волны непрерывного HeNe лазера 632.8 нм.

2. Показано, что использование Ми-резонансных полупроводниковых наночастиц α-Fe_2O_3, поддерживающих оптический нагрев и нанотермометрию посредством комбинационного рассеяния света, в задаче адресной доставки лекарственных средств, способствует значительному понижению пороговой интенсивности накачки для фотоиндуцированного разрушения полимерного носителя лекарственного препарата и последующего вызволения противоопухолевого средства внутрь клетки карциномы. Наночастицы α-Fe_2O_3 использовались в качестве мишени для лазерного возбуждения в ближнем ИК-диапазоне для эффективного преобразования света в тепло в стенках полимерных носителей лекарств и в качестве прямого оптического датчика температуры за счет термочувствительного Рамановского рассеяния. В качестве доказательства применения данной концепции была продемонстрирована *in vitro* успешная доставка и оптически-индуцированный разрыв полимерного носителя посредством лазерного нагрева наночастиц α-Fe_2O_3 с последующим высвобождением противоопухолевого лекарственного средства винкристина. Предложенная система работала при умеренном значении лазерной интенсивности 4.0×10^4 Вт·см$^{-2}$.
3. Показано, что одиночные нанодиски из аморфного гидрогенизированного кремния с диаметрами от 300 до 450 нм, выращенные литографическими методами на стеклянной подложке, могут претерпевать фотоиндуцированные фазовые переходу в поликристаллическую фазу за счет эффективного оптического нагрева. В то же время, такой фазовый переход детектируется посредством комбинационного рассеяния света, а форма наночастицы при контролируемом нагреве и фазовом переходе не изменяется, что подтверждено СЭМ изображениями до и после отжига.
4. Показано, что двумерное картирование распределения интенсивности комбинационного рассеяния света от асимметричного олигомера, со-

стоящего из трех одинаковых кремниевых нанодисков, позволяет получать структуру распределения «горячих точек» ближнего электромагнитного поля оптических мод таких наноструктур. А изменение линейной поляризации накачки на 90 градусов, приводит к оптическому переключению распределения ближнего поля моды, которое также детектируется в дальнем зоне посредством комбинационного рассеяния света.

5. Показано, что одиночный кремниевый наноцилиндр высотой 600 нм и диаметров 475 нм, расположенный на сапфировой подложке, поддерживает переход от режима спонтанного комбинационного рассеяния света к режиму вынужденного излучения при непрерывной накачке HeNe лазером на длине волны 632.8 нм и интенсивностью накачки $I_0 = 0.4$ МВт/см^2 за счет оптимизированных добротностей собственных мод, возбуждаемых на длине волны накачки и излучения стоксовой компоненты, а также за счет увеличенного теплоотвода в подложку за счет выбора материала с высокой теплопроводностью.

Основные публикации по теме диссертации:

[A1] **Zograf G. P.**, Petrov M. I., Zuev D. A., Dmitriev P. A., Milichko V. A., Makarov S. V., Belov P. A. Resonant nonplasmonic nanoparticles for efficient temperature-feedback optical heating //Nano Letters. – 2017. – Т. 17. – №. 5. – С. 2945-2952.

[A2] **Zograf G. P.**, Timin A. S., Muslimov A. R., Shishkin I. I., Nominé A., Ghanbaja J., Ghosh P., Li Q., Zyuzin M. V., Makarov S. V. All-Optical Nanoscale Heating and Thermometry with Resonant Dielectric Nanoparticles for Controllable Drug Release in Living Cells //Laser & Photonics Reviews. – 2020. – Т. 14. – №. 3. – С. 1900082.

[A3] Milichko V. A., Zuev D. A., Baranov D. G., **Zograf G. P.**, Volodina K., Krasilin A. A., Mukhin I. S., Dmitriev P. A., Vinogradov V. V., Makarov S. V., Belov P. A. Metal-dielectric nanocavity for real-time tracing molecular events with temperature feedback //Laser & Photonics Reviews. – 2018. – Т. 12. – №. 1. – С. 1700227.

[A4] **Zograf G. P.**, Yu Y. F., Baryshnikova K. V., Kuznetsov A. I., Makarov

S. V. Local crystallization of a resonant amorphous silicon nanoparticle for the implementation of optical nanothermometry //JETP Letters. – 2018. – Т. 107. – №. 11. – С. 699-704.

[A5] Aouassa M., Mitsai E., Syubaev S., Pavlov D., Zhizhchenko A., Jadli I., Hassayoun L., **Zograf G.**, Makarov S., Kuchmizhak, A . Temperature-feedback direct laser reshaping of silicon nanostructures //Applied Physics Letters. – 2017. – Т. 111. – №. 24. – С. 243103.

[A6] Baryshnikova K. V., Frizyuk K. S., **Zograf G. P**, Makarov S. V., Baranov M. A., Zuev D. A., Milichko V. A., Mukhin I.S., Petrov M. I., Evlyukhin A. B. Revealing low-radiative modes of nanoresonators with internal raman scattering //JETP Letters. – 2019. – Т. 110. – №. 1. – С. 25-30.

[A7] **Zograf G. P.** et al. Stimulated Raman Scattering from Mie-Resonant Subwavelength Nanoparticles //Nano Letters. – 2020. – Т. 20. – №. 8. – С. 5786-5791.

[A8] **Zograf G. P.**, Petrov M. I., Makarov S. V. Coating of Au nanoparticle by Si shell for enhanced local heating //JPhCS. – 2017. – Т. 929. – №. 1. – С. 012072.

[A9] **Zograf G. P.** et al. Gap size impact on metal-dielectric nanocavity heater properties //AIP Conference Proceedings. – AIP Publishing LLC, 2017. – Т. 1874. – №. 1. – С. 030043.

[A10] **Zograf G.**, Makarov S., Petrov M. Doping of resonant silicon nanodisks for efficient optical heating in the near-infrared range //JPhCS. – 2020. – Т. 1461. – №. 1. – С. 012201.

Благодарности. В заключение хочу выразить огромную искреннюю благодарность моему научному руководителю С.В. Макарову за поддержку и помощь в моих исследованиях, за обсуждение результатов, научное руководство и наставничество. Отдельно хочу отметить труд И.С. Мухина, Ф.Е. Комиссаренко, В. Руцкой и А. Кузнецова по созданию экспериментальных образцов. М.И. Петровf и Ю.С. Кившаря благодарю за уникальную возможность участвовать в реализации их многочисленных идей и за источник мотивации. П.А. Дмитриева, А.К. Самусева, А.А. Богдано-

ва, М.И. Петрова благодарю за приглашение в магистратуру Университета ИТМО еще в далеком 2015 году. Хочется отдельно выразить благодарность П.А. Белову, И.В. Мельчаковой и всему коллективу физико-технического факультета Университета ИТМО за теплые 5 лет работы. Также хочу отдельно поблагодарить «Физико-техническую школу» им. Ж. И. Алфёрова, Санкт-Петербургский Политехнический Университет Петра Великого, ФТИ им. Иоффе и моего первого научного руководителя – В.И.Николаева за знакомство с наукой и за влияние на мои первые научные шаги. Наконец, я благодарю авторов шаблона *RussianPhd-LaTeX-Dissertation-Template* за их помощь в завершении диссертации, а также моих друзей и семью за их терпение и поддержку.

Fin.

Synopsis

THESIS OVERVIEW

Background and motivation. The possibility for remote and non-invasive study of inherent properties of the objects and structures at micro- and nanoscale has been of great interest for researchers in the last half-century. The idea of creating sensors that would give precise and comprehensive information on the objects they were attached to was a guiding star for many years.

One of the possible solutions was proposed in 1973 by Martin Fleischmann, Patrick J. Hendra, and A. James McQuillan, when the authors observed a sufficient increase of the Raman scattering signal by placing pyridine on a roughened silver substrate - this effect was later named SERS (surface-enhanced Raman scattering) [1]. Initially, Raman scattering is a very weak optical effect occurring in semiconductors or molecules due to inelastic scattering either on lattice vibrations or chemical bonds vibrations, providing a footprint spectrum for any given molecule or composition, but it could be increased by a several orders of magnitude due to electromagnetic near-field enhancement [2, 3] allowing for detection of traces of single molecules. Thus, the plasmonic nanoparticles for SERS sensing attracted great interest [4]. The goal of sensing applications lied not only in finding presence of any substance, but also in detecting thermal data. The temperature measurement at the nanoscale and the ability of local manipulation of the temperature with a simultaneous possibility of distinguishing the compositions by means of Raman scattering was a fruitful topic for the research [5].

Recently, it was demonstrated that single plasmonic nanoparticles can support nanothermometry, efficient optical heating, and serve as a SERS sensor at once [6]. However, the Prof. Michel Orrit group faced a major drawback due to the very long acquisition time of the signal, several minutes, therefore limiting plasmonic nanorod applicability. Another limiting factor for plasmonic nanostructures as a thermal sensor is the lack of inherent Raman signal,

which requires additional fabrication or manipulations for acquiring the data.

On the other hand, in recent years dielectric nanophotonics gained high interest due to the ability of concentrating light inside nanoscale resonators by means of Mie resonances or other high-quality factor states, in contrast with plasmonic nanoantennas, allowing creation of subwavelength nanolasers [7, 8], empowered nonlinear light generation [9–11], enhanced photoluminescence [12, 13], near-field hot-spots [14, 15], and many other applications [16]. Due to the excitation of different optical resonant modes inside semiconductor nanostructures upon laser irradiation, considerable field enhancement can be observed. Moreover, these structures turn out to be highly efficient for optical heating and thermometry at moderate intensities. Based on the inherent Raman scattering of semiconductor and dielectric nanostructures, whose intensity can be drastically improved by matching resonant conditions [17, 18], one can achieve efficient optical heating, nanothermometry, and near-field enhancement, allowing the detection of molecular events at the nanoscale.

The thesis is devoted to the creation and the study the sensing platform alternative to plasmonics for efficient optical heating, thermometry and enhancement of the Raman scattering based on all-dielectric and semiconductor resonant nanostructures. The thesis covers the analysis of different shapes and geometries of nanostructures, a number of materials robust to optical heating and thermometry, different substrate materials and various surrounding media, the enhancement of the Raman scattering from the nanoparticles improved either by resonant conditions or by means of stimulated emission, the optical states probing and near-field distributions study.

The main goals of this work are

- Development of the approach for simultaneous optical heating and thermometry based on resonantly enhanced Raman scattering from dielectric and semiconductor nanostructures.
- Demonstration of the optically induced amorphous to polycrystalline phase transition in semiconductor nanostructures with the possibility for *in situ* phase state detection via Raman scattering.

- Probing the optical states of the semiconductor nanostructures by means of resonantly enhanced Raman scattering from the far-field region.
- Demonstration and realization of the transition from spontaneous to stimulated Raman scattering regimes from isolated single nanoparticle empowered by Mie resonances.

The scientific statements presented for the defence:

- Resonant optical excitation of Mie modes in a semiconductor nanoparticle with balanced radiation and non-radiation losses provides the most effective optical heating in comparison with other loss ratios for the given optical mode.
- Optical heating by a continuous wave laser source of a semiconductor Mie resonant nanostructure induces a phase transition from an amorphous to a polycrystalline state and enables *in situ* tracing of such a transition by means of Raman scattering.
- Two-dimensional Raman scattering intensity mapping of a resonant semiconductor nanostructure allows the probing of the excited optical modes in it from the electromagnetic far-field region and provides the near field "hot-spots" spatial distribution pattern of the eigenmode at the pump wavelength.
- The transition from spontaneous Raman scattering to stimulated scattering regime occurs upon excitation of high-Q optical resonant modes, both at the pump wavelength and at the Stokes Raman scattering wavelength, with optimized mode coupling efficiencies and their spatial overlapping at the pump the radiation wavelengths in a single crystalline silicon nanocylinder with optimized heat sink to the substrate.

Key novelty of this work includes but is not limited by the following points:

1. The first experimental demonstration of simultaneous continuous wave HeNe (632.8 nm) laser-induced optical heating and nanoscale thermometry by resonant Raman-active semiconductor nanostructures.

2. The first demonstration of the Mie resonant semiconductor nanoparticle optical heating and nanothermometry via Raman scattering for drug delivery applications. The α-Fe_2O_3 nanoparticles were used as the target for near-IR laser excitation for efficient conversion of light to heat in the walls of polymer drug agents and as the direct optical temperature probe via thermally-sensitive Raman scattering. As the proof of concept, the successful *in vitro* delivery and remote optically-induced thermal rupture of the polymer carrier was shown by means of laser heating of the target α-Fe_2O_3 nanoparticles with subsequent release of the antitumour drug agent vincristine. The proposed system worked at the moderate laser intensity value as low as 4.0×10^4 W cm^{-2}.
3. The first demonstration of *in situ* local controllable optically-induced phase transition from amorphous to polycrystalline state of silicon nanodisks on a glass substrate with temperature and phase optical feedback via Raman scattering.
4. The first demonstration of the qualitative probing of electromagnetic near-field hot spots distribution of optical modes in resonant semiconductor nanostructures by means of two-dimensional Raman scattering intensity spatial and spectral mapping.
5. The first experimental observation of the transition from spontaneous to stimulated Raman scattering regime from isolated single crystalline silicon nanocylinder.

Scientific and practical importance of the work lies in the fact is that the author proposed a novel approach for optical heating and thermometry with nanoscale spatial resolution by means of single Raman-active resonant semiconductor nanoparticle. The proposed platform on 'all-in-one' nanoparticle that serves both as a temperature probe and a nanoheater does not require any additional functionalizations or fabrication steps, it uses single excitation source both for enhanced optical heating and Raman scattering, it is robust and supports repeated cycles of usage. Such approach demonstrated its applicability in advanced bio-medical application, for drug delivery systems for cancer treatment with remote all-optical thermal release trigger.

Such a thermometry approach based on the spectral shift of the Raman scattering signal of nanostrucutres upon intense laser irradiation with subsequent optical heating found a very promising application for *in situ* crystalline-state modification of the nanostructures. The Raman scattering serves both as a thermal probe and a crystallinity state probe, thus, the sufficient optical heating of an amorphous silicon nanodisk on a glass substrate can result in phase transition from amorphous to polycrystalline state. The fabrication of crystalline nanostructures on glass SiO_2 remains quite challenging, therefore, the approach of steady precise optical heating of amorphous silicon nanodisks on a glass substrate with *in situ* probe of the temperature and the crystal state can solve the fabricational difficulty for some cases and applications.

As it was mentioned above, the Raman scattering is an efficient probing approach for temperature measurements and crystal-state evaluation, but the intensity of the Raman scattering can also serve as a probe for the electromagnetic power density stored in the nanostructures. The spatial mapping of the Raman scattering intensity of a zig-zag oligomer consisting of three nanodisks of the same size show the switching of the 'hot-spot' distribution upon changing the polarization of the incident excitation. The essential benefit of this approach is that it does not require any tip-assisted techniques, uses only a single laser for the excitation of Raman scattering and detects the signal in the far-field domain. Such fast and proper quality information on the electromagnetic 'hot-spots' distribution along the nanostructure surface might be useful for rapid analysis of the nanostructure's optical states or can serve as a platform for selective excitation of the biological or polymers in the gaps of the zig-zag oligomer.

Finally, the Raman scattering is a rather weak process, but it can be significantly improved by matching resonant conditions. Moreover, the Raman scattering intensity can be additionally increased by the transition from spontaneous to stimulated Raman scattering regime. Such transition observed in sub-micron (in all three dimensions), subwavelength nanodisk can pave the way for highly effective Raman-based nanosensors.

Reliability and validity of the obtained results is ensured by modern research methods and on the reproducibility of the measurement results, and is also confirmed by the good agreement between the experimental data, the numerical modeling and analytical results.

Implementation of the obtained results. The author of the thesis owns the patent of the Russian Federation registry №.177658 for the utility model "nonlinear dielectric nanoantenna", registered on 05.03.2018, the concept of which is based on the principles and results obtained within the framework of the thesis. Moreover, the concept of the semiconductor–based optical heating and thermometry demonstrated its applicability for real drug delivery systems.

Approbation. The main results of the work were presented and discussed at Russian and International conferences, such as: Ioffe Institute Winter School on semiconductor physics 2016, Zelenogorsk, Russia (poster); International School and Conference 'Saint-Petersburg Open 2016, 2017, 2019', Saint-Petersburg, Russia (poster); International conference 'Days on Diffraction' 2016 (poster), 2017 (oral), 2018 (oral), Saint-Petersburg, Russia; METANANO International Conference 2016, Anapa, Russia (poster); Russian congress "Science of the future – science of the young" 2016, Kazan, Russia (poster); METANANO International conference 2017, Vladivostok, Russia (oral); International conference NANOP 2017, Barcelona, Spain (oral); METANANO International Conference 2018, Sochi, Russia (oral); International summer school 'Nicolas Cabrera' on 'advanced light manipulation at nanoscale' 2018, Miraflores de la Sierra, Madrid, Spain (poster); International conference ICMAT 2019, Singapore (poster); METANANO International conference 2019, Saint-Petersburg, Russia (oral); METANANO International conference 2020 (online, oral); OSA Advanced Photonics Congress 2020 (online, oral); as well as at the scientific seminars at ITMO University, North Ossetian State University, Zhejiang University, Queensland University of Technology.

Publications. The main results of the thesis are described in 10 scientific pa-

pers included in the list of the Higher Attestation Commission of the Russian Federation, including 7 articles in scientific journals indexed by the scientific databases Scopus and Web of Science, and 3 peer-reviewed conference proceedings indexed by the scientific databases Scopus and Web of Science.

Author contribution. The contribution of the author consists of measurements and processing of experimental results (dark-field scattering spectra, Raman scattering spectra), an essential part of the numerical simulation of optical properties of the investigated nanostructures, the implementation of a numerical model of the optical heating of a semiconductor nanostructure, participation in the formulation of research objectives, and the writing of scientific papers.

The structure and scope of the thesis. The thesis consists of an introduction, five chapters, conclusion, and a list of references. The total volume of the thesis is 112 pages, including bibliography with 158 references. The work contains 36 figures and 1 table, placed inside the chapters.

MAIN CONTENTS OF THE WORK

First chapter presents a brief overview of the proposed and used in the research experimental and theoretical approaches; describes the necessity of every particular method and describes their applicability for different cases; proves the relevance of the method for the conducted research.

Second chapter of the thesis discusses the optimal conditions for the optical heating of the resonant spherical semiconductor nanoparticles.

The optimization of Mie resonances with material parameters can result in highly laser heating of all-dielectric nanoparticles.

The basic principle of light heating and absorption for a single spherical nanoparticle in homogeneous surrounding environment was developed and tested before [19, 20].

All-dielectric nanoparticles can support strong resonant responses in the visible range, therefore, their light absorption can vary dramatically. In

this regard, the analytical solution for the continuous-wave laser heating of a single spherical NP can take into account the resonant nature of the NP. As a result, the exact solution for the temperature increase of the spherical NP with diameter D in a steady-state heat diffusion equation, infinite external boundary conditions and a pre-defined plane-wave source with incident intensity (I), the NP absorption cross-section (C_{abs}) defined by Mie theory, the known thermal conductivity of the surrounding medium κ_2, in case the thermal conductivity of the NP is much greater than that of the environment, can be found as follows:

$$\delta T_{NP} = \frac{IC_{abs}}{2\pi\kappa_2 D}. \tag{5}$$

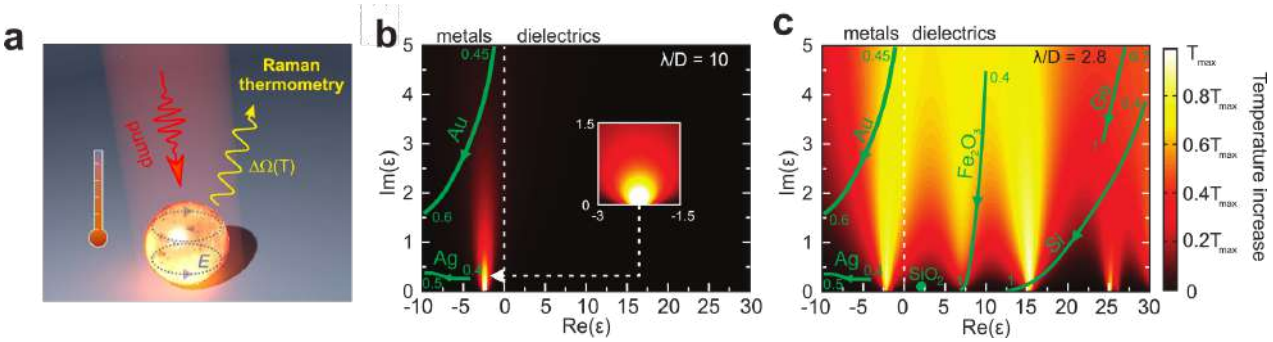

Figure 1 — **Optical heating of spherical NPs.** (a) Schematic of the optical heating and thermometry concept. Calculation results for theoretical optical heating in homogeneous aerial environment for single spherical NPs with fixed wavelength/diameter ratios λ/D as a function of various real and imaginary parts of the permittivity: (b) $\lambda/D = 10$; (c) $\lambda/D = 2.8$. The green arrowed lines in b) and c) correspond to values of Re(ε) and Im(ε) for specific real material dispersions. The direction of the arrows corresponds to increase of the wavelength. The numbers indicate the wavelength region in microns. Adopted from [21].

The results of the optical heating calculations can be found in the colormaps depicted in Fig. 1(b,c). The optical heating temperature for spherical nanoparticle in aerial media of different real (from -10 to 30) and imaginary (from 0 to 5) parts of permittivity in case of small nanospheres (wavelength/diameter ration = 10) are shown in Fig. 1(b), and the same calculations, but for the larger NPs, where the wavelength-to-diameter ratio is 2.8, are shown in Fig. 1(c). While the size of the NP is still too small to support Mie resonances, only nanospheres with negative real part of permittivity (metals)

support optical heating, which one can clearly see from Fig. 1(b). However, upon increasing the diameter of the NPs until wavelength-to-diameter ratios reaches $\lambda/D = 2.8$ (Fig. 1(c)), the hot sopts appear in the region of positive real part of the permittivity, which correspond to the dielectric and semiconductor materials. This happens due to excitation of different Mie modes in the nanosphere. What is more fascinating about this results is that the increase of the imaginary part of the permittivity does not necessarily lead to the total increase of the optical heating temperature.

For deeper understanding of the underlying physics and the explanation of the origin for efficient optical heating of materials that are considered to be lossless, i.e. all-dielectrics and semiconductors, upon resonant laser excitation of Mie modes, one should start the consideration from the classical general expression for the absorbed electromagnetic power P:

$$P = \frac{1}{2}\mathrm{Re}\int_V \mathbf{J}^*(\mathbf{r})\mathbf{E}(\mathbf{r})dV \tag{6}$$

where $\mathbf{J}(\mathbf{r})$ stands for the current density, $\mathbf{E}(\mathbf{r})$ is the electric field inside the object, and the integration is performed over the volume of the considered nanoobject V. The expression in Eq. 6 gives understanding that the higher electromagnetic field inside the nanoobject and higher the current density is, the greater the total absorbed power is. Moreover, one should keep in the mind that $\mathbf{J} = \sigma\mathbf{E}$ and $\sigma = \varepsilon_0\omega\mathrm{Im}(\varepsilon)$, where ε_0 is the vacuum permittivity, ω is the incident light frequency and σ is the electric conductivity.

The integration of Eq. 6 over an arbitrary NP volume supporting Mie modes allows to modify the Eq. 6 in terms of an effective mode volume V_{eff} and spatially-averaged field enhancement factor $F = < |E|^2 > /|E_0|^2$, which gives information on the amount of energy that can be stored inside the NP and where $|E_0|$ is the incident electric field magnitude. Therefore, one can modify Eq. 6 for the total absorbed power as follows:

$$P \sim \sigma F^2 \, V_{\mathrm{eff}}. \tag{7}$$

The total absorbed power now has 3 different independent contribution factors σ, F^2 and V_{eff}, which all have significant influence on total optical

heating temperature δT_{NP}. The following subsections will consider all the factors separately.

The nonradiative losses factor. As it was shown by the expression in the Eq. (7), the increased Ohmic losses do not necessary raise the total absorption of light by the NP, the same goes for the total optical heating. If we consider the increase of the imaginary part of the permittivity, that would necessary lead to increase of the electric conductivity; however it would also significantly affect the resonance quality factor Q by reducing it, therefore lowering the σF^2 factor. Thereby it should be examined in more details.

The optical resonances can be described by the 'toy model' of the oscillator with friction, with some assumptions. Therefore, near the optical resonance frequency ω_0, the field enhancement factor F can be expressed as $F \sim 1/\left(\omega_0^2 - \omega^2 - i\omega\gamma\right)$, where γ stands the total optical losses of the system. If one looks more closely, the total optical losses have two general contributions: $\gamma = \gamma_{\text{rad}} + \gamma_{\text{ohmic}}$, *radiative* and *nonradiative* (or *Ohmic*) losses. The nonradiative part is proportional to $\text{Im}(\varepsilon)$, thus σF^2 factor at the resonant frequency ω_0 is proportional to $\sim \gamma_{\text{Ohmic}}/(\gamma_{\text{Ohmic}} + \gamma_{\text{rad}})^2$, thereby, one can see that very high Ohmic losses lead the total absorbed power to zero.

The direct and pretty simple assumptions lead to following: at the certain value of γ_{rad}, the maximum value that the factor $(\sigma F^2)_{\max}$ can reach $\sim 1/(4\gamma_{\text{rad}})$. The maximum value is achieved when the $\gamma_{\text{Ohmic}} \approx \gamma_{\text{rad}}$. Radiation losses γ_{rad} can be minimized by taking a resonant nanoparticle whose size is much smaller than the wavelength λ. This can be obtained in case of plasmonic NP supporting localized surface plasmon resonance (LSPR) with a given plasma frequency ω_p, where $\gamma_{\text{rad}} \ll \gamma_{\text{Ohmic}}$. At the LSPR, the γ_{rad} is equal to $\approx \omega_0^3/\omega_p^2(\pi D/\lambda)^3$. This analysis leads to the fact that γ_{rad} is relatively small compared to ω_0 due to the ratio $(D/\lambda)^3$.

Indeed, these predictions and estimation are proven analytically and can be seen in Fig. 1(b), where in case of relatively small NPs ($\lambda/D = 10$) the resonance occurs only in the region of negative real part of the permittivity $\text{Re}(\varepsilon)$, and highest temperature value is achieved at relatively small values of imaginary part of the permittivity $\text{Im}(\varepsilon)$, where $\gamma_{\text{Ohmic}} \approx \gamma_{\text{rad}}$.

The opposite scenario appears for bigger NPs, which can be seen in the Fig. 1(c). The presence of the hot spots for optical heating in positive range of real part of the permittivity means that semiconductor NPs can be optically heated very efficiently. For example, radiation losses γ_{rad} for dipole modes is rather high, and highest temperature is achieved at bigger Ohmic losses. On the other hand, if one considers higher-order resonances, e.g. MQ, one should expect smaller γ_{rad}, and, therefore, the optimal laser heating would appear lower values of γ_{Ohmic}. The latter one can bee seen for higher $\text{Re}(\varepsilon)$ in Figs. 1(b,c).

Effective mode volume factor. Another factor that contributes greatly to the total absorption of light by the NP and, therefore, contributes to the heating, is the effective resonant optical mode volume inside the nanoresonator V_{eff}. In the general case, the larger the nanoparticle size is - the greater the optical heating. However, one should note that V_{eff} can significantly vary such an assumption. If one considers a plasmonic nanoparticle, where the real part of the permittivity is negative ($\text{Re}(\varepsilon)<0$), the skin-layer depth starts to govern the effective mode volume. Namely, the typical skin depth, i.e. the distance where the light propagates inside the material with decrease in field magnitude by e times, for plasmonic materials is hardly greater than $\delta \approx 20$ nm in the visible range. Therefore, the V_{eff} for plasmonic nanoparticle is defined by the skin depth as follows: $V_{\text{eff}} \approx \pi D^2 \delta$. In contrast to the plasmonic materials and NPs, the dielectric and semiconductor ones are mostly transparent to the light in the visible range, therefore the effective mode volume is ususally of the order of the physical volume of the NP. To be more precise, for Mie type resonance, the effective mode volumes can be defined as $V_{\text{eff}} \approx \pi D^3/6$.

The straightforward conclusion that comes from the effective mode analysis is that for dielectric and semiconductor nanoresonators, the increase of the size of the nanoresonator increases the optical heating temperature. The same approach for the plasmonic ones is much less effective.

The general conclusion for such an analysis of optical heating of semiconductor and all-dielectric nanostructures can be described as follows: the efficient optical heating in resonant semiconductor and all-dielectric nanopar-

ticles can be achieved when the balance of the losses is obeyed, i.e. radiative and Ohmic losses are equal. Since the inherent Ohmic losses in all-dielectric materials are low, one should consider bigger particles that support high-order, high-Q, narrow optical modes that also possess low radiative loss channel. In contrast, the plasmonic ones are showing the best performance when the sizes of the NPs are rather small [19].

Optical heating with temperature feedback. The major advantage of the crystalline semiconductors over the plasmonic materials is the presence of the Raman scattering, which can be efficiently used as a thermal probe. Moreover, resonant crystalline NPs supporting Mie modes can dramatically increase the Raman scattering intensity by two orders of magnitude [17], which subsequently can provide direct Raman-shift based thermometry. Indeed, the optical heating of a single nanoresonator can be seen from the Raman scattering spectra as a spectral blue-shift upon higher temperatures, as shown in Fig. 2(a). Moreover, it was well studied both theoretically and experimentally by M. Balaknski *et al.* [22] that due to anharmonic effects in lattice vibrations, spectral line position of Raman scattering is known to be thermally sensitive. Indeed, the frequency of optical phonon line responsible for Raman scattering (Ω) is governed by the temperature as follows:

$$\Omega(T) = \Omega_0 + A\left(1 + \frac{2}{e^x - 1}\right) + B\left(1 + \frac{3}{e^y - 1} + \frac{3}{(e^y - 1)^2}\right), \qquad (8)$$

where Ω_0 = 528 cm^{-1}, A = -2.96 cm^{-1}, B = -0.174 cm^{-1}, $x = \hbar\Omega_0/2kT, y = \hbar\Omega_0/3kT$ for crystalline silicon [22].

The straightforward correspondence between the Raman scattering spectral position and the temperature provides great opportunity for Raman nanothermometry [23].

Fig. 2(a) depicts the spectral shift of the Raman spectra upon increased incident laser intensity. One can determine from the Eq. 8 that the spectral blue-shift from ambient conditions to 509 cm^{-1} corresponds to the optical heating by $\Delta T \approx 600$ K. Moreover, the method based on Raman nanothermometry and optical heating allows for precise sub-μm resolution 2D mapping of the temperature distribution of the nanoobjects by means of fine positioning

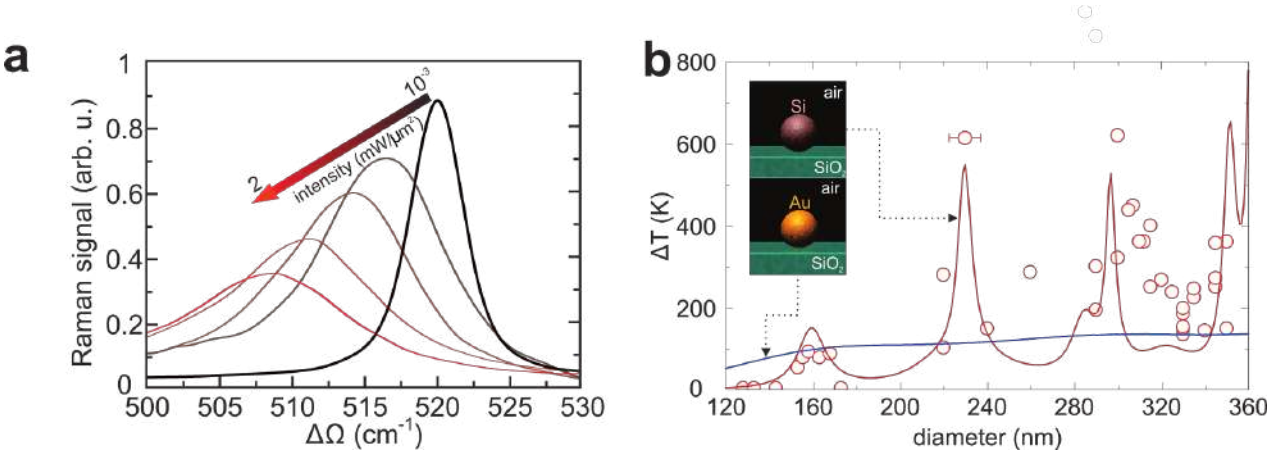

Figure 2 — **Laser heating and Raman thermometry of c-Si NPs.** a) Experimental Raman scattering spectra for a 350 nm diameter spherical c-Si NP on a glass substrate. b) Experimental (red circles) and numerically calculated (red solid lines) optical heating of spherical c-Si NPs. Blue lines corresponds to spherical gold NPs optical heating. The considered wavelength $\lambda = 633$ nm and light intensity $I_0 = 2$ mW/μm^2. Adopted from [21].

with piezo-stage. It is worth noticing, that during the experimental studies, no irreversible changes of phase, shape or size of the NPs were oberved.

The method described in this section, based on thermally sensitive Raman scattering, allows one to examine the temperature of the NP made of various semiconductor materials, under arbitrary laser excitation, for various values of other properties, and, what's more important, in a very broad temperature range of up to 1000 K, as shown in Fig. 2(b). The optical heating and Raman nanothermometry are in great agreement with the theoretical calculations and the results are reproducable. It should be notec, that the experimental data was well described without taking into account thermo-optical nonlinear effects in the nanoresonator materials, which actually might sufficiently change the refractive index, thermal conductivity of the heated materials and, therefore, the optical resonances and optical heating performance [24].

It was shown theoretically and proven experimentally that the optical heating of the c-Si NPs is very sensitive to the resonant conditions, therefore the optical heating is strongly dependent on the diameter of the nanospheres, as one can see from Fig. 2(b). The general concept is that the more precise one can tune the NPs size to the resonant condition, the stronger Raman shift

will be observed in the experiment, therefore, the stronger optical heating is achieved. The Fig. 2(b) shows pronounced resonant behavior from which one can conclude that low-order optical modes (ED) do not support highly efficient optical heating (roughly 160 nm in diameter), however at 230 nm diameter, the c-Si nanoparticle possesses MQ optical resonance. The higher-order modes appearing in larger NPs do not sufficiently improve the optical heating performance. Thereby, one can conclude that for the case of optical heating of single crystalline silicon nanosphere by HeNe CW-632.8 nm laser, the most optimal condition is the MQ mode.

Application of the optical heating for drug delivery systems. As it was already mentioned before, the tight 'union' between nanophotonics and biomedicine resulted in a wide range of unprecedented applications of optical concepts in real life. In recent decades, nanophotonics and biophotonics were mostly associated with plasmonic structures and nanoparticles - either due to their outstanding light-to-heat conversion properties [26] or electromagnetic field localization [27]. However, in the past few years, more and more bio-applications of nanophotonics are taking place basing on all-dielectric materials and optical responses [28–30]. The approach on using all-dielectric nanophotonics for biomedical applications is mostly based on excitation of single optical Mie modes or their combinations and collective resonances. One of the possible advantages of all-dielectric structures for biomedical applications is the ability for temperature probing via Raman scattering or PL signal. In this section we suggest using all-dielectric nanoparticles for optical thermal trigger for drug release in microcarrier systems for targeted medicine delivery.

The implementation of α-Fe_2O_3 resulted in the direct temperature measurement of the drug release from the capsule. The measurement by means of Raman thermometry showed that the mean value of the capsule rupture is roughly 170^o (Fig. 3(c)). Worth noticing, that on a scale of $5\mu m$ distance from the nanoparticle, the temperature decreases by one order of magnitude.

As a proof of concept, the delivery and optical rupture of the polymer drug carrier and subsequent release of anticancer drug vincristine (VCR) with lowered near-IR laser of of 4.0×10^4 W/cm^2 intensity, operating in biological

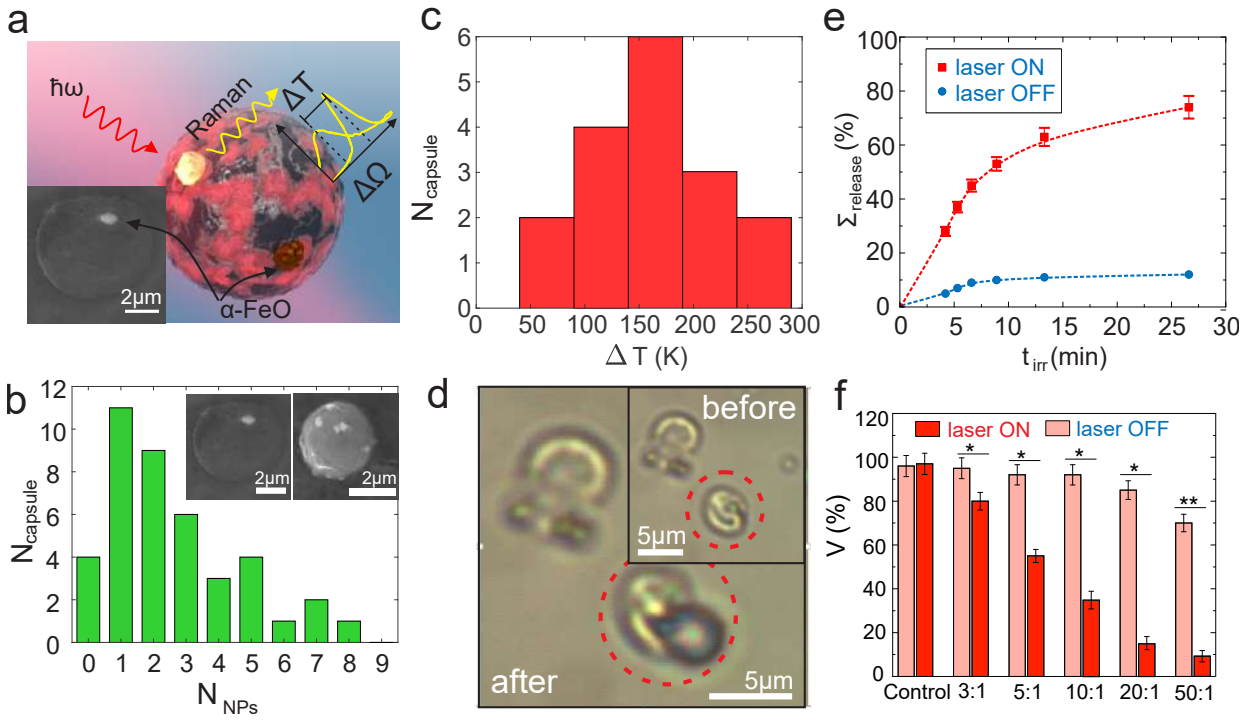

Figure 3 — **Polymer drug carriers with embedded α-Fe_2O_3 nanoparticles.** (a) Schematic of the concept for drug delivery systems based on microcapsules with α-Fe_2O_3 NPs embedded into the wall for photothermal activation of the drug release process. (b) Histogram of the quantity of α-Fe_2O_3 nanoparticles successfully trapped in the polymer carrier wall. Inset: Typical SEM images of the fabricated capsules. Scale bar is 2 μm. (c) Histogram of the observed capsule rupture upon laser radiation. The temperature values were obtained via Raman thermometry. (d) Bright-field microscopy images of the capsule before and after laser irradiation. (e) Released VCR concentration as the function of time with laser irradiation (red) and without (blue). (f) CC viability after the target-delivery experiments with laser-induced activation of the drug release. Red columns correspond to CC, pink columns correspond to the stem cells (control). Different columns correspond to different initial polymer capsules concentration. Adopted from [31].

tissue transparency window, by means of efficient optical heating and nanothermometry of α-Fe_2O_3 NPs, was shown. The biological tests are performed on two primary cell types: (i) carcinoma cells, as an example of malignant tumor, and (ii) human stem cells, as a model of healthy cells (Fig. 3(e,f)).

Further, this concept was proven experimentally for carcinoma cells. The capsule loaded with anti-tumour drug VCR successfully released the drug agent upon laser irradiation and subsequent thermally-induced rupture of the capsule (Fig. 3(e,f)). Moreover, the laser intensities were rather moderate, so

that the control cells (stem cells) were relatively unaffected. The biological part of the work was done by Dr. Mikhail Zyuzin and Dr. Alexander Timin and can be found in [31].

In conclusion to the chapter, it was shown that a single Mie resonant semiconductor nanoparticle can serve as a simple and "all-in-one" (heater-thermometer) nanoplatform which supports effective ligh-to-heat energy conversion and broad-range temperature sensing. In particular, such a nanosystem demonstrated its efficiency for biomedical applications requiring photothermal interaction.

The third chapter describes the implementation of Raman scattering of light for investigating and stimulating the photothermal phase transition in single nanocavities.

It was shown that simultaneous laser heating of nanothermometry using thermosensitive Raman scattering from resonant semiconductor nanoparticles can be applicable for a number of nanophotonics applications associated with photothermal processes. In this chapter, crystallization of optically resonant nanodisks from amorphous silicon caused by local optical heating was studied. The phase transition and temperature control were performed using Raman scattering. It was found that the temperature of the onset of the phase transition from the amorphous to the crystalline state for a single silicon nanodisk is about 900°C. Further, the polycrystalline nanodisk has already demonstrated the possibility of multiple reversible optical heating in the temperature range 300÷1000 K.

The process of phase transition from amorphous to crystalline phase for a silicon nanodisk is shown in Fig. 4(a). To ensure and control the phase transition in a single nanodisk, first, a Raman spectrum was obtained in the so-called "cold" mode, at a pumping intensity of 0.06 MW/cm^2, such that the disk temperature visually did not change. Then this disk was subjected to more intense irradiation with a helium-neon laser (0.39 MW/cm^2), which induced a phase transition. At temperatures of about 600÷800 °C, the nanodisk began to change from the amorphous to the polycrystalline phase, as can be seen from the figure. The crystallization temperature values coincide with the

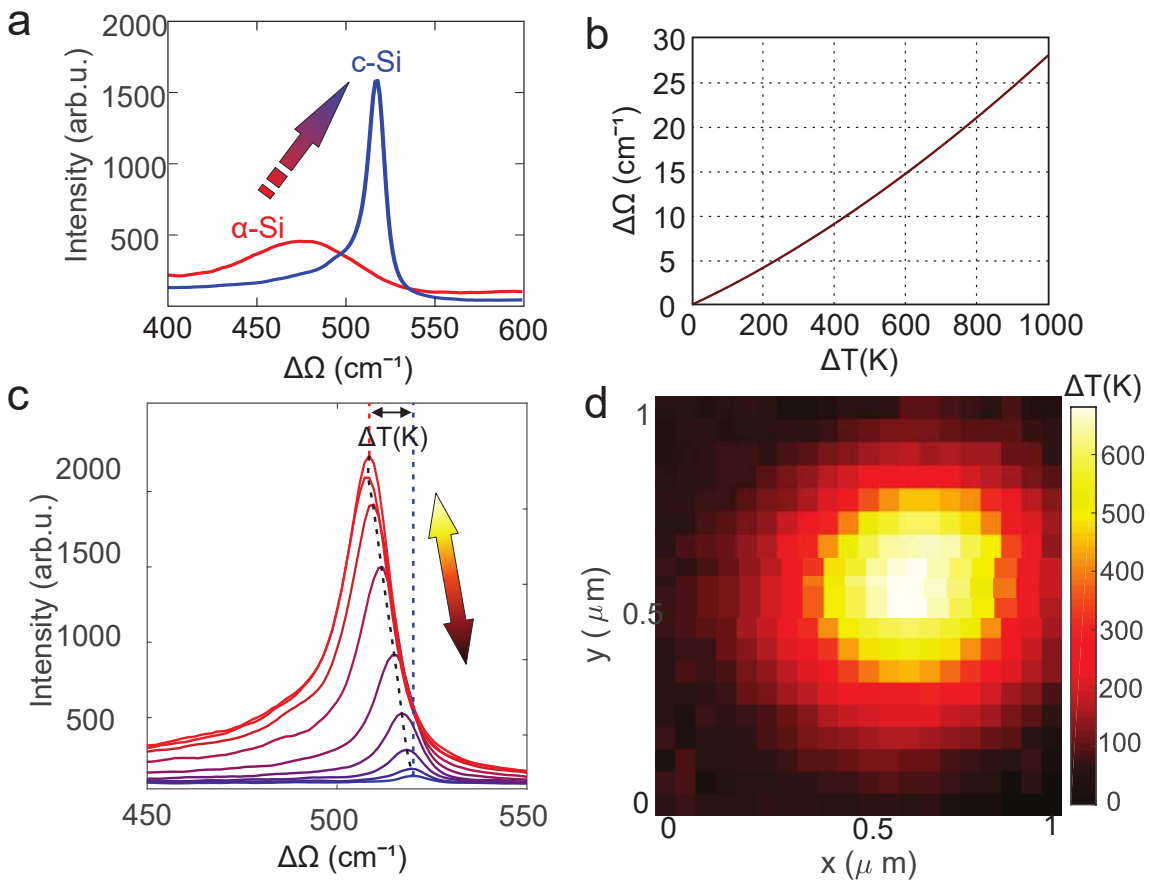

Figure 4 — **Photothermal annealing of a silicon nanodisk.** (a) Raman spectra of a nanodisk before and after laser exposure. (b) Theoretical temperature dependence of the spectral shift of the phonon line of crystalline silicon (see equation 8). (c) Raman spectra of a single polycrystalline nanodisk at various pump intensities. (d) Spatial distribution of the optical heating temperature depending on the position of the source relative to a single nanodisk. Taken from [32].

known ones [33], and the heating temperature is comparable to those previously achieved at a similar pump power, but for spherical nanoparticles [21].

Fig. 4(b) shows the direct temperature dependence of the spectral position of the Raman scattering of crystalline silicon at different temperatures. The Raman spectra after annealing resemble polycrystalline silicon because [33]: first, they exhibit asymmetry with respect to the spectral position, which is noticeably manifested at higher disk heating temperatures; second, the characteristic spectral FWHMs of Raman peaks exceed 10 cm^{-1} even at low intensities, while for single-crystal silicon this value does not exceed 5 cm^{-1}.

Fig. 4 (d) shows an example of two-dimensional mapping of the distri-

bution of optical heating of a single nanoobject, depending on the position of the laser source and the collection area.

This method allows fast and non-invasive local induction of phase transitions in amorphous materials using optical heating and control of the degree of crystallinity and temperature by means of Raman scattering. This approach is especially useful for second-harmonic generation [10] and broadband photoluminescence [34].

In conclusion to this chapter, it was shown that Raman scattering can be efficient both for thermometry and crystalline phase probe. As a proof of concept, it was shown that the silicon metasurface made of individual nanopillars can be modified via efficient optical heating. Due to the temperature localization in the tip of the nanopillar, which is proven theoretically, the melting can occur with great spatial precision and without modification of the closest neighbours.

Chapter four covers the ability of Raman scattering to qualitatively probe optical states of semiconductor nanostructures from the far-field.

By 'qualitative' we understand the detection of the general features and pattern of the near-field distribution of the optical modes of the nanostructure without any quantitative estimations.

As it was already shown before, resonant all-dielectric and semiconductor nanostructures are a powerful tool for near-field localization outside and inside the nanoresonators, as well as enhancement of the emission from them. Recently, various designs of light-emitting nanoantennas and metasurfaces with controllable intensity and far-field patterns were proposed. Here we demonstrate switching of near-field distribution in a silicon oligomer by changing polarization of the incident light generating Raman photons. Silicon nanodisks in the proposed designs support dipolar Mie resonances, coupled differently depending on the incident polarization. Since the incident polarization allows for control of the coupling between different pairs of nanodisks, the spatial distribution of Raman scattering is strongly dependent on the local field enhancement factor. We believe that such approach will pave the way for simplification both of excitation and detection of optical states.

Here we propose a method for optical far-field probing of optical states near-field hot spots based on Raman spectrometry. It was previously shown that Raman scattering can be used for detecting optical states, either non-radiating [35, 36] or bright modes (radiating) of the different order [17, 21]. We show theoretically and prove experimentally that chiral [37, 38] photonic designs that support topological edge states [39] can be probed via linear inelastic scattering on optical phonons - Raman scattering. We believe that the revealed approach can be further extended on other topologically trivial and non-trivial designs, and would benefit from the Raman technique that allow one to simultaneously optically heat and measure the temperature in real-time by the spectral shift of the Stokes signal [22]; thus, the thermally non-linear photonic state switching [40] might take place.

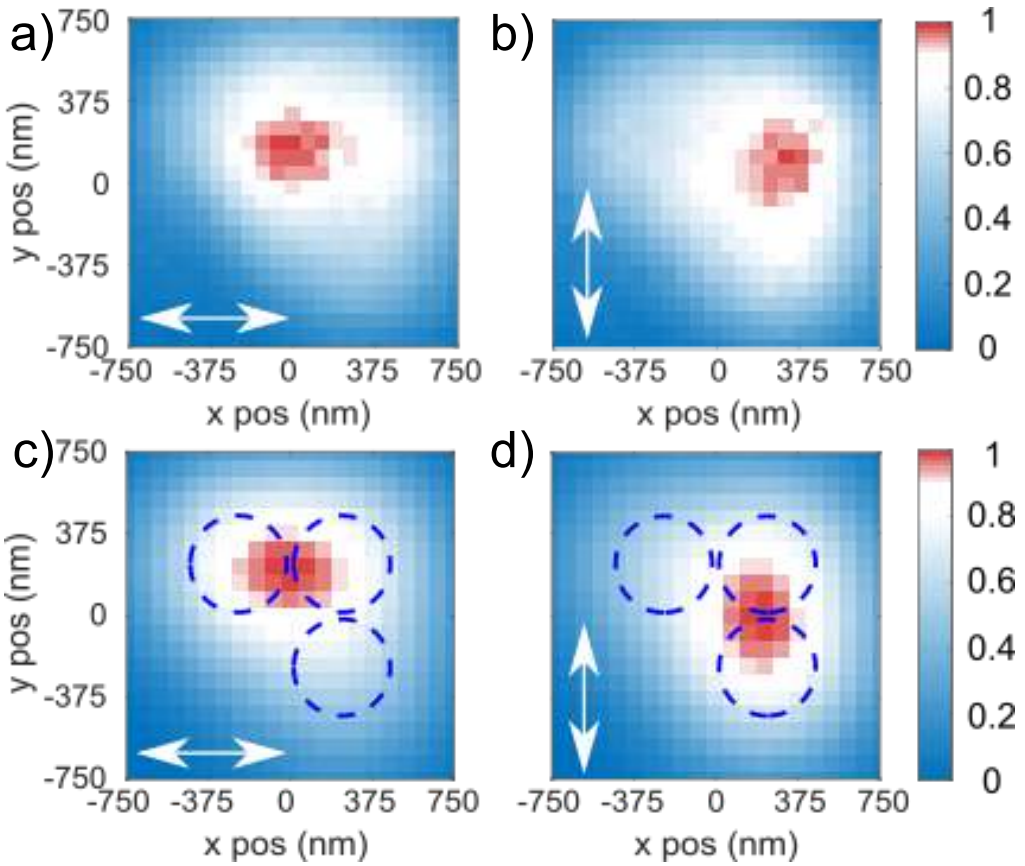

Figure 5 — **Polarization-induced hot-spot switching of the near-field distribution probed by Raman scattering mapping.** (a,b) Experimental and (c,d) theoretical distribution of Raman scattering from an oligomer for (a,c) horizontal and (b,d) vertical polarizations along the surface of the sample. Dashed line correspond to the location of oligomer consisting of separate nanodisks.

The experimental study of the predicted polarization-dependent local-

ization of Raman intensity on a zigzag oligomer chain of 3 disks is shown in Fig. 5. The calculation results in the polarizations x and y are the same as in the experiment in Fig. 5. The color map is selected so that the optical switching is the easier to notice. The Raman patterns are in full agreement with the predicted ones. The localization of the Raman response is shifted either to one or another edge, similar to the calculation and the measured experimental near-field distribution by means of scanning near-field optical microscopy (SNOM). Thus, we believe that for the first time we showed the probing from the far field of the optical states through the Raman scattering.

In conclusion to the chapter, it was shown that Raman scattering can serve as an optical states probing tool for resonant nanostructures. The proposed method can provide information regarding the light power absorbed by the nanoresonator, as well as give the qualitative information of the electromagnetic spatial distribution within the nanostructure.

Chapter five is devoted to the first demonstration of the transition from spontaneous Raman scattering to the stimulated emission regime achieved on a single submicron nanocylinder.

Resonant dielectric structures have emerged recently as a new platform for subwavelength non-plasmonic photonics. It was suggested and demonstrated that magnetic and electric Mie resonances can substantially enhance many effects at the nanoscale, including spontaneous Raman scattering. Here we demonstrate stimulated Raman scattering (SRS) for isolated crystalline silicon (c-Si) nanoparticles and observe experimentally a transition from spontaneous to stimulated scattering manifested in a nonlinear growth of the signal intensity above a certain pump threshold. At the Mie resonance, the light gets confined within a small volume of the resonant mode with electromagnetic fields enhanced inside the c-Si nanoparticle due to its high refractive index, which leads to an overall strong SRS signal at low pump intensities. Our finding paves the way to the development of efficient Raman nanolasers for multifunctional photonic metadevices.

Figure 6(b) shows typical experimental dependencies of Raman scattering signal on pump intensity. At low intensities, spontaneous Raman scat-

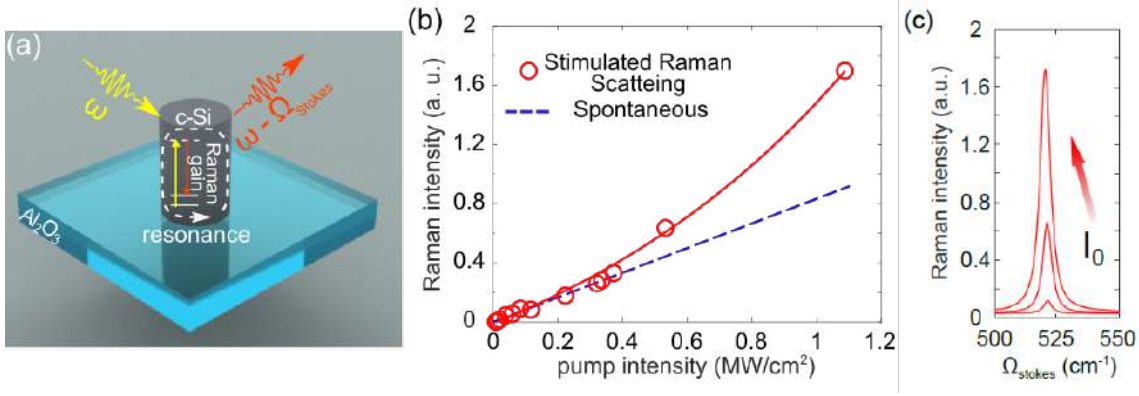

Figure 6 — **Experimental stimulated Raman scattering from c-Si nanoparticles.** (a) Schematic view of a Si nanoparticle excited with a laser light. (b) Experimental Raman scattering intensities at different pumps for the resonant 475-nm nanoparticle (red circles) and nonresonant 445-nm nanoparticle (blue dashed line). The red line corresponds to an exponential fitting.(c) Experimental Raman scattering spectra. The arrow demonstrates the higher intensity value from spectrum to spectrum. Adopted from [41].

tering dominates, being characterized by a linear dependence on the incident power, as was demonstrated earlier with c-Si nanoparticles [17, 21]. However, at higher intensities (higher than 0.3 MW/cm^2), we observe a nonlinear growth of the Raman scattering signal for the nanodisk with diameter 475 nm, which is not observed for other nanodisks with diameters 250÷800 nm, see a dashed blue line in Fig. 6(b). This sharp difference characterizes the SRS regime.

In conclusion to this chapter, the first observation was reported of the stimulated Raman scattering from subwavelength crystalline silicon nanoparticles enhanced by Mie-type resonances. The importance of critical optimization of the Q factors of nanoparticles, and thermal conductivity of a substrate to achieve a strong optical response and avoid overheating at higher intensities was revealed. It is believed that the provided finding will be useful for advanced applications of resonant dielectric nanophotonics for nanoscale thermometry and biosensing, and we envision further studies of the stimulated Raman scattering in various nanophotonic designs [7, 11, 42].

The thesis is devoted to the creation and the study of the alternative to the plasmonics sensing platform for efficient optical heating, thermometry and enhancement of the Raman scattering based on all-dielectric and semi-

conductor resonant nanostructures. The thesis covers the analysis of different shapes and geometries of the nanostructures, a number of materials robust to optical heating and thermometry, different substrate materials and various surrounding media were considered, the enhancement of the Raman scattering from the nanoparticles improved either by resonant conditions or by means of stimulated emission, and the optical states probing and near-field distributions study.

Summary of the main results:

1. It has been shown that spherical crystalline silicon nanoparticles with diameters from 100 to 400 nm, possessing Mie resonances in the visible range, are able to support effective optical heating and thermometry via Raman scattering at a wavelength of a CW HeNe laser of 632.8 nm.
2. It has been shown that the use of Mie resonant semiconductor α-Fe_2O_3 nanoparticles supporting optical heating and nanothermometry by means of Raman scattering in the targeted drug delivery systems contributes to a significant decrease in the threshold of pump intensity for photoinduced rupture of polymer carrier of the drug and subsequent release of the anticancer agent into carcinoma cells. The α-Fe_2O_3 nanoparticles were used as the target for near-IR laser excitation for efficient conversion of light to heat in the walls of polymer drug agents and as the direct optical temperature probe via thermally sensitive Raman scattering. As the proof of concept, the successful *in vitro* delivery and remote optically induced thermal rupture of the polymer carrier by means of laser heating of the target α-Fe_2O_3 nanoparticles with subsequent release of the antitumour drug agent vincristine was shown. The proposed system worked at the moderate laser intensity value as low as 4.0×10^4 W cm^{-2}.
3. It was shown that single amorphous hydrogenated silicon nanodisks with diameters from 300 to 450 nm, fabricated by lithographic methods on a glass substrate, can undergo a photoinduced phase transition to the polycrystalline phase due to efficient optical heating. At the same time, such a phase transition can be controlled and detected by means of

Raman scattering, and the shape of the nanoparticle does not change under controlled heating and phase transition, which is confirmed by SEM images before and after annealing.

4. It was shown that two-dimensional mapping of the intensity distribution of Raman scattering from an asymmetric oligomer, consisting of three identical silicon nanodisks, makes it possible to obtain the structure of the distribution of electromagnetic near-fiel hot spots of optical modes in such nanostructures. A change in the linear polarization of the pump by 90 degrees leads to optical switching of the near field distribution of the mode, which is also detected from the far-field by means of Raman scattering.
5. It was shown that a single silicon nanocylinder 600 nm in height and 475 nm in diameter placed on a sapphire substrate supports the transition from spontaneous Raman scattering mode to stimulated emission regime under continuous pumping of a HeNe laser at a wavelength of 632.8 nm and a pump intensity $I_0 = 0.4$ MW/cm^2 due to the optimized Q-factors of the eigenmodes excited at the pump and emission of the Stokes Raman scattering wavelengths, as well as due to increased heat sink to the substrate with high thermal conductivity.

Main research publications:

[A1] **Zograf G. P.**, Petrov M. I., Zuev D. A., Dmitriev P. A., Milichko V. A., Makarov S. V., Belov P. A. Resonant nonplasmonic nanoparticles for efficient temperature-feedback optical heating //Nano Letters. – 2017. – . 17. – №. 5. – . 2945-2952.

[A2] **Zograf G. P.**, Timin A. S., Muslimov A. R., Shishkin I. I., Nominé A., Ghanbaja J., Ghosh P., Li Q., Zyuzin M. V., Makarov S. V. All-Optical Nanoscale Heating and Thermometry with Resonant Dielectric Nanoparticles for Controllable Drug Release in Living Cells //Laser & Photonics Reviews. – 2020. – . 14. – №. 3. – . 1900082.

[A3] Milichko V. A., Zuev D. A., Baranov D. G., **Zograf G. P.**, Volodina K., Krasilin A. A., Mukhin I. S., Dmitriev P. A., Vinogradov V. V., Makarov

S. V., Belov P. A. Metal-dielectric nanocavity for real-time tracing molecular events with temperature feedback //Laser & Photonics Reviews. – 2018. – . 12. – №. 1. – . 1700227.

[A4] **Zograf G. P.**, Yu Y. F., Baryshnikova K. V., Kuznetsov A. I., Makarov S. V. Local crystallization of a resonant amorphous silicon nanoparticle for the implementation of optical nanothermometry //JETP Letters. – 2018. – . 107. – №. 11. – . 699-704.

[A5] Aouassa M., Mitsai E., Syubaev S., Pavlov D., Zhizhchenko A., Jadli I., Hassayoun L., **Zograf G.**, Makarov S., Kuchmizhak, A . Temperature-feedback direct laser reshaping of silicon nanostructures //Applied Physics Letters. – 2017. – . 111. – №. 24. – . 243103.

[A6] Baryshnikova K. V., Frizyuk K. S., **Zograf G. P**, Makarov S. V., Baranov M. A., Zuev D. A., Milichko V. A., Mukhin I.S., Petrov M. I., Evlyukhin A. B. Revealing low-radiative modes of nanoresonators with internal raman scattering //JETP Letters. – 2019. – . 110. – №. 1. – . 25-30.

[A7] **Zograf G. P.** et al. Stimulated Raman Scattering from Mie Resonant Subwavelength Nanoparticles //Nano Letters. – 2020. – . 20. – №. 8. – . 5786-5791.

[A8] **Zograf G. P.**, Petrov M. I., Makarov S. V. Coating of Au nanoparticle by Si shell for enhanced local heating //JPhCS. – 2017. – . 929. – №. 1. – . 012072.

[A9] **Zograf G. P.** et al. Gap size impact on metal-dielectric nanocavity heater properties //AIP Conference Proceedings. – AIP Publishing LLC, 2017. – . 1874. – №. 1. – . 030043.

[A10] **Zograf G.**, Makarov S., Petrov M. Doping of resonant silicon nanodisks for efficient optical heating in the near-infrared range //JPhCS. – 2020. – . 1461. – №. 1. – . 012201.

Acknowledgements. In conclusion, I would like to express my sincere gratitude to my scientific adviser Prof. S.V. Makarov for support and assistance throughout my research, for discussion of the results, and scientific guidance and mentoring. Credits to I. Mukhin, F. Komissarenko, V. Rutckaia

and A. Kuznetsov for providing the samples; M.I. Petrov and Yu.S. Kivshar for a unique opportunity to participate in the implementation of their many ideas and for a source of motivation; P. Dmitriev and A. Samusev for promoting department of physics of ITMO University, and A. Bogdanov and M. Petrov for inviting me to ITMO University master's program back in 2015; the collaborators from all over the world and the entire team of the Physics and Engineering Department of ITMO University, headed by P.A. Belov and I.V. Melchakova. Also I would like to mention the crucial impact to my first scientific steps from "Physical-Technical High School" named after Zh. I. Alfyorov, Peter the Great St.Petersburg Polytechnic University and Ioffe Institute and my first supervisor V.I. Nikolaev. Finally, I thank the authors of the *RussianPhd-LaTeX-Dissertation-Template* template for their help in completing the dissertation, and my friends and family for their patience and support.

Fin.

INTRODUCTION

Background and motivation. The possibility for remote and non-invasive study of inherent properties of the objects and structures at micro- and nanoscale has been of great interest for researchers in the last half-century. The idea of creating sensors that would give precise and comprehensive information on the objects they were attached to was a guiding star for many years.

One of the possible solutions was proposed in 1973 by Martin Fleischmann, Patrick J. Hendra, and A. James McQuillan, when the authors observed a sufficient increase of the Raman scattering signal by placing pyridine on a roughened silver substrate - this effect was later named SERS (surface-enhanced Raman scattering) [1]. Initially, Raman scattering is a very weak optical effect occurring in semiconductors or molecules due to inelastic scattering either on lattice vibrations or chemical bonds vibrations, providing a footprint spectrum for any given molecule or composition, but it could be increased by a several orders of magnitude due to electromagnetic near-field enhancement [2, 3] allowing for detection of traces of single molecules. Thus, the plasmonic nanoparticles for SERS sensing attracted great interest [4]. The goal of sensing applications lied not only in finding presence of any substance, but also in detecting thermal data. The temperature measurement at the nanoscale and the ability of local manipulation of the temperature with a simultaneous possibility of distinguishing the compositions by means of Raman scattering was a fruitful topic for the research [5].

Recently, it was demonstrated that single plasmonic nanoparticles can support nanothermometry, efficient optical heating, and serve as a SERS sensor at once [6]. However, the Prof. Michel Orrit group faced a major drawback due to the very long acquisition time of the signal, several minutes, therefore limiting plasmonic nanorod applicability. Another limiting factor for plasmonic nanostructures as a thermal sensor is the lack of inherent Raman signal, which requires additional fabrication or manipulations for acquiring the data.

On the other hand, in recent years dielectric nanophotonics gained high interest due to the ability of concentrating light inside nanoscale resonators by means of Mie resonances or other high-quality factor states, in contrast with plasmonic nanoantennas, allowing creation of subwavelength nanolasers [7, 8], empowered nonlinear light generation [9–11], enhanced photoluminescence [12, 13], near-field hot-spots [14, 15], and many other applications [16]. Due to the excitation of different optical resonant modes inside semiconductor nanostructures upon laser irradiation, considerable field enhancement can be observed. Moreover, these structures turn out to be highly efficient for optical heating and thermometry at moderate intensities. Based on the inherent Raman scattering of semiconductor and dielectric nanostructures, whose intensity can be drastically improved by matching resonant conditions [17, 18], one can achieve efficient optical heating, nanothermometry, and near-field enhancement, allowing the detection of molecular events at the nanoscale.

The thesis is devoted to the creation and the study the sensing platform alternative to plasmonics for efficient optical heating, thermometry and enhancement of the Raman scattering based on all-dielectric and semiconductor resonant nanostructures. The thesis covers the analysis of different shapes and geometries of nanostructures, a number of materials robust to optical heating and thermometry, different substrate materials and various surrounding media, the enhancement of the Raman scattering from the nanoparticles improved either by resonant conditions or by means of stimulated emission, the optical states probing and near-field distributions study.

The main goals of this work are

- Development of the approach for simultaneous optical heating and thermometry based on resonantly enhanced Raman scattering from dielectric and semiconductor nanostructures.
- Demonstration of the optically induced amorphous to polycrystalline phase transition in semiconductor nanostructures with the possibility for *in situ* phase state detection via Raman scattering.
- Probing the optical states of the semiconductor nanostructures by means of resonantly enhanced Raman scattering from the far-field region.

- Demonstration and realization of the transition from spontaneous to stimulated Raman scattering regimes from isolated single nanoparticle empowered by Mie resonances.

The scientific statements presented for the defence

- Resonant optical excitation of Mie modes in a semiconductor nanoparticle with balanced radiation and non-radiation losses provides the most effective optical heating in comparison with other loss ratios for the given optical mode.
- Optical heating by a continuous wave laser source of a semiconductor Mie resonant nanostructure induces a phase transition from an amorphous to a polycrystalline state and enables *in situ* tracing of such a transition by means of Raman scattering.
- Two-dimensional Raman scattering intensity mapping of a resonant semiconductor nanostructure allows the probing of the excited optical modes in it from the electromagnetic far-field region and provides the near field "hot-spots" spatial distribution pattern of the eigenmode at the pump wavelength.
- The transition from spontaneous Raman scattering to stimulated scattering regime occurs upon excitation of high-Q optical resonant modes, both at the pump wavelength and at the Stokes Raman scattering wavelength, with optimized mode coupling efficiencies and their spatial overlapping at the pump the radiation wavelengths in a single crystalline silicon nanocylinder with optimized heat sink to the substrate.

Key novelty of this work includes but is not limited by the following points:

1. The first experimental demonstration of simultaneous continuous wave HeNe (632.8 nm) laser-induced optical heating and nanoscale thermometry by resonant Raman-active semiconductor nanostructures.
2. The first demonstration of the Mie resonant semiconductor nanoparticle optical heating and nanothermometry via Raman scattering for drug delivery applications. The α-Fe_2O_3 nanoparticles were used as the target

for near-IR laser excitation for efficient conversion of light to heat in the walls of polymer drug agents and as the direct optical temperature probe via thermally-sensitive Raman scattering. As the proof of concept, the successful *in vitro* delivery and remote optically-induced thermal rupture of the polymer carrier was shown by means of laser heating of the target α-Fe_2O_3 nanoparticles with subsequent release of the antitumour drug agent vincristine. The proposed system worked at the moderate laser intensity value as low as 4.0×10^4 W cm^{-2}.

3. The first demonstration of *in situ* local controllable optically-induced phase transition from amorphous to polycrystalline state of silicon nanodisks on a glass substrate with temperature and phase optical feedback via Raman scattering.
4. The first demonstration of the qualitative probing of electromagnetic near-field hot spots distribution of optical modes in resonant semiconductor nanostructures by means of two-dimensional Raman scattering intensity spatial and spectral mapping.
5. The first experimental observation of the transition from spontaneous to stimulated Raman scattering regime from isolated single crystalline silicon nanocylinder.

Scientific and practical importance of the work lies in the fact is that the author proposed a novel approach for optical heating and thermometry with nanoscale spatial resolution by means of single Raman-active resonant semiconductor nanoparticle. The proposed platform on 'all-in-one' nanoparticle that serves both as a temperature probe and a nanoheater does not require any additional functionalizations or fabrication steps, it uses single excitation source both for enhanced optical heating and Raman scattering, it is robust and supports repeated cycles of usage. Such approach demonstrated its applicability in advanced bio-medical application, for drug delivery systems for cancer treatment with remote all-optical thermal release trigger.

Such a thermometry approach based on the spectral shift of the Raman scattering signal of nanostrucutres upon intense laser irradiation with subse-

quent optical heating found a very promising application for *in situ* crystalline-state modification of the nanostructures. The Raman scattering serves both as a thermal probe and a crystallinity state probe, thus, the sufficient optical heating of an amorphous silicon nanodisk on a glass substrate can result in phase transition from amorphous to polycrystalline state. The fabrication of crystalline nanostructures on glass SiO_2 remains quite challenging, therefore, the approach of steady precise optical heating of amorphous silicon nanodisks on a glass substrate with *in situ* probe of the temperature and the crystal state can solve the fabricational difficulty for some cases and applications.

As it was mentioned above, the Raman scattering is an efficient probing approach for temperature measurements and crystal-state evaluation, but the intensity of the Raman scattering can also serve as a probe for the electromagnetic power density stored in the nanostructures. The spatial mapping of the Raman scattering intensity of a zig-zag oligomer consisting of three nanodisks of the same size show the switching of the 'hot-spot' distribution upon changing the polarization of the incident excitation. The essential benefit of this approach is that it does not require any tip-assisted techniques, uses only a single laser for the excitation of Raman scattering and detects the signal in the far-field domain. Such fast and proper quality information on the electromagnetic 'hot-spots' distribution along the nanostructure surface might be useful for rapid analysis of the nanostructure's optical states or can serve as a platform for selective excitation of the biological or polymers in the gaps of the zig-zag oligomer.

Finally, the Raman scattering is a rather weak process, but it can be significantly improved by matching resonant conditions. Moreover, the Raman scattering intensity can be additionally increased by the transition from spontaneous to stimulated Raman scattering regime. Such transition observed in sub-micron (in all three dimensions), subwavelength nanodisk can pave the way for highly effective Raman-based nanosensors.

Reliability and validity of the obtained results is ensured by modern research methods and on the reproducibility of the measurement results, and

is also confirmed by the good agreement between the experimental data, the numerical modeling and analytical results.

Implementation of the obtained results. The author of the thesis owns the patent of the Russian Federation registry №.177658 for the utility model "nonlinear dielectric nanoantenna", registered on 05.03.2018, the concept of which is based on the principles and results obtained within the framework of the thesis. Moreover, the concept of the semiconductor–based optical heating and thermometry demonstrated its applicability for real drug delivery systems.

Approbation. The main results of the work were presented and discussed at Russian and International conferences, such as: Ioffe Institute Winter School on semiconductor physics 2016, Zelenogorsk, Russia (poster); International School and Conference 'Saint-Petersburg Open 2016, 2017, 2019', Saint-Petersburg, Russia (poster); International conference 'Days on Diffraction' 2016 (poster), 2017 (oral), 2018 (oral), Saint-Petersburg, Russia; METANANO International Conference 2016, Anapa, Russia (poster); Russian congress "Science of the future – science of the young" 2016, Kazan, Russia (poster); METANANO International conference 2017, Vladivostok, Russia (oral); International conference NANOP 2017, Barcelona, Spain (oral); METANANO International Conference 2018, Sochi, Russia (oral); International summer school 'Nicolas Cabrera' on 'advanced light manipulation at nanoscale' 2018, Miraflores de la Sierra, Madrid, Spain (poster); International conference ICMAT 2019, Singapore (poster); METANANO International conference 2019, Saint-Petersburg, Russia (oral); METANANO International conference 2020 (online, oral); OSA Advanced Photonics Congress 2020 (online, oral); as well as at the scientific seminars at ITMO University, North Ossetian State University, Zhejiang University, Queensland University of Technology.

Publications. The main results of the thesis are described in 10 scientific papers included in the list of the Higher Attestation Commission of the Russian Federation, including 7 articles in scientific journals indexed by the scientific

databases Scopus and Web of Science, and 3 peer-reviewed conference proceedings indexed by the scientific databases Scopus and Web of Science.

Author contribution. The contribution of the author consists of measurements and processing of experimental results (dark-field scattering spectra, Raman scattering spectra), an essential part of the numerical simulation of optical properties of the investigated nanostructures, the implementation of a numerical model of the optical heating of a semiconductor nanostructure, participation in the formulation of research objectives, and the writing of scientific papers.

The structure and scope of the thesis. The thesis consists of an introduction, five chapters, conclusion, and a list of references. The total volume of the thesis is 112 pages, including bibliography with 158 references. The work contains 36 figures and 1 table, placed inside the chapters.

CHAPTER 1. EXPERIMENTAL AND THEORETICAL METHODS

This chapter is devoted to the main experimental and theoretical approaches used in the research. Sections on the three main methods are distinguished: (i) theoretical, (ii) experimental, (iii) fabrication and characterization. All the methods were already invented and described. The author adopted the approaches for particular tasks and problems. The theoretical models are created by the author, experiments were conducted personally, and the fabrication with characterization were done together with the collaborators (for details, see section acknowledgments).

1.1 Theoretical studies

1.1.1 Mie theory

The spherical geometry is the simplest yet one of the most popular shapes in nanophotonics since the first demonstration of Mie resonance in single silicon nanospheres [43, 44]. For this case, one should consider Mie theory in order to study electromagnetic resonant properties of the nanosphere.

Maxwell equations Ordinary light scattering problem [45, 46] is devoted to calculating the scattering cross-section of a defined particle (with a given size, shape, optical properties). To be precise, we are going to solve problems with plane harmonic incident waves, which is not actually a general solution, but we can represent every single field with its Fourier image, which is a combination of plane waves (thanks to linearity of Maxwell equations).

Considering ($\mathbf{E}_1$;$\mathbf{H}_1$) - field inside the particle; ($\mathbf{E}_2$;$\mathbf{H}_2$) - surrounding particle field, which can be described as a combination of incident ($\mathbf{E}_i$;$\mathbf{H}_i$) and scattered ($\mathbf{E}_s$;$\mathbf{H}_s$) fields.

$$\mathbf{E}_2 = \mathbf{E}_i + \mathbf{E}_s \qquad \mathbf{H}_2 = \mathbf{H}_i + \mathbf{H}_s \tag{1.1}$$

where,

$$\mathbf{E}_i = \mathbf{E}_0 \exp(i\mathbf{k}\cdot\mathbf{x} - i\omega t) \qquad \mathbf{H}_i = \mathbf{H}_0 \exp(i\mathbf{k}\cdot\mathbf{x} - i\omega t) \tag{1.2}$$

$\mathbf{k}$ is the wave vector, defined by environment.
Maxwell equations for this case will slightly transform : $\frac{d}{dt} \to -i\omega$

$$\nabla\cdot\mathbf{E} = 0 \qquad \nabla\cdot\mathbf{H} = 0 \tag{1.3}$$

$$\nabla\times\mathbf{E} = i\frac{\omega}{c}\mu\mathbf{H} \qquad \nabla\times\mathbf{H} = -i\frac{\omega}{c}\varepsilon\mathbf{E} \tag{1.4}$$

($\mathbf{D}$ and $\mathbf{B}$ are replaced by $\mathbf{D} = \varepsilon\ \mathbf{E}$ and $\mathbf{B} = \mu\ \mathbf{H}$) By applying curl operator to Eq. 1.4 we get :

$$\nabla\times(\nabla\times\mathbf{E}) = i\frac{w}{c}\mu\nabla\times\mathbf{H} = \frac{\omega^2}{c^2}\mu\varepsilon\mathbf{E} \tag{1.5}$$

$$\nabla\times(\nabla\times\mathbf{H}) = \frac{w^2}{c^2}\mu\varepsilon\mathbf{H} \tag{1.6}$$

By definition, double cross product of ∇ with a vector $\mathbf{A}$ equals to (using $\mathbf{B}\cdot\mathbf{A}\cdot\mathbf{C} - \mathbf{C}\cdot\mathbf{A}\cdot\mathbf{B}$ rule):

$$\nabla\times(\nabla\times\mathbf{A}) = \nabla\cdot(\nabla\cdot\mathbf{A}) - \nabla^2\mathbf{A} \tag{1.7}$$

The first term in brackets in Eq.1.7 is exactly divergence of a vector. It means that upon applying this expansion to the pair of $\mathbf{E}$ and $\mathbf{H}$ it will turn to zero; also remembering Eq. 1.3, 1.5, 1.6 and knowing that $\varepsilon\mu = \mathrm{n}^2$ the squared refractive index and wave vector $\mathbf{k} = \mathrm{n}\cdot\frac{\omega}{c}$, one can get:

$$\nabla^2\mathbf{E} + k^2\mathbf{E} = 0 \qquad \nabla^2\mathbf{H} + k^2\mathbf{H} = 0 \tag{1.8}$$

Now that the equations are obtained, it is necessary to define the boundary conditions. Tangential components of the electromagnetic field in every single point of surface of the particle should be continuous. This leads to:

$$[\mathbf{E}_2 - \mathbf{E}_1]\times\hat{\mathbf{n}} = 0 \qquad [\mathbf{H}_2 - \mathbf{H}_1]\times\hat{\mathbf{n}} = 0 \tag{1.9}$$

Vector $\hat{\mathbf{n}}$ is the outer normal vector to the surface S of the particle.

Eigenfunctions of scalar wave equation for a spherical particle

Plane-wave scattering by a single spherical particle was rigorously solved as shown below.

Let's introduce a vector function $\mathbf{M}$ through some constant vector $\mathbf{c}$ and scalar potential φ :

$$\mathbf{M} = \nabla \times (\mathbf{c}\varphi) \tag{1.10}$$

Recalling that divergence of a curl equals zero:

$$\nabla \cdot \mathbf{M} = 0 \tag{1.11}$$

and :

$$\nabla^2\mathbf{M} + k^2\mathbf{M} = \nabla \times [\mathbf{c}(\nabla^2\varphi + k^2\varphi)] \tag{1.12}$$

$\mathbf{M}$ is a solution to vector wave equation only when φ is a solution to a scalar wave equation:

$$\nabla^2\varphi + k^2\varphi = 0 \tag{1.13}$$

Function $\mathbf{N}$ is introduced as well:

$$\mathbf{N} = \frac{\nabla \times \mathbf{M}}{k} \tag{1.14}$$

It also satisfies the wave equation:

$$\nabla^2\mathbf{N} + k^2\mathbf{N} = 0 \tag{1.15}$$

The pair of functions $\mathbf{N}$ and $\mathbf{M}$ is called wave harmonics, which have the same properties as electromagnetic field. So the problem is now "simplified" to calculation of scalar potential φ.

Let's start considering this problem with defining a scalar wave equation for the scalar potential in spherical coordinates.

$$\frac{1}{r^2}\frac{\partial}{\partial r}(r^2\frac{\partial\varphi}{\partial r}) + \frac{1}{r^2\sin\theta}\frac{\partial}{\partial\theta}(\sin\theta\frac{\partial\varphi}{\partial\theta}) + \frac{1}{r^2\sin^2\theta}\frac{\partial^2\varphi}{\partial\phi^2} + k^2\phi = 0 \tag{1.16}$$

One can search for a solution in this particular form:

$$\varphi = R(r)\Theta(\theta)\Phi(\phi) \tag{1.17}$$

By inserting Eq. 1.17 into Eq. 1.16, three separate equations will be obtained:

$$\frac{\partial^2\Phi}{\partial\phi^2} + m^2\Phi = 0 \tag{1.18}$$

$$\frac{1}{\sin\theta}\frac{\partial}{\partial\theta}(\sin\theta\frac{\partial\Theta}{\partial\theta}) + \Big[n(n+1) - \frac{m^2}{\sin^2\theta}\Big] = 0 \tag{1.19}$$

$$\frac{\partial}{\partial r}(r^2\frac{\partial R}{\partial r}) + [k^2r^2 - n(n+1)]R = 0 \tag{1.20}$$

Constants n and m are expansion indices and they should be defined through initial conditions on φ. Solution for Eq. 1.18 is :

$$\Phi_{even} = \cos m\phi \qquad\qquad \Phi_{odd} = \sin m\phi \tag{1.21}$$

Solution for Θ in Eq. 1.19 are Legendre functions (orthogonal functions) :

$$\Theta = P_n^m(\cos\theta) \tag{1.22}$$

In Eq. 1.20 solution for $\rho = kr$:

$$j_n(\rho) = \sqrt{\frac{\pi}{2\rho}}J_{n+1/2}(\rho) \tag{1.23}$$

$$y_n(\rho) = \sqrt{\frac{\pi}{2\rho}}Y_{n+1/2}(\rho) \tag{1.24}$$

$J_n(\rho)$ and $Y_n(\rho)$ are Bessel functions of first and second order (N_n is often used instead of Y_n). So these solutions are spherical Bessel functions. Linear combination of Bessel functions is also a solution. Often it's very convenient to use Hankel spherical functions (third-order spherical Bessel).

$$h_n^{(1)} = j_n(\rho) + iy_n(\rho) \qquad\qquad h_n^{(2)} = j_n(\rho) - iy_n(\rho) \tag{1.25}$$

Now, the scalar function is defined as following:

$$\varphi_{emn} = \cos m\phi \, P_n^m(\cos\theta) z_n(kr) \tag{1.26}$$

$$\varphi_{omn} = \sin m\phi \, P_n^m(\cos\theta) z_n(kr) \tag{1.27}$$

Where z_n is any of the spherical Bessel functions. Now, using following relations, let's define $\mathbf{M}$ and $\mathbf{N}$ wave harmonics through φ :

$$\mathbf{M}_{emn} = \nabla \times (\mathbf{c}\varphi_{emn}) \qquad \mathbf{M}_{omn} = \nabla \times (\mathbf{c}\varphi_{omn}) \tag{1.28}$$

$$\mathbf{N}_{emn} = \frac{\nabla \times \mathbf{M}_{emn}}{k} \qquad \mathbf{N}_{omn} = \frac{\nabla \times \mathbf{M}_{omn}}{k} \tag{1.29}$$

Expansion of the incident wave in wave harmonics series Without loss of generality, one can consider the problem of an x-polarized plane wave scattering on a spherical particle. In spherical coordinates, a plane wave is written as:

$$\mathbf{E}_i = \mathbf{E}_0 e^{i\mathbf{k}\cdot\mathbf{r}\cos\theta} \widehat{\mathbf{e}}_x \tag{1.30}$$

where

$$\widehat{\mathbf{e}}_x = \sin\theta\cos\phi \, \hat{\mathbf{e}}_r + \cos\theta\cos\phi \, \hat{\mathbf{e}}_\theta - \sin\phi \, \hat{\mathbf{e}}_\phi \tag{1.31}$$

Rather obvious but bulky steps for series representation are left out:

$$\mathbf{E}_i = E_0 \sum_{n=1}^{\infty} i^n \frac{2n+1}{n(n+1)} (\mathbf{M}_{o1n}^{(1)} - i\mathbf{N}_{e1n}^{(1)}) \tag{1.32}$$

By calculating curl of Eq. 1.32, magnetic field series expansion can be obtained:

$$\mathbf{H}_i = \frac{-k}{\omega\mu} E_0 \sum_{n=1}^{\infty} i^n \frac{2n+1}{n(n+1)} (\mathbf{M}_{e1n}^{(1)} + i\mathbf{N}_{o1n}^{(1)}) \tag{1.33}$$

Remembering boundary conditions in Eq. 1.9:

$$[\mathbf{E}_i + \mathbf{E}_s - \mathbf{E}_1] \times \hat{\mathbf{e}}_r = 0 \qquad [\mathbf{H}_i + \mathbf{E}_s - \mathbf{H}_1] \times \hat{\mathbf{e}}_r = 0 \tag{1.34}$$

It is also possible to expand into series the scattered light and light inside the particle:

$$\mathbf{E}_1 = \sum_{n=1}^{\infty} E_n(c_n \mathbf{M}_{o1n}^{(1)} - i d_n \mathbf{N}_{e1n}^{(1)});\ \mathbf{H}_1 = \frac{-k}{\omega \mu_1} \sum_{n=1}^{\infty} E_n(d_n \mathbf{M}_{e1n}^{(1)} + i c_n \mathbf{N}_{o1n}^{(1)}) \tag{1.35}$$

Where $E_n = E_0 i^n \frac{2n+1}{n(n+1)}$ and μ_1 is the permeability of the sphere. For scattered light, we have the following expansion:

$$\mathbf{E}_s = \sum_{n=1}^{\infty} E_n(i a_n \mathbf{N}_{e1n}^{(3)} - b_n \mathbf{M}_{o1n}^{(3)});\ \mathbf{H}_s = \frac{k}{w\mu} \sum_{n=1}^{\infty} E_n(i b_n \mathbf{M}_{o1n}^{(3)} + a_n \mathbf{N}_{e1n}^{(3)}) \tag{1.36}$$

Top index (1) stands for j_n, i.e. the spherical Bessel function and index (3) is for the first-order Hankel $h_n^{(1)}$ (third-order spherical Bessel).

Defining scattering coefficients For every given n there are four coefficients that should be defined: a_n, b_n, c_n, d_n. Let's define them through the boundary conditions :

$$E_{i\theta} + E_{s\theta} = E_{1\theta} \qquad E_{i\phi} + E_{s\phi} = E_{1\phi} \tag{1.37}$$

$$H_{i\theta} + H_{s\theta} = H_{1\theta} \qquad H_{i\phi} + H_{s\phi} = H_{1\phi} \tag{1.38}$$

For the following coefficients x is the diffraction parameter and m is the relative refractive index

$$x = ka = \frac{2\pi \mathrm{n} a}{\lambda} \qquad\qquad m = \frac{k_1}{k} = \frac{\mathrm{n}_1}{\mathrm{n}} \tag{1.39}$$

solutions for the field inside the particle :

$$c_n = \frac{\mu_1 j_n(x)[x h_n^{(1)}(x)]' - \mu_1 h_n^{(1)}(x)[x j_n(x)]'}{\mu_1 j_n(mx)[x h_n^{(1)}(x)]' - \mu h_n^{(1)}(x)[mx j_n(mx)]'} \tag{1.40}$$

$$d_n = \frac{\mu_1 m j_n(x)[x h_n^{(1)}(x)]' - \mu_1 m h_n^{(1)}(x)[x j_n(x)]'}{\mu m^2 j_n(mx)[x h_n^{(1)}(x)]' - \mu_1 h_n^{(1)}(x)[mx j_n(mx)]'} \tag{1.41}$$

for scattered light :

$$a_n = \frac{\mu m^2 j_n(mx)[x j_n(x)]' - \mu_1 j_n(mx)[x j_n(mx)]'}{\mu m^2 j_n(mx)[x h_n^{(1)}(x)]' - \mu_1 h_n^{(1)}(x)[mx j_n(mx)]'} \tag{1.42}$$

$$b_n = \frac{\mu_1 m j_n(x)[x j_n(x)]' - \mu j_n(x)[mx j_n(mx)]'}{\mu_1 j_n(mx)[x h_n^{(1)}(x)]' - \mu h_n^{(1)}(x)[mx j_n(mx)]'} \tag{1.43}$$

Scattering coefficients can be slightly simplified with Riccati-Bessel functions :

$$\psi_n(\rho) = \rho j_n(\rho) \qquad\qquad \xi_n(\rho) = \rho h_n^{(1)}(\rho) \tag{1.44}$$

and assuming that permeability of the particle is equal to that of the environment:

$$a_n = \frac{m\psi_n(mx)\psi_n'(x) - \psi_n(x)\psi_n'(mx)}{m\psi_n(mx)\xi_n'(x) - \xi_n(x)\psi_n'(mx)} \tag{1.45}$$

$$b_n = \frac{\psi_n(mx)\psi_n'(x) - m\psi_n(x)\psi_n'(mx)}{\psi_n(mx)\xi_n'(x) - m\xi_n(x)\psi_n'(mx)} \tag{1.46}$$

Cross-sections Summing up all the above, the calculation of scattering and extinction cross-sections can be done through the following (W is the power flux, I_i is the incident light intensity) :

$$C_{sca} = \frac{W_{sca}}{I_i} = \frac{2\pi}{k^2}\sum_{n=1}^{\infty}(2n+1)(|a_n|^2 + |b_n|^2) \tag{1.47}$$

$$C_{ext} = \frac{W_{ext}}{I_i} = \frac{2\pi}{k^2}\sum_{n=1}^{\infty}(2n+1)Re(a_n + b_n) \tag{1.48}$$

$$C_{abs} = C_{ext} - C_{sca}, \tag{1.49}$$

where a_n are the electric modes and b_n are the magnetic ones.

Case of layered spheres (core-shells) The problem of light scattering on single concentric spheres (sphere with a homogeneous layer), the core-shell particles, also has an exact solution in Mie theory. However, the scattering coefficients have some modifications as follows:

$$a_n = \frac{\psi_n(y)\left[\psi_n'(m_2y) - A_n\chi_n'(m_2y)\right] - m_2\psi_n'(y)\left[\psi_n(m_2y) - A_n\chi_n(m_2y)\right]}{\xi_n(y)\left[\psi_n'(m_2y) - A_n\chi_n'(m_2y)\right] - m_2\xi_n'(y)\left[\psi_n(m_2y) - A_n\chi_n(m_2y)\right]}$$
$$b_n = \frac{m_2\psi_n(y)\left[\psi_n'(m_2y) - B_n\chi_n'(m_2y)\right] - \psi_n'(y)\left[\psi_n(m_2y) - B_n\chi_n(m_2y)\right]}{m_2\xi_n(y)\left[\psi_n'(m_2y) - B_n\chi_n'(m_2y)\right] - \xi_n'(y)\left[\psi_n(m_2y) - B_n\chi_n(m_2y)\right]}, \tag{1.50}$$

where:

$$A_n = \frac{m_2\psi_n(m_2x)\,\psi_n'(m_1x) - m_1\psi_n'(m_2x)\,\psi_n(m_1x)}{m_2\chi_n(m_2x)\,\psi_n'(m_1x) - m_1\chi_n'(m_2x)\,\psi_n(m_1x)}$$
$$B_n = \frac{m_2\psi_n(m_1x)\,\psi_n'(m_2x) - m_1\psi_n(m_2x)\,\psi_n'(m_1x)}{m_2\chi_n'(m_2x)\,\psi_n(m_1x) - m_1\psi_n'(m_1x)\,\chi_n(m_2x)}. \tag{1.51}$$

and $\psi_n(\rho),\ \chi_n(\rho),\ \xi_n(\rho)$ are the Riccati-Bessel functions, a is the core radius, b is the shell radius, m_1 and m_2 are the relative refractive indices of a sphere and a shell, $x = ka,\ y = kb$.

Therefore, the following steps in defining the total scattering, absorption and extinction cross-sections remain the same as for conventional sphere. The same solution steps should be also taken for optical heating in homogeneous media, as will be discussed further.

1.1.2 Optical heating of nanospheres in homogeneous media with continuous wave source

Important question of physics of light scattering is 'how strong does the incident light heat the particle?' It is obvious that not only mechanical, but optical properties are linked with with the NPs temperature as well.

Absorption cross-section for spherical NP can be derived through Mie-theory, whereas temperature increase should be derived through heat diffusion equations. Heat power absorbed by NP can be described through its absorption cross-section C_{abs} and light source intensity I:

$$Q = C_{abs}I \tag{1.52}$$

C_{abs} for spherical NPs is shown above. In case of more complex shapes, it is reasonable to calculate heat generation inside the NP through the integral of power density $q(\mathbf{r})$:

$$Q = \int_V q(\mathbf{r}) d^3 r, \tag{1.53}$$

where:

$$q(\mathbf{r}) = \frac{\omega}{2} \mathrm{Im}[\varepsilon(\omega)] \varepsilon_0 |E(\mathbf{r})|^2 \tag{1.54}$$

Next step is to define temperature distributions $T(\mathbf{r})$ inside and outside the NP. For this case we need to solve the heat diffusion equation:

$$\nabla \cdot [\kappa_1(\mathbf{r}) \nabla T_1(\mathbf{r})] = -q(\mathbf{r}) \quad \text{inside} \quad \text{NP} \tag{1.55}$$

$$\nabla \cdot [\kappa_2(\mathbf{r}) \nabla T_2(\mathbf{r})] = 0 \quad \text{outside} \quad \text{NP} \tag{1.56}$$

Where q in our case is $\frac{Q}{V} = \frac{3Q}{4\pi a^3}$, κ_1 and κ_2 are thermal conductivities of the particle and the medium, respectively. Let's assume that κ_1 and κ_2 are homogeneous in space. It means that Eq.1.55 in case of spherical symmetry and stationary problem transforms into:

$$\frac{1}{r^2} \frac{\partial}{\partial r} r^2 \frac{\partial T_1}{\partial r} = -\frac{q(\mathbf{r})}{\kappa_1} \quad \text{inside} \quad \text{NP} \tag{1.57}$$

$$\frac{1}{r^2} \frac{\partial}{\partial r} r^2 \frac{\partial T_2}{\partial r} = 0 \quad \text{outside} \quad \text{NP} \tag{1.58}$$

Owing to high thermal conductivity κ_1 of the nanoparticle material, the distribution of the heating power inside the nanoparticle is highly homogeneous and can be set as a constant $q(\mathbf{r}) = q$. This simplifies Eq. 1.57, where temperature inside the nanoparticle is a function of only radius (r).

After some straightforward calculations the following is achieved:

$$T_1 = -\frac{qr^2}{6\kappa_1} - \frac{C_1}{r} + C_1' \quad \text{inside} \quad \text{NP} \tag{1.59}$$

$$T_2 = -\frac{C_2}{r} + C_2' \quad \text{outside} \quad \text{NP} \tag{1.60}$$

General solutions are shown above; after applying to them the boundary conditions, considering the case with a perfect thermal contact, the results are:

$$T_1|_{r=a} = T_2|_{r=a} \tag{1.61}$$

$$-\kappa_1 \frac{\partial T_1}{\partial r}|_{r=a} = -\kappa_2 \frac{\partial T_2}{\partial r}|_{r=a} \tag{1.62}$$

There are some physical limitations:

$$T_2|_{r\to\infty} \to T_0 \Rightarrow C_2' = T_0 \tag{1.63}$$

$$T_1|_{r=0} < \infty \Rightarrow C_1 = 0 \tag{1.64}$$

Hence:

$$-\frac{qa^2}{6\kappa_1} + C_1' = -\frac{C_2}{a} + T_0 \tag{1.65}$$

$$-\frac{qa}{3} = \frac{C_2\kappa_2}{a^2} \tag{1.66}$$

Thus, we obtain:

$$C_2 = -\frac{qa^3}{3\kappa_2} \tag{1.67}$$

$$C_1' = \frac{qa^2}{3\kappa_2} + \frac{qa^2}{6\kappa_1} + T_0 \tag{1.68}$$

So, the temperature distributions are the following:

$$T_1 = \frac{qa^2}{6\kappa_1}(1 - \frac{r^2}{a^2}) + \frac{qa^2}{3\kappa_2} + T_0 \quad \text{inside} \quad \text{NP} \tag{1.69}$$

$$T_2 = \frac{qa^3}{3\kappa_2 r} + T_0 \quad \text{outside} \quad \text{NP} \tag{1.70}$$

Taking into account Eq.1.53 leads to:

$$T_1 = \frac{Q}{8\pi\kappa_1 a}(1 - \frac{r^2}{a^2}) + \frac{Q}{4\kappa_2 a} + T_0 \quad \text{inside} \quad \text{NP} \tag{1.71}$$

$$T_2 = \frac{Q}{4\pi\kappa_2 r} + T_0 \quad \text{outside} \quad \text{NP} \tag{1.72}$$

Solutions for these equations for a NP with radius a are:

$$\delta T(r) = \delta T_{NP}\frac{a}{r} \quad r > a \tag{1.73}$$

$$\delta T(r) \approx \delta T_{NP} \quad r < a \tag{1.74}$$

δT_{NP} - temperature increase in NP. For spherical NP, temperature increase is related to the absorbed heat, so:

$$\delta T_{NP} = \frac{C_{abs} I}{4\pi\kappa_2 a}. \tag{1.75}$$

In case of other non-spherical, but preserving the axial symmetry, structures for optical heating, the formula for temperature estimation was proposed by Prof. de Abajo, Prof. Quidant and Prof. Baffou [20]. The method is based on calculation of the volume of a disk, spheroid, rod, thorus or ellipsoid nanoparticle and the derivation of the radius of the nanosphere of equivalent value. The method is in a great agreement with exact numerical calculations, and it requires considerably less time.

1.1.3 Numerical calculations for inhomogeneous media

In case of non-spherical nanoparticles in non-homogeneous surrounding media under excitation more complicated than a linearly polarized plane-wave, the numerical commercial software was used. The COMSOL Multiphysics packages for electromagnetic full-wave modeling and heat transfer in solid-state physics were used to determine elastic scattering of the light from finite-size nanoobjects on different substrates, electromagnetic field enhancement inside and outside the nanostructures and temperature distribution.

The numerical calculations of light interaction with complicated structures for elastic scattering and optical heating were carried out by means of full-wave 3D modelling. Depending on the geometry and the symmetry of the problem, i.e. a cylindrical nanoparticle with vertical incidence and linear polarization of light, the dimension of the problem could be reduced down to 2D without losing the quality and precision of the solution, but improving the calculation speed, thus reducing the time.

A standard model for elastic light scattering and linear absorption consisted of a computational domain presented by a sphere with a radius 5 times greater than the wavelength considered in the calculation. The walls of the computational domain were extended by 1/10 of the radius by PML-layer (perfectly-matched layer) in order to reduce non-physical reflections of light with non-normal incidence with respect to the computational domain wall. The lower hemisphere is playing the role of a substrate made of different materials (glass, quartz, metal etc.), on top of which the nanostructures are placed. The upper half of the computational domain is aerial medium. The background excitation, i.e. an electromagnetic wave propagating from the upper half on to the substrate, was chosen to be either a linearly polarized plane wave or a Gaussian beam with a variable focal spot and beam waist. The standard physics toolbox is chosen to be electromagnetic waves - frequency domain (ewfd). Scattering boundary conditions are selected for all the outer boundaries.

In case of optical heating, the multiphysics toolbox was used alongside with heat transfer in solid-state physics package. In these circumstances, the frequency-stationary study steps are selected. After the calculation of electromagnetic wave absorption by a nanostructure, the power density absorbed by the nanostructure is used as a heat source for the second step of the solution - stationary heat diffusion problem in solids.

The 2D method of heat diffusion in solids and light scattering was adopted from [48] and realized with assistance of Daniil Ryabov, Kirill Koshelev and Dr. Andrey Bogdanov. The 3D method was proposed by the author of the thesis.

1.2 Optical experiments

The proposed theoretical methods reflect what was measured during the research, therefore, the theoretical methods are reproducing the conditions of the experiments. There were two main experimental setups and techniques for the investigation.

1.2.1 Elastic dark-field scattering

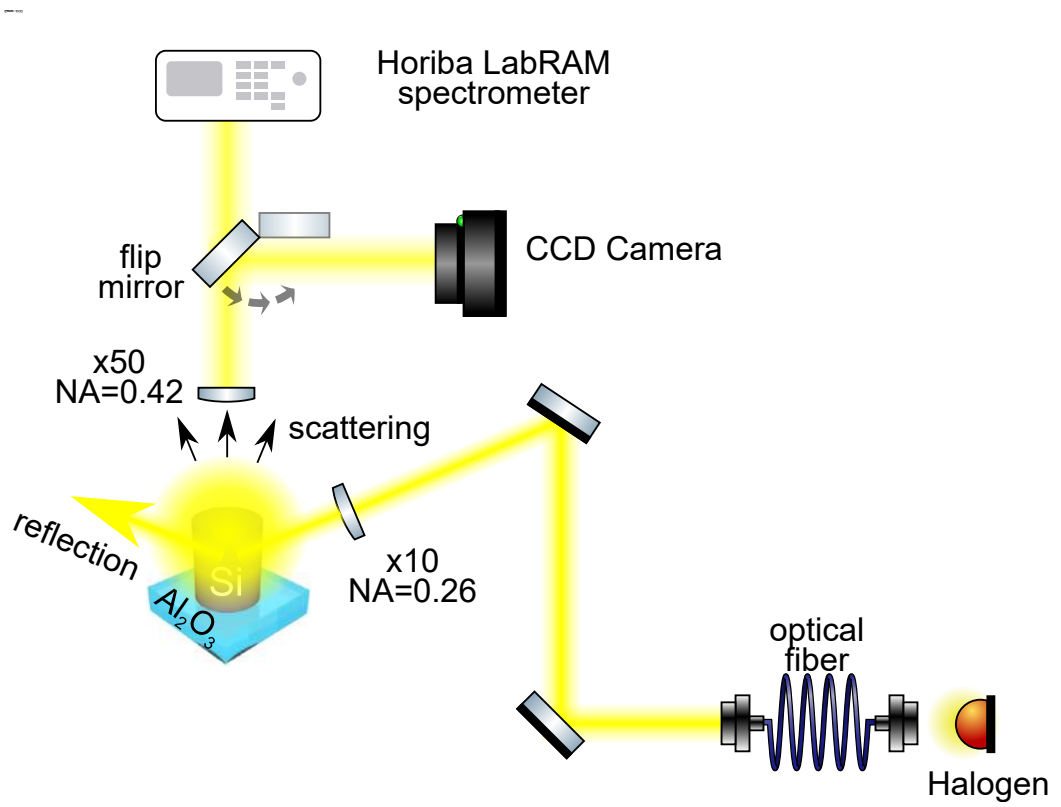

Figure 1.1 — Schematic of the experimental dark-field optical spectroscopy setup.

The experimental elastic light scattering spectra were obtained by means of the confocal setup for dark-field scattering spectroscopy. The schematic of the setup is shown in Fig. 1.1. The broadband white light source (halogen lamp HL-2000), coupled through the optical fiber, illuminates the sample through the x10 NA 0.26 lens (Mitutoyo Plan Apo NIR) with oblique incidence angle from 65 to 67 degrees with respect to the normal of the surface. The light enters the setup through the collimator with a Glan prism, which rotates the linear polarization of light from s-pol to p-pol. Further, the scattered light is collected through the upper lens x50 NA 0.42 (Mitutoyo Plan Apo NIR). The benefit of such scheme is that the geometrically reflected light is not being collected by the lens, only the light that has interacted with the nanoresonator is scattered in the upper direction. Further, the collected signal is analyzed by Horiba LabRAM spectrometer with a grating of 150 g/mm for fast detection; for higher spectral precision, 1800 g/mm was used. The positioning and the visualization of the sample was controlled via CCD camera

Canon 400D. For precise positioning micrometer screw stage was used.

1.2.2 Stokes Raman scattering

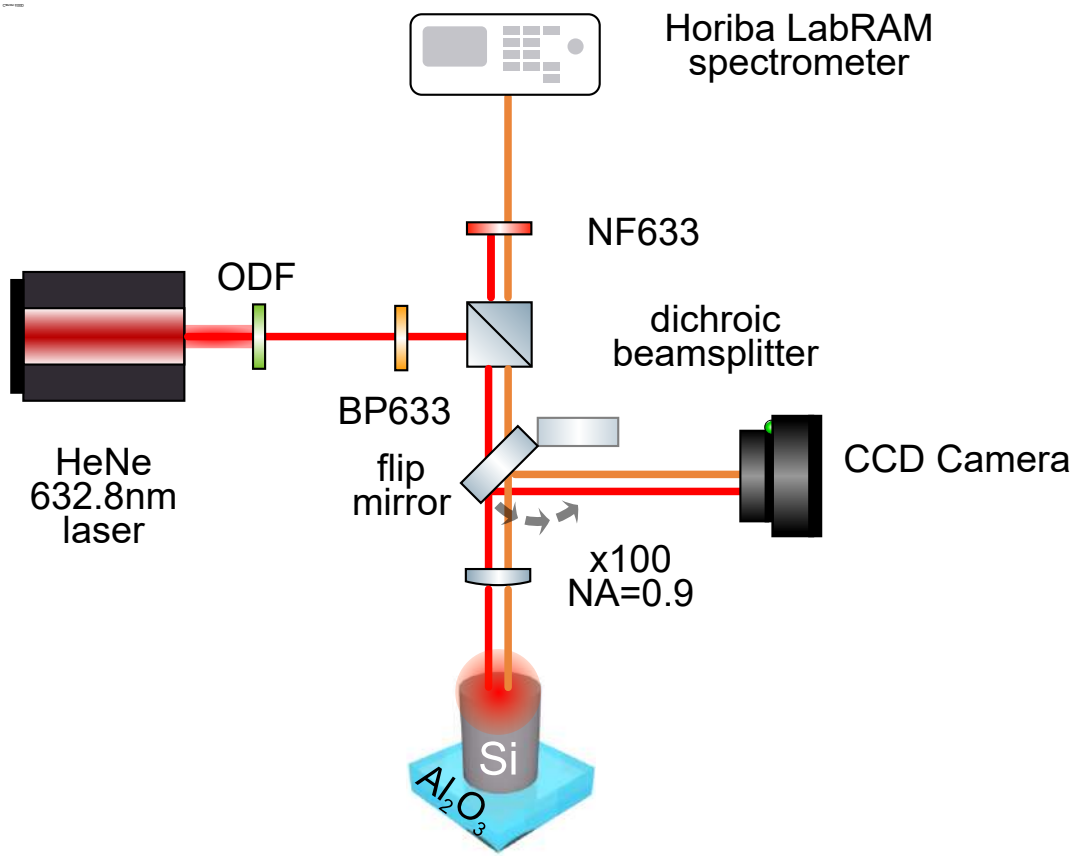

Figure 1.2 — Schematic of the experimental Raman scattering setup.

The experimental setup for Raman scattering and optical heating in nanoresonators is schematically shown in Fig. 1.2. The optical scheme of the setup is similar to the one for dark-field scattering, but the excitation and the collection comes from the upper channel. The HeNe (Melles Griot) linearly polarized laser system with a central wavelength of 632.8 nm and a very sharp peak (beam spectral width less than 0.01 nm) was used.. The excitation goes through the set of neutral optical density filters (ODF) to vary the outgoing laser intensity and then propagates throught the band-pass filter (BP633) which cut any but the 632.8 nm wavelengthns and filters all the possible alterations in the wavelengths. Subsequently, the beam goes from the flipping semi-transparent mirror both to the CCD camera Canon 400D to control the laser-sample position and to the sample through the x100 NA 0.9 (Mitutoyo Plan Apo HR) lens. After hitting the sample, the laser beam reflects

back to the lens in the upper direction without changing its wavelength, and also excites the shifted signal - Raman scattering, which is also collected by the same lens. Further, the mixture of the laser and the Raman scattering reaches the notch-filter (NF633) that permits every wavelength but the 632.8 nm through, therefore only the shifted wavelengths reach the Horiba LabRAM spectrometer for further analysis. The collected signal is further directed on to the 150 g/mm grating for quick analysis, and for deep analysis with high spectral resolution, the 1800 g/mm grating is used.

1.2.3 Raman thermometry

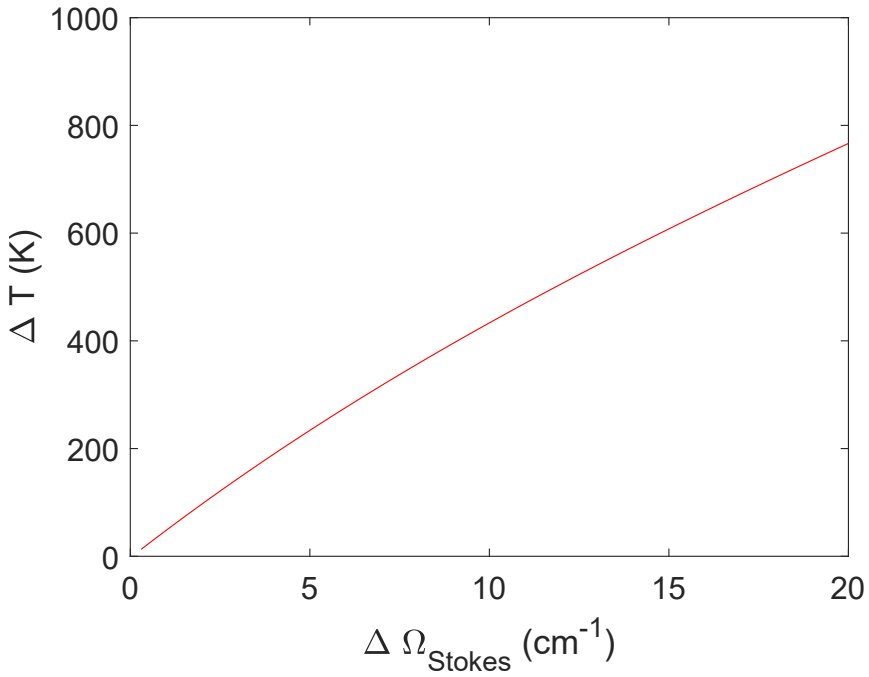

Figure 1.3 — Theoretical correspondence between the Raman spectral shift with reference values - the spectral position at room temperature and the temperature of the nanoobject.

The Raman scattering from the nanoobject can serve for the detection of the local temperature. The presence of the active optical phonons in semiconductors like silicon, allow a pronounced and strong Raman signal at various ambient conditions. Moreover, the presence of the Mie-resonances can significantly increase the signal up to several orders of magnitude [17], therefore being a potential platform for direct nanoscale temperature measurement, since the spectral position of the Raman scattering is highly sensitive to the temperature of the material due to anharmonic effects in lattice vibrations [22].

Fig. 1.3 depicts the correspondence between the temperature and the relative spectral shift of the Raman line for crystalline silicon. Theoretically such relation was obtained by M. Balkanski *et al.* [22] as follows:

$$\Omega(T) = \Omega_0 + A\left(1 + \frac{2}{e^x - 1}\right) + B\left(1 + \frac{3}{e^y - 1} + \frac{3}{(e^y - 1)^2}\right), \qquad (1.76)$$

where Ω_0 = 528 cm^{-1}, A = -2.96 cm^{-1}, B = -0.174 cm^{-1}, $x = \hbar\Omega_0/2kT, y = \hbar\Omega_0/3kT$ for crystalline silicon [22]. This function is plotted in Fig. 1.3.

The difference of the Raman Stokes shift between low-power pump and high-power pump can be converted to the difference of the temperatures (see Fig. 1.3).

1.3 Fabrication and characterization

Of course, the plethora of geometrical shapes of the nanostructures is limited only the researchers' imagination, thus, the shapes proposed in this thesis were mostly quasi-spherical and quasi-cylindrical, as they are the most well-studied and relatively easy to fabricate. "Quasi" refers to the fact that the actual shapes of the nanosctructures obtained from the scanning electron microscopy (SEM) images are neither perfectly spherical nor cylidrical, however, the theoretical calculations of the optical responses or the occuring effects is well described with nanospheres and nanodisks.

1.3.1 Scanning electron microscopy

The morphology, shapes and sizes of the fabricated nanostrucutres were studied by a standard scanning electron microscopy (SEM) system with an electron microscope (Crossbeam 1540 XB, Carl Zeiss).

Most of the SEM images were obtained by Dr. Filipp Komissarenko.

1.3.2 Femtosecond laser ablation fabrication

The spherically-shaped single silicon polycrystalline nanoparticles can be fabricated by means of femtosecond laser ablation [50]. The sphere-like

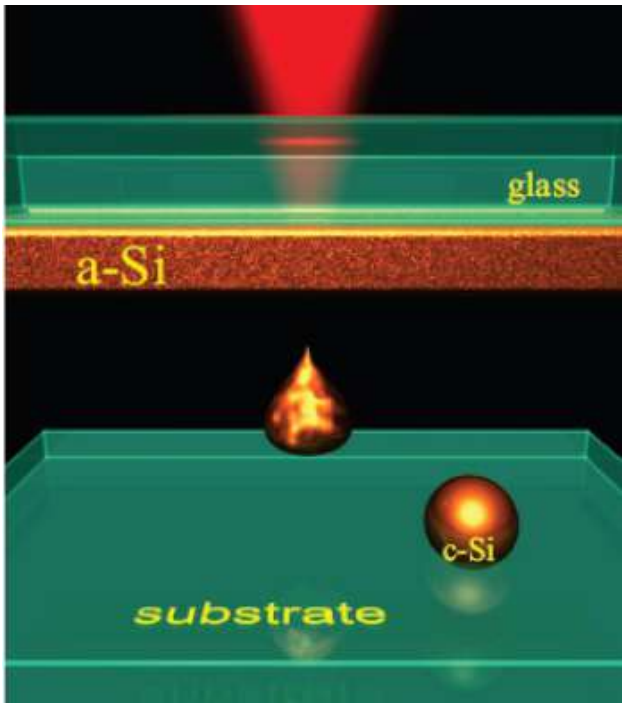

Figure 1.4 — Schematic image of laser-induced forward transfer of silicon crystalline nanoparticles [49].

single polycrystalline silicon nanoparticles were fabricated by means of the so called 'laser-induced forward transfer' method. The basic principle of the method is following [21, 49]: there are two substrates - the donor one, which 'produces' the nanospheres upon intense femtosecond laser irradiation, and the acceptor one, which 'catches' those nanoparticles. Both substrates are Menzel glass coverslips, and the donor one has a deposited homogeneous 100 nm thick amorphous hydrogenized silicon layer. The layer is prepared via plasma-enhanced chemical vapor deposition (PECVD) method from a precursor gas SiH_3, resulting in about 10% of initial concentration of hydrogen. The aerial gap between the substrates can be varied, but usually is about 10 μm. The retraction from the surface and ultrafast boiling (ablation) of the amorphous silicon layer was carried out by commercial Avesta Project TeMa-150 Yb-doped solid-state femtosecond laser with operating central wavelength $\lambda = 1050$ nm, whose repetition rate is 80 MHz and pulse duration is 150 fs. The laser was working in the quasi-single pulse regime, which was provided by a commercial pulse picker system Avesta Project and focused by a 10x lens with NA 0.28 (Mitutoyo Plan Apo) on a a-Si layer with a focal spot diameter of 4-5 μm. As a result of fs-laser interaction with the donor substrate film,

the polycrystalline sphere-like nanoparticles were 'catched' by the acceptor substrate with the size range of 100÷400 nm in diameter.

1.3.3 Lithographical fabrication

In case of cylindrical shapes of the nanoparticles and nanostructures, different lithographical techniques already proved their efficiency. Therefore, only the details differ: whether the substrate were sapphire or SiO_2.

To fabricate the cylindrical zig-zag patterned nanostructures that were studied in the chapter devoted to the optical states probing with Raman scattering, first, an amorphous silicon film of 165 nm thickness was deposited on a quartz substrate using the chemical vapor deposition method (Plasmalab System 380, Oxford Instruments). Electron beam lithography (Elionix, 100 kV) is carried out using a resist (HSQ, Dow Corning, XR-1541-006). The unirradiated portion of HSQ is removed with tetramethylammonium hydroxide (TMAH, 25%). The sample is then etched (Plasmalab System 100, Oxford) to create arrays of silicon nanodisks on a quartz substrate.

In case of a sapphire substrate, where nanodisks were studied for the ability of stimulated Raman scattering another lithographical technique was used. A set of single-crystal silicon nanoparticles (nanopillars and nanodisks) with different diameters placed on sapphire (Al_2O_3) substrates are fabricated by using a top-down technique. An epitaxial structure is grown by molecular beam epitaxy at 600° C using the Stranski-Krastanov growth mode. A set of isolated nanoparticle resonators with with a 10-nm step in diameters is created on the grown epitaxial structure by applying focused gallium ion beam (FIB) milling using a FEI Versa 3D dual beam system. Adjustment of ion current down to 1.5 pA allows to obtain nearly vertical side walls of the nanoparticles.

The proposed lithographical fabrications were done by Dr. Viktoriia Rutckaia, Prof. Arseniy Kuznetsov, Dr. Filipp Komissarenko and Prof. Ivan Mukhin.

Chapter conclusions

This chapter includes most of the fabrication steps for the nanostructures studied in the research, and the characterization techniques and experimental setups for investigation of the effects proposed in the thesis. The proposed methods allow a full study of resonant optical properties of the nanostructures and give comprehensive information regarding their ability for thermally sensitive enhanced Raman response.

CHAPTER 2. MIE-RESONANT OPTICAL HEATING AND RAMAN NANOTHERMOMETRY

2.1 Light-matter interaction at nanoscale

Study of interaction of structured light with micro- and nanoscale solid-state objects gave a boost for development of an alternative platform to conventional electronic devices and signal processing – optical and photonic devices [51]. In order to understand the underlying physics, one should start from characteristic light-matter interaction timescales and intensity scale.

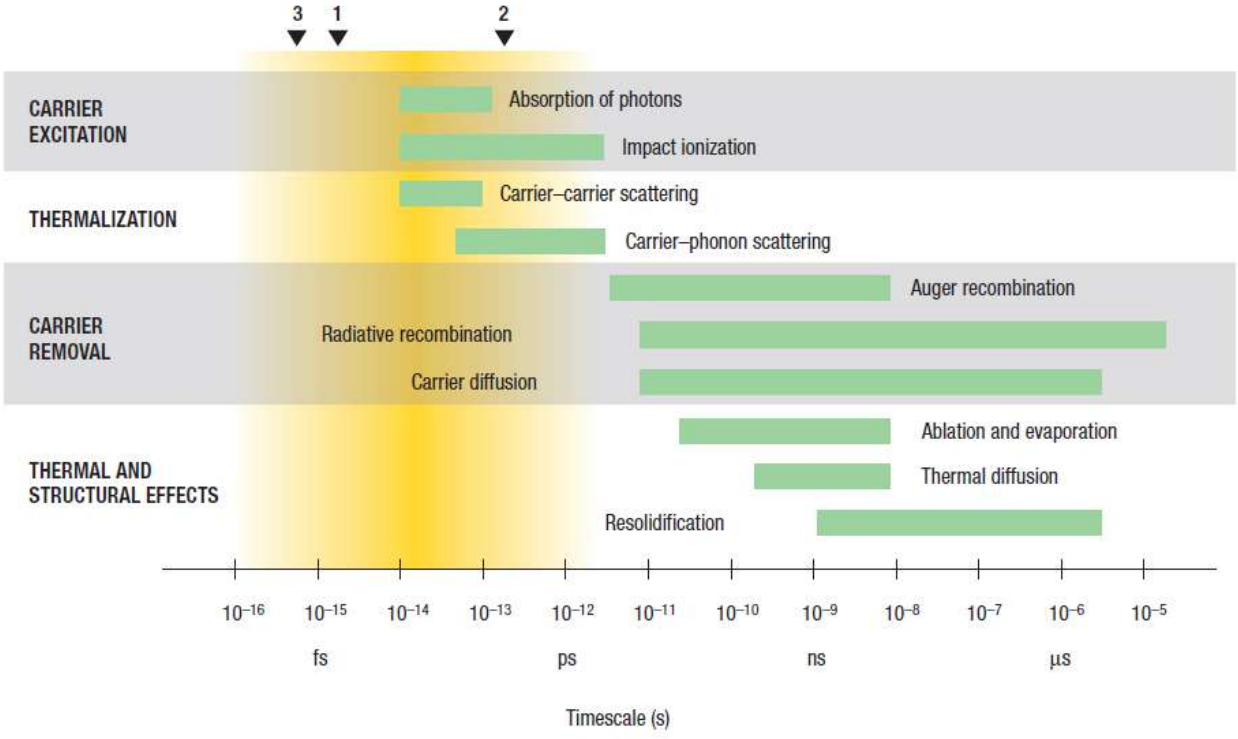

Figure 2.1 — Schematic of different photon-matter interaction timescales. Adopted from [52].

Fig. 2.1, adopted from [52], depicts typical timescales of laser-pulse-excited electron and lattice processes in solid-state materials. The fastest processes are related to electron (carriers) absorption of light and their thermalization. Further, carrier removal mechanisms follow, and the last are thermal and structural effects, which appear of nano- and microsecond scales. In this work, the main results and effects are obtained in stationary state, which

means that the characteristic times are of the order of seconds and the system is in stable condition.

Important feature shown in Fig. 2.1 is thermal and structural effects under intense laser irradiation. They can be schematically described as given in Fig. 2.2.

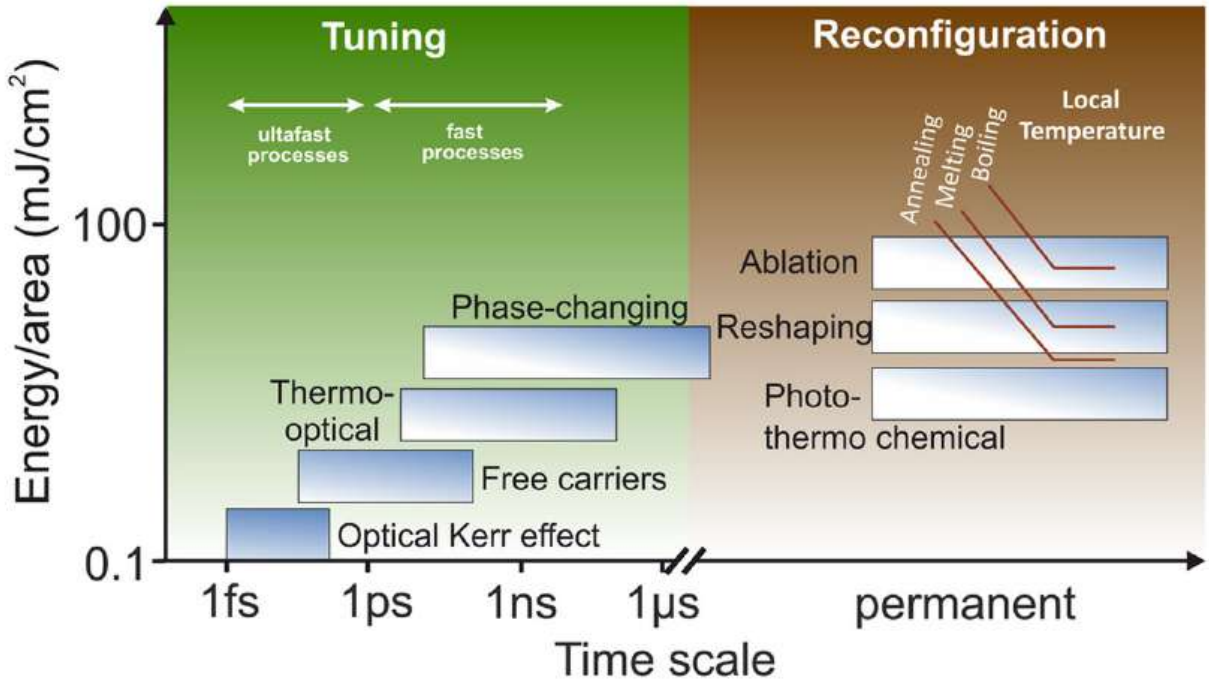

Figure 2.2 — Schematic of different photon-matter interaction timescales. Adopted from [53].

Laser irradiation of solid-state materials can initiate various micro- and macroscopic processes, especially if sharply focused. In such systems, optically-induced electromagnetic nonlinear reversible and irreversible processes of different timescale occur. The fastest nonlinear process among the reversible processes that allows tuning of properties, and, therefore, of optical response, is optical Kerr nonlinearity, which manifests in alteration of refractive index proportional to the square of the field and happens due to the interaction of a high intensity electromagnetic field with the material [54]. A relatively slower process of free carriers generation appears due to electron-hole plasma excitation during light-stimulated band transitions [55]. Other light-induced nonlinear processes occur due to the conversion of light energy to thermal energy resulting in thermo-optical effect or crystalline phase transition [56], for example, the processes in GST materials.

A different type of laser-matter interaction is reconfiguration or irreversible change of structure due to high-intensity laser field applied to the material that results in the release of thermal energy. The first example of irreversible light-stimulated transition is photo-thermo chemical catalysis. Laser excitation of the structures induces some chemical reactions that alter the chemical structure of the material, and, thus, its optical properties [57–59]. Another basic example of irreversible reconfiguration is reshaping due to melting of the material, and the last but not the least is laser ablation at high-intensity laser illumination with ultrafast boiling of the material [60].

This section gave a basic understanding of different timescales and intensities that stand for light-matter interaction. More details will be described later for specific topics.

2.2 Resonant all-dielectric nanophotonics

The section is devoted to the milestone works of the field. Since the main focus of the dissertation is stressed on semiconductor resonant structures for Raman scattering, it is crucial to have general knowledge of the related researches. All-dielectric nanophotonic mostly studies single optically resonant nanostructures - nanoantennas or nanoresonators, and structures supporting collective resonances - metasurfaces [16].

One of the main advantages of finite-size objects that support resonances – nanoresonators – is the ability to localize and enhance electromagnetic field either inside or in the near-field region, therefore substantially enhancing and improving performance for other light emission applications.

Fig. 2.3 depicts use of basic type of resonances - Mie-type - in different light interactions with nanoresonators. After the first experimental observation of ED and MD Mie-resonances in elastic scattering of single all-dielectric nanoparticles [43,44] (Fig. 2.3(a,b)), such approach was used for other optical effects. For example, MD resonance gives a two-fold increase in Raman scattering signal of single silicon nanoparticle in comparison with non-resonant case [17] (Fig. 2.3(e)). Similar performance was observed for nonlinear generation of light, namely second- [10] and third-harmonic generation [9] from

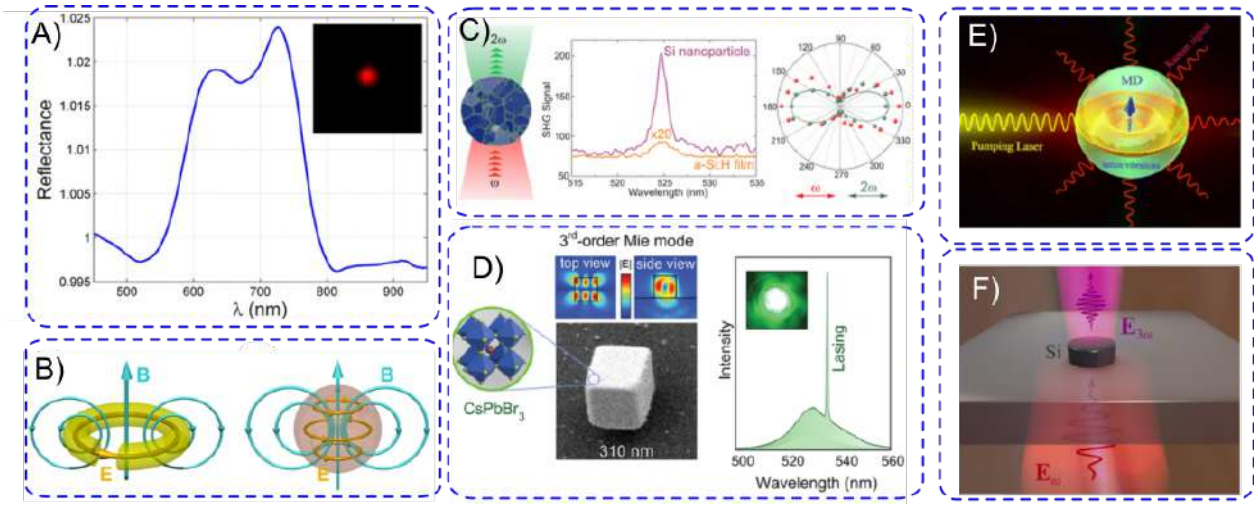

Figure 2.3 — **Mie-resonances in nanophotonics.** a) First experimental observation of Mie-type electric and magnetic dipole resonances (ED, MD) in elastic scattering on single silicon nanoparticle [44] b) Electromagnetic field structure and dipole moments orientation for ED and MD [43] c) Enhanced second-harmonic generation from single silicon nanoparticle supporting Mie resonances [10]. d) Mie-resonant lasing action in all-dielectric perovskite nanocube [7]. e) Schematic of Mie-enhanced Raman scattering from single silicon nanoparticles [17]. f) Schematic of Mie-enhanced third-harmonic generation from single all-dielectric nanodisk [9].

a single resonant all-dielectric nanoparticle, giving significant improvement in efficiency of the generation after reaching resonant conditions (Fig. 2.3(a,d)). At last, it is worth mentioning, that Mie-type resonances can possess relatively high quality factor, therefore they are a possible platform for subwavelength nanolasers [7] (Fig. 2.3(d)).

The described examples of resonantly enhanced optical processes were mostly obtained using the so-called bright modes, i.e. the resonant states that emit light in the far-field, and, therefore, can be externally excited. However, several fruitful approaches have been proposed for achievement of high electromagnetic field localization within the nanoresonator, based on destructive interference in the far-field. Such peculiar optical effects can be obtained via anapole modes or by excitation of a quasi-bound state in the continuum (q-BIC).

Fig. 2.4 depicts application of dark modes in nanophotonics. For example, anapole state in a single silicon nanodisk, with near-zero scattering, supports enhanced Raman scattering [35], or enhanced third-harmonic gener-

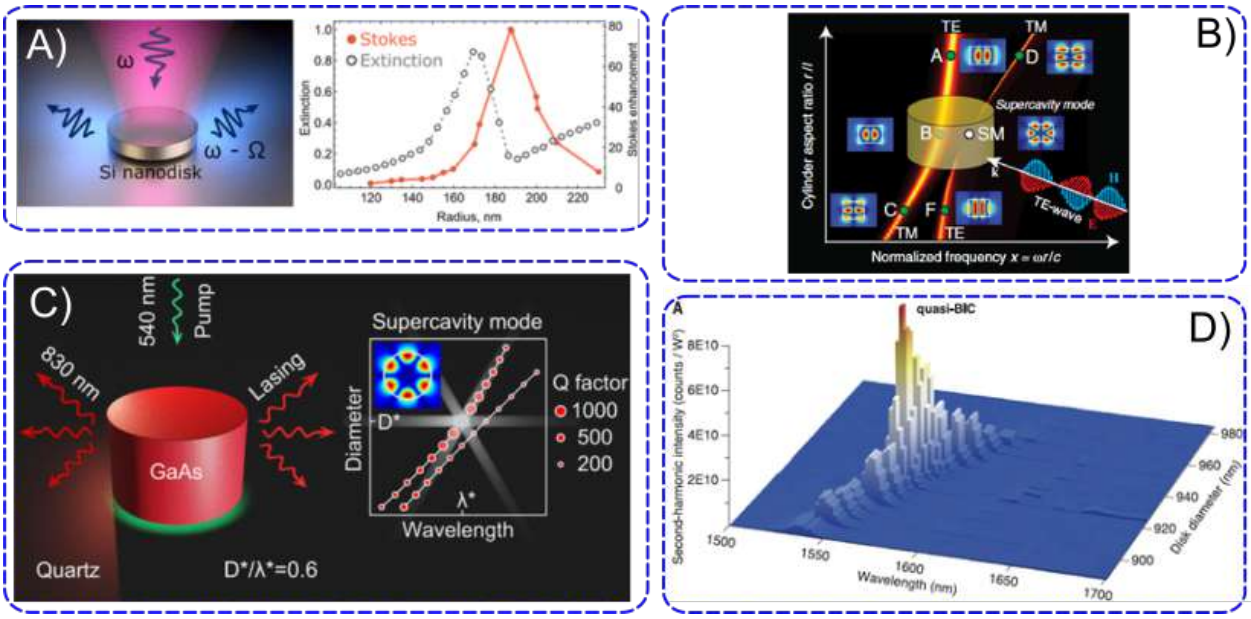

Figure 2.4 — **Dark modes in nanophotonics.** a) Anapole-enhanced Raman scattering from a single silicon nanodisk [35]. b) The schematic of the concept of quasi-BIC state in a single nanoresonator [48]. c) The schematic of BIC-induced lasing in a single all-dielectric nanodisk [8]. d) Enhanced second-harmonic generation from single nanodisk supporting supercavity mode [11].

ation [61]. Another example of dark-mode is the supercavity mode, or quasi-BIC mode supporting very high-Q resonances [48], which making them attractive for nonlinear light generation, such as lasing [8] and record-efficiency second-harmonic generation [11].

Different variations of shapes and excited optical modes in the nanoresonators can be outstanding in performance: namely, for directional scattering [62, 63], for excitation of non-radiating states [64], for extreme thermo-optical tuning [40], enhanced photovoltaic efficiency [65] and improved photoluminescence [12, 13].

The approaches described in this section that are based on single nanoresonators can be extended to collective resonances - metasurfaces. However, this dissertation is mostly devoted to single nanoparticles. Thus, the metasurfaces in nanophotonics field will not be covered.

This section covers main applications of resonant states in single nanoparticles for different nanophotonics areas.

Material (Units)	Melting Temperature	Heat Capacitance	Thermal Conductivity	Thermo-optical coefficient	Thermal expansion coefficient	Eg
	K	J/(g K)	W/(m K)	1e-6 1/K	1e-6 1/K	eV
Si (c)	1687 [66]	0.713 [66]	1.56 [66]	250(>2 mkm) 150 (>2mkm) [67]	2.616 [66]	1.14(i) [68]
Si (a)	1400 [69]	21 J/mol/K [69]	0.018 [70]	-147+485i(@633) 271+225i(@752) [71] +imaginary part	∼1 [72]	1.14(i) [68]
Ge	1210.4 [66]	0.3295 [66]	0.6 [66]	400(>2 mkm) 400-500 (>2mkm) [67]	5.75 [66]	0.67(i) [68]
GaAs	1513 [66]	0.327 [66]	0.45 [66]	250 (@1.15 mkm) [67]	6.03 [66]	1.43(d) [68]
GaP	1730 [66]	0.313 [66]	0.77 [66]	160 (@0.63 mkm) [67]	4.89 [66]	2.26(d) [68]
CdTe	1365 [66]	0.211 [66]	0.075 [66]	147(@1.15 mkm) [67]	4.7 [66]	1.49(d) [68]
PbTe	1197	0.0031 [73]	0.0198 [73]	-1.4e3 (>6mkm[1]) [74]	19.8 [75]	0.32(d) [75]
Ge2Sb2Te5 (a,c)	900K (a->c ∼400K) [76, 77]	0.212 [78]	0.0019, 0.0057-0.015 [79]	a: \deltaK = (1.17+-0.03)*10-5 K-1 \delta n = 3.5*1e-5 c: \deltaK = 1.13*1e-4 \delta n = -6.5*1e-5 (@1.55 um) [56]	2 – 7 [80]	0.95(d) [68]
$MAPbCl_3$	380 C [81]	0.492 [82]	0.0046 [82]	300 [82]	30 [83]	3.15 [82]
Au	1337 [5]	0.129 [5]	3.18 [5]	-300 – -700 [84]	14 [85]	Metals
Ag	1235 [5]	0.24 [5]	4.29 [5]	-300 – -700 [86]	18.9 [85]	
Al	933 [5]	0.9 [5]	2.37 [5]	thermoreflectance @780nm	23.3 [85]	

Table 2.1 — Properties of the common materials for thermophotonic applications. Parameters are taken at ambient conditions if not noted elsewise.

2.3 Introduction to all-dielectric thermal nanophotonics

In recent years, dielectric nanophotonics gained high interest due to the ability for light concentration inside the nanoscale resonators, in contrast with plasmonic nanoantennas. Due to the excitation of different optical resonant modes inside the semiconductor nanostructures upon laser irradiation, considerable field enhancement can be possibly observed. However, these structures turn out to be highly efficient for optical heating and thermometry at moderate intensities. In this review, we cover the recent progress in the field of newly arising all-dielectric thermal nanophotonics, which contains theoretical approach in optimization of optical heating process, as well as experimental verification and simultaneous thermometry at the nanoscale. We believe that such approach can serve as an effective platform for single-step optical heating-nanothermometry applications and overcome major drawbacks of thermoplasmonics in general.

Here we discuss the main physical properties of bulk semiconductor and dielectric materials, which have key importance in the relation to thermophotonics. We will consider direct and indirect semiconductors as common

materials used in nanophotonics, and also will focus on actively developing phase-changing GST materials and halide-perovskite materials. The list of the discussed materials along with their parameters are summarized in Table 2.1. We also provide the data for typical metals for future comparison with the thermoplasmonics.

The resonant response of nanostructures is one of the main requirements for their utilization in nanophotonic systems. In the absence of surface plasmon resonances, which are typical for highly conductive nanomaterials, the non-plasmonic nanostructures possess the dielectric-type Mie resonances defined by the geometric condition for resonant wavelength $\lambda_0 \sim \mathrm{n}D$, where n is the real part of the refractive index of the nanoresonator material, and D is the linear size of the nanostructure (for nanospheres - diameter). Thus, the non-plasmonic materials efficient enough for nanophotonics applications are usually selected among high-index materials [87], which provides compact and high-Q resonators. The high refractive index is usually achieved in narrow band-gap materials [88], which also defines their spectral operation region as above the band edge, where the losses can be extremely high, thus suppressing any optical resonances. Nevertheless, for the thermo-optical applications, losses play a dual role: on the one hand, they destroy the resonances, and on the other hand, they are responsible for thermal heating.

2.3.1 Tunable optical losses

The origin of optical losses in non-plasmonic materials in visible and infrared regions is mainly related to the mechanisms of inter-band or intra-band electron absorption. While the former are related to valence-to-conduction band transitions or to excitonic transitions, the latter are connected to absorption of light by free carriers present in semiconductors.

A beneficial property of non-plasmonic materials is their ability for tuning the optical losses. Although the inter-band losses are normally provided by the band structure of the solid and hardly can be varied, the excitonic absorption can be varied in a wide range by tuning the excitonic transition in perovskite materials [89, 90]. More conventional methods of intra-band ab-

sorption tuning require doping - intentional introduction of impurities into an intrinsic semiconductor for the purpose of modulating its electrical, optical and structural properties, thus allowing effective alternation of the band structure [91, 92]. In Fig. 2.5 the spectral dependences of the optical absorption in c-Si and GaAs are shown for different values of the doping level. One can see that for the short-wavelength region the interband indirect optical transition govern the optical losses and are almost independent of the doping level. For the photon energy below the band gap, the intra-band free carrier absorption becomes dominant, and doping drastically increases the absorpion. Despite that, in the whole spectral region of interest the optical losses of gold prevail over the losses in the semiconductors. The doping of semiconductors also results in the change of the real part of the refractive index, which stays relatively low in the visible-NIR spectral regions. The ability to tune the losses can be efficiently used for controlling the optical heating of the nanostructure, which will be discussed in details below.

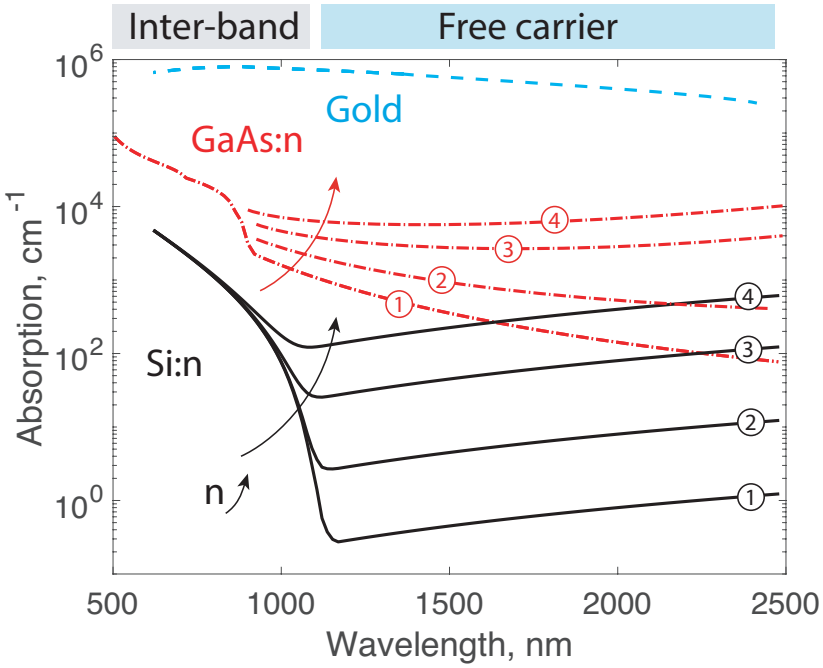

Figure 2.5 — **Light absorption in Au, c-Si:n, and GaAs:n.** The absorption curves for different level of doping are shown: $1 \div 10^{-17}\text{cm}^{-3}$; $2 \div 10^{-18}\text{cm}^{-3}$; $3 \div 10^{-19}\text{cm}^{-3}$; $4 \div 5 \cdot 10^{-18}\text{cm}^{-3}$;

2.3.2 Light emission as a thermometry tool

The non-metallic materials provide the intense sources of light emission. Photoluminescence and Raman scattering are of strong interest within this section. These mechanisms are defined by the crystalline and electronic structure of the materials and are highly sensitive to the temperature changes, which underpins the nanoscale thermometry.

The probing of photoluminescence temperature works as following: a direct band-gap quantum dot or nanostructure absorbs incident light with subsequent exciton generation and further re-emits light, according to the excitonic energy and the band gap. Different thermal conditions in the surrounding media result in spectral and intensity shifts of the photoluminescence spectrum, which can be detected and converted into the temperature [93–95].

Another example of thermally sensitive light emission from semiconductor structures is Raman scattering. Generally, Raman response is inelastic scattering of incident light on crystal lattice phonon, thus, the higher the purity and crystallinity of a nanostructure are, the higher the quality factor and intensity of the Raman response. The Raman scattering allows measuring temperature either by the spectral shift of the Stokes signal [21, 22] or by Stokes/anti-Stokes ratio [96]. However, single resonant semiconductor nanoparticle can significantly enhance Raman scattering by more than 100 times compared to the non-resonant case [17], thus making the detection of temperature via comparison of Stokes and anti-Stokes scattering signals complicated.

It is worth mentioning that the proposed thermally sensitive light emission processes allow temperature detection both at relatively low and high laser pump intensities. High intensities and temperature broadens the emission spectra and lowers the Q-factor, making detection quite challenging.

There are plethora of optical techniques for thermometries at nanoscale; however, we believe that the most applicable methods for single resonant nanostructures are based on intrinsic Raman scattering (see Sec. 1.2.3 for more details) and photoluminescence of the nanoresonators. First, such methods do not require extra functionalization or fabrication steps - the generated

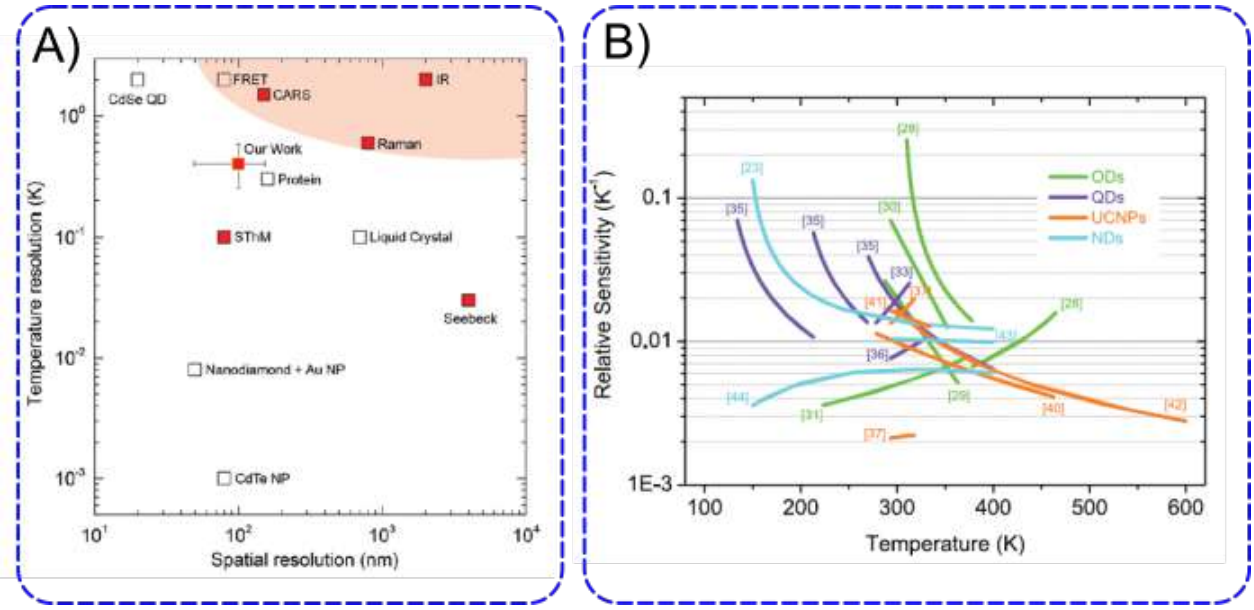

Figure 2.6 — a) Resolution and precision comparison of optical thermometry techniques adopted from [30]. B) Comparison of sensitivities for optical thermometries based on quantum dots, up-conversion nanoparticles and nano-diamonds [97].

signal is inherent to the material. Secondly, thermometry cycles are unlimited, contrary to the thermometries based on dye molecules. At last, a single laser source can be used both for pumping of the optical heating and Raman or PL generation. The spatial resolution of the thermometry based on PL or Raman scattering is mostly governed by the sizes of the structures, whereas the temperature resolution is limited by the spectral width of the emitted signal and the resolution of the spectrometer. Comparative analysis for various thermometry techniques is shown in Fig. 2.6.

Another Raman nanothermometry approach is based on the comparison of Stokes and anti-Stokes signal intensities. It is known that anti-Stokes/Stokes Raman signals ratio increases with growth of the temperature of crystallized dielectrics (e.g. silicon [98]). Because of Boltzman distribution of phonons population, an exponential dependence on temperature is observed for this ratio:

$$\frac{I_A}{I_S} = e^{-\frac{\hbar\omega_0}{kT}}, \tag{2.1}$$

where I_A and I_S are the intensities of anti-Stokes and Stokes signals, respectively, $\hbar$ is the reduced Planck constant, ω_0 is optical phonon frequency of silicon, k is Boltzmann constant and T is temperature.

Remarkably, Raman signal can be strongly enhanced at optical resonances in all-dielectric designs [17, 35, 41, 99]. However, this property can reduce the accuracy of such an intensity-based method as Stokes/anti-Stokes thermometry at high temperatures because of thermo-refractive effects, which change resonant properties of dielectric nanostructures and, thus, the efficiencies of Raman scattering at different wavelengths in a different manner.

The last thermometry based on Raman scattering that is worth mentioning for single resonant nanoparticles is the combination of optical and mechanical processes. The tweezed silicon nanorod can exhibit mechanical rotation, and the heating temperature of the nanorod trapped by the laser source can be extracted both via Raman scattering and analysis of the rotational motion.

This section covers basic principles of light emission from all-dielectric and semiconductor nanoparticles. The analysis and the understanding of the connection between emission and thermal properties of the particles allows one to extract the temperature profile of the object at the nanoscale with sub-10 Kelvin resolution.

2.3.3 Thermo-optical effect

At the elevated temperatures, the optical constants of the solids generally cannot be considered as constant and start to depend on temperature, which is referred to as *thermo-optical effect*. There are several physical mechanisms lying in the origin of this effect. One of the most important is related to the dependence of the electronic band gap on the temperature [100] due to the thermal expansion of lattice. This effect, along with the temperature-dependent Fermi level, gives the most significant contribution in thermo-optical effect in semiconductor materials. Another contribution is related to the increased scattering rate of electrons in solids due to the enhanced phonon scattering, however, this mechanism is more important in metals, where the electron concentration stays almost constant.

Upon the alterations in the temperature, both real and imaginary parts

of the refractive index change according to the following expression:

$$\Delta n \;=\; \Gamma(T - T_0), \quad \Gamma = \left.\frac{d\mathrm{n}}{dT}\right|_{T_0} \tag{2.2}$$

where Γ is the complex thermooptical coefficient. A conventional semiconductor, such as crystalline silicon, possesses a relatively high Γ. The value for the real part is $4.5{\cdot}10^{-4}$ K^{-1} and the imaginary part is $0.1{\cdot}10^{-4}$ K^{-1} [101, 102]. In comparison, other conventional semiconductor, GaAs, possesses 4 time lower value of the thermooptical coefficient. The values of the thermo-optical coefficients are summarized in Table 1. One can notice that the most of the semiconductor materials have a positive real part of Γ. Thermal expansion leads to larger interatomic distances and, thus, to weaker interaction between the electronic states and consequent decrease in the band gap. The well-known general law describing the temperature dependence of the band gap is as follows:

$$E_g(T) = E_g(0) - \frac{\alpha T^2}{T + \beta},$$

where α and β are material-dependent constants. The simple reasons related to thermal expansion provide that for the majority of materials $\alpha > 0$, which results in positive thermo-optical coefficient $\Gamma' > 0$. However, there is a number of materials where the temperature dependence of the band gap has anomalous form and, for instance, $\alpha < 0$ resulting in $\Gamma' < 0$. One can see that PbTe is one of such materials, with negative thermo-optical constant being several times higher in absolute values [74, 103] compared to others materials. Recently, a high negative thermo-optical constant of lead halide perovskites was also reported [82].

From the point of heating a resonant nanostructure, the temperature change of the refractive index leads to thermal drift of the resonant wavelength:

$$\frac{\Delta\lambda_0}{\lambda_0} \sim \left(\frac{1}{\mathrm{n}}\frac{d\mathrm{n}}{dT} + \frac{1}{D}\frac{dD}{dT}\right)\Delta T.$$

Here, the first term corresponds to thermo-optical coefficient, while the second one is related to thermal expansion coefficient and related change in geometrical size of the nanostructure. It allows, for instance, the tuning from non-

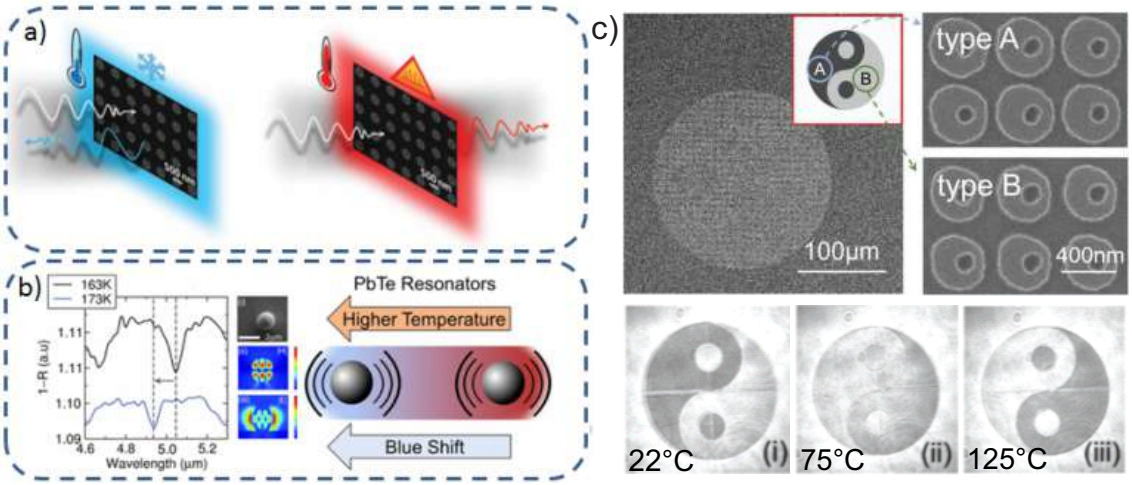

Figure 2.7 — **Thermal tuning of metaoptical devices.** a) Illustration of the temperature effect on the far-field optical properties of metasurfaces by employing the actual scanning electron microscope (SEM) image. By cooling or heating the metasurface sample, one can operate in either the reflection or transmission regime, respectively [104]. b) Ultrawide spectral tuning of resonances via heating of semiconductor meta-atoms [103]. c) Upper row: SEM images of the fabricated Yin-Yang pattern with slightly different geometries of the two parts. Lower row: optical images of the metasurfaces obtained at 784 nm at different temperatures [105].

radiating to super-radiating states as shown in [40] on a single nanoresonator. From Table 2.1 one can see that normally, the thermal expansion coefficient is smaller than the thermo-optical constant, but their contributions to the relative wavelength shift may be comparable. The recent findings show that among other materials, perovskite structures may possess quite high value of thermal expansion coefficient $250 \cdot 10^{-6}$ K^{-1} [83].

Among the possible applications for thermo-optical effect is the tuning of the optical resonances spectral position in an ultrawide range, as shown in Fig. 2.7(b). At higher temperatures, the meta-atom's optical response shows a significant blue shift [103]. Same feature can be realized for full transparency - full reflection switching for all-dielectric metasurfaces [104]. Similar approach can be realized for asymmetric meta-atoms for application in visualization, as shown for a metasurface of Yin-Yang shape [105].

This section briefly covers some of the works related to thermo-optical tuning of light responses of nanophotonic structures, showing the potential of such approach for efficient reversible tuning.

2.3.4 Temperature-driven phase transition

Another advantage in comparison to the plasmonics related to the possible degree of freedom for tunable optical heating and resonant response inherent for semiconductors is temperature-driven phase transitions. Schematically, we will divide them into four main thermally-driven phase-transitions: i) melting ii) crystalline-to-amorphous transition (annealing) iii) reversible phase transitions in GST or similar materials iv) crystalline lattice phase transitions in perovskite-like structures.

Upon intense laser irradiation materials tend to experience changes in their properties and structure when the local temperature exceeds the threshold value. Such changes in the properties upon reaching certain temperature are called phase transition. A conventional and well-known example of a phase transition is the melting-crystallization process. The process is reciprocal and the material can melt and recrystallize upon heating and cooling, respectively.

However, there are also different types of phase transitions that are not manifested by visual differences and hardly can be detected. These types of phase transition occur between crystalline and amorphous phases of the material. Such phase transitions in materials supporing glass-transition effect are very prospective for designing new photonic nanostructures.

The described phase transitions were demonstrated in c-Si spherical NPs, that were fabricated by a fs-laser forward transfer [50, 106]. The transition from a-Si to c-Si is manifested optically via slight changes in the refractive index in the visible and near-IR spectral range. The nature of the process is the following: in the c-Si state, the electron transitions in the range from 1.1 eV to 3.4 eV are indirect, thus the radiative transition can be only phonon-assisted. In contrast, in the a-Si state, the wave vector conservation is not supported, thus making these transitions possible, which results in the stronger optical response [107].

If we consider the numbers - the values for the permittivities in both cases - crystalline and amorphous, they differ quite a bit: $\varepsilon_{\mathrm{a-Si}} = 16.5$ to $\varepsilon_{\mathrm{c-Si}} = 14$ in the visible range. Spectrally, such difference in permittivities can shift the position of the Mie resonance in scattering response more than

50 nm as shown in Fig. 2.8(a) [50]. Zywietz *et al.* printed an equidustant array of the a-Si nanospheres. The fabricated nanospheres supported the same MD Mie response in the same wavelength region. However, the subsequent laser-induced phase transition to c-Si state in the array of these a-Si NPs resulted in spectral shift of the Mie-resonances, therefore changing the color of its microscopic scattering images. This behavior was also employed to modify locally optical properties of individual a-Si nanoparticles to create a picture "Si" as shown in Fig. 2.8(b).

Further, the approach of local thermally-induced phase switching was applied to record various complicated colorful patterns with amorphous Si nanoparticles prepared by nanolithography [108]. This method is quite useful because it allows creating of c-Si nanoparticles on an arbitrary substrate (e.g. glass) without employing silicon-on-insulator or silicon-on-sapphire technologies nor any transfer techniques. Additionally, this technique allowed for local laser annealing of amorphous silicon nanoparticles with *in situ* control of temperature and crystalline state via generated Raman signal analysis [32].

There is another example of phase transitions that should be mentioned. The special compound of germanium (Ge), antimony (Sb) and tellurium (Te) - shortly GST - support non-volatile reversible amorphous-to-crystalline phase transitions forth and back. Such modulations between crystalline and amorphous phases in GST materials attracted a great attention in last years.

In contrast to the moderate change in optical and electrical properties of amorphous and crystalline phases of silicon, amorphous and crystalline GST alloys have significant differences in permittivities [109, 110]. This alteration of permittivity upon phase transition is highly attractive for nanophotonics application. For example, the optical response can be significantly tuned spectrally with the crystallization process as shown in Fig. 2.8(c) [111] and can be modulated from complete reflection to complete transmission for metasurfaces made GST disks as shown in Fig. 2.8(d) [112].

Due to low losses for $\lambda > 1.5$ μm, the GST-based nanophotonic designs employing optical resonances can operate in the near-infrared range.

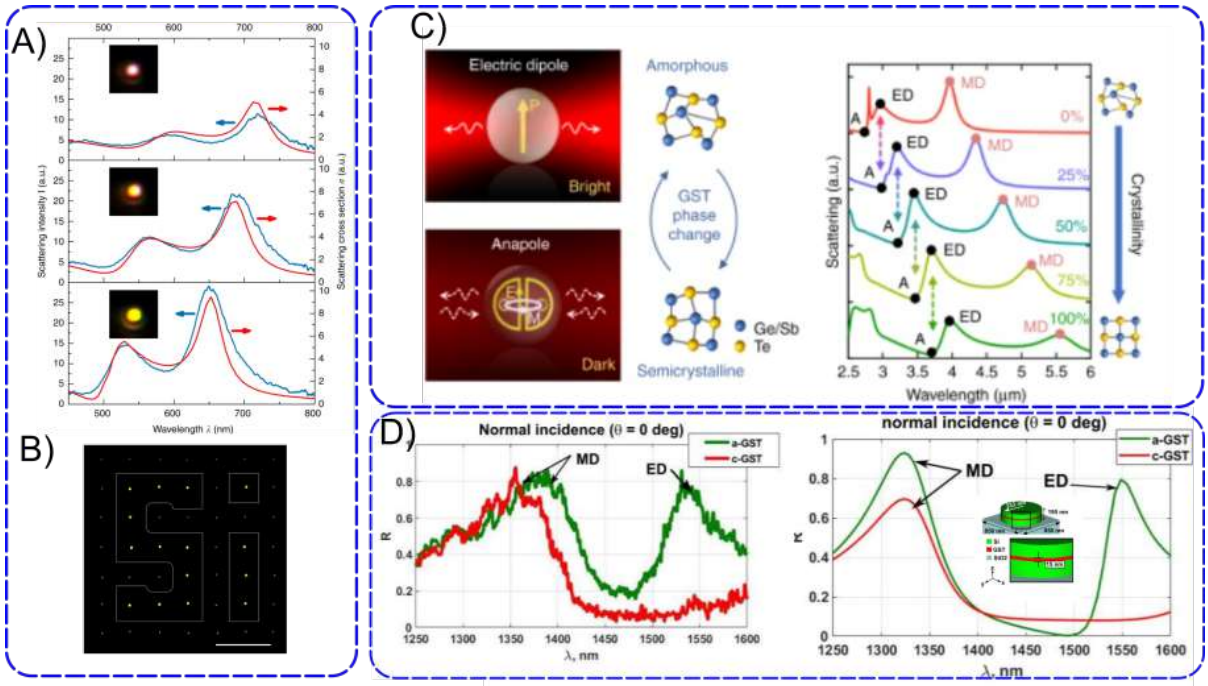

Figure 2.8 — **Phase-changing of nanoparticles.** a) Experimental (blue) and theoretical (red) scattering spectra of spherical Si nanoparticles. b) Dark-field image of the fs-laser printed Si NPs. The nanoparticles in the 'Si' shape figure are crystallized by another laser pulse [50]. c) Numerical scattering spectra of a single GST nanodisk for different crystalline states [111]. d) The reflection spectra for the metasurface fabricated of hybrid Si/GST nanodisks, supporting phase transitions that are manifested by the modulation of the reflection [112].

Recently, it was demonstrated that a metasurface working in the near-IR region where the optical losses for GST materials are low, can support low-order resonances [113]. The fabricated metasurface was designed so that it supported resonant features both for transmission and reflection at $\lambda = 2\mu$m for specific polarization, and non-resonant behavior for other linear polarizations. However, for shorter wavelengths, the structure did not support scattering in non-zero diffraction orders [114], therefore acting as a metamaterial [113].

In the work of Tian *et al.* [111], it was demonstrated that the structures from GST material can support a number of different optical Mie-modes and allow for active *in situ* tunability. The significant difference in dielectric permittivities of the crystalline and amorphous phases resulted in a broadband ($\Delta\lambda/\lambda \sim 15\%$) spectral shift of the resonance position (see Fig. 2.8(c)).

In order to shift from IR to visible range, a new concept in all-dielectric

optical metasurfaces was introduced and experimentally validated based on a hybrid combination of high-index and low-loss dielectric building blocks with embedded subwavelength inclusions of chalcogenide phase-change materials. [112] By using this hybrid approach, the authors were able not only to provide on-demand dynamic control of light amplitude, but also to deliver a very high efficiency of operation over a very wide spectral range by a judicious material choice. The authors demonstrated the flexibility and universality of our approach by the design and development of hybrid metasurfaces for applications as switchable spectral filters in the near-infrared and dynamic color generation in the visible spectrum.

2.4 Laser heating and Raman nanothermometry by Mie-resonant nanostructures

This section is devoted to the main analysis of the optical heating phenomena of all-dielectric and semiconductor nanoresonators, which were considered as lossless and inefficient in light-to-heat conversion applications. The optimization of Mie-resonances with material parameters can result in highly laser heating of all-dielectric nanoparticles.

The basic principle of light heating and absorption for single spherical nanoparticle in homogeneous surrounding environment was developed and tested before [19, 20].

All-dielectric nanoparticles can support strong resonant responses in the visible range, therefore, their light absorption can vary dramatically. In this regard, the analytical solution for the continuous-wave laser heating of a single spherical NP can take into account the resonant nature of the NP. As a result, the exact solution for the temperature increase of the spherical NP with diameter D in a steady-state heat diffusion equation, infinite external boundary conditions and a pre-defined plane-wave source with incident intensity (I), the NP absorption cross-section (C_{abs}) defined by Mie theory, the known thermal conductivity of the surrounding medium κ_2, in case the thermal conductivity of the NP is much greater than that of the environment, can be found as follows:

$$\delta T_{NP} = \frac{IC_{abs}}{2\pi\kappa_2 D}. \tag{2.3}$$

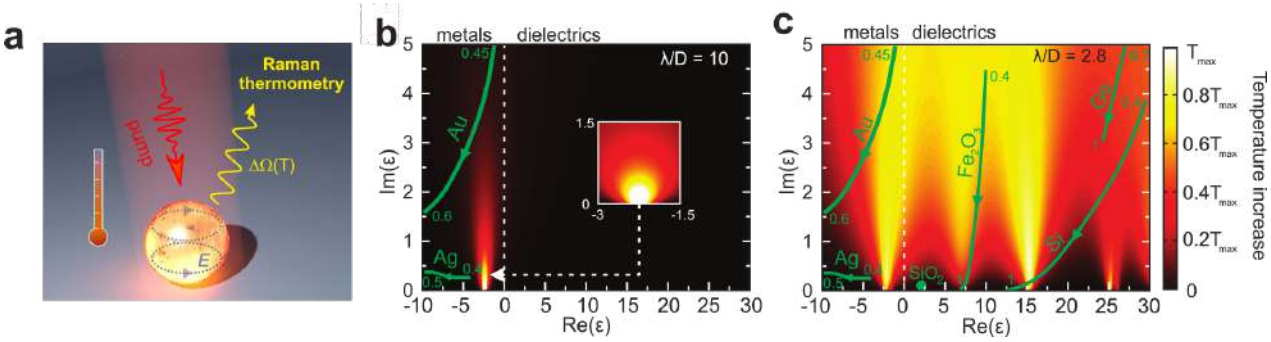

Figure 2.9 — **Optical heating of spherical NPs.** (a) Schematic of the optical heating and thermometry concept. Calculation results for theoretical optical heating in homogeneous aerial environment for single spherical NPs with fixed wavelength/diameter ratios λ/D as a function of various real and imaginary parts of the permittivity: (b) $\lambda/D = 10$; (c) $\lambda/D = 2.8$. The green arrowed lines in b) and c) correspond to values of $\mathrm{Re}(\varepsilon)$ and $\mathrm{Im}(\varepsilon)$ for specific real material dispersions. The direction of the arrows corresponds to increase of the wavelength. The numbers indicate the wavelength region in microns. Adopted from [21].

The results of the optical heating calculations can be found in the colormaps depicted in Fig. 2.9(b,c). The optical heating temperature for spherical nanoparticle in aerial media of different real (from -10 to 30) and imaginary (from 0 to 5) parts of permittivity in case of small nanospheres (wavelength/diameter ration = 10) are shown in Fig. 2.9(b), and the same calculations, but for the larger NPs, where the wavelength-to-diameter ratio is 2.8, are shown in Fig. 2.9(c). While the size of the NP is still too small to support Mie resonances, only nanospheres with negative real part of permittivity (metals) support optical heating, which one can clearly see from Fig. 2.9(b). However, upon increasing the diameter of the NPs until wavelength-to-diameter ratios reaches $\lambda/D = 2.8$ (Fig. 2.9(c)), the hot sopts appear in the region of positive real part of the permittivity, which correspond to the dielectric and semiconductor materials. This happens due to excitation of different Mie modes in the nanosphere. What is more fascinating about this results is that the increase of the imaginary part of the permittivity does not necessarily lead to the total increase of the optical heating temperature.

For deeper understanding of the underlying physics and the explanation

of the origin for efficient optical heating of materials that are considered to be lossless, i.e. all-dielectrics and semiconductors, upon resonant laser excitation of Mie modes, one should start the consideration from the classical general expression for the absorbed electromagnetic power P:

$$P = \frac{1}{2}\mathrm{Re}\int_V \mathbf{J}^*(\mathbf{r})\mathbf{E}(\mathbf{r})dV \tag{2.4}$$

where $\mathbf{J}(\mathbf{r})$ stands for the current density, $\mathbf{E}(\mathbf{r})$ is the electric field inside the object, and the integration is performed over the volume of the considered nanoobject V. The expression in Eq. 2.4 gives understanding that the higher electromagnetic field inside the nanoobject and higher the current density is, the greater the total absorbed power is. Moreover, one should keep in the mind that $\mathbf{J} = \sigma\mathbf{E}$ and $\sigma = \varepsilon_0\omega\mathrm{Im}(\varepsilon)$, where ε_0 is the vacuum permittivity, ω is the incident light frequency and σ is the electric conductivity.

The integration of Eq. 2.4 over an arbitrary NP volume supporting Mie modes allows to modify the Eq. 2.4 in terms of an effective mode volume V_{eff} and spatially-averaged field enhancement factor $F = < |E|^2 > / |E_0|^2$, which gives information on the amount of energy that can be stored inside the NP and where $|E_0|$ is the incident electric field magnitude. Therefore, one can modify Eq. 2.4 for the total absorbed power as follows:

$$P \sim \sigma F^2 \, V_{\text{eff}}. \tag{2.5}$$

The total absorbed power now has 3 different independent contribution factors σ, F^2 and V_{eff}, which all have significant influence on total optical heating temperature δT_{NP}. The following subsections will consider all the factors separately.

The nonradiative losses factor. As it was shown by the expression in the Eq. (2.5), the increased Ohmic losses do not necessary raise the total absorption of light by the NP, the same goes for the total optical heating. If we consider the increase of the imaginary part of the permittivity, that would necessary lead to increase of the electric conductivity; however it would also significantly affect the resonance quality factor Q by reducing it, therefore lowering the σF^2 factor. Thereby it should be examined in more details.

The optical resonances can be described by the 'toy model' of the oscillator with friction, with some assumptions. Therefore, near the optical resonance frequency ω_0, the field enhancement factor F can be expressed as $F \sim 1/\left(\omega_0^2 - \omega^2 - i\omega\gamma\right)$, where γ stands the total optical losses of the system. If one looks more closely, the total optical losses have two general contributions: $\gamma = \gamma_{\text{rad}} + \gamma_{\text{ohmic}}$, *radiative* and *nonradiative* (or *Ohmic*) losses. The nonradiative part is proportional to $\text{Im}(\varepsilon)$, thus σF^2 factor at the resonant frequency ω_0 is proportional to $\sim \gamma_{\text{Ohmic}}/(\gamma_{\text{Ohmic}} + \gamma_{\text{rad}})^2$, thereby, one can see that very high Ohmic losses lead the total absorbed power to zero.

The direct and pretty simple assumptions lead to following: at the certain value of γ_{rad}, the maximum value that the factor $(\sigma F^2)_{\text{max}}$ can reach $\sim 1/(4\gamma_{\text{rad}})$. The maximum value is achieved when the $\gamma_{\text{Ohmic}} \approx \gamma_{\text{rad}}$. Radiation losses γ_{rad} can be minimized by taking a resonant nanoparticle whose size is much smaller than the wavelength λ. This can be obtained in case of plasmonic NP supporting localized surface plasmon resonance (LSPR) with a given plasma frequency ω_p, where $\gamma_{\text{rad}} \ll \gamma_{\text{Ohmic}}$. At the LSPR, the γ_{rad} is equal to $\approx \omega_0^3/\omega_p^2(\pi D/\lambda)^3$. This analysis leads to the fact that γ_{rad} is relatively small compared to ω_0 due to the ratio $(D/\lambda)^3$.

Indeed, these predictions and estimation are proven analytically and can be seen in Fig. 2.9(b), where in case of relatively small NPs ($\lambda/D = 10$) the resonance occurs only in the region of negative real part of the permittivity $\text{Re}(\varepsilon)$, and highest temperature value is achieved at relatively small values of imaginary part of the permittivity $\text{Im}(\varepsilon)$, where $\gamma_{\text{Ohmic}} \approx \gamma_{\text{rad}}$.

The opposite scenario appears for bigger NPs, which can be seen in the Fig. 2.9(c). The presence of the hot spots for optical heating in positive range of real part of the permittivity means that semiconductor NPs can be optically heated very efficiently. For example, radiation losses γ_{rad} for dipole modes is rather high, and highest temperature is achieved at bigger Ohmic losses. On the other hand, if one considers higher-order resonances, e.g. MQ, one should expect smaller γ_{rad}, and, therefore, the optimal laser heating would appear lower values of γ_{Ohmic}. The latter one can bee seen for higher $\text{Re}(\varepsilon)$ in Figs. 2.9(b,c).

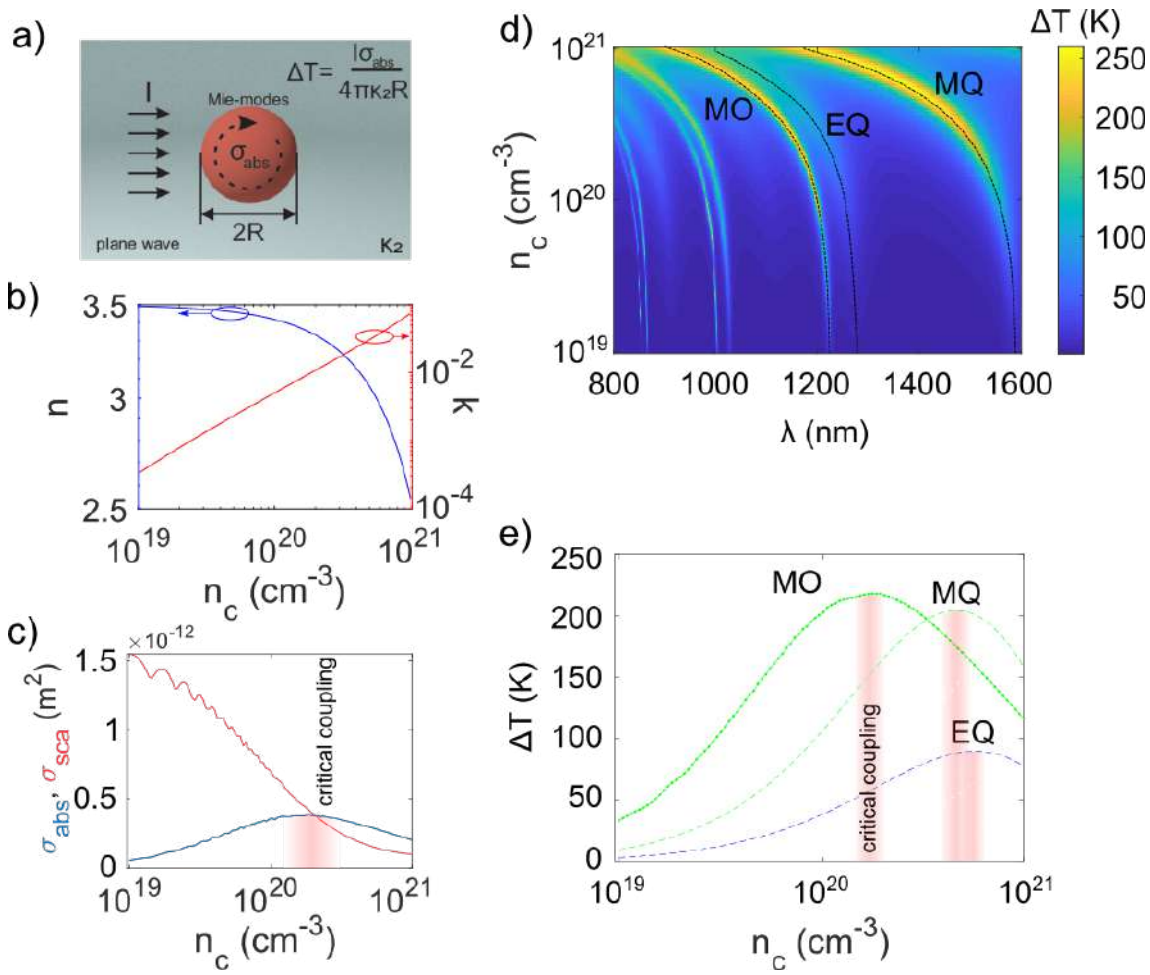

Figure 2.10 — **Semiconductor doping.** a) Schematic of a spherical nanoparticle optical heating by plane wave irradiation in homogeneous media. Picture adopted from [31]. b) Real (blue) and imaginary (red) parts of refractive index as a function of doped free carriers concentration. c) Maximum values of scattering (red) and absorption (blue) cross-sections in 800 to 1600 nm excitation wavelength at different doping levels for magnetic octopole (MO) mode only. d) Optical heating temperature of single spherical nanoparticle with 315 nm radius with refractive index defined by b) and c) as a function of doping level. e) Optical heating of spherical nanoparticle as a function of doping carrier concentration at a certain optical mode - MO, MQ, EQ - magnetic octopole, magnetic quadrupole, electric quadrupole modes, respectively.

One of the possible ways to vary the nonradiative losses of the nanoresonator and, thus, the nonradiative losses of optical mode, is to dope the nanoresonator material with free carriers before fabrication. Doping of a single conventional semiconductor nanoparticle is still quite a challenging task except for some nanostructures based on hybrid halide perovskites, where one can achieve a drastic change in the optical and conductive properties by in-

situ nanoparticles doping [90]. In this regard, for doping, one should consider the films that would be subsequently reshaped by lithography techniques into metasurfaces and nanoparticles. However, in order to show only the proof of concept, we will consider calculation of optical heating without loss of generality of the statement. Strickly speaking, a resonant silicon nanodisk is a more reasonable structure for consideration, but, nevertheless, the excited optical modes in the nanodisks are similar to those that can be excited in nanospheres, and the total optical heating can be also analytically estimated by using the expression from [20].

To start with, it is necessary to estimate the effect of doping on optical and conductive properties of the material, since it impacts significantly on optical properties [115]. The free carrier contribution to the semiconductors permittivity is described by a Drude model [116]:

$$\varepsilon' = \varepsilon_\infty \Big(1 \; - \; \frac{\omega_p^2 \tau^2}{1+\omega^2\tau^2}\Big) \tag{2.6}$$

$$\varepsilon'' = \frac{\varepsilon_\infty \omega_p^2 \tau}{\omega(1+\omega^2\tau^2)} \; , \tag{2.7}$$

where the plasma frequency ω_p and scattering time τ are defined as $\omega_p = \sqrt{\frac{Ne^2}{m_c \varepsilon_\infty \varepsilon_0}}$ and $\tau = \frac{\mu m_c}{e}$, where N is the free carrier concentration, e is the electron charge, m_c is the conductivity effective mass and for n-type doping of silicon $m_c = 0.26 \cdot m_e, m_e$ is the electron mass, ε_0 and ε_∞ are the permittivity of free space and the high-frequency permittivity, respectively, and μ is the free carrier mobility.

The mobilities of carriers, both electrons and holes, have similar dependence on the introduced doping: at relatively low values of doping concentrations, the mobility remains almost constant and is mostly limited by phonon scattering. Upon reaching higher doping concentrations, the mobility lowers due to the scattering on the ionized doping atoms. The real mobility value also strongly depends on the type of dopant.

The mobility at a particular doping density is obtained from the following empiric expression:

$$\mu = \mu_{min} + \frac{\mu_{max} - \mu_{min}}{1 + \big(\frac{N}{N_r}\big)^\alpha} \; , \tag{2.8}$$

where fitting parameters for phosphorous doping of silicon $\mu_{min} = 68.5\ cm^2/V \cdot s$, $\mu_{max} = 1414\ cm^2/V \cdot s$, $N_r = 9.2 \cdot 10^{16}\ cm^{-3}$, $\alpha = 0.711$.

The mobility of the carriers and concentration affects the permittivity of the material according to the Eq. 2.6. A slight change of the real part of permittivity affects the spectral position and quality factor of the resonance, as one can see in Fig. 2.10(d) where temperature of the nanosphere of 315nm radius under plane wave illumination (as schematically depicted in Fig. 2.10(a) is shown. The imaginary part of refractive index defines the absorption in bulk material and, therefore, optical heating. One can notice the blue shift of the excited optical modes with increase of the doping level. This occurs due to decrease of the refractive index as one can see from Fig. 2.10(b). On the other hand, the increase of the free carriers with doping level increases dramatically the imaginary part of the refractive index, thus lowering the Q-factor of the mode, therefore spectrally broaden the resonance. However, after reaching certain level of carriers concentration, further doping does not boost optical heating, therefore it means that higher nonradiative losses do not necessarily lead to enhanced absorption and optical heating.

The latter one is explicitly shown in Fig. 2.10(e) where optical heating at certain optical modes MO, MQ, EQ (magnetic octopole, magnetic quadrupole, electric quadrupole modes, respectively) for different levels of doping is shown. Each particular optical mode is described by its radiative losses γ_{rad} and non-radiative losses, which are mostly Ohmic due to Joule heating γ_{Ohmic}. The latter one is defined by the imaginary part of refractive index, therefore by doped carriers concentration. In general, the higher the optical mode order is the better its quality factor and lower the radiative losses γ_{rad}. Thus, the balance between the radiative and non-radiative losses occurs at lower doping concentrations. Indeed, for higher order and higher Q-factor MO mode, the optimal optical heating is being reached at lower doping levels, whereas for MQ and EQ losses match at higher doping concentration. This result is consistent with previous predictions for plasmonic [117] and all-dielectric [118] nanoparticles described by Prof. Tribelsky and co-authors. The so-called ultimate absorption (UA) regime is being realized, where absorption

matches scattering, as manifested in [118], therefore, the most efficient optical heating occurs at the same conditions. The Fig. 2.10(c) depicts the maximum scattering cross-section and the maximum absorption cross-section of a single spherical nanoparticle of 315 nm radius at different values of doping for MO contribution only. Such an approach has already been successfully employed by the author in case of nanodisk resonator optical heating [119].

Effective mode volume factor. Another factor that contributes greatly to the total absorption of light by the NP and, therefore, contributes to the heating, is the effective resonant optical mode volume inside the nanoresonator V_{eff}. In the general case, the larger the nanoparticle size is - the greater the optical heating. However, one should note that V_{eff} can significantly vary such an assumption. If one considers a plasmonic nanoparticle, where the real part of the permittivity is negative ($\text{Re}(\varepsilon)<0$), the skin-layer depth starts to govern the effective mode volume. Namely, the typical skin depth, i.e. the distance where the light propagates inside the material with decrease in field magnitude by e times, for plasmonic materials is hardly greater than $\delta \approx 20$ nm in the visible range. Therefore, the V_{eff} for plasmonic nanoparticle is defined by the skin depth as follows: $V_{\text{eff}} \approx \pi D^2 \delta$. In contrast to the plasmonic materials and NPs, the dielectric and semiconductor ones are mostly transparent to the light in the visible range, therefore the effective mode volume is ususally of the order of the physical volume of the NP. To be more precise, for Mie type resonance, the effective mode volumes can be defined as $V_{\text{eff}} \approx \pi D^3/6$.

The straightforward conclusion that comes from the effective mode analysis is that for dielectric and semiconductor nanoresonators, the increase of the size of the nanoresonator increases the optical heating temperature. The same approach for the plasmonic ones is much less effective.

The general conclusion for such an analysis of optical heating of semiconductor and all-dielectric nanostructures can be described as follows: the efficient optical heating in resonant semiconductor and all-dielectric nanoparticles can be achieved when the balance of the losses is obeyed, i.e. radiative and Ohmic losses are equal. Since the inherent Ohmic losses in all-dielectric materials are low, one should consider bigger particles that support high-order,

high-Q, narrow optical modes that also possess low radiative loss channel. In contrast, the plasmonic ones are showing the best performance when the sizes of the NPs are rather small [19].

Optical heating with temperature feedback. The major advantage of the crystalline semiconductors over the plasmonic materials is the presence of the Raman scattering, which can be efficiently used as a thermal probe. Moreover, resonant crystalline NPs supporting Mie modes can dramatically increase the Raman scattering intensity by two orders of magnitude [17], which subsequently can provide direct Raman-shift based thermometry. Indeed, the optical heating of a single nanoresonator can be seen from the Raman scattering spectra as a spectral blue-shift upon higher temperatures, as shown in Fig. 2.11(a). Moreover, it was well studied both theoretically and experimentally by M. Balaknski *et al.* [22] that due to anharmonic effects in lattice vibrations, spectral line position of Raman scattering is known to be thermally sensitive. Indeed, the frequency of optical phonon line responsible for Raman scattering (Ω) is governed by the temperature as follows:

$$\Omega(T) = \Omega_0 + A\left(1 + \frac{2}{e^x - 1}\right) + B\left(1 + \frac{3}{e^y - 1} + \frac{3}{(e^y - 1)^2}\right), \qquad (2.9)$$

where Ω_0 = 528 cm^{-1}, A = -2.96 cm^{-1}, B = -0.174 cm^{-1}, $x = \hbar\Omega_0/2kT, y = \hbar\Omega_0/3kT$ for crystalline silicon [22].

The straightforward correspondence between the Raman scattering spectral position and the temperature provides great opportunity for Raman nanothermometry [23].

Fig. 2.11(a) depicts the spectral shift of the Raman spectra upon increased incident laser intensity. One can determine from the Eq. 2.9 that the spectral blue-shift from ambient conditions to 509 cm^{-1} corresponds to the optical heating by $\Delta T \approx 600$ K. Moreover, the method based on Raman nanothermometry and optical heating allows for precise sub-μm resolution 2D mapping of the temperature distribution of the nanoobjects by means of fine positioning with piezo-stage. It is worth noticing, that during the experimental studies, no irreversible changes of phase, shape or size of the NPs were oberved.

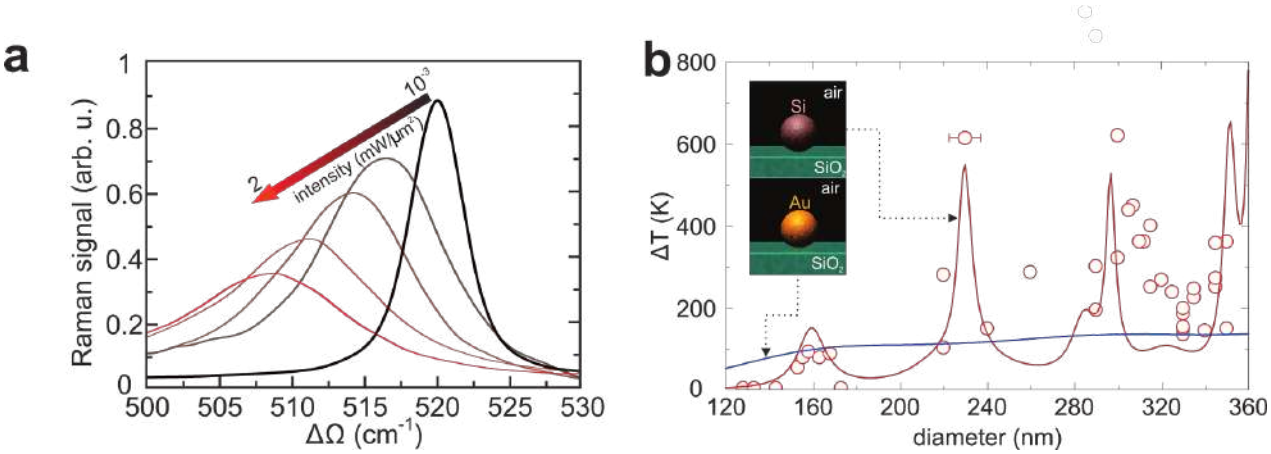

Figure 2.11 — **Laser heating and Raman thermometry of c-Si NPs.** a) Experimental Raman scattering spectra for a 350 nm diameter spherical c-Si NP on a glass substrate. b) Experimental (red circles) and numerically calculated (red solid lines) optical heating of spherical c-Si NPs. Blue lines corresponds to spherical gold NPs optical heating. The considered wavelength $\lambda = 633$ nm and light intensity $I_0 = 2$ mW/μm^2. Adopted from [21].

The method described in this section, based on thermally sensitive Raman scattering, allows one to examine the temperature of the NP made of various semiconductor materials, under arbitrary laser excitation, for various values of other properties, and, what's more important, in a very broad temperature range of up to 1000 K, as shown in Fig. 2.11(b). The optical heating and Raman nanothermometry are in great agreement with the theoretical calculations and the results are reproducable. It should be notec, that the experimental data was well described without taking into account thermo-optical nonlinear effects in the nanoresonator materials, which actually might sufficiently change the refractive index, thermal conductivity of the heated materials and, therefore, the optical resonances and optical heating performance [24].

It was shown theoretically and proven experimentally that the optical heating of the c-Si NPs is very sensitive to the resonant conditions, therefore the optical heating is strongly dependent on the diameter of the nanospheres, as one can see from Fig. 2.11(b). The general concept is that the more precise one can tune the NPs size to the resonant condition, the stronger Raman shift will be observed in the experiment, therefore, the stronger optical heating is achieved. The Fig. 2.11(b) shows pronounced resonant behavior from which

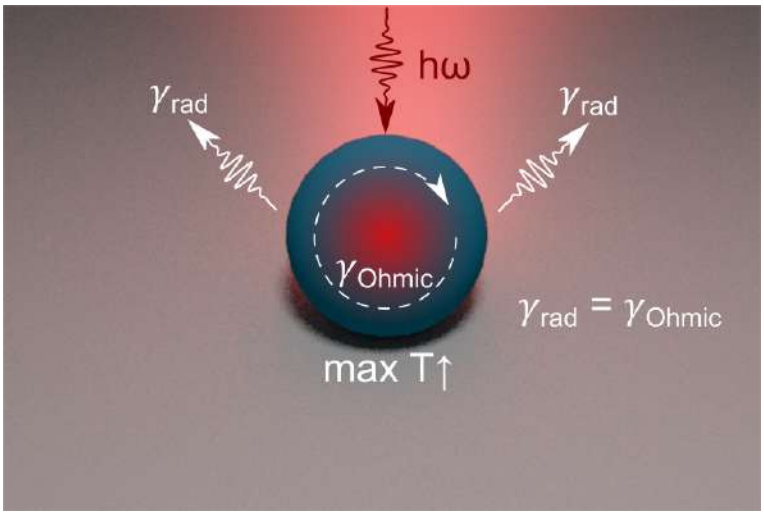

Figure 2.12 — Schematic of basic principle of the optical heating of the all-dielectric nanoresonators.

one can conclude that low-order optical modes (ED) do not support highly efficient optical heating (roughly 160 nm in diameter), however at 230 nm diameter, the c-Si nanoparticle possesses MQ optical resonance. The higher-order modes appearing in larger NPs do not sufficiently improve the optical heating performance. Thereby, one can conclude that for the case of optical heating of single crystalline silicon nanosphere by HeNe CW-632.8 nm laser, the most optimal condition is the MQ mode.

Such optical heating of a single resonant all-dielectric nanoparticle already demonstrated its applicability for coversion of solar energy into heat [120–122]. Moreover, such laser heating might be prospective for astrophysics applications [123].

This section covers the main aspects of optical heating of a single resonant all-dielectric nanoparticle under CW laser illumination. The basic principle described in is shown in Fig. 2.12 , where light excites optical modes in the nanoresonator, and reaching the balance between radiative and non-radiative channel of losses, the most efficient optical heating is realized. The next sections and chapters mostly follow this concept of the efficient light-to-heat conversion in a single nanoresonator.

2.5 Hybrid plasmonic-dielectric nanostructures for enhanced optical heating and sensitive Raman thermometry

Single homogeneous nanoresonators made of all-dielectric materials described in previous sections are not the only selection for simultaneous optical heating and temperature probing via Raman response. Recently, dimer or hybrid structures combining advantages both of plasmonic and all-dielectric materials, with a high degree of electromagnetic field localization, attracted a great attention among the nanophotonics researchers [124].

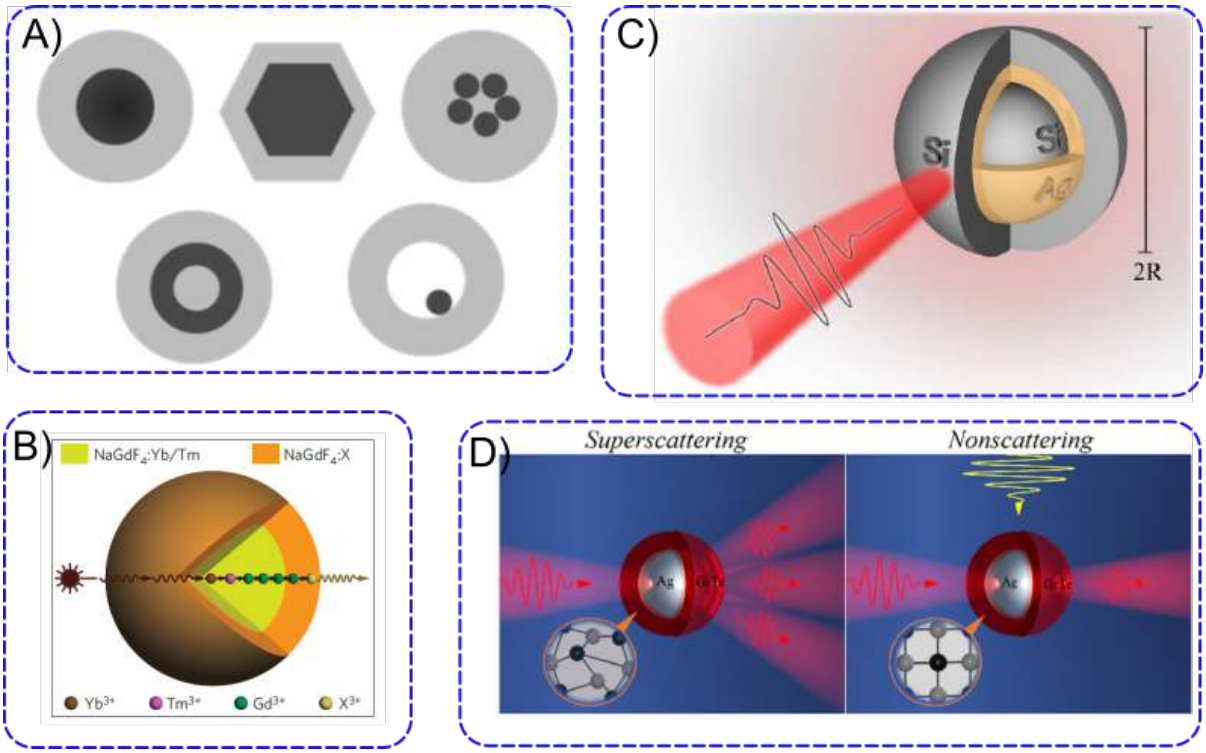

Figure 2.13 — **Core-shell nanoparticles in nanophotonics.** a) Schematic of typical core-shell nanoparticles, namely, spherical, hexagonal, multiple cores in a single shell, nanomatryoshka, hollow centre of the shell with a movable core. Adopted from [126]. b) Schematic of a core-shell nanoparticle for upconversion photoluminescence [127]. c) Schematic of the optimization of light absoprtion by a single multi-layered sphere [128]. d) Tunability of core-shell scattering with phase-changing materials from non-radiating to super-radiating state [129].

The system consisting of two resonators, made either of the same or different material, closely located in space, is called a dimer strucutre. Such dimer structures already demonstrated their efficiency in nonlinear light generation [125], field localization [14] and sensing [15]. However, such systems are

difficult for implementation in some applications that require the use without the substrates. Thus, the simplest case of hybrid nanoantenna for advanced light manipulation is a spherical core-shell nanoparticle consisting of a spherical core and a hollow homogeneous concentric shell made of another material.

Fig. 2.13 depicts some of the applications of core-shell structures in nanophotonics. Some of them might not support Mie-resonances in the visible range and enhance optical effects due to material and surface properties [127](see Fig. 2.13(b)). The other type of core-shell nanoparticles, supporting Mie-resonances in the visible range, allow for advanced light manipulation through the intereference of the optical modes, thus realizing superabsorption regime [128], shown in Fig. 2.13(c). Indeed, the optimization of geometrical parameters of the nanoresonator can lead to optimized light absorption [130]. Moreover, such core-shell strcutures allow switching from superscattering to non-scattering regimes due to reversible phase transition in GST shell material [129], as briefly shown in Fig. 2.13(d) or unidirectional scattering [131].

In this section, we focus mainly on the metal-semiconductor (gold-silicon) hybrid core-shell nanospheres for realization of efficient optical heating.

The approach for calculation of the scattering and absorption, which mostly governs the total optical heating, is based on the method described in sections 1.1.1 and 1.1.2.

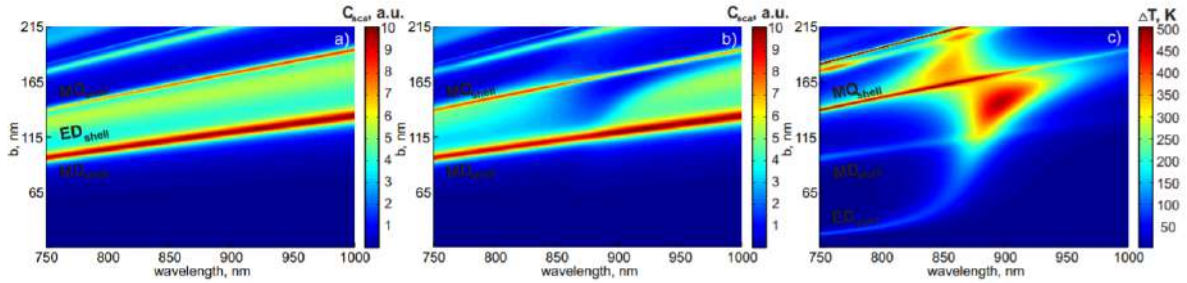

Figure 2.14 — **Optical heating of core-shell nanoparticles** a) Total scattering cross-section of a single silicon nanosphere with a hollow center of 15 nm radius. b) Total scattering cross-section of a single core-shell nanoparticle of silicon shell with a core made of 15-nm radius gold nanosphere. c) Optical heating of a single core-shell nanoparticle of silicon shell with a core made of 15-nm radius gold nanosphere. Adopted from [132]

Fig. 2.14 depicts theoretical study of a gold-silicon core-shell nanopar-

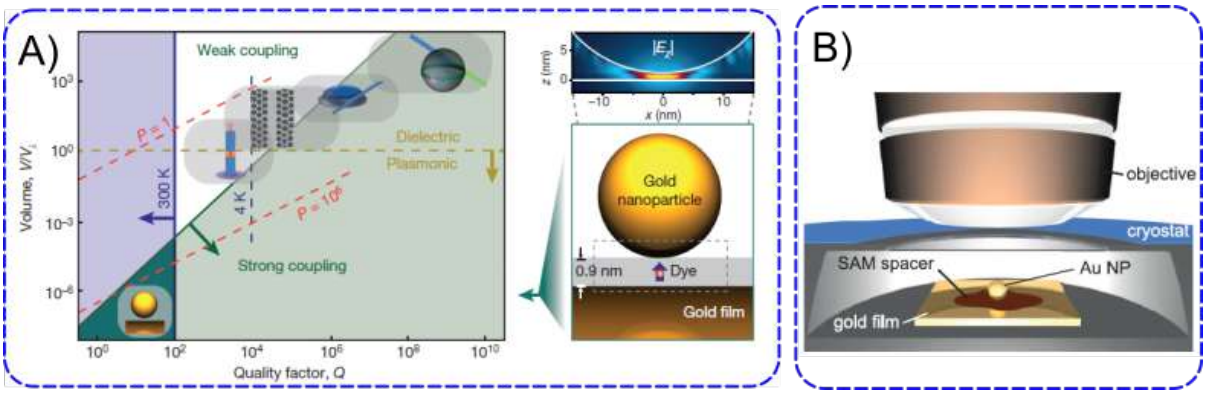

Figure 2.15 — **Plasmonic gap nanocavities.** a) Effective mode volume versus quality factor of the resonator and a schematic of the plasmonic nanocavity [133]. b) Plasmon nanocavity for single molecule sensing [134].

ticle in terms of optical heating and scattering. The left colormap map shows the total scattering cross-section of light by a single hollow silicon nanosphere with various radii. The radius of air space inside the silicon shell is 15 nm. This is done in order to show the contribution of golden core to the total scattering and absorption. One can see from Fig. 2.14(b) that spectral region between 850 and 900 nm, with radii between 115 nm and 165 nm, shows a decrease in the scattering signal for core-shell strucutre with fixed golden core radius in comparison to the case of a hollow silicon shell. This means that the excited optical modes inside the core and shell destructively interfere in the far-field scattering domain, and this results in a better absorption and electromagnetic field localization inside the core-shell which one can see from the Fig. 2.14(c), where optical heating of such a core-shell structure is shown. Strictly speaking, in order to determine such an optical state, one should carry out the mode decomposition of the scattering response; however, according to the section 2.2, such nanophtonics behaviour might be considered as 'anapole-like'. Therefore, core-shell nanospheres give enough degrees of freedom for theoretical realization of anapole-enhanced resonant optical heating [132].

Another interesting example for possible hybrid approaches for efficient optical heating and thermometry is based on gap cavities.

Fig. 2.15 depicts plasmonic gap nanocavities, which are formed with a plasmonic resonant nanoparticle and a plasmonic substrate (a surface). The

substrate covered with plasmonic material acts as a reflector that strongly enhances the field in between the surface and nanoparticle, resulting in a very high-Q resonance. The dye molecules or other organic materials play a role of a neutral density spacer between the substrate and the sphere, thus extremely localizing the electromagnetic field in a very tight volume [133, 134]. Other types of plasmonic structures for enhanced sensing are dimer or trimer structures consisting of similar nanoparticles that allow enhanced fluorescence [135] or Raman scattering [136]. Even though it was shown that gold nanoparticles can support thermometry [6], the collection time and applicability in real problems remains quite challenging. In this regard, non-plasmonic sensing platforms based on semiconductor materials with Raman-active phonons can provide optical efficient thermometry. First, semiconductor resonant nanostrucutres already demonstrated great performance in biological applications including enhanced Raman response [15, 137], molecular bar-coding [28, 29], enhanced fluorescence of single molecules [138] and many other biosensing examples [139].

In this section, we propose a hybrid plasmon-dielectric platform for simultaneous optical heating and thermometry based on a nanogap cavity: a silicon nanosphere placed on top of a golden surface with proteins on the surface of the substrate playing the role of a spacer.

The proposed system, analyzed in the Fig. 2.16, consists of a silicon spherical nanoparticle, supporting Mie-resonance in the visible and substrate with a homogeneous gold layer deposited on the surface. Since the laser excitation source used for excitation of Raman scattering in this work was HeNe CW laser with a wavelength of 632.8 nm, it was necessary to calculate local electromagnetic field enhancement and distribution within the nanogap. The field enhancement spectrum for different sizes of the NP and the distribution shown in Fig. 2.16(a,b), demonstrate pronounced resonant peaks, which correspond to specific optical modes excited in the silicon nanosphere. The best performance in such systems was observed at the ED resonance. This happens due to the polarization of the nanosphere and the fact that induced dipole moment interacts with the gold substrate, resulting in a significant en-

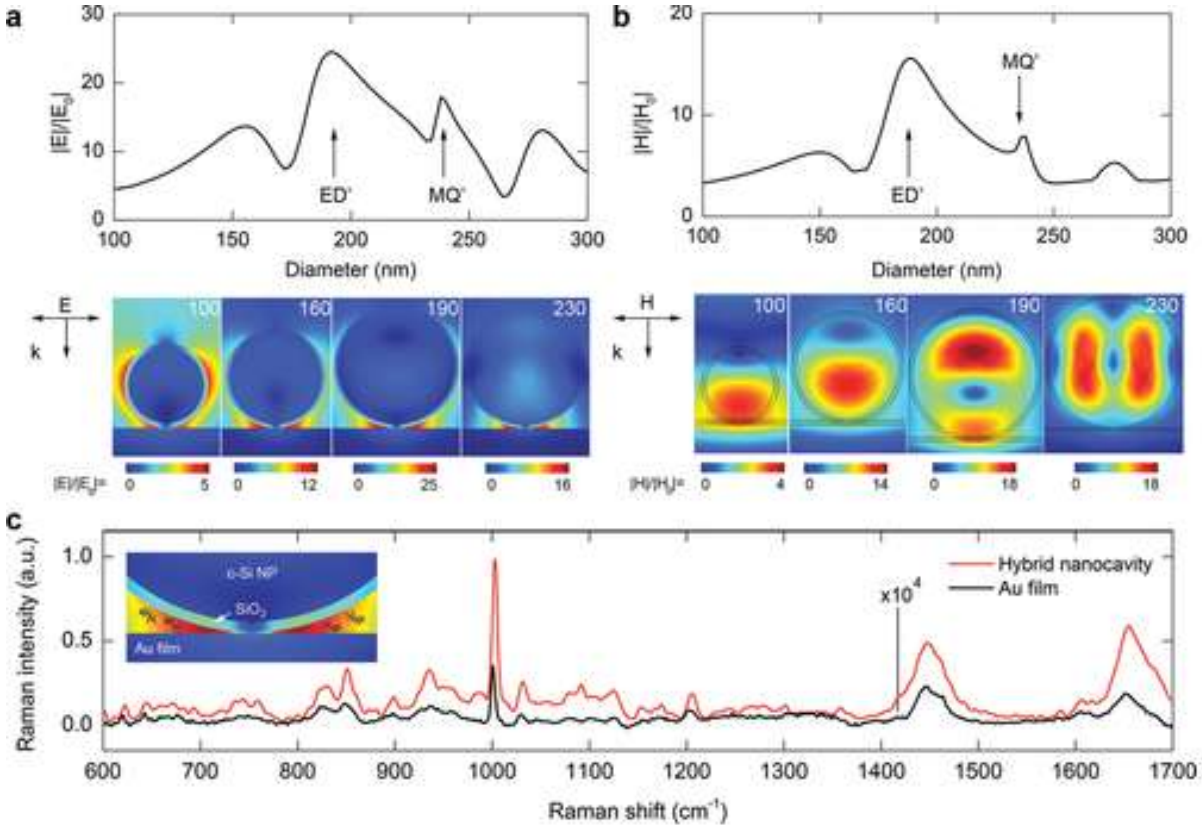

Figure 2.16 — **Hybrid Si-Au nanogap cavity.** a) Maximum electric and b) magnetic field magnitude normalized over the magnitude of the incident field for excitation at a wavelength of 633 nm. Insets depict the field distribution for different linear polarizations. c) Experimental Raman scattering spectra of protein molecule inside the nanogap (red line) and on a gold substrate without silicon nanoparticle (black line, scale factor x10^4). Adopted from [30].

hancement of the elctromagnetic field inside the nanogap. Such an excited ED optical state demonstrates a dramatic enhancement of the Raman scattering signal from the protein molecule located inside the nanogap, showing the 4-fold improvement of the signal. Moreover, the silicon nanosphere serves as temperature indicator of the whole system, making it possible to probe the temperature of the protein unfolding process *in situ*, which was experimentally shown in [30].

Another peculiar aspect of such a system is the optical heating performance. The trade-off between the efficient electromagnetic field enhancement for sensing applications and avoiding hyperthermia for proteins in the nanogap remains a challenge. For this purpose, a theoretical analysis of optical heating in such a system was carried out in numerical commercial software COMSOL

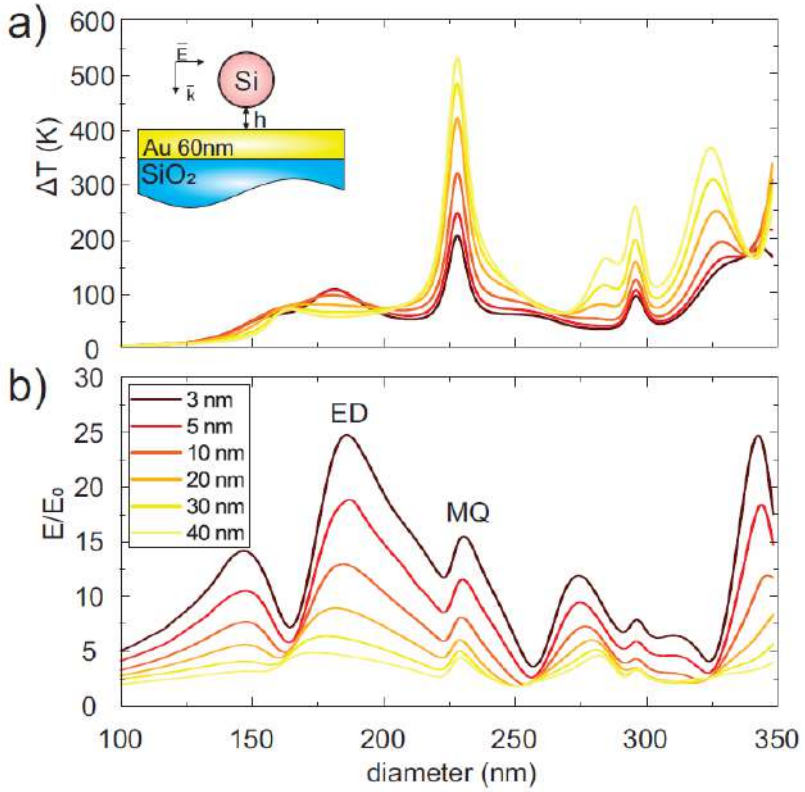

Figure 2.17 — **Nano-gap size impact on optical heating.** a) Maximum temperature of the NP and b) electric field magnitude in the hybrid nanogap consisting of a silicon nanosphere and a gold layer on top of the substrate. Adopted from [140].

Multiphysics. Fig. 2.17 depicts the calculated maximum temperature of the NP for varying distance h between the NP and the surface. The distance h increased up to 40 nm dramatically lowers the electromagnetic field enhancement since the resonant coupling appears in the near-field region between the ED mode of the silicon sphere and the gold layer. However, this distance increases the aerial medium that surrounds the NP and, therefore, strongly lowers the thermal conductivity, thus resulting in higher final temperature of the NP. On the other hand, if one decreases the gap size down to several nanometers, the field enhancement will dramatically increase, with a sufficient decrease of optical heating efficiency. The limit case of nanosphere in contact with the gold layer without any spacers will result in roughly negligible optical heating, since the gold layer will play a role of an infinite heat sink with great thermal conductivity with respect to the silicon sphere [140].

This section was devoted to the basic and general properties of simple hybrid metal-dielectric structures for advanced optical heating and sensing via

Raman scattering.

2.6 Advanced bio-medical applications

As it was already mentioned before, the tight 'union' between nanophotonics and biomedicine resulted in a wide range of unprecedented applications of optical concepts in real life. In recent decades, nanophotonics and biophotonics were mostly associated with plasmonic structures and nanoparticles - either due to their outstanding light-to-heat conversion properties [26] or electromagnetic field localization [27]. However, in the past few years, more and more bio-applications of nanophotonics are taking place basing on all-dielectric materials and optical responses [28–30]. The approach on using all-dielectric nanophotonics for biomedical applications is mostly based on excitation of single optical Mie modes or their combinations and collective resonances. One of the possible advantages of all-dielectric structures for biomedical applications is the ability for temperature probing via Raman scattering or PL signal. In this section we suggest using all-dielectric nanoparticles for optical thermal trigger for drug release in microcarrier systems for targeted medicine delivery.

There is a number of possible prominent and prospective applications for resonant all-dielectric nanoparticles created for optically-responsive delivery sytems [141].

Fig. 2.18 schematically depicts possible optically-responsive delivery systems before and after interaction with laser, starting from conventional single plasmonic nanoparticles functionalized with drug agents, which can be activated via light-to-heat conversion by means of absorbed laser irradiation. The same concepts is used with dielectric nanoparticles - either solid, porous or unevenly shaped structures, they release drug agents upon photoactivation. More complicated carrier systems, for instance, are based on polymer carriers with drug agents located inside the carrier. The drug release is realized through the the rupture of the capsule by laser radiation. The use of plasmonic or semiconductor target nanoparticles lowers the effect on biological tissues, since they require less light energy to achieve the sufficient temperature in order to break the capsule wall. We believe that such approach with

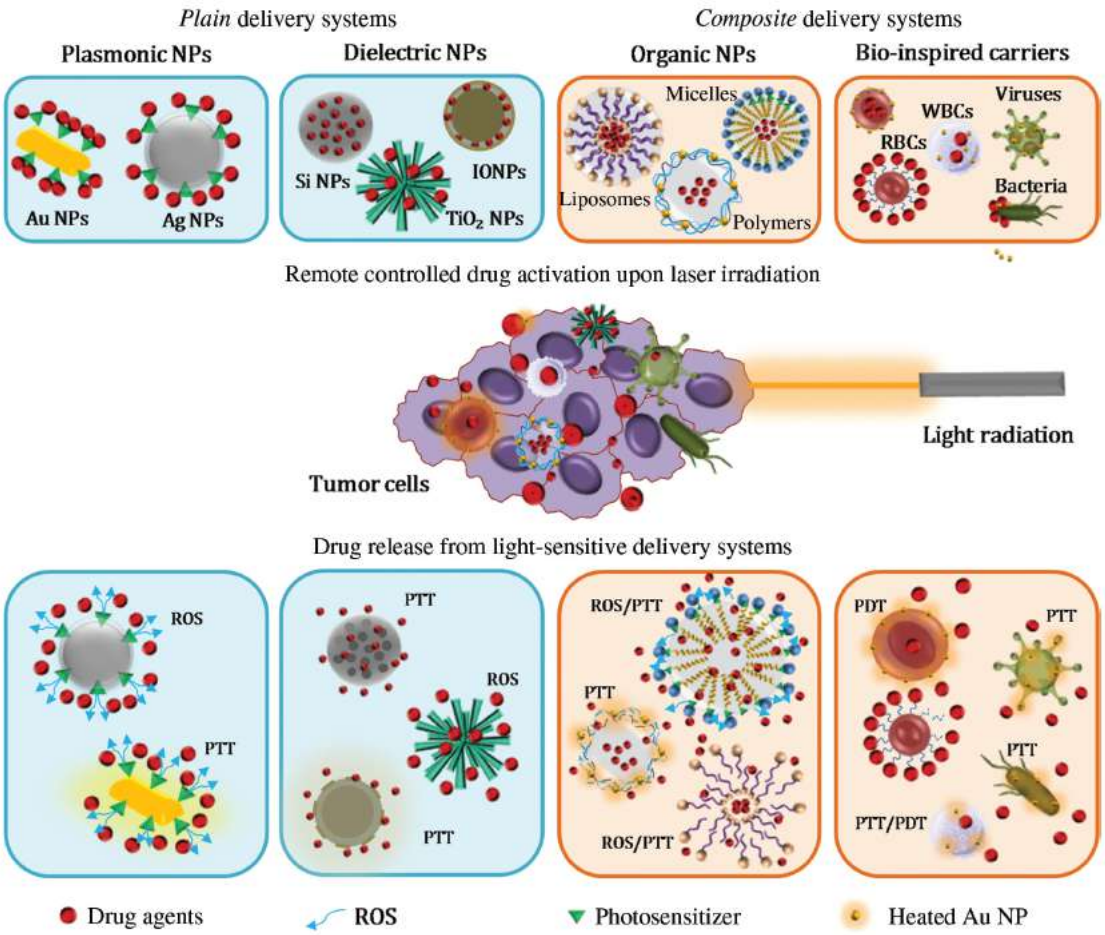

Figure 2.18 — **Optically-responsive carrier systems.** Schematic of optically-responsive carrier systems for targeted drug delivery. Adopted from [141].

a combination of temperature responsive resonant semiconductor NPs and microcarrier systems might be very efficient.

In this regard, we start our analysis from the selection of non-cytotoxic semiconductor materials that would i) support resonances in the visible range, keeping the subwavelength size, ii) be Raman active in order to measure temperature in a fully optical way and iii) have proper value of optical losses for efficient conversion of light to thermal energy.

According to Fig. 2.9(c), crystalline silicon and iron-oxide (α-Fe_2O_3) nanoparticles might be promising candidates for efficient optical heating in aqueous media. Moreover, α-Fe_2O_3 serve to be a great material from cytotoxic point of view [142] because it is compatible for bio-applications. As one can see from Fig. 2.19, α-Fe_2O_3 NPs demonstrate a great advantage compared to gold and silicon nanospheres during optical heating in aqueous medium. It is manifested via broader spectral region of optical heating and higher values

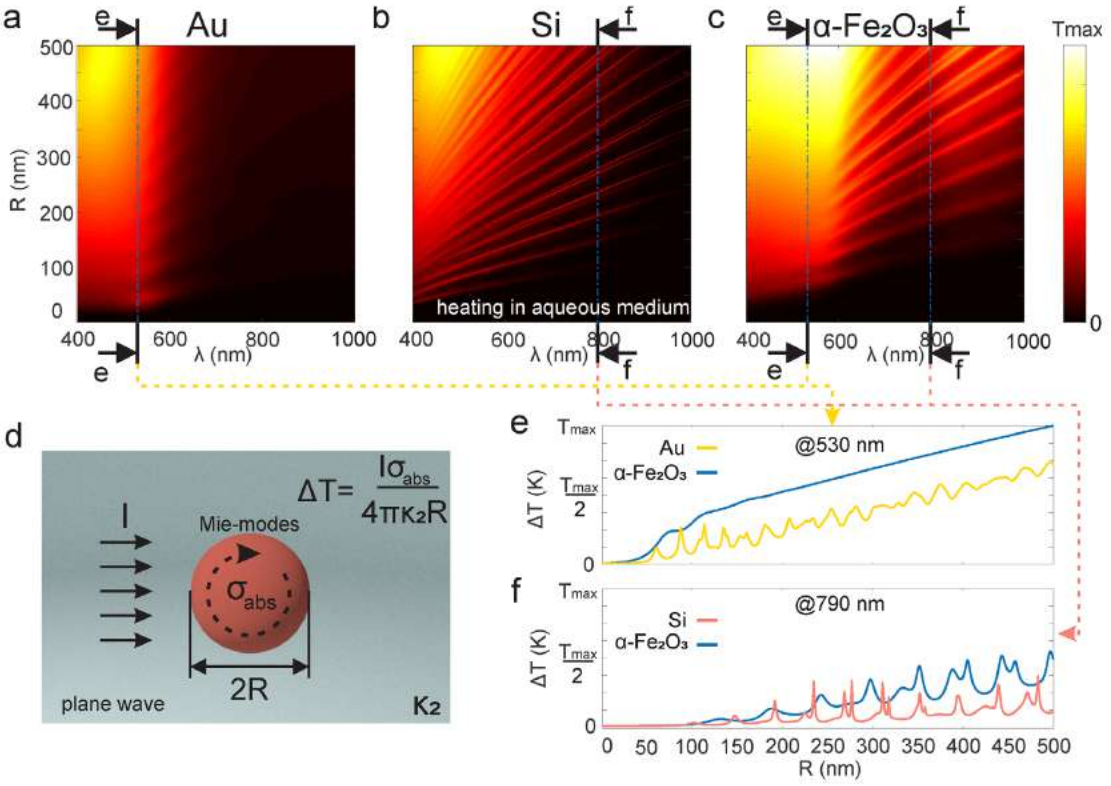

Figure 2.19 — **Optimization of heating parameters.** Optical heating of spherical nanoparticles with various radii in a homogeneous aqueous medium for a) gold, b) silicon and c) α-Fe_2O_3 materials. d) Schematic of the calculation of optical heating. Comparison of optical heating between α-Fe_2O_3 NPs with e) gold NPs at 530 nm and f) silicon at near-IR 790 nm. Adopted from [31].

of obtained temperature, thus making α-Fe_2O_3 NPs a perfect candidate for optical heating and sensing in bio-applications. Another advantage of α-Fe_2O_3 NPs over silicon is the higher number of Raman-active phonon lines [143], which allow a more precise temperature measurement via averaging the values obtained from the individual Raman response line.

Further, such α-Fe_2O_3 NPs were embedded into the walls of polymer drug agent carrier as shown in Fig. 2.20(a). The presence of the NP plays the role of a target for laser heating and further rupture of the capsule.

The implementation of α-Fe_2O_3 resulted in the direct measurement of the temperature of the drug release from the capsule. The measurement by means of Raman thermometry showed that the mean value of the capsule rupture temperature is roughly 170^o. Worth noticing that on a scale of $5\mu m$ distance from the nanoparticle, the temperature decreases by an order

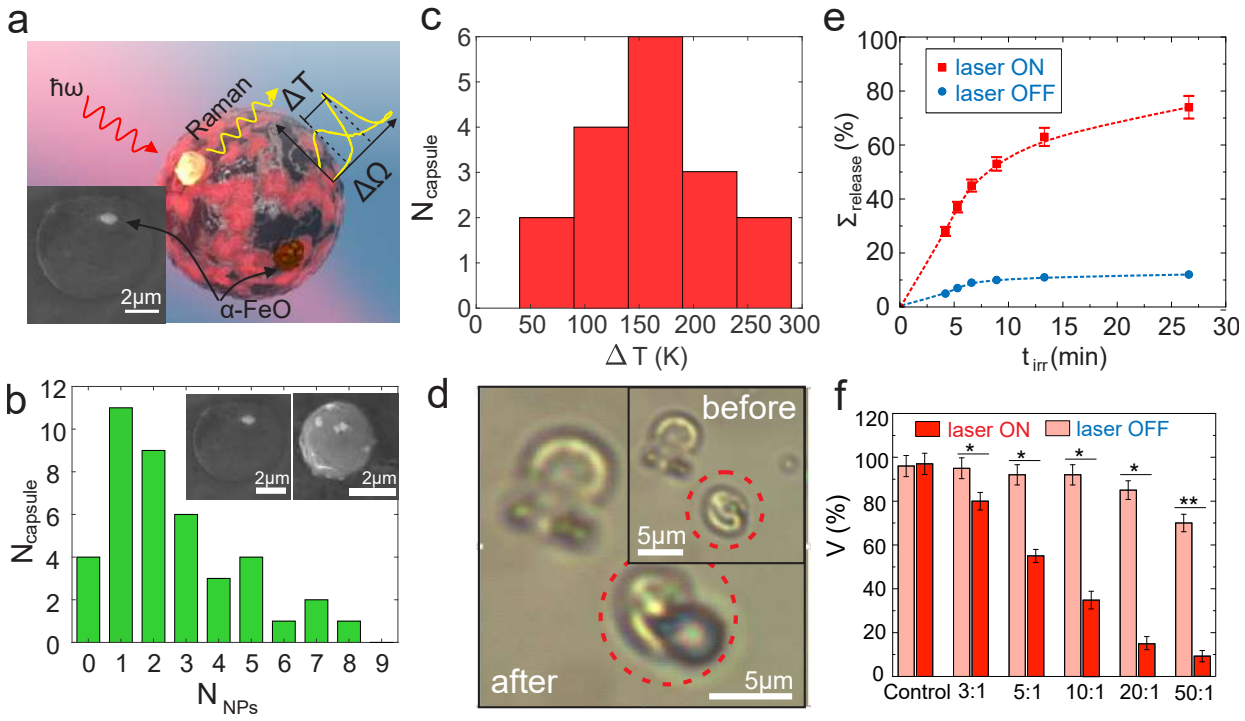

Figure 2.20 — **Polymer drug carriers with embedded α-Fe_2O_3 nanoparticles.** a) Schematic of the concept for drug delivery systems based on microcapsules with α-Fe_2O_3 NPs embedded into the wall for photothermal activation of the drug release process. (b) Histogram of the quantity of α-Fe_2O_3 nanoparticles successfully trapped in the polymer carrier wall. Inset: Typical SEM images of the fabricated capsules. Scale bar is 2 μm. (c) Histogram of the observed capsule rupture upon laser radiation. The temperature values were obtained via Raman thermometry. (d) Bright-field microscopy images of the capsule before and after laser irradiation. (e) Released VCR concentration as the function of time with laser irradiation (red) and without (blue). (f) CC viability after target delivery experiments with laser induced activation of the drug release. Red columns correspond to CC, pink columns correspond to the stem cells (control). Different columns correspond to different initial polymer capsules concentration. Adopted from [31].

of magnitude.

As a proof of concept, the delivery and optical rupture of the polymer drug carrier and subsequent release of anticancer drug vincristine (VCR) with lowered near-IR laser of of 4.0×10^4 W/cm^2 intensity, operating in biological tissue transparency window, by means of efficient optical heating and nanothermometry of α-Fe_2O_3 NPs, was shown. The biological tests are performed on two primary cell types: (i) carcinoma cells, as an example of malignant tumor, and (ii) human stem cells, as a model of healthy cells (Fig. 3(e,f)).

Further, this concept was proven experimentally for carcinoma cells. The capsule loaded with anti-tumour drug VCR successfully released the drug agent upon laser irradiation and subsequent thermally-induced rupture of the capsule (Fig. 3(e,f)). Moreover, the laser intensities were rather moderate, so that the control cells (stem cells) were relatively unaffected. The biological part of the work was done by Dr. Mikhail Zyuzin and Dr. Alexander Timin and can be found in [31].

Chapter conclusions

In conclusion to the chapter, it was shown that a single Mie-resonant semiconductor nanoparticle can serve as a simple and "all-in-one" (heater-thermometer) nanoplatform which supports effective ligh-to-heat energy conversion and broad-range of temperature sensing. In particular, such nanosystem demonstrated its efficiency for bio-medical applications requiring photothermal interaction.

The scientific statement presented for the defence:

- Resonant optical excitation of Mie modes in a semiconductor nanoparticle with balanced radiation and non-radiation losses provides the most effective optical heating in comparison with other loss ratios for the given optical mode.

Key novelty includes, but is not limited by:

- The first experimental demonstration of simultaneous continuous wave HeNe (632.8 nm) laser-induced optical heating and nanoscale thermometry by resonant Raman-active semiconductor nanostructures.
- The first demonstration of the Mie resonant semiconductor nanoparticle optical heating and nanothermometry via Raman scattering for drug delivery applications. The α-Fe_2O_3 nanoparticles were used as the target for near-IR laser excitation for efficient conversion of light to heat in the walls of polymer drug agents and as the direct optical temperature probe via thermally-sensitive Raman scattering. As the proof of concept, the successful *in vitro* delivery and remote optically-induced thermal rupture of the polymer carrier was shown by means of laser heating of the target

α-Fe_2O_3 nanoparticles with subsequent release of the antitumour drug agent vincristine. The proposed system worked at the moderate laser intensity value as low as 4.0×10^4 W cm^{-2}.

The main results of the chapter are published in papers [21, 30, 31, 119, 132, 140].

CHAPTER 3. CONTROLLABLE PHASE TRANSITIONS STIMULATED BY LASER HEATING AND PROBED BY RAMAN NANOTHERMOMETRY

As it was described earlier, the material and structure properties can be tuned laser-induced processes: glass-like transitions and melting-solidification. In this chapter, both methods will be covered for controllable laser annealing and melting of the nanoresonators with the Raman scattering feedback that serves both as a thermal probe and the crystalline-phase probe.

3.1 Controllable laser-induced amorphous-to-crystalline phase transition in single nanoresonators

It was shown that simultaneous laser heating of semiconductor nanostrucutre and nanothermometry using thermally-sensitive Raman scattering can be promising for a number of nanophotonics applications associated with photothermal processes. In this chapter, crystallization of optically resonant nanodisks made of amorphous silicon, caused by local optical heating, was studied. The phase transition and temperature control were performed using Raman scattering. It was found that the temperature of the onset of the phase transition from the amorphous to the crystalline state for a single silicon nanodisk is about 900°C. Further, the polycrystalline nanodisk has already demonstrated the possibility of multiple reversible optical heating in the temperature range 300÷1000 K.

Indeed, the substrate material plays a significant role for resonant optical heating in two ways: first, high-index substrates lower the optical contrast with the nanoresonator material, therefore decreasing the Q-factor of the resonances, and second, the substrate is the dominant thermal sink for the heat leakage from the nanoparticle upon laser heating. Therefore, a high-index sapphire substrate with a relatively high thermal conductivity in comparison with fused silica or glass is a much worse candidate for the efficient optical heating at moderate incident laser intensities. Moreover, if the proposed

fs-laser fabrication of quasi-spherical NPs of different semiconductor materials [12, 49, 50] is not sensitive to the selection of the donor substrate material, the lithographical methods are highly sensitive to the substrate material used for growth of the structures. Indeed, if one needs a planar nanostructure based on high-crystalline pure semiconductor, for example, a topological chain of nanodisks [144], it is necessary to use lithography growth techniques. In the case of nanolithography methods, the substrate material on which fabrication (growth) and etching of nanostructures will be realized plays a crucial role. For instance, the growth of c-Si nanostructures on a glass substrate remains a challenge. In this regard, the fabrication of the a-Si nanostructures with subsequent laser-induced thermo-annealing is a possible attractive solution, which already has been proven theoretically [145]. For this case, Raman scattering will serve both as a thermal probe, as it was shown in the previous section, and as a crystalline phase probe. Moreover, the proposed 2D mapping of the intensity distribution of the Raman scattering, along with the temperature distribution mapping, allows for a fast analysis of the shape of the nanoresonator, for instance, the nanodisk one.

The process of phase transition from amorphous to crystalline phase for a silicon nanodisk is shown in Fig. 3.1(a). To ensure and control the phase transition in a single nanodisk, first, a Raman spectrum was obtained in the so-called "cold" mode, at a pumping intensity of 0.06 MW/cm^2, such that the disk temperature visually did not change. Then this disk was subjected to more intense irradiation with a helium-neon laser (0.39 MW/cm^2), which induced a phase transition. At temperatures of about 600÷800 °C, the nanodisk began to change from the amorphous to the polycrystalline phase, as can be seen from the figure. The crystallization temperature values coincide with the known ones [33], and the heating temperature is comparable to those previously achieved at a similar pump power, but for spherical nanoparticles [21].

Fig. 3.1(b) shows the direct temperature dependence of the spectral position of the Raman scattering of crystalline silicon at different temperatures. The Raman spectra after annealing resemble polycrystalline silicon because [33]: first, they exhibit asymmetry with respect to the spectral po-

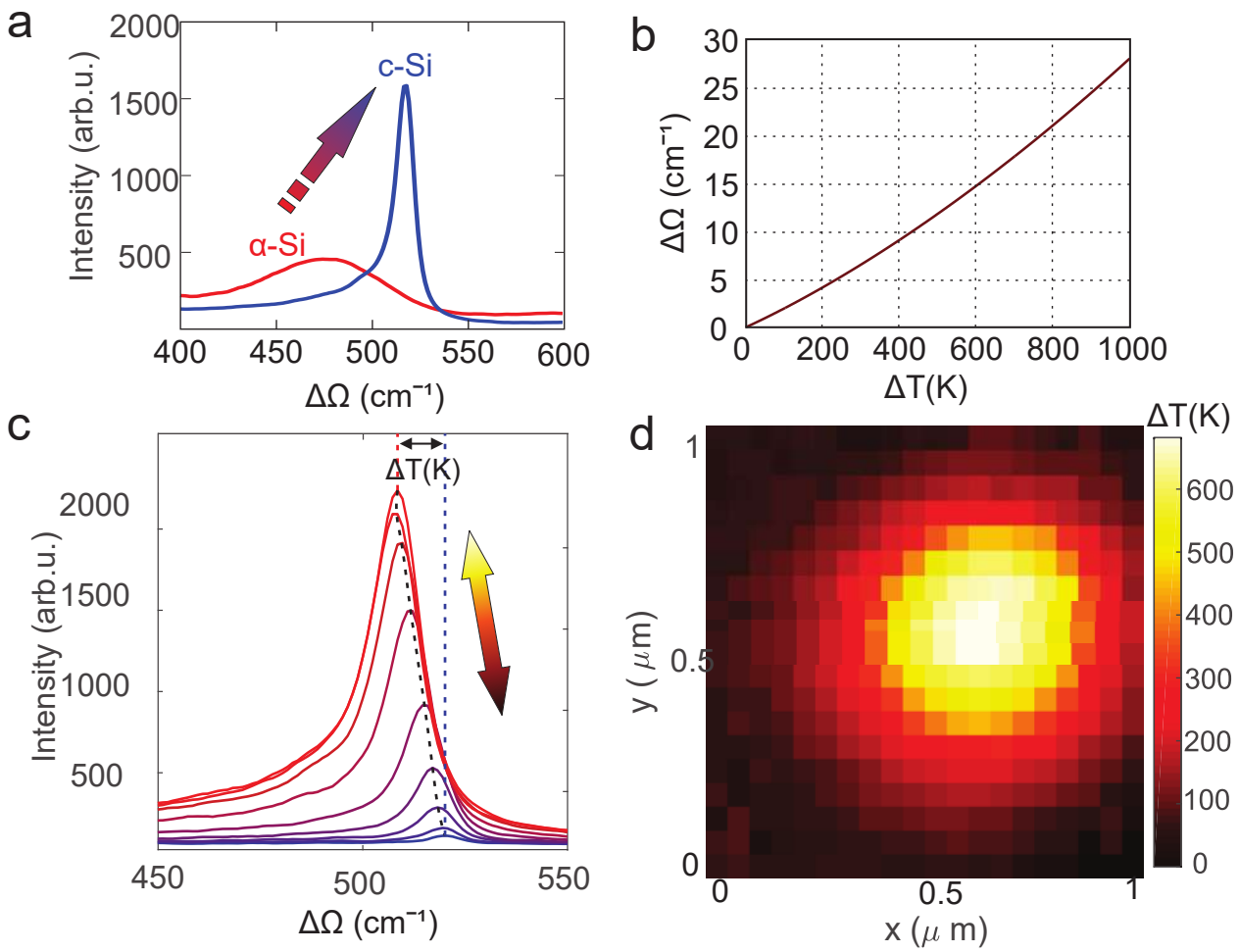

Figure 3.1 — **Photothermal annealing of a silicon nanodisk.** (a) Raman spectra of a nanodisk before and after laser exposure. (b) Theoretical temperature dependence of the spectral shift of the phonon line of crystalline silicon (see equation 8). (c) Raman spectra of a single polycrystalline nanodisk at various pump intensities. (d) Spatial distribution of the optical heating temperature depending on the position of the source relative to a single nanodisk. Taken from [32].

sition, which is noticeably manifested at higher disk heating temperatures; second, the characteristic spectral FWHMs of Raman peaks exceed 10 cm^{-1} even at low intensities, while for single-crystal silicon this value does not exceed 5 cm^{-1}.

Fig. 3.1(d) shows an example of two-dimensional mapping of the distribution of optical heating of a single nanoobject, depending on the position of the laser source and the collection area.

This method allows fast and non-invasive local induction of phase transitions in amorphous materials using optical heating and control of the degree of crystallinity and temperature by means of Raman scattering. This ap-

proach is especially useful for second-harmonic generation [10] and broadband photoluminescence [34].

Moreover, while the advantage of the fs-laser ablation method is the possibility to choose an acceptor substrate fast and without complications, the advantage of nanolithographic methods is the accuracy in specifying the geometry and dimensions of nanostructures. Therefore it is crucial to propose a method of annealing from a-Si state to c-Si state without any irreversible changes of the shape of the nanostructures. The set of the test single a-Si nanodisks underwent laser annealing with control SEM images before and after the exposure.

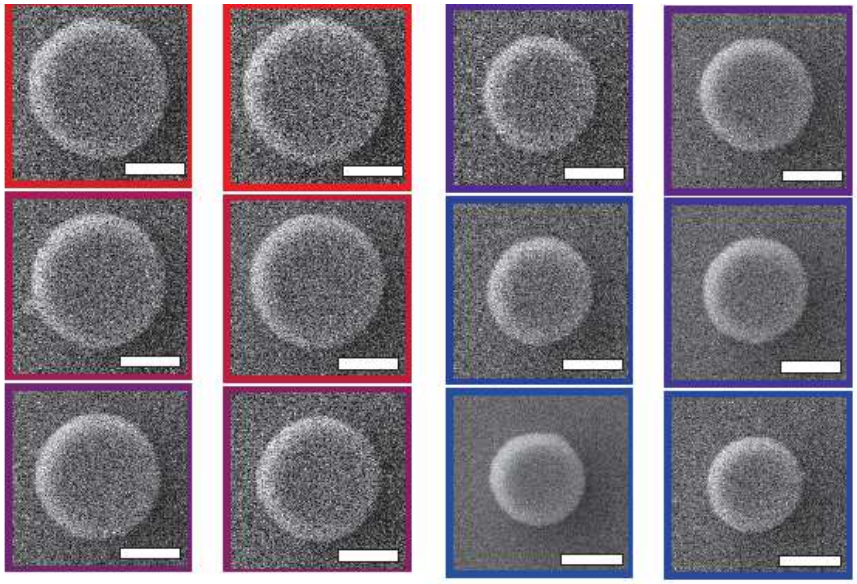

Figure 3.2 — **Nanodisks SEM images.** SEM images of the fabricated nanodisks. The colors from red to blue schematically correspond to the diameter, from larger to smaller. The squares of the same color correspond to the same nanodisk before (left) and after (right) laser annealing.

For the fabrication of cylindrical nanostructures studied in this section, first, an amorphous silicon film of 165 nm thickness is deposited on a quartz substrate using the method of plasma-chemical vapor deposition (Plasmalab System 380, Oxford Instruments). Electron beam lithography (Elionix, 100 kV) was performed using resist (HSQ, Dow Corning, XR-1541-006). The unirradiated portion of the HSQ is removed with tetramethylammonium hydroxide (TMAH, 25%). The sample is then etched (Plasmalab System 100, Oxford) to create arrays of silicon nanodisks on a quartz substrate [146].

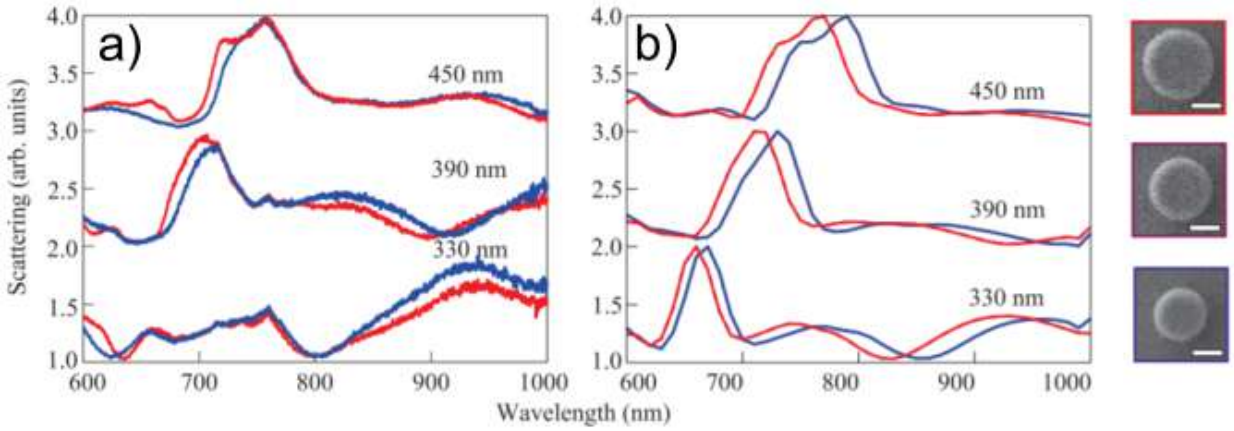

Figure 3.3 — **Nanodisks dark-field scatering spectra.** a) Experimental and b) theoretical dark-field scattering spectra before (blue) and after (red) laser annealing. Insets depict SEM images of the specific nanodisk. Adopted from [32].

Single nanodisks were made so that they would support optical resonances in the visible region of the spectrum. In the process of local annealing with a CW HeNe laser, the geometry of the nanoparticles did not change, which was confirmed by the SEM results in Fig. 3.2. Thus, the proposed method makes it possible to convert amorphous silicon nanostructures into crystalline ones by optical heating.

This method allows fast and non-invasive local induction of phase transitions in amorphous materials using optical heating and control of the degree of crystallinity and temperature by means of Raman scattering. This approach is especially useful for second-harmonic generation [10] and broadband photoluminescence [34].

3.2 Controllable laser heating for local melting of the nanostructures

The section 3.1 considered the optical heating temperature that enables glass-like amorphous-to-crystalline phase transitions, however, upon increasing the intensity and overcoming the melting threshold temperature, one can achieve the controllable melting of the nanoresonator. Indeed, intense and sharply focused laser excitation can lead to the thermally-induced reshaping of the metasurfaces, therefore tuning the optical response [147].

The precise controllable melting of the material or the modification

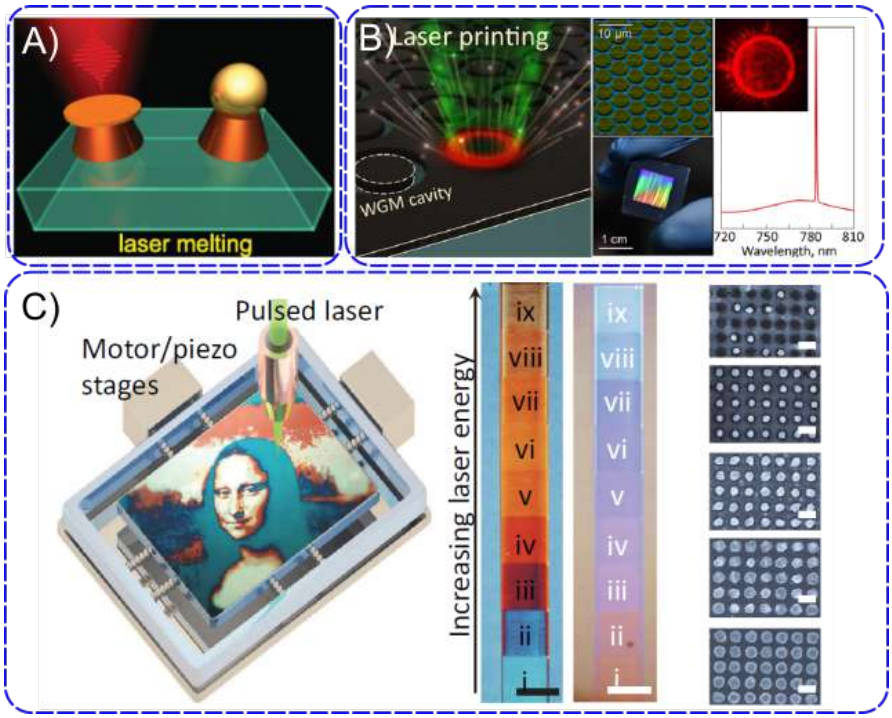

Figure 3.4 — **Controllable laser melting for nanophotonics applications.** a) Laser modification of the golden nanocap for fine tuning of the optical response [148]. b) Laser printing of the donut-shape resonators on the perovskite films for lasing from the WGM cavities [149]. c) Laser modification for colouring applications [147].

of the metasurfaces is a powerful tool for nanophotonics applications, which includes the fabrication of the whispering gallery mode (WGM) persovskite lasers [149] (see Fig. 3.4(b)), the melting of the plasmonic cap of the hybrid nanoresonator for dense optical data storage and signal processing [148] (see Fig. 3.4(a)), and different colouring applications for micro- and nanometer precise image visualization [147] 3.4(c)). These effects appear due to changes of the resonators' shapes, and, thus, the tuning of their optical response.

However, most of such examples of surface modifications or micro- and nanoresonators shape changes appear due to highly intense ultrafast laser irradiation, which does not allow the *in situ* control of the crystalline phase or the shape of the object. In this section, the method based on CW laser heating of semiconductor nanoresonators with simultaneous control of the meting process is proposed.

The case of the CW laser modification with direct temperature and crystalline phase probe of the silicon metasurface made of single nanopillars is shown in Fig. 3.5. One can see that upon higher laser excitation intensity, the

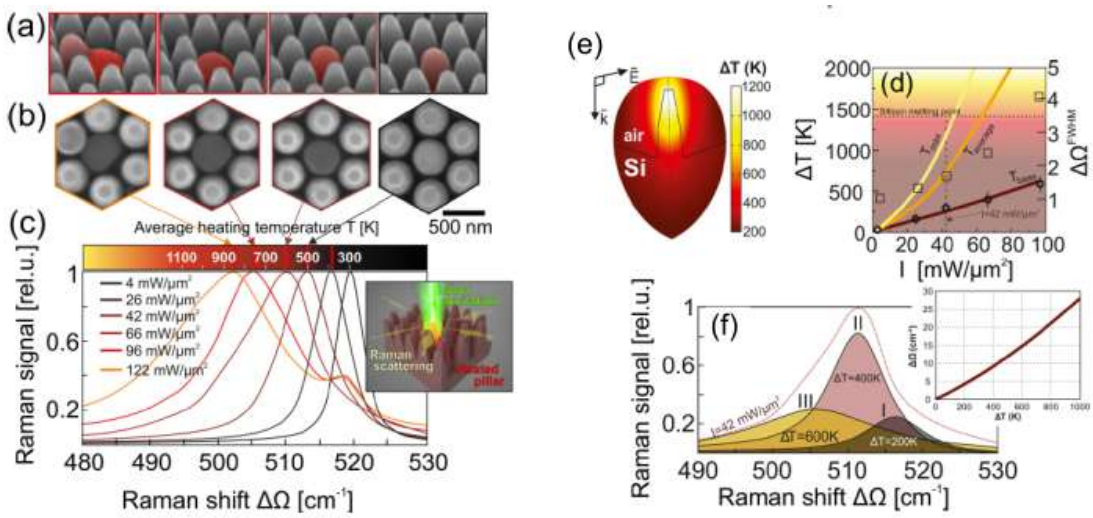

Figure 3.5 — **Laser melting with Raman feedback.** SEM images from the a) side and the b) top. c) Experimental Raman scattering spectra at elevated intensities. d) Numerical calculation of the optical heating temperature of the base (brown), average of the pillar (orange) and maximum value (yellow). Squares correspond to experimental points at different intensities. e) Typical temperature profile for resonant optical heating. f) Raman scattering spectrum with three separate contributions. Adopted from [150].

Raman spectra broadens and undergoes a blue shift (see Fig. 3.5(c)). Moreover, there are two features that should be noted from the spectra. Firstly, the presence of the right shoulder peak, which corresponds to crystalline silicon at room temperature (spectral position 520 cm^{-1}). This occurs due to non-homogeneous temperature distribution in a single nanopillar, which can be seen from the theoretical analysis in Fig. 3.5(d,e). Secondly, the wide left shoulder, which can be explained via melting of the nanoresonator and, therefore, lowering the crystalline lattice order. Indeed, the SEM images after laser treatment of corresponding laser intensities show irreversible shape modification due to the overheating and subsequent melting, as shown in Fig. 3.5(a,b).

Chapter conclusions

In conclusion to this chapter, it was shown that Raman scattering can be efficient both for thermometry and crystalline phase probe. As a proof of concept, it was shown that the silicon metasurface made of individual nanopillars can be modified via efficient optical heating. Due to the temperature localization in the tip of the nanopillar, which is proven theoretically, the

melting can occur with great spatial precision and without modification of the closest neighbours.

The scientific statement presented for the defence:

- Optical heating by a continuous wave laser source of a semiconductor Mie resonant nanostructure induces a phase transition from an amorphous to a polycrystalline state and enables *in situ* tracing of such a transition by means of Raman scattering.

Key novelty includes, but is not limited to:

- The first demonstration of *in situ* local controllable optically-induced phase transition from amorphous to polycrystalline state of silicon nanodisks on a glass substrate with temperature and phase optical feedback via Raman scattering.

The main results of the chapter are presented in works [32, 150].

CHAPTER 4. RAMAN PHOTONICS STATES PROBING

This chapter covers the ability of Raman scattering to qualitatively probe the optical resonant states of the semiconductor nanostructures non-invasively from the far-field region. It was shown in previous chapters that Raman thermometry can support the regime for 2D temperature distribution scan over the nanostructure by implementing the precise positioning piezo-stage.

By 'qualitative' we understand the detection of the general features and pattern of the near-field distribution of the optical modes of the nanostructure without any quantitative estimations.

As it was already shown before, resonant all-dielectric and semiconductor nanostructures are a powerful tool for near-field localization outside and inside the nanoresonators, as well as enhancement of the emission from them. Recently, various designs of light-emitting nanoantennas and metasurfaces with controllable intensity and far-field patterns were proposed. Here we demonstrate switching of near-field distribution in a silicon oligomer by changing polarization of the incident light generating Raman photons. Silicon nanodisks in the proposed designs support dipolar Mie resonances, coupled differently depending on the incident polarization. Since the incident polarization allows for control of the coupling between different pairs of nanodisks, the spatial distribution of Raman scattering is strongly dependent on the local field enhancement factor. We believe that such approach will pave the way for simplification both of excitation and detection of optical states.

Indeed, the Raman scattering is a powerful tool for the detection of the non-radiating optical states - anapole ones [35].

The basic principle of the dark-modes probing is shown in Fig. 4.1(a,b). If the nanoparticle supports elastic scattering in the far-field domain for specific conditions, the excitation wavelength or the substrate material, the mode is called bright. However, some optical modes do not necessarily show good coupling in the far-field scattering, therefore they are non-scattering, or, in

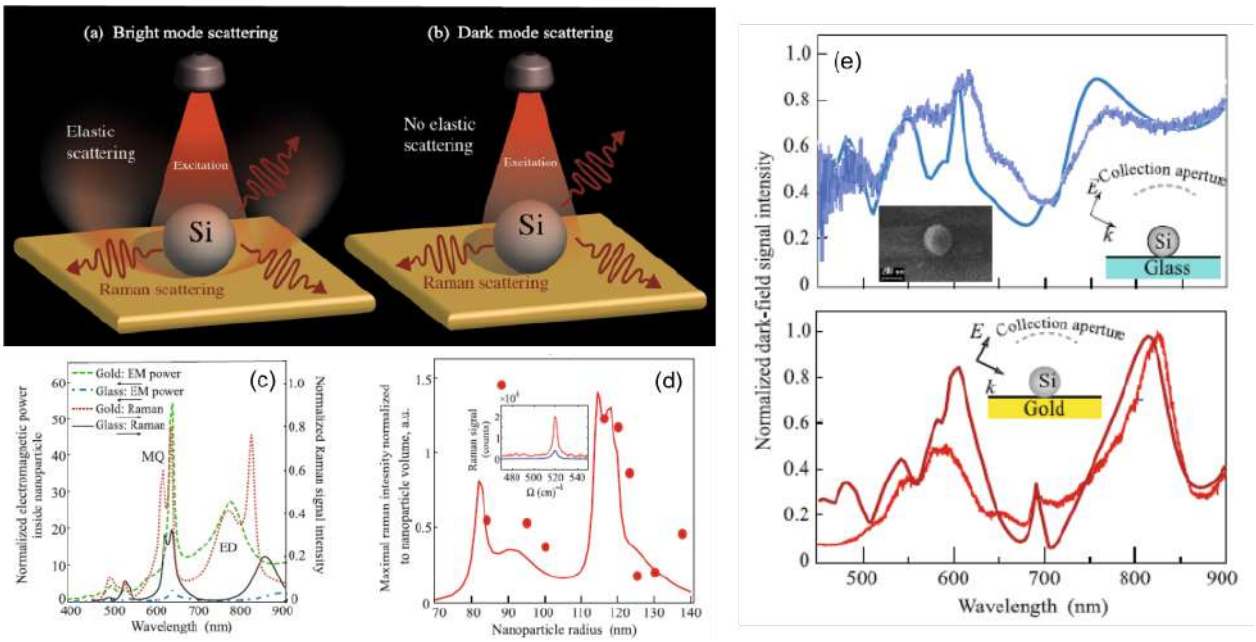

Figure 4.1 — **Raman probing of anapole states in single NP.** (a,b) Schematic of the bright and dark-mode scattering. (c) Theoretical calculation of Raman intensity response at different wavelengths in a single NP of a 115 nm radius on a glass or gold substrate. (d) Experimental and theoretical results of Raman scattering from single a nanosphere at 633 nm pump for various NPs radius. e) Experimental and theoretical DF scattering spectra of single silicon NPs on glass (upper) and gold (lower) substrates. Adopted from [36].

other words, dark modes. On the other hand, the mode might not be coupled to the far-field radiation, but still be able to be resonant. In this case, one can probe such modes by active light-emitting signal - luminescence [13] or Raman scattering [35, 36]. Both processes are very sensitive to the power absorbed by the resonator, therefore the emitted signal is proportional to the electromagnetic power inside the nanoresonator. In case of c-Si NPs, the Raman scattering is a dominant emitting process. Indeed, the elastic scattering at the Raman excitation and emitting wavelengths of 633 and 654 nm exhibits a pronounced dip both for gold and glass substrates, shown in Fig. 4.1(e). However, at the same time, the absorbed electromagnetic power and, therefore, the Raman scattering demonstrate resonant behavior as seen both from calculation and experiment, as it is shown in Fig. 4.1(c,d).

The concept of the Raman probing can be extended from the bright/dark modes detection to the polarization-dependent states in asymmetric nanostructures. In this regard, the zig-zag oligomer consisting of three

identical amorphous silicon nanodisks was considered.

Here we propose a method for optical far-field probing of near-field hot spots of the optical states based on Raman spectroscopy. It was previously shown that Raman scattering can be used for detecting optical states, either non-radiating [35,36] or bright modes (radiating) of the different order [17,21]. We show theoretically and prove experimentally that chiral [37, 38] photonic designs that support topological edge states [39] can be probed via linear inelastic scattering on optical phonons - Raman scattering. We believe that the proposed approach can be further extended to other topologically trivial and non-trivial designs and would benefit from the Raman technique that allows one to simultaneously optically heat particles and measure their temperature in real time by the spectral shift of the Stokes signal [22], thus, thermally non-linear photonic state switching [30] might take place.

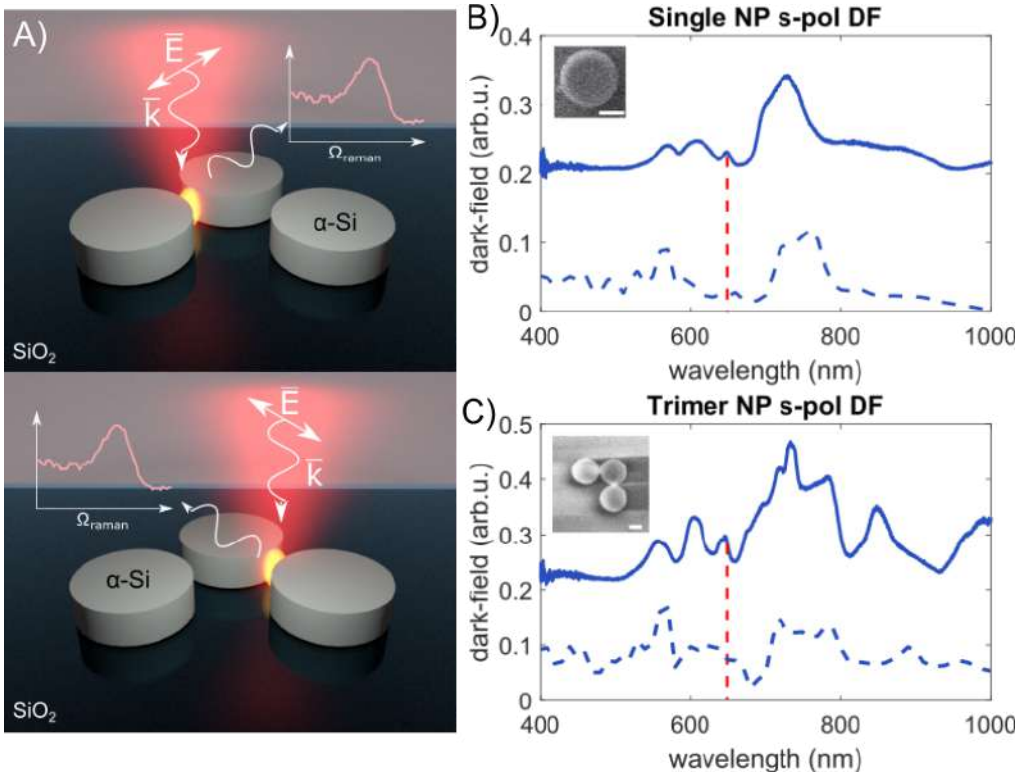

Figure 4.2 — **a-Si oligomer Raman probing concept.** a) Schematic of the Raman-probed hot-spot switching concept. Experimental and theoretical DF scattering spectra for b) a single nanodisk and c) an asymmetric oligomer consisting of the identical nanodisks of 420 nm in diameter and 165 nm in height.

Fig. 4.2(a) depicts the proposed concept, which is based on 2D mapping of Raman scattering intensity, that will show the dependence of the signal

distribution on the excitation polarization. The building block for the oligomer was chosen as a-Si nanodisk of 165 nm in height and 420 nm in diameter, which supports optical resonance in the visible range and shows a pronounced peak at the HeNe laser wavelength 632.8 nm, as shown in Fig. 4.2(b). The same resonant features can be seen for the case of the zig-zag oligomer, shown in Fig. 4.2(c).

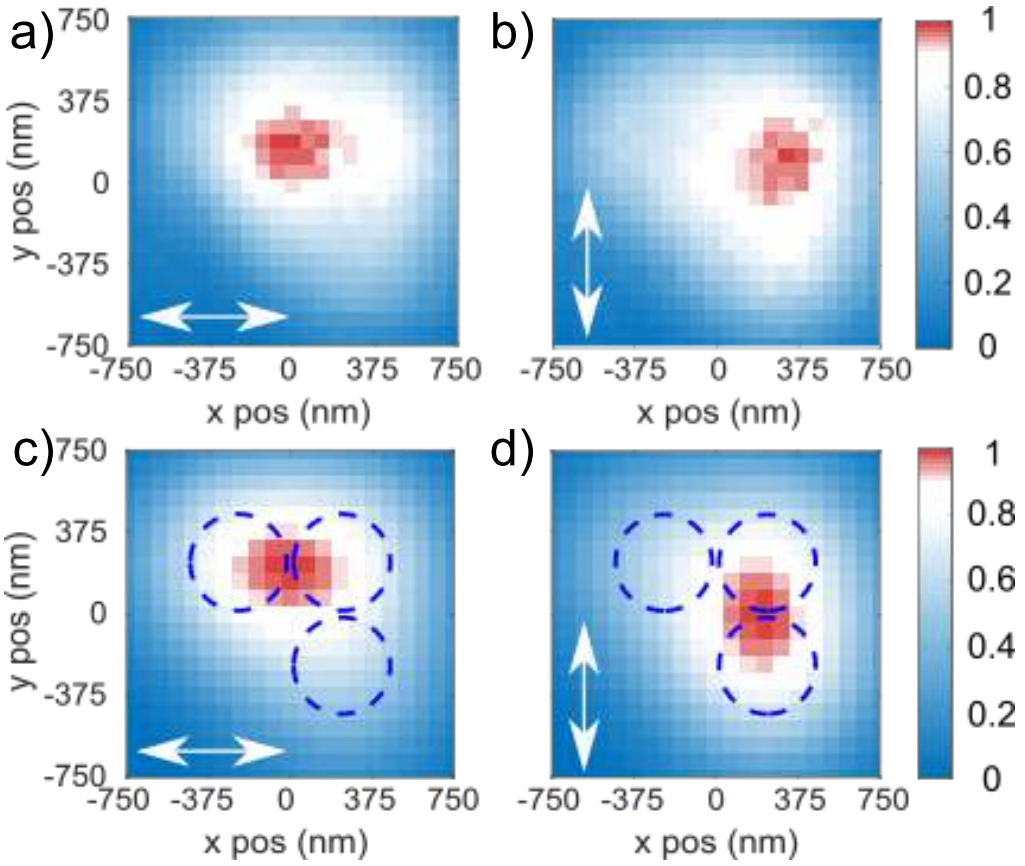

Figure 4.3 — **Polarization-induced hot-spot switching of the near-field distribution probed by Raman scattering mapping.** (a,b) Experimental and (c,d) theoretical distribution of Raman scattering from an oligomer for (a,c) horizontal and (b,d) vertical polarizations along the surface of the sample. Dashed line correspond to the location of oligomer consisting of separate nanodisks.

The experimental study of the predicted polarization-dependent localization of Raman intensity on a zigzag oligomer chain of 3 disks is shown in Fig. 4.3. The calculation results in the polarizations x and y are the same as in the experiment in Fig. 4.3. The color map is selected so that the optical switching is the easier to notice. The Raman patterns are in full agreement with the predicted ones. The localization of the Raman response is shifted either to one or another edge, similar to the calculation and the measured

experimental near-field distribution by means of scanning near-field optical microscopy (SNOM). Thus, we believe that for the first time we showed the probing from the far field of the optical states through the Raman scattering.

Chapter conclusions

In conclusion to the chapter, it was shown that Raman scattering can serve a probing tool of optical states for resonant nanostructures. The proposed method can provide information regarding the light power absorbed by the nanoresonator, and give the qualitative information about the electromagnetic spatial distribution within the nanostructure.

The scientific statement presented for the defence:

- Two-dimensional Raman scattering intensity mapping of a resonant semiconductor nanostructure allows the probing of the excited optical modes in it from the electromagnetic far-field region and provides the near field "hot-spots" spatial distribution pattern of the eigenmode at the pump wavelength.

Key novelty includes, but is not limited to:

- The first demonstration of the qualitative probing of electromagnetic near-field hot spots distribution of optical modes in resonant semiconductor nanostructures by means of two-dimensional Raman scattering intensity spatial and spectral mapping.

The main results of the chapter are published in the paper [36].

CHAPTER 5. STIMULATED RAMAN SCATTERING FROM SINGLE RESONANT NANODISK

Chapter five is devoted to the first experimental realization and demonstration of the transition from spontaneous Raman scattering to the stimulated emission regime on a single sub-micron nanodisk.

Generally, stimulated Raman scattering, or SRS, is a powerful tool for various optical and nanophotonic applications. Indeed, one of the most popular semiconductor materials for microelectronics and photonics is silicon, however, its indirect band gap is a serious disadvantage, because the transitions with photons emitted without an additional k-vector from a phonon are unlikely. Thus, silicon acting as an efficient emitter or light generator was considered ti be as a unicorn, that doesn't appear in nature. Of course, there are nonlinear light-generation processes: sum-frequency generation such as SHG, THG or higher-harmonics generation [151]. But in case of nano- and micro-objects, these processes are of very low probability. In this regard, the Raman scattering appears to be a very prospective effect for the generation of new frequencies of light for silicon or other indirect semiconductors. Generally, the Raman scattering itself is a very low probability process, however, the optical resonance can significantly enhance its intensity [17, 18]. Moreover, one can overcome the limitation that one excitation photon cannot excite more than one Raman photon by stimulated Raman emission. Indeed, stimulated Raman emission is one of the possible keys for substantial increase of the efficiency of Raman scattering, and, therefore, its intensity.

Fig. 5.1 depicts some of the important applications of stimulated Raman scattering. The stimulated Raman emission regime is an important milestone between spontaneous scattering and lasing. It was already shown that all-silicon waveguide systems support Raman lasing [152]. The Raman spectra in the Fig. 5.1(a) shows the narrowing of the line and intensity increased by 5 orders of magnitude upon reaching the lasing regime. The same effect was observed in optical waveguide, where silicon micro-sphere supporting high-Q

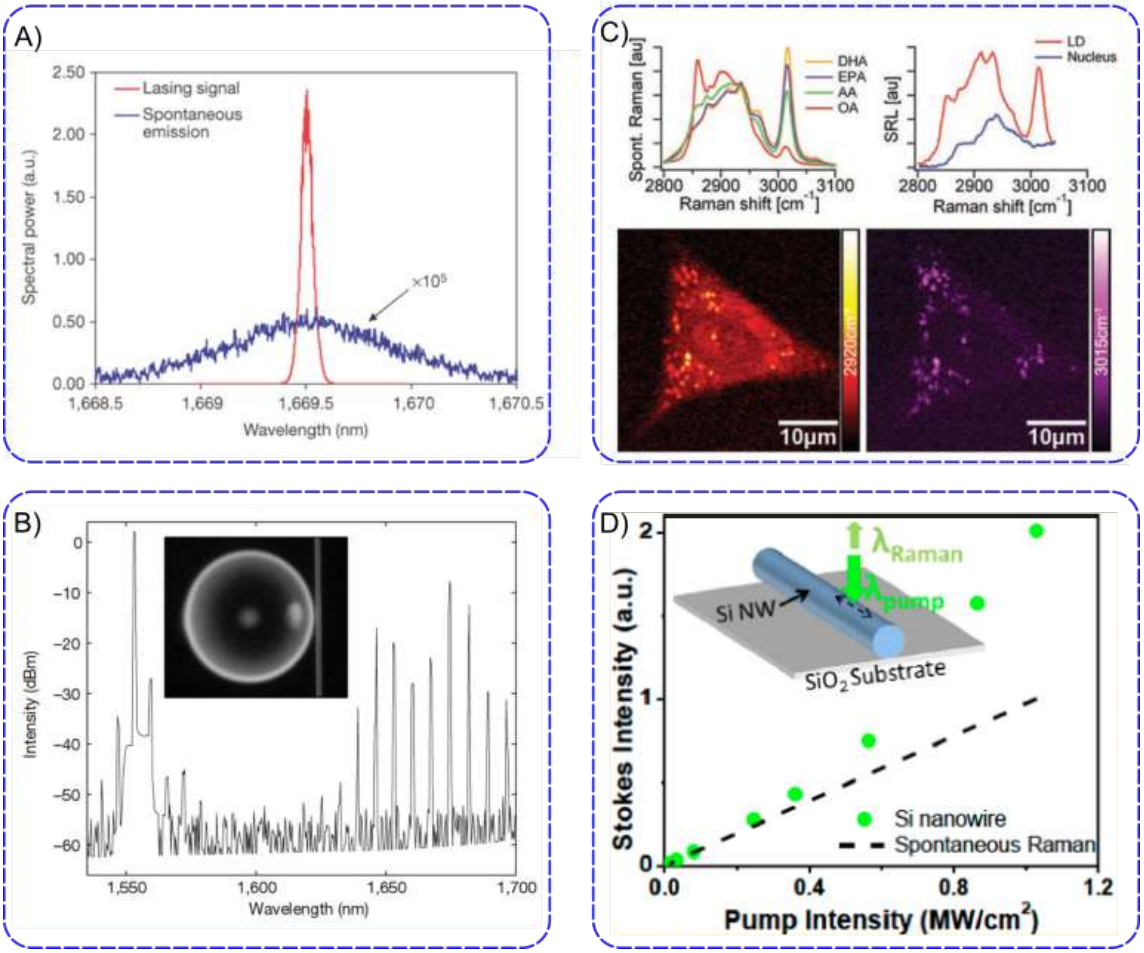

Figure 5.1 — **Stimulated Raman scattering applications.** a) All silicon Raman laser on waveguide cavity [152]. b) Ultra-low-threshold laser based on a silicon microcavity [153]. c) The demonstration of biological cell imaging with stimulated Raman scattering [154]. c) The stimulated Raman scattering from single nanowire [155].

modes served as a gain media. This effect resulted in lowering the lasing threshold [153] of lasing emission, as seen from Fig. 5.1(b). Other examples of nonlinear Raman generation include, but are not limited by label-free biological imaging and sensing [154] (see Fig. 5.1(c)), of the transition from a spontaneous to a stimulated regime of Raman emission in a single nanowire with a sub-μm cross-section and length over 10 μm length [155] (Fig. 5.1(d)). Moreover, nonlinear Raman emission allows for sub-diffractional imaging [156–158]. However, if one wants to reduce the size of the nanoobject, that supports stimulated Raman scattering, they should take into account several general steps.

Stimulated Raman scattering is a threshold process that requires specific excitation pump intensity which is defined by [153] and the formula can be observed in the red box in the Fig. 5.2. It might seem that a proper laser

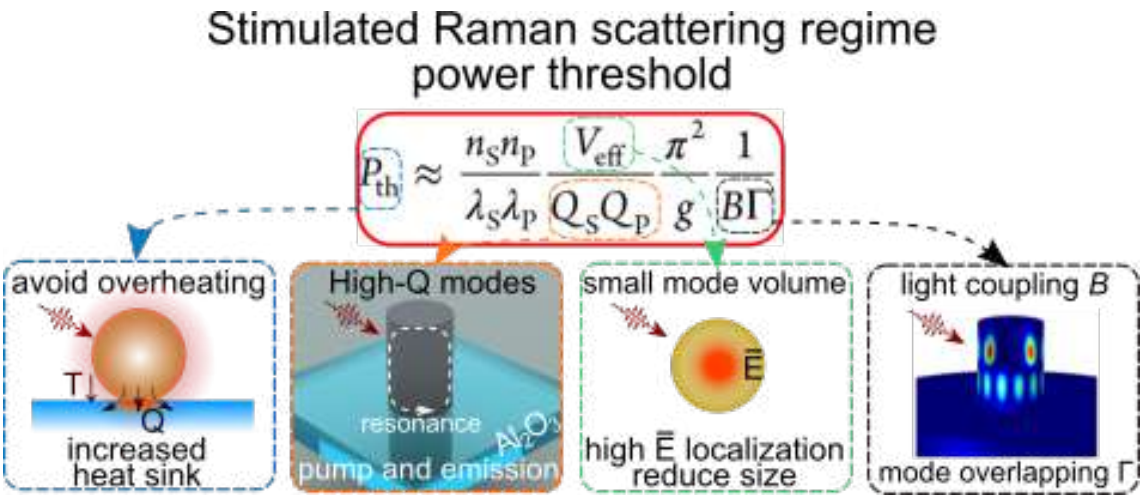

Figure 5.2 — **Schematic of reaching stimulated Raman emission regime threshold.**

excitation is sufficient to achieve stimulated Raman emission, but, unfortunately, it is always not true. In order to realize stimulated scattering in the single nanoresonator, one should try to lower the threshold power as much as possible, otherwise the nanoresonator will suffer from optical heating, as it was already shown in previous sections. Therefore, an optimized heat sink to the substrate should be realized. In this case, highly thermal conductive sapphire was chosen to be a substrate for the c-Si nanodisk. Second, the pump threshold might be reduced via the excitation of high-Q modes both at pump wavelength and at the Raman emission wavelength. One should also reduce the effective mode volume by ensuring the tight localization of the field inside the nanoresonator. Finally, the excitation light should be coupled as good possible, and the pump and emission optical modes should not be orthogonal to one another, as it is required that they should overlap as much as possible.

If the first parameter, the substrate material, is selected at the fabrication step, the other three key factors for achieving stimulated Raman scattering should be analyzed in more detail theoretically.

Fig. 5.3(a) depicts the theoretical calculation of the optical modes quality factor of a single crystalline silicon nanocylinder with fixed height of 600 nm. The diameters were varied in the range of 200÷500 nm, in order to keep the sizes in all dimensions subwavelength and sub-micron. The optimized geometry was selected as the cylinder with a 475 nm diameter. It supported the highest Q-factor resonances both at pump and emission wavelengths. It

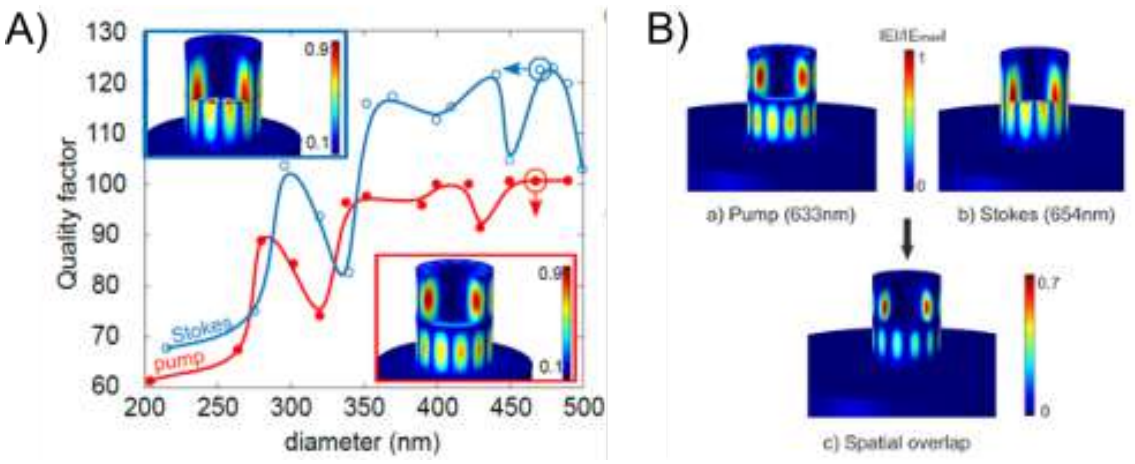

Figure 5.3 — **Theoretical mode analysis of the nanoresonator.** (a) Theoretical results on quality factor calculations for c-Si cylindrical nanoresonator of 600 nm in height at 633 wavelength. Red dots corresond to pump wavelength (633 nm), blue circles correspond to Raman emission wavelength (∼654 nm). Insets depict the electromagnetic field distribution for a specific mode. (b) The results of modes of an optimized-size nanoresonator at pump and emission spatial overlapping. Adopted from [41].

is also important that the the spectral overlapping of the modes was of the value of $\Gamma = 0.784$, and the mode coupling efficiency was $B = 2.41$. The selected cylinder of a 475 nm diameter was further studied by means of Raman scattering at different excitation intensities.

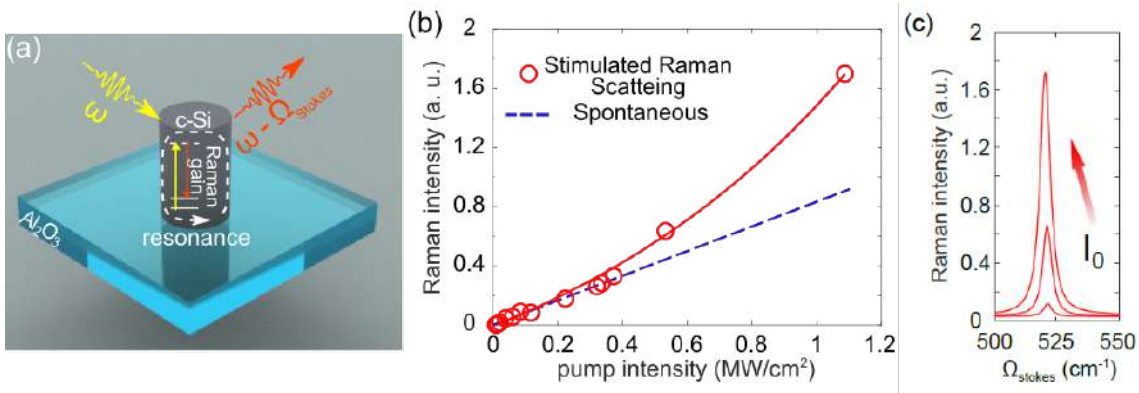

Figure 5.4 — **Experimental stimulated Raman scattering from c-Si nanoparticles.** (a) Schematic view of a Si nanoparticle excited with a laser light. (b) Experimental Raman scattering intensities at different pumps for the resonant 475-nm nanoparticle (red circles) and nonresonant 445-nm nanoparticle (blue squares). The red line corresponds to an exponential fitting.(c) Experimental Raman scattering spectra. The arrow demonstrates the higher intensity value from spectrum to spectrum. Adopted from [41].

Fig. 5.4(b) shows typical experimental dependencies of Raman scatter-

ing signal vs. pump intensity. At low intensities, spontaneous Raman scattering dominates, being characterized by a linear dependence on the incident power, as was demonstrated earlier with c-Si nanoparticles [17, 21]. However, at higher intensities (higher than 0.3 MW/cm^2), we observe a nonlinear growth of the Raman scattering signal for the nanodisk with diameter 475 nm, which is not observed for other nanodisks with diameters 250÷800 nm, see the dashed line with blue squares in Fig. 5.4(b). This sharp difference characterizes the SRS regime. It is worth noticing that the optimized substrate material (sapphire) with an increased thermal sink, along with a lowered pump threshold for the stimulated regime, allowed to keep the nanocylinder at moderate temperatures which can be seen from Fig. 5.4(c), where the explicit Raman spectra are shown. Upon higher laser intensities, the spectral position of the peak undergoes only a slight blue shift, which corresponds to sub-200 K optical heating.

Chapter conclusions

In conclusion to this chapter, the first observation of the stimulated Raman scattering from subwavelength crystalline silicon nanoparticles enhanced by Mie-type resonances was reported. The importance of critical optimization of the Q-factors of nanoparticles and thermal conductivity of a substrate for achieving a strong optical response and avoid overheating at higher intensities was revealed. It is believed that the provided finding will be useful for advanced applications of resonant dielectric nanophotonics for nanoscale thermometry and biosensing, and we plan further studies of the stimulated Raman scattering in various nanophotonic designs [7, 11, 42].

The scientific statement presented for the defence:

- The transition from spontaneous Raman scattering to stimulated scattering regime occurs upon excitation of high-Q optical resonant modes, both at the pump wavelength and at the Stokes Raman scattering wavelength, with optimized mode coupling efficiencies and their spatial overlapping at the pump the radiation wavelengths in a single crystalline silicon nanocylinder with optimized heat sink to the substrate.

Key novelty includes, but is not limited to:

- The first experimental observation of the transition from spontaneous to stimulated Raman scattering regime from isolated single crystalline silicon nanocylinder.

The main results of the chapter are published in the paper [41].

CONCLUSION

The thesis is devoted to the creation and the study of the alternative to the plasmonics sensing platform for efficient optical heating, thermometry and enhancement of the Raman scattering based on all-dielectric and semiconductor resonant nanostructures. The thesis covers the analysis of different shapes and geometries of the nanostructures, a number of materials robust to optical heating and thermometry, different substrate materials and various surrounding media were considered, the enhancement of the Raman scattering from the nanoparticles improved either by resonant conditions or by means of stimulated emission, and the optical states probing and near-field distributions study.

Summary of the main results:

1. It has been shown that spherical crystalline silicon nanoparticles with diameters from 100 to 400 nm, possessing Mie resonances in the visible range, are able to support effective optical heating and thermometry via Raman scattering at a wavelength of a CW HeNe laser of 632.8 nm.
2. It has been shown that the use of Mie resonant semiconductor α-Fe_2O_3 nanoparticles supporting optical heating and nanothermometry by means of Raman scattering in the targeted drug delivery systems contributes to a significant decrease in the threshold of pump intensity for photoinduced rupture of polymer carrier of the drug and subsequent release of the anticancer agent into carcinoma cells. The α-Fe_2O_3 nanoparticles were used as the target for near-IR laser excitation for efficient conversion of light to heat in the walls of polymer drug agents and as the direct optical temperature probe via thermally sensitive Raman scattering. As the proof of concept, the successful *in vitro* delivery and remote optically induced thermal rupture of the polymer carrier by means of laser heating of the target α-Fe_2O_3 nanoparticles with subsequent release of the antitumour drug agent vincristine was shown. The proposed system worked at the moderate laser intensity value as low as 4.0×10^4 W cm^{-2}.

3. It was shown that single amorphous hydrogenated silicon nanodisks with diameters from 300 to 450 nm, fabricated by lithographic methods on a glass substrate, can undergo a photoinduced phase transition to the polycrystalline phase due to efficient optical heating. At the same time, such a phase transition can be controlled and detected by means of Raman scattering, and the shape of the nanoparticle does not change under controlled heating and phase transition, which is confirmed by SEM images before and after annealing.
4. It was shown that two-dimensional mapping of the intensity distribution of Raman scattering from an asymmetric oligomer, consisting of three identical silicon nanodisks, makes it possible to obtain the structure of the distribution of electromagnetic near-fiel hot spots of optical modes in such nanostructures. A change in the linear polarization of the pump by 90 degrees leads to optical switching of the near field distribution of the mode, which is also detected from the far-field by means of Raman scattering.
5. It was shown that a single silicon nanocylinder 600 nm in height and 475 nm in diameter placed on a sapphire substrate supports the transition from spontaneous Raman scattering mode to stimulated emission regime under continuous pumping of a HeNe laser at a wavelength of 632.8 nm and a pump intensity $I_0 = 0.4$ MW/cm^2 due to the optimized Q-factors of the eigenmodes excited at the pump and emission of the Stokes Raman scattering wavelengths, as well as due to increased heat sink to the substrate with high thermal conductivity.

Main research publications:

[A1] **Zograf G. P.**, Petrov M. I., Zuev D. A., Dmitriev P. A., Milichko V. A., Makarov S. V., Belov P. A. Resonant nonplasmonic nanoparticles for efficient temperature-feedback optical heating //Nano Letters. – 2017. – . 17. – №. 5. – . 2945-2952.

[A2] **Zograf G. P.**, Timin A. S., Muslimov A. R., Shishkin I. I., Nominé A., Ghanbaja J., Ghosh P., Li Q., Zyuzin M. V., Makarov S. V. All-Optical

Nanoscale Heating and Thermometry with Resonant Dielectric Nanoparticles for Controllable Drug Release in Living Cells //Laser & Photonics Reviews. – 2020. – . 14. – №. 3. – . 1900082.

[A3] Milichko V. A., Zuev D. A., Baranov D. G., **Zograf G. P.**, Volodina K., Krasilin A. A., Mukhin I. S., Dmitriev P. A., Vinogradov V. V., Makarov S. V., Belov P. A. Metal-dielectric nanocavity for real-time tracing molecular events with temperature feedback //Laser & Photonics Reviews. – 2018. – . 12. – №. 1. – . 1700227.

[A4] **Zograf G. P.**, Yu Y. F., Baryshnikova K. V., Kuznetsov A. I., Makarov S. V. Local crystallization of a resonant amorphous silicon nanoparticle for the implementation of optical nanothermometry //JETP Letters. – 2018. – . 107. – №. 11. – . 699-704.

[A5] Aouassa M., Mitsai E., Syubaev S., Pavlov D., Zhizhchenko A., Jadli I., Hassayoun L., **Zograf G.**, Makarov S., Kuchmizhak, A . Temperature-feedback direct laser reshaping of silicon nanostructures //Applied Physics Letters. – 2017. – . 111. – №. 24. – . 243103.

[A6] Baryshnikova K. V., Frizyuk K. S., **Zograf G. P**, Makarov S. V., Baranov M. A., Zuev D. A., Milichko V. A., Mukhin I.S., Petrov M. I., Evlyukhin A. B. Revealing low-radiative modes of nanoresonators with internal raman scattering //JETP Letters. – 2019. – . 110. – №. 1. – . 25-30.

[A7] **Zograf G. P.** et al. Stimulated Raman Scattering from Mie-Resonant Subwavelength Nanoparticles //Nano Letters. – 2020. – . 20. – №. 8. – . 5786-5791.

[A8] **Zograf G. P.**, Petrov M. I., Makarov S. V. Coating of Au nanoparticle by Si shell for enhanced local heating //JPhCS. – 2017. – . 929. – №. 1. – . 012072.

[A9] **Zograf G. P.** et al. Gap size impact on metal-dielectric nanocavity heater properties //AIP Conference Proceedings. – AIP Publishing LLC, 2017. – . 1874. – №. 1. – . 030043.

[A10] **Zograf G.**, Makarov S., Petrov M. Doping of resonant silicon nanodisks for efficient optical heating in the near-infrared range //JPhCS. – 2020. – . 1461. – №. 1. – . 012201.

Acknowledgements. In conclusion, I would like to express my sincere gratitude to my scientific adviser Prof. S.V. Makarov for support and assistance throughout my research, for discussion of the results, and scientific guidance and mentoring. Credits to I. Mukhin, F. Komissarenko, V. Rutckaia and A. Kuznetsov for providing the samples; M.I. Petrov and Yu.S. Kivshar for a unique opportunity to participate in the implementation of their many ideas and for a source of motivation; P. Dmitriev and A. Samusev for promoting department of physics of ITMO University, and A. Bogdanov and M. Petrov for inviting me to ITMO University master's program back in 2015; the collaborators from all over the world and the entire team of the Physics and Engineering Department of ITMO University, headed by P.A. Belov and I.V. Melchakova. Also I would like to mention the crucial impact to my first scientific steps from "Physical-Technical High School" named after Zh. I. Alfyorov, Peter the Great St.Petersburg Polytechnic University and Ioffe Institute and my first supervisor V.I. Nikolaev. Finally, I thank the authors of the *RussianPhd-LaTeX-Dissertation-Template* template for their help in completing the dissertation, and my friends and family for their patience and support.

Fin.

LIST OF ACRONYMS AND SYMBOLS

NP	Nanoparticle
DF	Dark-field scattering
CW	Continuous wave laser
PML	Perfectly matched layers
PEC	Perfect electric conductor
ED, MD	Electric dipole and magnetic dipole
EQ, MQ	Electric quadrupole and magnetic quadrupole
SRS	Stimulated Raman scattering
SEM	Scanning electron microscopy
TEM	Transmission electron microscopy
AFM	Atomic force microscopy
SERS	Surface-enhanced Raman scattering
CC	Carcinoma cells
λ	Wavelength in vacuum
ε	Dielectric permittivity
n	Refractive index

BIBLIOGRAPHY

1. M. Fleischmann, P. Hendra, and A. McQuillan, "Raman spectra of pyridine adsorbed at a silver elec," *Chemical physics letters*, vol. 26, no. 2, 1974.
2. E. Le Ru, E. Blackie, M. Meyer, and P. G. Etchegoin, "Surface enhanced raman scattering enhancement factors: a comprehensive study," *The Journal of Physical Chemistry C*, vol. 111, no. 37, pp. 13794–13803, 2007.
3. D.-K. Lim, K.-S. Jeon, H. M. Kim, J.-M. Nam, and Y. D. Suh, "Nanogap-engineerable raman-active nanodumbbells for single-molecule detection," *Nature materials*, vol. 9, no. 1, pp. 60–67, 2010.
4. L. A. Lane, X. Qian, and S. Nie, "Sers nanoparticles in medicine: from label-free detection to spectroscopic tagging," *Chemical reviews*, vol. 115, no. 19, pp. 10489–10529, 2015.
5. G. Baffou and R. Quidant, "Thermo-plasmonics: using metallic nanostructures as nano-sources of heat," *Laser & Photonics Reviews*, vol. 7, no. 2, pp. 171–187, 2013.
6. A. Carattino, M. Caldarola, and M. Orrit, "Gold nanoparticles as absolute nanothermometers," *Nano Letters*, vol. 18, no. 2, pp. 874–880, 2018.
7. E. Tiguntseva, K. Koshelev, A. Furasova, P. Tonkaev, V. Mikhailovskii, E. V. Ushakova, D. G. Baranov, T. Shegai, A. A. Zakhidov, Y. Kivshar, *et al.*, "Room-temperature lasing from mie-resonant non-plasmonic nanoparticles," *ACS Nano*, 2020.
8. V. Mylnikov, S. T. Ha, Z. Pan, V. Valuckas, R. Paniagua-Dominguez, H. V. Demir, and A. I. Kuznetsov, "Lasing action in single subwavelength particles supporting supercavity modes," *ACS Nano*, 2020.
9. M. R. Shcherbakov, D. N. Neshev, B. Hopkins, A. S. Shorokhov, I. Staude, E. V. Melik-Gaykazyan, M. Decker, A. A. Ezhov, A. E. Miroshnichenko, and I. Brener, "Enhanced third-harmonic generation in silicon nanoparticles driven by magnetic response," *Nano Letters*, vol. 14, no. 11, pp. 6488–6492, 2014.

10. S. V. Makarov, M. I. Petrov, U. Zywietz, V. Milichko, D. Zuev, N. Lopanitsyna, A. Kuksin, I. Mukhin, G. Zograf, and E. Ubyivovk, "Efficient second-harmonic generation in nanocrystalline silicon nanoparticles," *Nano Letters*, vol. 17, no. 5, pp. 3047–3053, 2017.
11. K. Koshelev, S. Kruk, E. Melik-Gaykazyan, J.-H. Choi, A. Bogdanov, H.-G. Park, and Y. Kivshar, "Subwavelength dielectric resonators for nonlinear nanophotonics," *Science*, vol. 367, no. 6475, pp. 288–292, 2020.
12. E. Tiguntseva, G. P. Zograf, F. E. Komissarenko, D. A. Zuev, A. A. Zakhidov, S. V. Makarov, and Y. S. Kivshar, "Light-emitting halide perovskite nanoantennas," *Nano Letters*, vol. 18, no. 2, pp. 1185–1190, 2018.
13. V. Rutckaia, F. Heyroth, A. Novikov, M. Shaleev, M. Petrov, and J. Schilling, "Quantum dot emission driven by mie resonances in silicon nanostructures," *Nano letters*, vol. 17, no. 11, pp. 6886–6892, 2017.
14. R. M. Bakker, D. Permyakov, Y. F. Yu, D. Markovich, R. Paniagua-Domínguez, L. Gonzaga, A. Samusev, Y. Kivshar, B. Lukyanchuk, and A. I. Kuznetsov, "Magnetic and electric hotspots with silicon nanodimers," *Nano Letters*, vol. 15, no. 3, pp. 2137–2142, 2015.
15. M. Caldarola, P. Albella, E. Cortés, M. Rahmani, T. Roschuk, G. Grinblat, R. F. Oulton, A. V. Bragas, and S. A. Maier, "Non-plasmonic nanoantennas for surface enhanced spectroscopies with ultra-low heat conversion," *Nature communications*, vol. 6, p. 7915, 2015.
16. A. I. Kuznetsov, A. E. Miroshnichenko, M. L. Brongersma, Y. S. Kivshar, and B. Luk'yanchuk, "Optically resonant dielectric nanostructures," *Science*, vol. 354, no. 6314, p. aag2472, 2016.
17. P. A. Dmitriev, D. G. Baranov, V. A. Milichko, S. V. Makarov, I. S. Mukhin, A. K. Samusev, A. E. Krasnok, P. A. Belov, and Y. S. Kivshar, "Resonant raman scattering from silicon nanoparticles enhanced by magnetic response," *Nanoscale*, vol. 8, no. 18, pp. 9721–9726, 2016.
18. K. Frizyuk, M. Hasan, A. Krasnok, A. Alú, and M. Petrov, "Enhancement of raman scattering in dielectric nanostructures with electric and magnetic mie resonances," *Physical Review B*, vol. 97, no. 8, p. 085414, 2018.

19. A. O. Govorov and H. H. Richardson, "Generating heat with metal nanoparticles," *Nano Today*, vol. 2, no. 1, pp. 30–38, 2007.

20. G. Baffou, R. Quidant, and F. J. Garcia de Abajo, "Nanoscale control of optical heating in complex plasmonic systems," *ACS Nano*, vol. 4, no. 2, pp. 709–716, 2010.

21. G. P. Zograf, M. I. Petrov, D. A. Zuev, P. A. Dmitriev, V. A. Milichko, S. V. Makarov, and P. A. Belov, "Resonant nonplasmonic nanoparticles for efficient temperature-feedback optical heating," *Nano letters*, vol. 17, no. 5, pp. 2945–2952, 2017.

22. M. Balkanski, R. Wallis, and E. Haro, "Anharmonic effects in light scattering due to optical phonons in silicon," *Physical Review B*, vol. 28, no. 4, p. 1928, 1983.

23. C. D. Brites, P. P. Lima, N. J. Silva, A. Millán, V. S. Amaral, F. Palacio, and L. D. Carlos, "Thermometry at the nanoscale," *Nanoscale*, vol. 4, no. 16, pp. 4799–4829, 2012.

24. G. T. Reed, G. Mashanovich, F. Gardes, and D. Thomson, "Silicon optical modulators," *Nature Photonics*, vol. 4, no. 8, pp. 518–526, 2010.

25. A. Yashchenok, A. Masic, D. Gorin, O. Inozemtseva, B. S. Shim, N. Kotov, A. Skirtach, and H. Möhwald, "Optical heating and temperature determination of core–shell gold nanoparticles and single-walled carbon nanotube microparticles," *Small*, vol. 11, no. 11, pp. 1320–1327, 2015.

26. G. Baffou, F. Cichos, and R. Quidant, "Applications and challenges of thermoplasmonics," *Nature Materials*, pp. 1–13, 2020.

27. W. L. Barnes, A. Dereux, and T. W. Ebbesen, "Surface plasmon subwavelength optics," *nature*, vol. 424, no. 6950, pp. 824–830, 2003.

28. A. Tittl, A. Leitis, M. Liu, F. Yesilkoy, D. Y. Choi, D. N. Neshev, Y. S. Kivshar, and H. Altug, "Imaging-based molecular barcoding with pixelated dielectric metasurfaces," *Science*, vol. 360, no. 6393, pp. 1105–1109, 2018.

29. F. Yesilkoy, E. R. Arvelo, Y. Jahani, M. Liu, A. Tittl, V. Cevher, Y. Kivshar, and H. Altug, "Ultrasensitive hyperspectral imaging and

biodetection enabled by dielectric metasurfaces," *Nature Photonics*, vol. 13, no. 6, pp. 390–396, 2019.

30. V. A. Milichko, D. A. Zuev, D. G. Baranov, G. P. Zograf, K. Volodina, A. A. Krasilin, I. S. Mukhin, P. A. Dmitriev, V. V. Vinogradov, S. V. Makarov, *et al.*, "Metal-dielectric nanocavity for real-time tracing molecular events with temperature feedback," *Laser & Photonics Reviews*, vol. 12, no. 1, p. 1700227, 2018.
31. G. P. Zograf, A. S. Timin, A. R. Muslimov, I. I. Shishkin, A. Nominé, J. Ghanbaja, P. Ghosh, Q. Li, M. V. Zyuzin, and S. V. Makarov, "All-optical nanoscale heating and thermometry with resonant dielectric nanoparticles for controllable drug release in living cells," *Laser & Photonics Reviews*, vol. 14, no. 3, p. 1900082, 2020.
32. G. P. Zograf, Y. F. Yu, K. V. Baryshnikova, A. I. Kuznetsov, and S. V. Makarov, "Local crystallization of a resonant amorphous silicon nanoparticle for the implementation of optical nanothermometry," *JETP Letters*, vol. 107, no. 11, pp. 699–704, 2018.
33. M. K. Hatalis and D. W. Greve, "Large grain polycrystalline silicon by low-temperature annealing of low-pressure chemical vapor deposited amorphous silicon films," *Journal of applied physics*, vol. 63, no. 7, pp. 2260–2266, 1988.
34. S. Makarov, I. Sinev, V. Milichko, F. Komissarenko, D. Zuev, E. Ushakova, I. Mukhin, Y. Yu, A. Kuznetsov, P. Belov, *et al.*, "Nanoscale generation of white light for ultrabroadband nanospectroscopy," *Nano letters*, vol. 18, no. 1, pp. 535–539, 2018.
35. D. G. Baranov, R. Verre, P. Karpinski, and M. Kall, "Anapole-enhanced intrinsic raman scattering from silicon nanodisks," *ACS Photonics*, vol. 5, no. 7, pp. 2730–2736, 2018.
36. K. Baryshnikova, K. Frizyuk, G. Zograf, S. Makarov, M. Baranov, D. Zuev, V. Milichko, I. Mukhin, M. Petrov, and A. Evlyukhin, "Revealing low-radiative modes of nanoresonators with internal raman scattering," *JETP Letters*, pp. 1–6, 2019.

37. K. Ullah, B. Garcia-Camara, M. Habib, X. Liu, A. Krasnok, S. Lepeshov, J. Hao, J. Liu, and N. Yadav, "Chiral all-dielectric trimer nanoantenna," *Journal of Quantitative Spectroscopy and Radiative Transfer*, vol. 208, pp. 71–77, 2018.

38. L. Lin, S. Lepeshov, A. Krasnok, T. Jiang, X. Peng, B. A. Korgel, A. Alù, and Y. Zheng, "All-optical reconfigurable chiral meta-molecules," *Materials Today*, vol. 25, pp. 10–20, 2019.

39. A. P. Slobozhanyuk, A. N. Poddubny, A. E. Miroshnichenko, P. A. Belov, and Y. S. Kivshar, "Subwavelength topological edge states in optically resonant dielectric structures," *Physical review letters*, vol. 114, no. 12, p. 123901, 2015.

40. T. Zhang, Y. Che, K. Chen, J. Xu, Y. Xu, T. Wen, G. Lu, X. Liu, B. Wang, X. Xu, *et al.*, "Anapole mediated giant photothermal nonlinearity in nanostructured silicon," *Nature communications*, vol. 11, no. 1, pp. 1–9, 2020.

41. G. P. Zograf, D. Ryabov, V. Rutckaia, P. Voroshilov, P. Tonkaev, D. V. Permyakov, Y. Kivshar, and S. V. Makarov, "Stimulated raman scattering from mie-resonant subwavelength nanoparticles," *Nano Letters*, vol. 20, no. 8, pp. 5786–5791, 2020.

42. S. T. Ha, Y. H. Fu, N. K. Emani, Z. Pan, R. M. Bakker, R. Paniagua-Domínguez, and A. I. Kuznetsov, "Directional lasing in resonant semiconductor nanoantenna arrays," *Nature Nanotechnology*, vol. 13, no. 11, pp. 1042–1047, 2018.

43. A. I. Kuznetsov, A. E. Miroshnichenko, Y. H. Fu, J. Zhang, and B. Luk'Yanchuk, "Magnetic light," *Scientific reports*, vol. 2, p. 492, 2012.

44. A. B. Evlyukhin, S. M. Novikov, U. Zywietz, R. L. Eriksen, C. Reinhardt, S. I. Bozhevolnyi, and B. N. Chichkov, "Demonstration of magnetic dipole resonances of dielectric nanospheres in the visible region," *Nano Letters*, vol. 12, no. 7, pp. 3749–3755, 2012.

45. G. Mie, "Beiträge zur optik trüber medien, speziell kolloidaler metallösungen," *Annalen der Physik*, vol. 330, no. 3, pp. 377–445, 1908.

46. C. F. Bohren and D. R. Huffman, *Absorption and scattering of light by small particles*. John Wiley & Sons, 2008.

47. J. G. Speight, *Lange's handbook of chemistry*, vol. 1. McGraw-Hill New York, 2005.

48. M. V. Rybin, K. L. Koshelev, Z. F. Sadrieva, K. B. Samusev, A. A. Bogdanov, M. F. Limonov, and Y. S. Kivshar, "High-q supercavity modes in subwavelength dielectric resonators," *Physical review letters*, vol. 119, no. 24, p. 243901, 2017.

49. P. Dmitriev, S. Makarov, V. Milichko, I. Mukhin, A. Gudovskikh, A. Sitnikova, A. Samusev, A. Krasnok, and P. Belov, "Laser fabrication of crystalline silicon nanoresonators from an amorphous film for low-loss all-dielectric nanophotonics," *Nanoscale*, vol. 8, no. 9, pp. 5043–5048, 2016.

50. U. Zywietz, A. B. Evlyukhin, C. Reinhardt, and B. N. Chichkov, "Laser printing of silicon nanoparticles with resonant optical electric and magnetic responses," *Nature communications*, vol. 5, p. 3402, 2014.

51. S. L. Chuang, *Physics of photonic devices*, vol. 80. John Wiley & Sons, 2012.

52. S. K. Sundaram and E. Mazur, "Inducing and probing non-thermal transitions in semiconductors using femtosecond laser pulses," *Nature Materials*, vol. 1, no. 4, pp. 217–224, 2002.

53. S. V. Makarov, A. S. Zalogina, M. Tajik, D. A. Zuev, M. V. Rybin, A. A. Kuchmizhak, S. Juodkazis, and Y. Kivshar, "Light-induced tuning and reconfiguration of nanophotonic structures," *Laser & Photonics Reviews*, vol. 11, no. 5, p. 1700108, 2017.

54. R. Righini, "Ultrafast optical kerr effect in liquids and solids," *Science*, vol. 262, no. 5138, pp. 1386–1390, 1993.

55. S. Makarov, S. Kudryashov, I. Mukhin, A. Mozharov, V. Milichko, A. Krasnok, and P. Belov, "Tuning of magnetic optical response in a dielectric nanoparticle by ultrafast photoexcitation of dense electron–hole plasma," *Nano letters*, vol. 15, no. 9, pp. 6187–6192, 2015.

56. M. Stegmaier, C. Ríos, H. Bhaskaran, and W. H. Pernice, "Thermo-optical effect in phase-change nanophotonics," *Acs Photonics*, vol. 3, no. 5, pp. 828–835, 2016.

57. M. A. Fox and M. T. Dulay, "Heterogeneous photocatalysis," *Chemical reviews*, vol. 93, no. 1, pp. 341–357, 1993.

58. A. Fujishima, T. N. Rao, and D. A. Tryk, "Titanium dioxide photocatalysis," *Journal of photochemistry and photobiology C: Photochemistry reviews*, vol. 1, no. 1, pp. 1–21, 2000.

59. M. R. Hoffmann, S. T. Martin, W. Choi, and D. W. Bahnemann, "Environmental applications of semiconductor photocatalysis," *Chemical reviews*, vol. 95, no. 1, pp. 69–96, 1995.

60. B. N. Chichkov, C. Momma, S. Nolte, F. Von Alvensleben, and A. Tünnermann, "Femtosecond, picosecond and nanosecond laser ablation of solids," *Applied physics A*, vol. 63, no. 2, pp. 109–115, 1996.

61. G. Grinblat, Y. Li, M. P. Nielsen, R. F. Oulton, and S. A. Maier, "Enhanced third harmonic generation in single germanium nanodisks excited at the anapole mode," *Nano Letters*, vol. 16, no. 7, pp. 4635–4640, 2016.

62. H. K. Shamkhi, K. V. Baryshnikova, A. Sayanskiy, P. Kapitanova, P. D. Terekhov, P. Belov, A. Karabchevsky, A. B. Evlyukhin, Y. Kivshar, and A. S. Shalin, "Transverse scattering and generalized kerker effects in all-dielectric mie-resonant metaoptics," *Physical review letters*, vol. 122, no. 19, p. 193905, 2019.

63. W. Liu, A. E. Miroshnichenko, D. N. Neshev, and Y. S. Kivshar, "Broadband unidirectional scattering by magneto-electric core–shell nanoparticles," *ACS Nano*, vol. 6, pp. 5489–5497, 2012.

64. A. E. Miroshnichenko, A. B. Evlyukhin, Y. F. Yu, R. M. Bakker, A. Chipouline, A. I. Kuznetsov, B. Luk'yanchuk, B. N. Chichkov, and Y. S. Kivshar, "Nonradiating anapole modes in dielectric nanoparticles," *Nature communications*, vol. 6, p. 8069, 2015.

65. A. Furasova, E. Calabró, E. Lamanna, E. Tiguntseva, E. Ushakova, E. Ubyivovk, V. Mikhailovskii, A. Zakhidov, S. Makarov, and A. Di Carlo, "Resonant silicon nanoparticles for enhanced light harvesting in halide

perovskite solar cells," *Advanced Optical Materials*, vol. 6, no. 21, p. 1800576, 2018.

66. S. Adachi, *Properties of semiconductor alloys: group-IV, III-V and II-VI semiconductors*, vol. 28. John Wiley & Sons, 2009.
67. G. Ghosh, *Handbook of optical constants of solids: Handbook of thermo-optic coefficients of optical materials with applications*. Academic Press, 1998.
68. M. Levinshtein, *Handbook series on semiconductor parameters*, vol. 1. World Scientific, 1997.
69. K. Tsang, H. Kui, and K. Chik, "Calorimetric studies of the heat capacity and relaxation of amorphous si prepared by electron beam evaporation," *Journal of applied physics*, vol. 74, no. 8, pp. 4932–4935, 1993.
70. B. Zink, R. Pietri, and F. Hellman, "Thermal conductivity and specific heat of thin-film amorphous silicon," *Physical review letters*, vol. 96, no. 5, p. 055902, 2006.
71. O. Yavas, N. Do, A. C. Tam, P. Leung, W. P. Leung, H. K. Park, C. P. Grigoropoulos, J. Boneberg, and P. Leiderer, "Temperature dependence of optical properties for amorphous silicon at wavelengths of 632.8 and 752 nm," *Optics letters*, vol. 18, no. 7, pp. 540–542, 1993.
72. K. Takimoto, A. Fukuta, Y. Yamamoto, N. Yoshida, T. Itoh, and S. Nonomura, "Linear thermal expansion coefficients of amorphous and microcrystalline silicon films," *Journal of non-crystalline solids*, vol. 299, pp. 314–317, 2002.
73. A. El-Sharkawy, A. Abou El-Azm, M. Kenawy, A. Hillal, and H. Abu-Basha, "Thermophysical properties of polycrystalline pbs, pbse, and pbte in the temperature range 300–700 k," *International journal of thermophysics*, vol. 4, no. 3, pp. 261–269, 1983.
74. T. Lewi, N. A. Butakov, H. A. Evans, M. W. Knight, P. P. Iyer, D. Higgs, H. Chorsi, J. Trastoy, J. D. V. Granda, I. Valmianski, *et al.*, "Thermally reconfigurable meta-optics," *IEEE Photonics Journal*, vol. 11, no. 2, pp. 1–16, 2019.

75. J. M. Skelton, S. C. Parker, A. Togo, I. Tanaka, and A. Walsh, "Thermal physics of the lead chalcogenides pbs, pbse, and pbte from first principles," *Physical Review B*, vol. 89, no. 20, p. 205203, 2014.

76. L. Balde, B. Legendre, and A. Balkhi, "Etude du diagramme d'equilibre entre phases du systeme ternaire germanium-etain-tellure," *Journal of alloys and compounds*, vol. 216, no. 2, pp. 285–293, 1995.

77. E. Morales-Sanchez, E. Prokhorov, J. Gonzalez-Hernandez, and A. Mendoza-Galvan, "Structural, electric and kinetic parameters of ternary alloys of gesbte," *Thin Solid Films*, vol. 471, no. 1-2, pp. 243–247, 2005.

78. J.-L. Battaglia, A. Kusiak, V. Schick, A. Cappella, C. Wiemer, M. Longo, and E. Varesi, "Thermal characterization of the si o 2-ge 2 sb 2 te 5 interface from room temperature up to 400 c," *Journal of Applied Physics*, vol. 107, no. 4, p. 044314, 2010.

79. H.-K. Lyeo, D. G. Cahill, B.-S. Lee, J. R. Abelson, M.-H. Kwon, K.-B. Kim, S. G. Bishop, and B.-k. Cheong, "Thermal conductivity of phase-change material ge 2 sb 2 te 5," *Applied Physics Letters*, vol. 89, no. 15, p. 151904, 2006.

80. C.-A. Jong, W. Fang, C.-M. Lee, and T.-S. Chin, "Mechanical properties of phase-change recording media: Gesbte films," *Japanese Journal of Applied Physics*, vol. 40, no. 5R, p. 3320, 2001.

81. B. Brunetti, C. Cavallo, A. Ciccioli, G. Gigli, and A. Latini, "On the thermal and thermodynamic (in) stability of methylammonium lead halide perovskites," *Scientific reports*, vol. 6, p. 31896, 2016.

82. T. Handa, H. Tahara, T. Aharen, and Y. Kanemitsu, "Large negative thermo-optic coefficients of a lead halide perovskite," *Science advances*, vol. 5, no. 7, p. eaax0786, 2019.

83. C. Ge, M. Hu, P. Wu, Q. Tan, Z. Chen, Y. Wang, J. Shi, and J. Feng, "Ultralow thermal conductivity and ultrahigh thermal expansion of single-crystal organic–inorganic hybrid perovskite ch3nh3pbx3 (x= cl, br, i)," *The Journal of Physical Chemistry C*, vol. 122, no. 28, pp. 15973–15978, 2018.

84. L. Sarkhosh, H. Aleali, R. Karimzadeh, and N. Mansour, "Large thermally induced nonlinear refraction of gold nanoparticles stabilized by cyclohexanone," *physica status solidi (a)*, vol. 207, no. 10, pp. 2303–2310, 2010.

85. F. Nix and D. MacNair, "The thermal expansion of pure metals: copper, gold, aluminum, nickel, and iron," *Physical Review*, vol. 60, no. 8, p. 597, 1941.

86. R. Karimzadeh and N. Mansour, "The effect of concentration on the thermo-optical properties of colloidal silver nanoparticles," *Optics & Laser Technology*, vol. 42, no. 5, pp. 783–789, 2010.

87. D. G. Baranov, D. A. Zuev, S. I. Lepeshov, O. V. Kotov, A. E. Krasnok, A. B. Evlyukhin, and B. N. Chichkov, "All-dielectric nanophotonics: the quest for better materials and fabrication techniques," *Optica*, vol. 4, no. 7, pp. 814–825, 2017.

88. P. Herve and L. Vandamme, "General relation between refractive index and energy gap in semiconductors," *Infrared physics & technology*, vol. 35, no. 4, pp. 609–615, 1994.

89. Q. A. Akkerman, V. D'Innocenzo, S. Accornero, A. Scarpellini, A. Petrozza, M. Prato, and L. Manna, "Tuning the optical properties of cesium lead halide perovskite nanocrystals by anion exchange reactions," *Journal of the American Chemical Society*, vol. 137, no. 32, pp. 10276–10281, 2015.

90. E. Y. Tiguntseva, D. G. Baranov, A. P. Pushkarev, B. Munkhbat, F. Komissarenko, M. Franckevicius, A. A. Zakhidov, T. Shegai, Y. S. Kivshar, and S. V. Makarov, "Tunable hybrid fano resonances in halide perovskite nanoparticles," *Nano letters*, vol. 18, no. 9, pp. 5522–5529, 2018.

91. S. C. Erwin, L. Zu, M. I. Haftel, A. L. Efros, T. A. Kennedy, and D. J. Norris, "Doping semiconductor nanocrystals," *Nature*, vol. 436, no. 7047, p. 91, 2005.

92. W. Spear and P. Le Comber, "Substitutional doping of amorphous silicon," *Solid state communications*, vol. 17, no. 9, pp. 1193–1196, 1975.

93. I. L. Medintz, H. T. Uyeda, E. R. Goldman, and H. Mattoussi, "Quantum dot bioconjugates for imaging, labelling and sensing," *Nature materials*, vol. 4, no. 6, p. 435, 2005.

94. G. W. Walker, V. C. Sundar, C. M. Rudzinski, A. W. Wun, M. G. Bawendi, and D. G. Nocera, "Quantum-dot optical temperature probes," *Applied Physics Letters*, vol. 83, no. 17, pp. 3555–3557, 2003.

95. S.-T. Ha, C. Shen, J. Zhang, and Q. Xiong, "Laser cooling of organic–inorganic lead halide perovskites," *Nature Photonics*, vol. 10, no. 2, p. 115, 2016.

96. Y. Hagiwara, K. Takahata, J. Torimoto, and J. Yamamoto, "Co2 raman thermometer improvement: Comparing hot band and stokes and anti-stokes raman scattering thermometers," *Journal of Raman Spectroscopy*, vol. 49, no. 11, pp. 1776–1781, 2018.

97. C. Bradac, S. F. Lim, H.-C. Chang, and I. Aharonovich, "Optical nanoscale thermometry: From fundamental mechanisms to emerging practical applications," *Advanced Optical Materials*, p. 2000183, 2020.

98. T. Hart, R. Aggarwal, and B. Lax, "Temperature dependence of raman scattering in silicon," *Physical Review B*, vol. 1, no. 2, p. 638, 1970.

99. I. Alessandri and J. R. Lombardi, "Enhanced raman scattering with dielectrics," *Chemical reviews*, vol. 116, no. 24, pp. 14921–14981, 2016.

100. N. W. Ashcroft and N. D. Mermin, *Solid state physics*. Holt, Reinhart and Winston, 1976.

101. G. Jellison Jr and F. Modine, "Optical functions of silicon between 1.7 and 4.7 ev at elevated temperatures," *Physical Review B*, vol. 27, no. 12, p. 7466, 1983.

102. A. Esser, K. Seibert, H. Kurz, G. Parsons, C. Wang, B. Davidson, G. Lucovsky, and R. Nemanich, "Ultrafast recombination and trapping in amorphous silicon," *J. Non-Cryst. Solids*, vol. 114, pp. 573–575, 1989.

103. T. Lewi, H. A. Evans, N. A. Butakov, and J. A. Schuller, "Ultrawide thermo-optic tuning of pbte meta-atoms," *Nano letters*, vol. 17, no. 6, pp. 3940–3945, 2017.

104. M. Rahmani, L. Xu, A. E. Miroshnichenko, A. Komar, R. Camacho-Morales, H. Chen, Y. Zárate, S. Kruk, G. Zhang, D. N. Neshev, *et al.*, "Reversible thermal tuning of all-dielectric metasurfaces," *Advanced Functional Materials*, vol. 27, no. 31, p. 1700580, 2017.

105. K. Zangeneh Kamali, L. Xu, J. Ward, K. Wang, G. Li, A. E. Miroshnichenko, D. Neshev, and M. Rahmani, "Reversible image contrast manipulation with thermally tunable dielectric metasurfaces," *Small*, p. 1805142, 2019.

106. S. Makarov, L. Kolotova, S. Starikov, U. Zywietz, and B. Chichkov, "Resonant silicon nanoparticles with controllable crystalline states and nonlinear optical responses," *Nanoscale*, vol. 10, no. 24, pp. 11403–11409, 2018.

107. J. D. Joannopoulos and G. Lucovsky, eds., *The Physics of Hydrogenated Amorphous Silicon II: Electronic and Vibrational Properties.* Berlin: Springer-Verlag, 1984.

108. L. Wang, Y. Rho, W. Shou, S. Hong, K. Kato, M. Eliceiri, M. Shi, C. P. Grigoropoulos, H. Pan, C. Carraro, *et al.*, "Programming nanoparticles in multiscale: optically modulated assembly and phase switching of silicon nanoparticle array," *ACS nano*, vol. 12, no. 3, pp. 2231–2241, 2018.

109. D. Lencer, M. Salinga, B. Grabowski, T. Hickel, J. Neugebauer, and M. Wuttig, "A map for phase-change materials," *Nature Mater.*, vol. 7, no. 12, pp. 972–977, 2008.

110. K. Shportko, S. Kremers, M. Woda, D. Lencer, J. Robertson, and M. Wuttig, "Resonant bonding in crystalline phase-change materials," *Nature Mater.*, vol. 7, no. 8, pp. 653–658, 2008.

111. J. Tian, H. Luo, Y. Yang, F. Ding, Y. Qu, D. Zhao, M. Qiu, and S. I. Bozhevolnyi, "Active control of anapole states by structuring the phase-change alloy ge 2 sb 2 te 5," *Nature communications*, vol. 10, no. 1, p. 396, 2019.

112. C. Ruiz de Galarreta, I. Sinev, A. M. Alexeev, P. Trofimov, K. Ladutenko, S. Garcia-Cuevas Carrillo, E. Gemo, A. Baldycheva,

J. Bertolotti, and C. David Wright, "Reconfigurable multilevel control of hybrid all-dielectric phase-change metasurfaces," 2020.

113. Q. Wang, E. T. F. Rogers, B. Gholipour, C.-M. Wang, G. Yuan, J. Teng, and N. I. Zheludev, "Optically reconfigurable metasurfaces and photonic devices based on phase change materials," *Nature Photonics*, vol. 10, no. 1, pp. 60–65, 2016.

114. M. V. Rybin, K. B. Samusev, S. Y. Lukashenko, Y. S. Kivshar, and M. F. Limonov, "Transition from two-dimensional photonic crystals to dielectric metasurfaces in the optical diffraction with a fine structure," *Sci. Rep.*, vol. 6, p. 30773, 2016.

115. T. Lewi, P. P. Iyer, N. A. Butakov, A. A. Mikhailovsky, and J. A. Schuller, "Widely tunable infrared antennas using free carrier refraction," *Nano letters*, vol. 15, no. 12, pp. 8188–8193, 2015.

116. C. Kittel and P. McEuen, *Introduction to solid state physics*, vol. 8. Wiley New York, 1976.

117. M. I. Tribelsky, "Anomalous light absorption by small particles," *EPL (Europhysics Letters)*, vol. 94, no. 1, p. 14004, 2011.

118. A. E. Miroshnichenko and M. I. Tribelsky, "Ultimate absorption in light scattering by a finite obstacle," *Physical review letters*, vol. 120, no. 3, p. 033902, 2018.

119. G. Zograf, S. Makarov, and M. Petrov, "Doping of resonant silicon nanodisks for efficient optical heating in the near-infrared range," *JPhCS*, vol. 1461, no. 1, p. 012201, 2020.

120. C. Ma, J. Yan, Y. Huang, C. Wang, and G. Yang, "The optical duality of tellurium nanoparticles for broadband solar energy harvesting and efficient photothermal conversion," *Science advances*, vol. 4, no. 8, p. eaas9894, 2018.

121. S. Ishii, R. P. Sugavaneshwar, K. Chen, T. D. Dao, and T. Nagao, "Solar water heating and vaporization with silicon nanoparticles at mie resonances," *Optical Materials Express*, vol. 6, no. 2, pp. 640–648, 2016.

122. S. Ishii, K. Chen, H. Okuyama, and T. Nagao, "Resonant optical absorption and photothermal process in high refractive index germanium

nanoparticles," *Advanced Optical Materials*, vol. 5, no. 5, p. 1600902, 2017.

123. G. Pirruccio, D. Rocco, C. De Angelis, G. Sorbello, D. Mascali, G. Torrisi, M. Frassetto, L. Malferrari, F. Odorici, C. Altana, *et al.*, "Numerical simulations on laser absorption enhancement in hybrid metallo-dielectric nanostructured targets for future nuclear astrophysics experiments," *AIP Advances*, vol. 10, no. 4, p. 045020, 2020.

124. S. I. Lepeshov, A. E. Krasnok, P. A. Belov, and A. E. Miroshnichenko, "Hybrid nanophotonics," *Physics-Uspekhi*, vol. 61, no. 11, p. 1035, 2019.

125. F. Timpu, N. R. Hendricks, M. Petrov, S. Ni, C. Renaut, H. Wolf, L. Isa, Y. Kivshar, and R. Grange, "Enhanced second-harmonic generation from sequential capillarity-assisted particle assembly of hybrid nanodimers," *Nano letters*, vol. 17, no. 9, pp. 5381–5388, 2017.

126. R. Ghosh Chaudhuri and S. Paria, "Core/shell nanoparticles: classes, properties, synthesis mechanisms, characterization, and applications," *Chemical reviews*, vol. 112, no. 4, pp. 2373–2433, 2012.

127. F. Wang, R. Deng, J. Wang, Q. Wang, Y. Han, H. Zhu, X. Chen, and X. Liu, "Tuning upconversion through energy migration in core–shell nanoparticles," *Nature materials*, vol. 10, no. 12, pp. 968–973, 2011.

128. K. Ladutenko, P. Belov, O. Peña-Rodríguez, A. Mirzaei, A. E. Miroshnichenko, and I. V. Shadrivov, "Superabsorption of light by nanoparticles," *Nanoscale*, vol. 7, no. 45, pp. 18897–18901, 2015.

129. S. Lepeshov, A. Krasnok, and A. Alù, "Nonscattering-to-superscattering switch with phase-change materials," *ACS Photonics*, vol. 6, no. 8, pp. 2126–2132, 2019.

130. V. Grigoriev, N. Bonod, J. Wenger, and B. Stout, "Optimizing nanoparticle designs for ideal absorption of light," *ACS photonics*, vol. 2, no. 2, pp. 263–270, 2015.

131. W. Liu, J. Zhang, B. Lei, H. Ma, W. Xie, and H. Hu, "Ultra-directional forward scattering by individual core-shell nanoparticles," *Optics express*, vol. 22, no. 13, pp. 16178–16187, 2014.

132. G. Zograf, M. Petrov, and S. Makarov, "Coating of au nanoparticle by si shell for enhanced local heating," *JPhCS*, vol. 929, no. 1, p. 012072, 2017.

133. R. Chikkaraddy, B. de Nijs, F. Benz, S. J. Barrow, O. A. Scherman, E. Rosta, A. Demetriadou, P. Fox, O. Hess, and J. J. Baumberg, "Single-molecule strong coupling at room temperature in plasmonic nanocavities," *Nature*, vol. 535, no. 7610, pp. 127–130, 2016.

134. F. Benz, M. K. Schmidt, A. Dreismann, R. Chikkaraddy, Y. Zhang, A. Demetriadou, C. Carnegie, H. Ohadi, B. de Nijs, R. Esteban, J. Aizpurua, and J. J. Baumberg, "Single-molecule optomechanics in "picocavities"," *Science*, vol. 354, no. 6313, pp. 726–729, 2016.

135. D. Punj, R. Regmi, A. Devilez, R. Plauchu, S. B. Moparthi, B. Stout, N. Bonod, H. Rigneault, and J. Wenger, "Self-assembled nanoparticle dimer antennas for plasmonic-enhanced single-molecule fluorescence detection at micromolar concentrations," *ACS photonics*, vol. 2, no. 8, pp. 1099–1107, 2015.

136. K. L. Wustholz, A.-I. Henry, J. M. McMahon, R. G. Freeman, N. Valley, M. E. Piotti, M. J. Natan, G. C. Schatz, and R. P. Van Duyne, "Structure-activity relationships in gold nanoparticle dimers and trimers for surface-enhanced raman spectroscopy," *Journal of the American Chemical Society*, vol. 132, no. 31, pp. 10903–10910, 2010.

137. I. Alessandri, "Enhancing raman scattering without plasmons: Unprecedented sensitivity achieved by TiO2 shell-based resonators," *Journal of the American Chemical Society*, vol. 135, no. 15, pp. 5541–5544, 2013.

138. R. Regmi, J. Berthelot, P. M. Winkler, M. Mivelle, J. Proust, F. Bedu, I. Ozerov, T. Begou, J. Lumeau, H. Rigneault, *et al.*, "All-dielectric silicon nanogap antennas to enhance the fluorescence of single molecules," *Nano letters*, vol. 16, no. 8, pp. 5143–5151, 2016.

139. A. Krasnok, M. Caldarola, N. Bonod, and A. Alú, "Spectroscopy and biosensing with optically resonant dielectric nanostructures," *Advanced Optical Materials*, vol. 6, no. 5, p. 1701094, 2018.

140. G. P. Zograf, D. A. Zuev, V. A. Milichko, and S. V. Makarov, "Gap size impact on metal-dielectric nanocavity heater properties," in *AIP Conference Proceedings*, vol. 1874, p. 030043, AIP Publishing LLC, 2017.

141. I. Koryakina, D. S. Kuznetsova, D. A. Zuev, V. A. Milichko, A. S. Timin, and M. V. Zyuzin, "Optically responsive delivery platforms: From the design considerations to biomedical applications," *Nanophotonics*, vol. 9, no. 1, pp. 39–74, 2020.

142. S. J. Soenen, U. Himmelreich, N. Nuytten, and M. De Cuyper, "Cytotoxic effects of iron oxide nanoparticles and implications for safety in cell labelling," *Biomaterials*, vol. 32, no. 1, pp. 195–205, 2011.

143. A. M. Jubb and H. C. Allen, "Vibrational spectroscopic characterization of hematite, maghemite, and magnetite thin films produced by vapor deposition," *ACS Applied Materials & Interfaces*, vol. 2, no. 10, pp. 2804–2812, 2010.

144. S. Kruk, A. Slobozhanyuk, D. Denkova, A. Poddubny, I. Kravchenko, A. Miroshnichenko, D. Neshev, and Y. Kivshar, "Edge states and topological phase transitions in chains of dielectric nanoparticles," *Small*, vol. 13, no. 11, p. 1603190, 2017.

145. S. Danesi and I. Alessandri, "Using optical resonances to control heat generation and propagation in silicon nanostructures," *Physical Chemistry Chemical Physics*, vol. 21, no. 22, pp. 11724–11730, 2019.

146. A. P. Slobozhanyuk, A. N. Poddubny, I. S. Sinev, A. K. Samusev, Y. F. Yu, A. I. Kuznetsov, A. E. Miroshnichenko, and Y. S. Kivshar, "Enhanced photonic spin hall effect with subwavelength topological edge states," *Laser & Photonics Reviews*, vol. 10, no. 4, pp. 656–664, 2016.

147. X. Zhu, W. Yan, U. Levy, N. A. Mortensen, and A. Kristensen, "Resonant laser printing of structural colors on high-index dielectric metasurfaces," *Science advances*, vol. 3, no. 5, p. e1602487, 2017.

148. D. A. Zuev, S. V. Makarov, I. S. Mukhin, V. A. Milichko, S. V. Starikov, I. A. Morozov, I. I. Shishkin, A. E. Krasnok, and P. A. Belov, "Fabrication of hybrid nanostructures via nanoscale laser-induced reshaping for

advanced light manipulation," *Adv. Mater.*, vol. 28, no. 16, pp. 3087–3093, 2016.

149. A. Zhizhchenko, S. Syubaev, A. Berestennikov, A. V. Yulin, A. Porfirev, A. Pushkarev, I. Shishkin, K. Golokhvast, A. A. Bogdanov, A. A. Zakhidov, *et al.*, "Single-mode lasing from imprinted halide-perovskite microdisks," *ACS nano*, vol. 13, no. 4, pp. 4140–4147, 2019.

150. M. Aouassa, E. Mitsai, S. Syubaev, D. Pavlov, A. Zhizhchenko, I. Jadli, L. Hassayoun, G. Zograf, S. Makarov, and A. Kuchmizhak, "Temperature-feedback direct laser reshaping of silicon nanostructures," *Applied Physics Letters*, vol. 111, no. 24, p. 243103, 2017.

151. G. Zograf, K. Koshelev, A. Zalogina, V. Korolev, D.-Y. Choi, M. Zurch, C. Spielmann, B. Luther-Davies, D. Kartashov, S. Makarov, *et al.*, "High-harmonic generation from metasurfaces empowered by bound states in the continuum," *arXiv preprint arXiv:2008.11481*, 2020.

152. H. Rong, A. Liu, R. Jones, O. Cohen, D. Hak, R. Nicolaescu, A. Fang, and M. Paniccia, "An all-silicon raman laser," *Nature*, vol. 433, no. 7023, pp. 292–294, 2005.

153. S. Spillane, T. Kippenberg, and K. Vahala, "Ultralow-threshold raman laser using a spherical dielectric microcavity," *Nature*, vol. 415, no. 6872, pp. 621–623, 2002.

154. C. W. Freudiger, W. Min, B. G. Saar, S. Lu, G. R. Holtom, C. He, J. C. Tsai, J. X. Kang, and X. S. Xie, "Label-free biomedical imaging with high sensitivity by stimulated raman scattering microscopy," *Science*, vol. 322, no. 5909, pp. 1857–1861, 2008.

155. D. Agarwal, M.-L. Ren, J. S. Berger, J. Yoo, A. Pan, and R. Agarwal, "Nanocavity-enhanced giant stimulated raman scattering in si nanowires in the visible light region," *Nano letters*, vol. 19, no. 2, pp. 1204–1209, 2019.

156. T. Würthwein, N. Irwin, and C. Fallnich, "Saturated raman scattering for sub-diffraction-limited imaging," *The Journal of chemical physics*, vol. 151, no. 19, p. 194201, 2019.

157. S. S. Kharintsev, A. V. Kharitonov, A. R. Gazizov, and S. G. Kazarian, "Disordered nonlinear metalens for raman spectral nanoimaging," *ACS Applied Materials & Interfaces*, vol. 12, no. 3, pp. 3862–3872, 2020.

158. S. S. Kharintsev, A. V. Kharitonov, A. M. Alekseev, and S. G. Kazarian, "Superresolution stimulated raman scattering microscopy using 2-enz nano-composites," *Nanoscale*, vol. 11, no. 16, pp. 7710–7719, 2019.

APPENDIX A. MAIN JOURNAL PAPERS

NANO LETTERS

Letter

pubs.acs.org/NanoLett

Resonant Nonplasmonic Nanoparticles for Efficient Temperature-Feedback Optical Heating

George P. Zograf,[†] Mihail I. Petrov,[*,†,‡] Dmitry A. Zuev,[†] Pavel A. Dmitriev,[†] Valentin A. Milichko,[†] Sergey V. Makarov,[*,†] and Pavel A. Belov[†]

[†]Department of Nanophotonics and Metamaterials, ITMO University, St. Petersburg 197101, Russia

[‡]Department of Physics and Mathematics, University of Eastern Finland, Yliopistokatu 7, 80101, Joensuu, Finland

Supporting Information

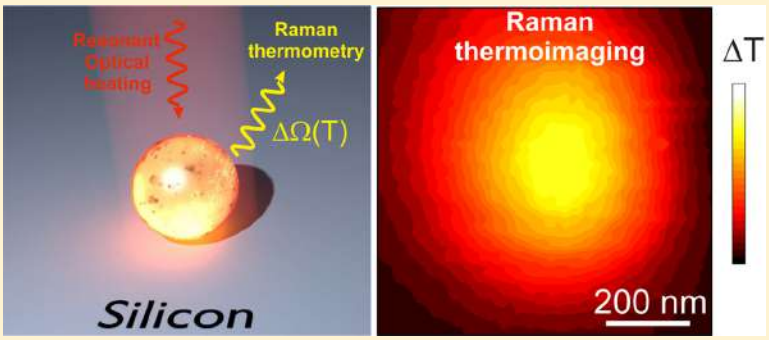

ABSTRACT: We propose a novel photothermal approach based on resonant dielectric nanoparticles, which possess imaginary part of permittivity significantly smaller as compared to metal ones. We show both experimentally and theoretically that a spherical silicon nanoparticle with a magnetic quadrupolar Mie resonance converts light to heat up to 4 times more effectively than similar spherical gold nanoparticle at the same heating conditions. We observe photoinduced temperature raise up to 900 K with the silicon nanoparticle on a glass substrate at moderate intensities (<2 mW/μm^2) and typical laser wavelength (633 nm). The advantage of using crystalline silicon is the simplicity of local temperature control by means of Raman spectroscopy working in a broad range of temperatures, that is, up to the melting point of silicon (1690 K) with submicrometer spatial resolution. Our CMOS-compatible heater−thermometer nanoplatform paves the way to novel nonplasmonic photothermal applications, extending the temperature range and simplifying the thermoimaging procedure.

KEYWORDS: *Optical heating, nanothermometry, magnetic optical resonances, silicon nanoparticle, Raman scattering*

High refractive index dielectrics with the absorption coefficient several orders of magnitude smaller than that of metals have become basic materials for fabrication of advanced optical devices.[1,2] This low-loss all-dielectric approach in nanophotonics is effective for localization of light at nanoscale,[3,4] wavefront manipulation,[5,6] perfect reflection,[7] coloring,[8] and holograms,[9] owing to strong magnetic and electric type optical resonances in visible and IR ranges. A biosensing approach with low light-to-heat conversion efficiency based on dielectric nanodimers, supporting high localization and strong enhancement of electric and magnetic fields outside the material, for example, in a nanogap,[3] has been developed[10−13] and applied for single molecule detection.[8] However, the resonant nanoparticles made from high refractive index dielectrics still have not been applied as nanoscale heaters remotely controlled using light.

In this Letter, we demonstrate that the concept of all-dielectric nanophotonics can be considered as an effective platform for optical heating with temperature-feedback. For this purpose, we utilize crystalline silicon nanoparticles possessing (i) high real part and relatively low imaginary part of permittivity; (ii) a high melting threshold (>1600 K); and (iii) enhanced Raman active phonon modes[14] being suitable for nanoscale thermometry[15] due to their high thermal sensitivity.[16] We demonstrate both experimentally and theoretically that optical field localization inside the silicon nanoparticle at a magnetic quadrupolar resonance provides efficient optical heating, despite its imaginary part of refractive index is two orders lower than that of metals. Moreover, the Raman nanothermometry allows for thermoimaging with submicrometer spatial resolution.

We compare this approach with thermoplasmonics[17−19] which is widely used currently for photothermal therapy,[20,21] photochemistry,[22] photocatalysis,[23,24] nanosurgery,[25] thermal imaging,[26] optofluidic,[27] and biosensing[28] owing to high Ohmic losses in metals. In Figure 1, we schematically show that

Received: January 14, 2017
Revised: April 7, 2017
Published: April 14, 2017

DOI: 10.1021/acs.nanolett.7b00183
Nano Lett. 2017, 17, 2945−2952

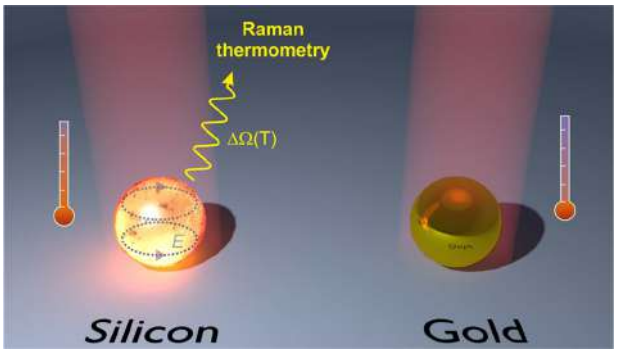

Figure 1. Concept. Schematic illustration of strong optical heating of silicon nanoparticle as compared to golden one.

spherical silicon nanoparticles can be more effectively heated as compared to spherical plasmonic ones due to better resonant properties discussed below, whereas intrinsic thermal-sensitive Raman modes in silicon simplify nanothermometry procedure. Indeed, metals do not allow to detect the temperature by itself, requiring usage of thermally sensitive nanoscale objects (dyes, quantum dots, rare earth doped dielectric nanoparticles, carbon nanotubes, and so forth)[29,30] or interferometry techniques based on temperature-dependent variation of refractive index of surrounding dielectric medium.[31,32]

Concept of Resonant Heating. In order to show that low optical losses inherent for most of dielectrics do not necessarily result in weak photoinduced heating of nanoparticles, we first discuss basic principles of light-to-heat conversion in nanoresonators.

General model for heating of a spherical nanoparticle from an arbitrary material (metals or dielectrics) by continuous laser illumination in a homogeneous medium was developed elsewhere.[17,33] We combine it with a simple analytical solution for light absorption by the nanoparticle from the Mie theory. As a result, the solution of a thermal diffusion equation in a steady-state regime with a heat source defined by the light intensity (I) and the nanoparticle absorption cross-section (C_{abs}) gives the following equation for temperature growth inside the nanoparticle

$$\delta T_{NP} = \frac{IC_{abs}}{2\pi\kappa_2 D} \tag{1}$$

where κ_2 is the thermal conductivity of the surrounding medium, which is significantly smaller than that of the nanoparticle; and D is the nanoparticle diameter. The details of derivation of this formula and calculations of the absorption cross-section can be found in Supporting Information.

The results of the calculations are shown in Figure 2, where the heating of dielectric and metallic nanoparticles of different sizes are compared. Namely, the dependence of temperature increase inside a nanoparticle with defined real ($\mathrm{Re}(\epsilon)$) and imaginary ($\mathrm{Im}(\epsilon)$) parts of permittivity is presented. These results give general conclusion that the relatively large dielectric nanoparticles can be heated as effective as plasmonic ones, whereas their $\mathrm{Im}(\epsilon)$ can be significantly smaller.

In order to provide deep understanding of the origin of strong heating of low-loss dielectrics, we consider the case of resonant heating, when an external wave is coupled with an eigenmode of the nanoparticle. The general expression for the absorbed electromagnetic power P is

$$P = \frac{1}{2}\mathrm{Re}\int_V J(r)E(r)\mathrm{d}V \tag{2}$$

where $J(r)$ is the current density, $E(r)$ is the electric field inside the material, and the integration is taken over the volume of the nanoobject V. From this formula, it follows that the stronger the electrical field inside the material, the higher the absorbed power. The heating itself is caused by the Ohmic losses determined by the electric conductivity σ, yielding $J = \sigma E$. Imaginary part of the permittivity determines the conductivity as $\sigma = \epsilon_0\omega\,\mathrm{Im}(\epsilon)$, where ϵ_0 and ω are the dielectric permittivity of vacuum and incident light frequency, respectively.

Integration in eq 2 over an arbitrary nanoparticle volume supporting eigenmodes allows to rewrite eq 2 in terms of an effective mode volume V_{eff} and spatially averaged field enhancement factor $F = \langle|E|^2\rangle/|E_0|^2$, which determines how much energy can be accumulated inside the nanoparticle and where $|E_0|$ is the incident electric field magnitude. Thus, we can rewrite eq 2 for the absorbed power as

$$P \sim \sigma F^2 V_{eff} \tag{3}$$

Each factor, σ, F^2, and V_{eff}, has a strong contribution to the nanoparticle heating δT_{NP}, which we will discuss separately.

Influence of Nonradiative Losses. From eq 3, it is clear that the increasing Ohmic losses do not necessarily lead to the rise of the light absorption by the nanoparticle. On one hand, the imaginary part of the permittivity increases the conductivity

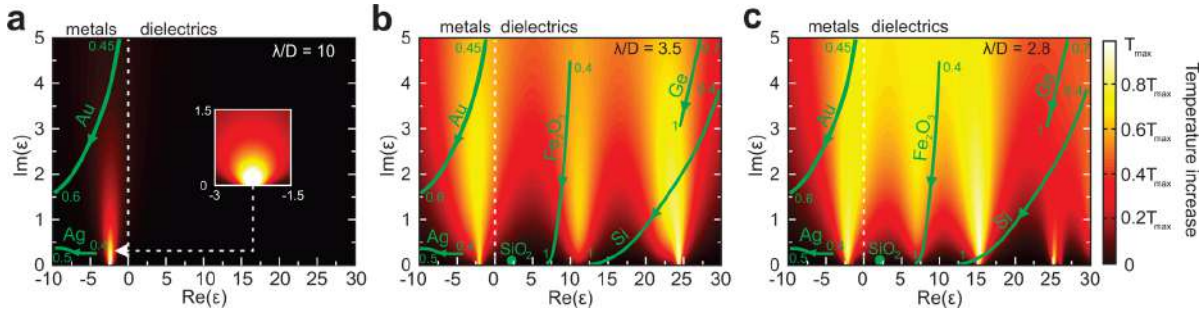

Figure 2. Resonant heating of a spherical nanoparticle. Theoretically calculated (Mie theory) heating maps for spherical nanoparticles with fixed wavelength (λ)/diameter (D) ratios for different real and imaginary parts of permittivity in homogeneous medium (air): (a) λ/D = 10; (b) λ/D = 3.5; (c) λ/D = 2.8. Green lines with arrows depict values of $\mathrm{Re}(\epsilon)$ and $\mathrm{Im}(\epsilon)$ for different materials (dispersion). The orientation of arrows corresponds to increase of wavelength from minimum to maximum indicated by numbers in microns.

DOI: 10.1021/acs.nanolett.7b00183
Nano Lett. 2017, 17, 2945−2952

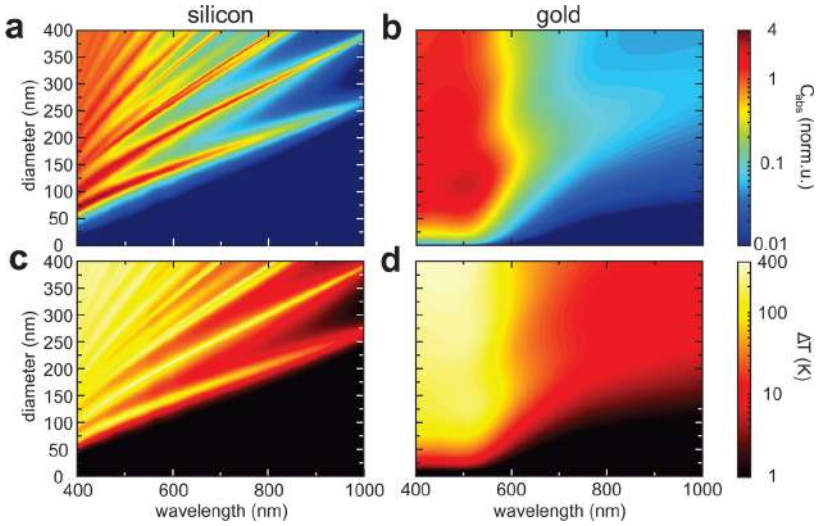

Figure 3. Optimization 2D maps for spherical nanoparticles in air. Theoretically calculated from Mie theory absorption cross-section maps normalized by geometrical area for (a) silicon and (b) gold nanoparticles. Theoretically calculated temperature maps for heating of (c) silicon and (d) gold spherical nanoparticles at light intensity I_0 = 0.1 mW/μm^2.

but on the other hand it suppresses the quality factor Q of the optical resonance; therefore, the factor σF^2 should be considered in more detail.

The field enhancement factor near the nanoparticle resonance ω_0 can be expressed as $F \sim 1/(\omega_0^2 - \omega^2 - i\omega\gamma)$, where γ defines the total optical losses. The optical losses include both radiative and nonradiative (or Ohmic) losses $\gamma = \gamma_{rad} + \gamma_{ohmic}$. The latter one is proportional to Im(ϵ), hence the factor σF^2 at the resonant frequency ω_0 is proportional to $\sigma F^2 \sim \gamma_{Ohmic}/(\gamma_{Ohmic} + \gamma_{rad})^2$, from which it is clear that for high Ohmic losses the absorbed power tends to zero. Thus, at fixed γ_{rad} the maximal value of this factor $(\sigma F^2)_{max} \sim 1/(4\gamma_{rad})$ can be achieved when $\gamma_{Ohmic} \approx \gamma_{rad}$. The radiative losses can be suppressed by considering resonant nanoparticle much smaller than the wavelength λ, which is the case of small plasmonic nanoparticles, where $\gamma_{rad} \ll \gamma_{Ohmic}$. At the surface plasmon resonance $\omega = \omega_0$, the radiative losses are equal to $\gamma_{rad} \approx \omega_0^3/\omega_p^2(\pi D/\lambda)^3$, where ω_p is the plasma frequency. This estimation formula gives small values for γ_{rad} compared to ω_0 due to the ratio $(D/\lambda)^3$. As shown in Figure 2a, for small nanoparticles the resonance occurs only in the region of negative Re(ϵ), and maximal temperature should be achieved at relatively small values of Im(ϵ), where $\gamma_{Ohmic} \approx \gamma_{rad}$. On the other hand, for bigger nanoparticles, which is the case of dielectric ones, the radiative losses for low order dipole modes are high and maximal heating is achieved at higher Ohmic losses (see Figure 2b,c). However, for higher order resonances, for example, quadrupole, one can expect small radiative losses and, thus, the maximal optimal heating for lower Ohmic losses that is seen for higher Re(ϵ) in Figure 2b,c. More quantitative analysis of the heating dependencies on Im(ϵ) at each resonance is shown in Figure.S1 in Supporting Information.

Influence of Effective Mode Volume. Another factor, which is important for the absorption of light, is the effective mode volume inside the nanoparticle V_{eff}. Generally, the larger the volume of an arbitrary nanoparticle, the stronger the heating. However, the effective mode volume can significantly affect this dependence. For plasmonic nanoparticles (Re(ϵ) < 0), the effective volume is defined by a skin depth, which is less than $\delta \approx 20$ nm for most of metals in the visible range.[34] Thus, the effective mode volume of plasmonic nanoparticles is $V_{eff} \approx \pi D^2\delta$. Opposite to metals, dielectrics support optical penetration depth much larger than the diameter of the nanoparticle in the visible range. The effective volumes of Mie-type modes are typically of the order of nanoparticle volume $V_{eff} \approx \pi D^3/6$. It means that the increase of the nanoparticle size is effective for the temperature increase in the case of dielectrics and less effective for the plasmonic nanoparticles.

On the basis of the presented general argumentation and calculations, we stress that the dielectric nanoparticles can be efficiently heated by light illumination when their radiative losses are equal to the Ohmic ones. Because dielectrics have low nonradiative losses, this condition is fulfilled for relatively big nanoparticles. On the contrary, plasmonic nanoparticles are expected to show the most effective heating for significantly smaller sizes.[17]

Comparison of Materials for Optical Heating. In order to make optical heating of dielectric nanoparticles as effective as the thermoplasmonic approach, it is crucial to choose the dielectric material with the most optimized parameters. One of the best materials for thermoapplications is silicon, because, according to Figure 2, one needs a dielectric with high Re(ϵ) and finite Im(ϵ) to achieve high light-to-heat conversion efficiencies in a broad spectral range. Moreover, silicon is considered to be a biocompatible material,[35] which makes its nanoparticles prospective for biophotonic applications.

Silicon can be effectively heated by light with the wavelengths less than 500 nm in the case of even relatively small nanoparticles (λ/D = 3.5) where Ohmic losses are high (Figure 2b).[15,36] However, even stronger heating can be achieved for slightly larger size (λ/D = 2.8) in the visible or IR ranges, where higher order modes are excited (Figure 2c).

The dependencies of heating on real and imaginary parts of permittivity of other materials (Au, Ag, Ge, Fe_2O_3, SiO_2) are also shown in Figure 2 and reflect current trends in searching new materials for the nanonscale optical heating.[37] The mentioned dielectric materials belong to different categories. SiO_2 is low refractive index dielectric with low Ohmic losses, which is obviously useless for optical heating, especially in water where the optical contrast is very low (see Figure.S2 in

DOI: 10.1021/acs.nanolett.7b00183
Nano Lett. 2017, 17, 2945−2952

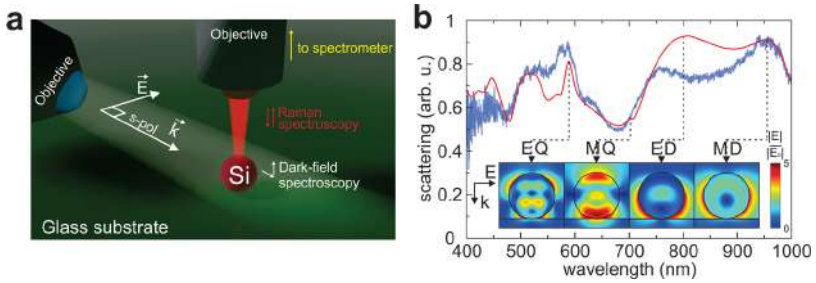

Figure 4. Optical properties of individual silicon nanoparticles. (a) Schematic of dark-field optical spectroscopy and micro-Raman spectroscopy setup. (b) Experimental and numerical scattering spectra for 260 nm spherical silicon nanoparticle in the dark-field scheme, the red line corresponds to numerical model. Insets: numerical electric near-field distribution at different resonances (see Supporting Information, for details of mode decomposition) upon plane wave illumination by s-polarized white light with an incident angle of 67°. For the electric field insets, a wavevector of an incident plane wave is oriented along a vertical axis.

Supporting Information). Midrefractive index dielectrics (e.g., Fe_2O_3[38] or Cu_2O) are more suitable for optical heating owing to less radiative losses (i.e., better optical contrast with a host medium) and higher Ohmic losses. Therefore, such nanoparticles with $\lambda/D = 2-3$ can be heated as strong as metallic ones of the same size (Figure 2c). However, they are still less effective as compared to silicon. Finally, germanium[34] as a high-refractive index dielectric possesses too high Ohmic losses in the visible and near-IR ranges, reducing Q-factor and field enhancement for the excited optical modes.

The most reasonable comparison of silicon should be done with gold nanoparticles, which are the most frequently used as biocompatible[18] nanoscale heat sources. Moreover, gold is much less oxidized under high temperatures as compared to other metals. In the "metals region" of Figure 2, gold is more appropriate for heating of larger particles as compared to silver owing to higher values of $\mathrm{Im}(\epsilon)$ in gold.

In Figure 3, there is the comparison of absorption and heating properties of silicon[34,39] and gold[40] spherical nanoparticles in air calculated basing on the Mie theory. The calculations show that the silicon nanoparticles are effectively heated at resonant conditions. Indeed, as we discussed above, the silicon nanoparticles demonstrate resonant heating behavior for certain wavelengths and sizes and even exceed maximum temperature values for gold in the IR range. The similar behavior is observed for nanoparticles in surrounding water as shown in Figure.S3 in Supporting Information, which makes silicon nanoparticles to be prospective for biological applications, where the nanoparticles are immersed in liquids.

Optical Properties of Silicon Nanoparticles. In order to prove that silicon nanoparticles can be effectively heated upon typical laser intensities, we experimentally study spherical silicon nanoparticles on a glass substrate. We fabricate an array of crystalline spherical silicon nanoparticles using laser printing method, which is based on laser-induced forward transfer technique from a thin amorphous silicon film, allowing to deposit crystalline nanospheres on arbitrary substrates[41] (for details, see Methods). The shape of the resulting nanoparticles is analyzed by means of scanning electron microscopy (SEM), whereas optical properties are studied by polarization-resolved dark-field microscopy,[42] as shown in Figure 4a. The details of nanoparticles' optical characterization is discussed in Methods.

Typical scattering spectrum of the individual silicon nanoparticle on the glass substrate is shown in Figure 4b. Our modeling of the scattering using Comsol Multiphysics allows reproduction of experimental conditions, that is, angles of *s*-polarized light incidence and signal collection. The spectra of nanoparticle in homogeneous air surrounding or on the substrate are slightly different, especially, when accounting for the aperture of a collecting objective (NA = 0.26). Therefore, magnetic quadrupole (MQ) is invisible in our experimental geometry (more details find in Figure S6 in Supporting Information), whereas multipole decomposition (see Figure.S4 in Supporting Information) gives pronounced MQ around $\lambda \approx 700$ nm. In turn, the electrical quadrupolar (EQ) mode as well as electric (ED) and magnetic (MD) dipolar modes are clearly seen in both cases, which makes it easy to interpret the experimental results, shown in Figure 4b. We determine the nanoparticles sizes by the positions of ED, MD, and EQ resonances in the dark-field spectra. The obtained diameters are slightly different from those of obtained by SEM. However, we rely on dark-field results due to presence of dioxide on the surface,[14] whereas SEM results are just to ensure the shape of the nanoparticles. The results of the modeling show that the filling factor for each mode is around 0.3−0.7 and the electric field enhancement is up to 5.

Optical Heating with Temperature Feedback. Unlike metals, crystalline silicon possess strong Raman signal at room temperature,[14] making it possible to provide direct Raman nanothermometry during optical heating as shown in Figure 5a. Indeed, the spectral position of a Raman line is known to be thermosensitive due to anharmonic effects in lattice vibrations.[16] Therefore, the frequency of optical phonon (Ω) responsible for Raman signal is dependent on temperature as

$$\Omega(T) = \Omega_0 + A\left(1 + \frac{2}{e^x - 1}\right) + B\left(1 + \frac{3}{e^y - 1} + \frac{3}{(e^y - 1)^2}\right) \quad (4)$$

where $\Omega_0 = 528\ \mathrm{cm}^{-1}$, $A = -2.96\ \mathrm{cm}^{-1}$, $B = -0.174\ \mathrm{cm}^{-1}$, $x = \hbar\Omega_0/2kT$, and $y = \hbar\Omega_0/3kT$ for crystalline silicon.[16] This function is plotted in Figure.S5 in Supporting Information.

Such direct connection of the Raman signal with temperature allows to provide Raman thermometry.[30] In Figure 5a, experimentally observed thermal-induced shift of the silicon Raman peak is presented. According to eq 4, the shift down to 509 cm^{-1} corresponds to the heating up to $\Delta T \approx 600$ K. As shown in Figure 5b,c, the proposed method allows reconstruction of two-dimensional (2D) temperature map with submicron resolution. It should be noted that we do not observe any irreversible changes after nanoparticles heating up to such high temperatures.

DOI: 10.1021/acs.nanolett.7b00183
Nano Lett. 2017, 17, 2945−2952

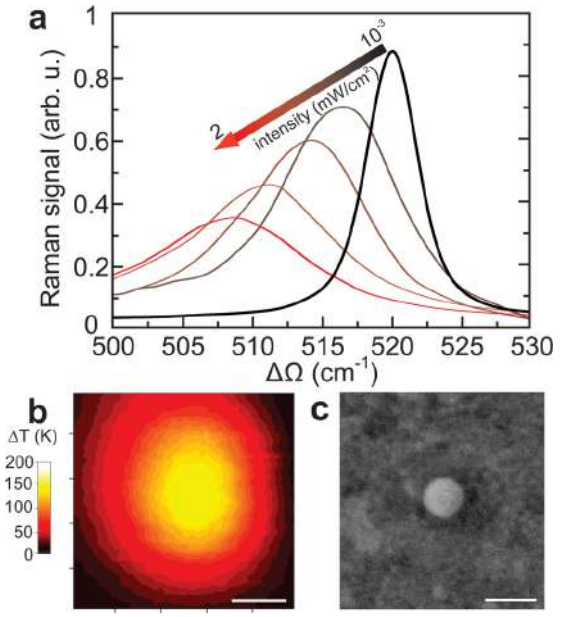

Figure 5. Raman nanothermometry. (a) Experimental Raman spectra for a spherical silicon nanoparticle with diameter 350 nm on a glass substrate. Thermal (b) and SEM (c) images of a silicon nanoparticle on a glass substrate. Scale bar is 200 nm, image (b) is obtained at laser intensity 2 mW/μm^2.

The method of Raman nanothermometry allows one to determine temperature for a given nanoparticle at a certain laser intensity in the broad range of temperatures, as shown in Figure 6a. The experimental results are in good agreement with the numerically obtained in Comsol Multiphysics dependence for a silicon nanosphere on a glass substrate. The case of the silicon nanoparticle on the substrate is intermediate between the cases of homogeneous air and glass host media (Figure 6a). The best agreement of the numerical calculations with the experimental data is achieved, when the nanoparticle has cut off segment with height 20 nm from the bottom contacting with the substrate. This shape is consistent with the process of the nanoparticles fabrication.[41] Indeed, laser printing implies melting of a thin film to produce a liquid droplet of silicon, which then falls to the surface and slightly wets it. We notice that experimental results are described well without taking into account thermo-optical nonlinear effects, which might change refractive index and thermal conductivity of heated materials.[43]

As shown in Figure 6b, heating of the silicon nanoparticle strongly depends on its diameter for the fixed wavelength. Generally, the more accurately nanoparticle size fulfills resonant conditions at given wavelength (λ = 633 nm), the stronger the Raman shift (i.e., higher temperature). At λ = 633 nm and $D \approx$ 160 nm, the MD excitation results in optical heating up to $\Delta T \approx$ 100 K at intensity 2 mW/μm^2. The next pronounced peak of temperature is related to excitation of MQ mode yielding $\Delta T \approx$ 600 K, which we observe both experimentally and numerically (Figure 6b). According to the multipole decomposition, the resonant heating of larger nanoparticles is related to EQ ($D \approx$ 290 nm) and mixture of the second orders of electric (a_{11}) and magnetic (b_{11}) dipolar modes around $D \approx$ 300 nm. Therefore, in order to find the most compact design and effective light-to-heat conversion efficiency, the silicon nanoparticle supporting MQ mode demonstrates the best characteristics.

We also compare numerically optical heating of silicon spherical nanoparticles with similar gold ones, which are frequently used in modern thermo-plasmonic applications.[18,19] The numerical calculations show that the optical heating of the gold nanosphere on the glass substrate does not strongly dependent on the optical resonances (blue curve in Figure 6b). Generally, the comparison shows that plasmonic spherical nanoparticles are heated effectively at small diameters (D < 150 nm), whereas large dielectric nanoparticles are much more effective than similar plasmonic ones. This conclusion is consistent with our previous analysis, where the quadrupole mode of the dielectric nanoparticle (Re(ϵ) > 0 and Im(ϵ) < 0.5) is more effective than a dipole mode in metals (Re(ϵ) < 0 and Im(ϵ) > 0.5). Indeed, due to large effective mode volume and high average field enhancement the maximum temperature of silicon nanoparticles ($\Delta T_{max} \approx$ 600 K) is much higher as compared to plasmonic ones ($\Delta T_{max} \approx$ 130 K) at equal light intensities and nanoparticles size.

Despite spherical gold nanoparticles are the most simple nanoobjects to produce, the optical heating of gold nanorods,[44,45] nanoshells,[20,46] and nanostars[47] can be more effective. In turn, the shape of silicon nanoparticles can be also optimized in order to achieve maximum light-to-heat conversion efficiencies. Moreover, most metals suffer from high values of Re(ϵ) and Im(ϵ) in the near-IR range[48] impeding their applicability. In opposite to metals, there are a lot of dielectric materials with desirable values of Im(ϵ) in the near-IR range, for example, in biological tissue transparency window. Therefore, we envision further development of the photothermal

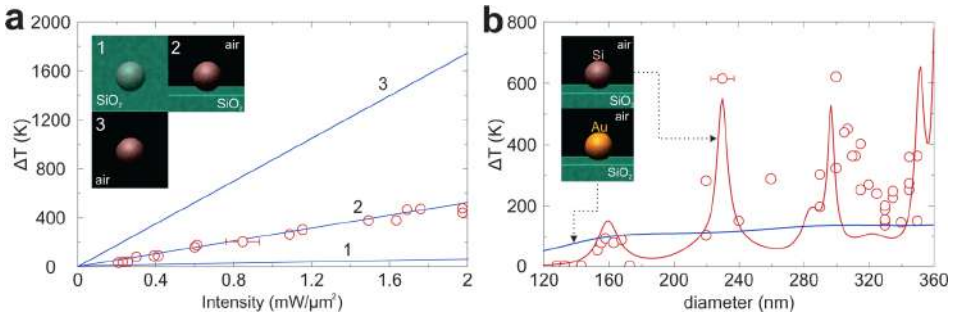

Figure 6. Resonant optical heating of silicon nanoparticles. (a) Experimental data (red circles) and numerical calculations (solid lines) for a spherical silicon nanoparticle with diameter 350 nm in different media. (b) Experimental (red circles) and numerically calculated (solid lines) optical heating of spherical silicon (red) and gold (blue) nanoparticles at wavelength λ = 633 nm and light intensity I_0 = 2 mW/μm^2.

DOI: 10.1021/acs.nanolett.7b00183
Nano Lett. 2017, 17, 2945−2952

applications based on nanoparticles and nanostructures made from low-loss high-refractive index dielectrics.

In conclusion, we have shown that a resonant silicon nanoparticle represents a simple and "all-in-one" (heater−thermometer) nanoplatform integrating effective photoinduced heat generation and broad-range temperature sensing. In particular, by using Raman nanothermometry we have revealed experimentally that at a magnetic quadrupolar optical resonance photoinduced heating of the spherical silicon nanoparticle can be four times more effective as compared to plasmonic nanospheres. We have found that the silicon nanoparticles can be effectively heated both in air and in water environment. Because the silicon nanoparticles with the quadrupolar mode can be fabricated by means of laser ablation at certain positions on arbitrary surfaces, they can be used for plenty of applications where strong and controllable optical heating around a single nanoparticle is crucial: nanosurgery, photochemistry, nanofabrication, as well as photothermal signal modulation.

Methods. *Fabrication of Nanoparticles.* Single silicon nanoparticles are fabricated by the laser-induced forward transfer method: an acceptor glass substrate (Menzel coverslips) is placed above a donor glass substrate with a deposited 100 nm film of amorphous hydrogenized silicon. The thin film is prepared via plasma enhanced chemical vapor deposition from a precursor gas SiH_3, yielding about 10% of initial concentration of hydrogen. The distance between substrates is about 10 μm. The radiation of ytterbium-doped femtosecond solid-state laser (TeMa-150, Avesta Poject, λ = 1050 nm, repetition rate 80 MHz, pulse duration 150 fs) in a single pulse mode provided by a pulse picker system (Avesta Poject) is focused by an infinity corrected objective (10×, NA = 0.28 Mitutoyo Plan Apo) on a thin film-glass interface into a spot with diameter 4.6 μm. The femtosecond-laser ablation yields spherical crystalline silicon nanopartiles on the acceptor substrate with the sizes in the range of 100−400 nm.

Dark-Field Scattering Spectra Measurements. In order to carry out measurements of scattering spectra we apply a dark-field scheme, where an infinity corrected objective (10×, NA = 0.26, Mitutoyo Plan Apo NIR) is used for illumination with a white light source (HL-2000 halogen lamp) of the sample under angle 67° to the surface normal (see Figure 4a). The second objective (50×, NA = 0.42 Mitutoyo Plan Apo NIR) placed perpendicularly to the sample surface is applied for scattering signal collection. The scattered signal is analyzed by a confocal system with a spectrometer (HORIBA LabRam HR) and cooled charge-coupled device (CCD) Camera (Andor DU 420A-OE 325) equipped with a 150 g/mm diffraction grating. The position of the nanoparticles is controlled by an additional CCD camera (Cannon 400 D).

Raman Scattering Measurements. The Raman spectra measurements are conducted utilizing the same registration system (HORIBA LabRam HR) with a 600 g/mm diffraction grating and 632.8 nm HeNe laser as a heating light source focused through a microscope objective (100×, NA = 0.9 Mitutoyo Plan Apo HR) to the sample surface. The objective is used for excitation and collection of the Raman signal. The sample with nanoparticles is placed on a piezo-stage (AIST-NT) providing a positioning accuracy of 10 nm during a thermal imaging process. The HeNe laser is chosen for Raman thermometry due to its high stability and narrow spectral width, yielding high accuracy of temperature measurements. Moreover, its wavelength almost within the biological tissue transparency window (650−1350 nm), making it useful for a number of bioapplications.

Numerical Calculations. Theoretical description of scattering spectra of silicon nanoparticles on a glass substrate as well as their optical heating are carried out numerically in a commercial software Comsol Multiphysics. Permittivities[39,40] and thermal properties[49] of all materials are taken elsewhere. Permittivity at wavelength 632.8 nm for silicon is $\varepsilon_{Si} = 15.072 + 0.152i$, for gold is $\varepsilon_{Au} = -11.573 + 1.259i$, and for glass is $\varepsilon_{glass} = 2.123 + 0i$. Thermal conductivities for air, water, and glass are taken as $\kappa_{air} = 0.022\frac{W}{m\cdot K}$, $\kappa_{water} = 0.6\frac{W}{m\cdot K}$, $\kappa_{glass} = 0.8\frac{W}{m\cdot K}$. Diameter of computational domain is chosen to be 2 μm. We define thermal boundary conditions as a heat flux through the computational domain surface $q = h(T_{ext} - T_{surf})$, where h for upper and bottom computational hemispheres are equal to $h_{up} = 2\kappa_{up}/D$ and $h_{bottom} = 2\kappa_{bottom}/D$, respectively, κ is the thermal conductivity, T_{ext} = 293 K is the external temperature, T is the calculated temperature near boundary of the computational domain. The bottom hemisphere plays a role of a substrate, when we consider inhomogeneous surrounding of the particle, whereas it is similar to the upper hemisphere in the case of homogeneous surrounding. In our model, all nanoparticles have cut off spherical segment of 20 nm thickness from the bottom.

■ ASSOCIATED CONTENT

Supporting Information

The Supporting Information is available free of charge on the ACS Publications website at DOI: 10.1021/acs.nanolett.7b00183. .

Model of optical heating of spherical nanoparticles; heating of spherical particles of dierent permittivities; heating in medium with higher refractive index and thermal conductivity (water and glass); mode decomposition; Raman shift; radiation pattern at magnetic quadrupole resonance (PDF)

■ AUTHOR INFORMATION

Corresponding Authors

*E-mail: m.petrov@metalab.ifmo.ru.

*E-mail: s.makarov@metalab.ifmo.ru.

ORCID

Mihail I. Petrov: 0000-0001-8155-9778

Sergey V. Makarov: 0000-0002-9257-6183

Notes

The authors declare no competing financial interest.

■ ACKNOWLEDGMENTS

The authors are thankful to Professor C. Simovski, Dr. A. Yulin, Dr. A. Bogdanov, and Dr. D. Baranov for useful discussions and comments and Dr. A. Gudovskih and Dr. I. Mukhin for silicon films deposition. Experimental part was financed by Russian Science Foundation (Grant 15-19-00172). Theoretical part was supported by Ministry of Education and Science of the Russian Federation (Grant 14.Y26.31.0010). S.V.M. acknowledges ITMO Fellowship Program. M.I.P. acknowledges support from Academy of Finland Grant 310753.

■ REFERENCES

(1) Kuznetsov, A. I.; Miroshnichenko, A. E.; Brongersma, M. L.; Kivshar, Y. S.; Luk'yanchuk, B. S. Optically resonant dielectric nanostructures. *Science* **2016**, *354*, aag2472.

(2) Jahani, S.; Jacob, Z. All-dielectric metamaterials. *Nat. Nanotechnol.* **2016**, *11*, 23−36.
(3) Bakker, R.; Permyakov, D.; Yu, Y. F.; Markovich, D.; Paniagua-Domínguez, R.; Gonzaga, L.; Samusev, A. K.; Kivshar, Y. S.; Luk'yanchuk, B. S.; Kuznetsov, A. I. Magnetic and electric hotspots with silicon nanodimers. *Nano Lett.* **2015**, *15*, 2137−2142.
(4) Sinev, I.; Iorsh, I.; Bogdanov, A.; Permyakov, D.; Komissarenko, F.; Mukhin, I.; Samusev, A. K.; Valuckas, V.; Kuznetsov, A. I.; Luk'yanchuk, B. S.; Miroshnichenko, A. E.; Kivshar, Y. S. Polarization control over electric and magnetic dipole resonances of dielectric nanoparticles on metallic films. *Laser & Photonics Reviews* **2016**, *10*, 799−806.
(5) Person, S.; Jain, M.; Lapin, Z.; Sáenz, J. J.; Wicks, G.; Novotny, L. Demonstration of zero optical backscattering from single nanoparticles. *Nano Lett.* **2013**, *13*, 1806−1809.
(6) Chong, K. E.; Staude, I.; James, A.; Dominguez, J.; Liu, S.; Campione, S.; Subramania, G. S.; Luk, T. S.; Decker, M.; Neshev, D. N.; Breger, I.; Kivshar, Y. S. Polarization-independent silicon metadevices for efficient optical wavefront control. *Nano Lett.* **2015**, *15*, 5369−5374.
(7) Moitra, P.; Slovick, B. A.; Li, W.; Kravchencko, I. I.; Briggs, D. P.; Krishnamurthy, S.; Valentine, J. Large-scale all-dielectric metamaterial perfect reflectors. *ACS Photonics* **2015**, *2*, 692−698.
(8) Proust, J.; Bedu, F.; Gallas, B.; Ozerov, I.; Bonod, N. All-Dielectric Colored Metasurfaces with Silicon Mie Resonators. *ACS Nano* **2016**, *10*, 7761−7767.
(9) Wang, L.; Kruk, S.; Tang, H.; Li, T.; Kravchenko, I.; Neshev, D. N.; Kivshar, Y. S. Grayscale transparent metasurface holograms. *Optica* **2016**, *3*, 1504−1505.
(10) Albella, P.; Poyli, M. A.; Schmidt, M. K.; Maier, S. A.; Moreno, F.; Sáenz, J. J.; Aizpurua, J. Low-loss electric and magnetic field-enhanced spectroscopy with subwavelength silicon dimers. *J. Phys. Chem. C* **2013**, *117*, 13573−13584.
(11) Albella, P.; Alcaraz de la Osa, R.; Moreno, F.; Maier, S. A. Electric and magnetic field enhancement with ultralow heat radiation dielectric nanoantennas: considerations for surface-enhanced spectroscopies. *ACS Photonics* **2014**, *1*, 524−529.
(12) Caldarola, M.; Albella, P.; Cortés, E.; Rahmani, M.; Roschuk, T.; Grinblat, G.; Oulton, R. F.; Bragas, A. V.; Maier, S. A. Non-plasmonic nanoantennas for surface enhanced spectroscopies with ultra-low heat conversion. *Nat. Commun.* **2015**, *6*, 7915.
(13) Huang, Z.; Wang, J.; Liu, Z.; Xu, G.; Fan, Y.; Zhong, H.; Cao, B.; Wang, C.; Xu, K. Strong-field-enhanced spectroscopy in silicon nanoparticle electric and magnetic dipole resonance near a metal surface. *J. Phys. Chem. C* **2015**, *119*, 28127−28135.
(14) Dmitriev, P. A.; Baranov, D. G.; Milichko, V. A.; Makarov, S. V.; Mukhin, I. S.; Samusev, A. K.; Krasnok, A. E.; Belov, P. A.; Kivshar, Y. S. Resonant Raman scattering from silicon nanoparticles enhanced by magnetic response. *Nanoscale* **2016**, *8*, 9721−9726.
(15) Mukherjee, S.; Givan, U.; Senz, S.; Bergeron, A.; Francoeur, S.; De La Mata, M.; Arbiol, J.; Sekiguchi, T.; Itoh, K. M.; Isheim, D. Phonon Engineering in Isotopically Disordered Silicon Nanowires. *Nano Lett.* **2015**, *15*, 3885−3893.
(16) Balkanski, M.; Wallis, R.; Haro, E. Anharmonic effects in light scattering due to optical phonons in silicon. *Phys. Rev. B: Condens. Matter Mater. Phys.* **1983**, *28*, 1928.
(17) Govorov, A. O.; Richardson, H. H. Generating heat with metal nanoparticles. *Nano Today* **2007**, *2*, 30−38.
(18) Dreaden, E. C.; Alkilany, A. M.; Huang, X.; Murphy, C. J.; El-Sayed, M. A. The golden age: gold nanoparticles for biomedicine. *Chem. Soc. Rev.* **2012**, *41*, 2740−2779.
(19) Baffou, G.; Quidant, R. Thermo-plasmonics: using metallic nanostructures as nano-sources of heat. *Laser & Photonics Reviews* **2013**, *7*, 171−187.
(20) Hirsch, L.; Stafford, R.; Bankson, J.; Sershen, S.; Rivera, B.; Price, R.; Hazle, J.; Halas, N. J.; West, J. Nanoshell-mediated near-infrared thermal therapy of tumors under magnetic resonance guidance. *Proc. Natl. Acad. Sci. U. S. A.* **2003**, *100*, 13549−13554.
(21) Lim, W. Q.; Gao, Z. Plasmonic nanoparticles in biomedicine. *Nano Today* **2016**, *11*, 168−188.
(22) Linic, S.; Aslam, U.; Boerigter, C.; Morabito, M. Photochemical transformations on plasmonic metal nanoparticles. *Nat. Mater.* **2015**, *14*, 567−576.
(23) Adleman, J. R.; Boyd, D. A.; Goodwin, D. G.; Psaltis, D. Heterogenous catalysis mediated by plasmon heating. *Nano Lett.* **2009**, *9*, 4417−4423.
(24) Christopher, P.; Xin, H.; Linic, S. Visible-light-enhanced catalytic oxidation reactions on plasmonic silver nanostructures. *Nat. Chem.* **2011**, *3*, 467−472.
(25) Urban, A. S.; Pfeiffer, T.; Fedoruk, M.; Lutich, A. A.; Feldmann, J. Single-step injection of gold nanoparticles through phospholipid membranes. *ACS Nano* **2011**, *5*, 3585−3590.
(26) Boyer, D.; Tamarat, P.; Maali, A.; Lounis, B.; Orrit, M. Photothermal imaging of nanometer-sized metal particles among scatterers. *Science* **2002**, *297*, 1160−1163.
(27) Donner, J. S.; Baffou, G.; McCloskey, D.; Quidant, R. Plasmon-assisted optofluidics. *ACS Nano* **2011**, *5*, 5457−5462.
(28) Zijlstra, P.; Paulo, P. M.; Orrit, M. Optical detection of single non-absorbing molecules using the surface plasmon resonance of a gold nanorod. *Nat. Nanotechnol.* **2012**, *7*, 379−382.
(29) Wang, S.; Westcott, S.; Chen, W. Nanoparticle luminescence thermometry. *J. Phys. Chem. B* **2002**, *106*, 11203−11209.
(30) Brites, C. D.; Lima, P. P.; Silva, N. J.; Millán, A.; Amaral, V. S.; Palacio, F.; Carlos, L. D. Thermometry at the nanoscale. *Nanoscale* **2012**, *4*, 4799−4829.
(31) Cognet, L.; Tardin, C.; Boyer, D.; Choquet, D.; Tamarat, P.; Lounis, B. Single metallic nanoparticle imaging for protein detection in cells. *Proc. Natl. Acad. Sci. U. S. A.* **2003**, *100*, 11350−11355.
(32) Baffou, G.; Bon, P.; Savatier, J.; Polleux, J.; Zhu, M.; Merlin, M.; Rigneault, H.; Monneret, S. Thermal imaging of nanostructures by quantitative optical phase analysis. *ACS Nano* **2012**, *6*, 2452−2458.
(33) Baffou, G.; Quidant, R.; Garcia de Abajo, F. J. Nanoscale control of optical heating in complex plasmonic systems. *ACS Nano* **2010**, *4*, 709−716.
(34) Palik, E. D. *Handbook of optical constants of solids*; Academic Press, 1998; Vol. *3*.
(35) Serda, R. E.; Gu, J.; Bhavane, R. C.; Liu, X.; Chiappini, C.; Decuzzi, P.; Ferrari, M. The association of silicon microparticles with endothelial cells in drug delivery to the vasculature. *Biomaterials* **2009**, *30*, 2440−2448.
(36) Ishii, S.; Sugavaneshwar, R. P.; Chen, K.; Dao, T. D.; Nagao, T. Solar water heating and vaporization with silicon nanoparticles at mie resonances. *Opt. Mater. Express* **2016**, *6*, 640−648.
(37) Aioub, M.; Panikkanvalappil, S. R.; El-Sayed, M. A. Platinum-Coated Gold Nanorods: Efficient Reactive Oxygen Scavengers That Prevent Oxidative Damage Toward Healthy, Untreated Cells During Plasmonic Photothermal Therapy. *ACS Nano* **2017**, *11*, 579.
(38) Mörl, K.; Röpke, U.; Knappe, B.; Lehmann, J.; Perthel, R.; Schröder, H. Optical properties of sputtered Fe 2 O 3 films. *Thin Solid Films* **1979**, *60*, 49−53.
(39) Aspnes, D.; Studna, A. Dielectric functions and optical parameters of si, ge, gap, gaas, gasb, inp, inas, and insb from 1.5 to 6.0 ev. *Phys. Rev. B: Condens. Matter Mater. Phys.* **1983**, *27*, 985.
(40) Johnson, P. B.; Christy, R.-W. Optical constants of the noble metals. *Phys. Rev. B* **1972**, *6*, 4370.
(41) Dmitriev, P.; Makarov, S.; Milichko, V.; Mukhin, I.; Gudovskikh, A.; Sitnikova, A.; Samusev, A.; Krasnok, A.; Belov, P. Laser fabrication of crystalline silicon nanoresonators from an amorphous film for low-loss all-dielectric nanophotonics. *Nanoscale* **2016**, *8*, 5043−5048.
(42) Permyakov, D.; Sinev, I.; Markovich, D.; Ginzburg, P.; Samusev, A.; Belov, P.; Valuckas, V.; Kuznetsov, A. I.; Luk'yanchuk, B. S.; Miroshnichenko, A. E.; Neshev, D. N.; Kivshar, Y. S. Probing magnetic and electric optical responses of silicon nanoparticles. *Appl. Phys. Lett.* **2015**, *106*, 171110.
(43) Reed, G. T.; Mashanovich, G.; Gardes, F.; Thomson, D. Silicon optical modulators. *Nat. Photonics* **2010**, *4*, 518−526.

DOI: 10.1021/acs.nanolett.7b00183
Nano Lett. 2017, 17, 2945−2952

(44) Huang, X.; El-Sayed, I. H.; Qian, W.; El-Sayed, M. A. Cancer cell imaging and photothermal therapy in the near-infrared region by using gold nanorods. *J. Am. Chem. Soc.* **2006**, *128*, 2115−2120.
(45) Mackey, M. A.; Ali, M. R.; Austin, L. A.; Near, R. D.; El-Sayed, M. A. The most effective gold nanorod size for plasmonic photothermal therapy: theory and in vitro experiments. *J. Phys. Chem. B* **2014**, *118*, 1319−1326.
(46) Hu, M.; Petrova, H.; Chen, J.; McLellan, J. M.; Siekkinen, A. R.; Marquez, M.; Li, X.; Xia, Y.; Hartland, G. V. Ultrafast laser studies of the photothermal properties of gold nanocages. *J. Phys. Chem. B* **2006**, *110*, 1520−1524.
(47) Rodríguez-Oliveros, R.; Sánchez-Gil, J. A. Gold nanostars as thermoplasmonic nanoparticles for optical heating. *Opt. Express* **2012**, *20*, 621−626.
(48) Lalisse, A.; Tessier, G.; Plain, J.; Baffou, G. Quantifying the Efficiency of Plasmonic Materials for Near-Field Enhancement and Photothermal Conversion. *J. Phys. Chem. C* **2015**, *119*, 25518−25528.
(49) Speight, J. G. *Lange's handbook of chemistry*; McGraw-Hill: New York, 2005; Vol. *1*.

DOI: 10.1021/acs.nanolett.7b00183
Nano Lett. 2017, 17, 2945−2952

ORIGINAL PAPER

LASER & PHOTONICS REVIEWS

www.lpr-journal.org

All-Optical Nanoscale Heating and Thermometry with Resonant Dielectric Nanoparticles for Controllable Drug Release in Living Cells

George P. Zograf, Alexander S. Timin, Albert R. Muslimov, Ivan I. Shishkin, Alexandre Nominé, Jaafar Ghanbaja, Pintu Ghosh, Qiang Li, Mikhail V. Zyuzin, and Sergey V. Makarov**

All-dielectric nanophotonics becomes a versatile tool for various optical applications, including nanothermometry and optical heating. Its general concept includes excitation of Mie resonances in nonplasmonic nanoparticles. However, the potential of resonant dielectric nanoparticles in drug delivery applications still has not been fully realized. Here, optically resonant dielectric iron oxide nanoparticles (α-Fe_2O_3 NPs) are employed for remote rupture of microcontainers used as a drug delivery platform. It is theoretically and experimentally demonstrated that α-Fe_2O_3 NPs have several advantages in light-to-heat energy conversion comparing to previously used materials, such as noble metals and silicon, due to the broader spectral range of efficient optical heating, and in enhancement of thermally sensitive Raman signal. The α-Fe_2O_3 NPs embedded into the wall of universal drug carriers, polymer capsules, are used to experimentally determine the local temperature of the capsule rupture upon laser irradiation (170 °C). As a proof of principle, the delivery and remote release of anticancer drug vincristine upon lowered laser irradiation (4.0×10^4 W cm^{-2}) using polymer capsules modified with the α-Fe_2O_3 NPs is shown. The biological tests are performed on two primary cell types: i) carcinoma cells, as an example of malignant tumor, and ii) human stem cells, as a model of healthy cells.

1. Introduction

Optically resonant dielectric nanoparticles (NPs) allowing for light localization at subwavelength scale attracted a lot of attention[1,2] during last years due to their excellent performance in a number of advanced optical applications. Namely, the resonant NPs made of silicon,[3,4] germanium,[5] III-V semiconductors,[6,7] or multicomponent materials[8–10] demonstrate outstanding optical characteristics owing to Mie resonances excited by incident laser field. Moreover, because of strong field enhancement inside the nonplasmonic (e.g., silicon) NPs, it is possible to both efficiently heat them by laser irradiation and measure local temperature via thermally sensitive Raman response,[11] which is also enhanced by several orders of magnitude.[12] With the resonant silicon NPs, the "all-in-one" concept was applied for simultaneous all-optical heating, sensing, and thermometry of small amount of protein molecules.[13] However, the full potential of resonant nonplasmonic NPs with both temperature and micrometer spatial control for more advanced bioapplications has not yet been realized.

Recent trends in various biomedical applications are related to incorporation of different NPs within nano- and microcarriers to obtain a composite platform with improved properties.[14] Among available delivery systems, polymer capsules are currently

G. P. Zograf, Dr. I. I. Shishkin, Dr. A. Nominé, Dr. M. V. Zyuzin, Dr. S. V. Makarov
Department of Physics and Engineering
ITMO University
Lomonosova 9, Saint-Petersburg 191002, Russia
E-mail: mikhail.zyuzin@metalab.ifmo.ru; s.makarov@metalab.ifmo.ru

Dr. A. S. Timin
Research School of Chemical and Biomedical Engineering
National Research Tomsk Polytechnic University
Lenin Avenue 30,, 634050 Tomsk, Russia

The ORCID identification number(s) for the author(s) of this article can be found under https://doi.org/10.1002/lpor.201900082

DOI: 10.1002/lpor.201900082

Dr. A. S. Timin, A. R. Muslimov
Peter The Great St. Petersburg Polytechnic University
Polytechnicheskaya str. 29, St. Petersburg 195251, Russia

A. R. Muslimov
First I. P. Pavlov State Medical University of St. Petersburg
L'va Tolstogo 6-8, Saint-Petersburg 197022, Russia

Dr. A. Nominé, Dr. J. Ghanbaja
Institute Jean Lamour (IJL)
Universite de Lorraine – CNRS
F-54000 Nancy, France

Dr. P. Ghosh, Dr. Q. Li
Laboratory of Integrated Photonics and Nanophotonics
Zhejiang University
Zhejiang 310027, China

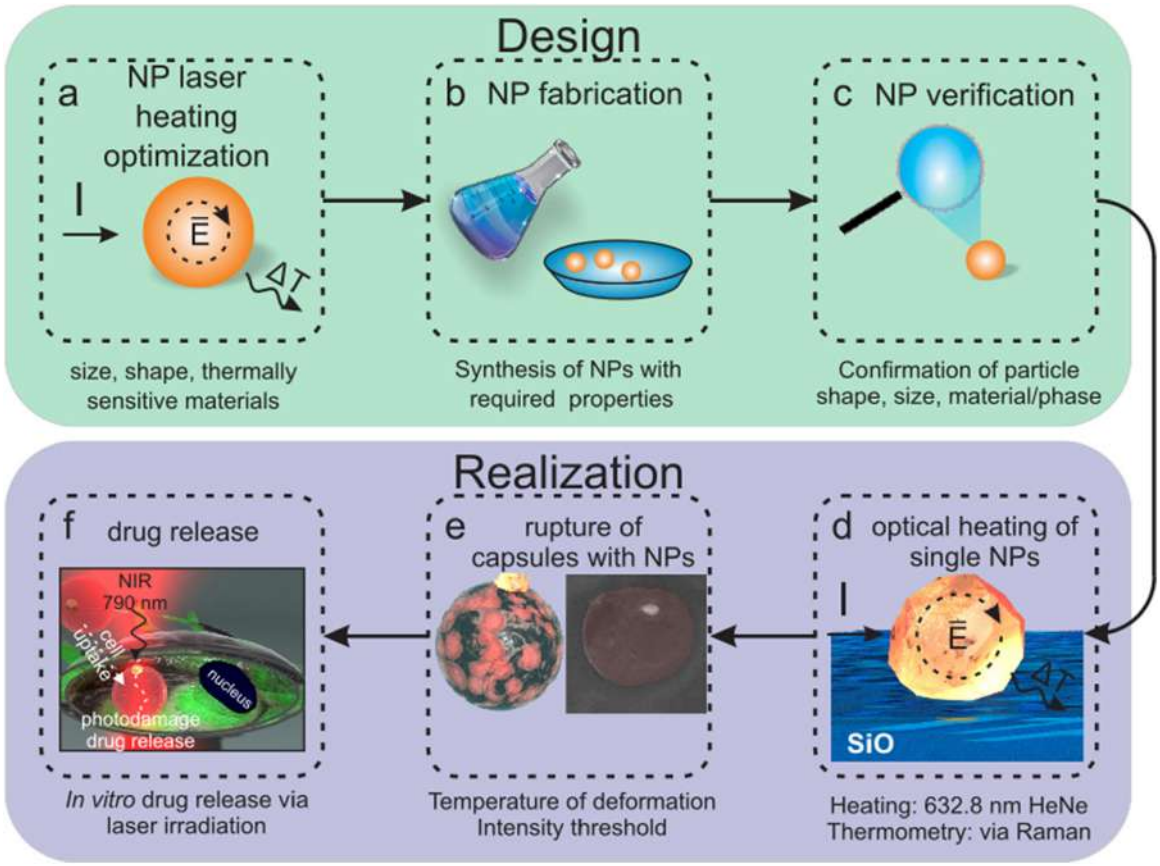

Figure 1. Schematic representation of iron oxide NPs implementation steps in this work. a) Simulation of optimal optical heating parameters. b) Synthesis of NPs with the required physicochemical properties. c) Characterization of obtained NPs. d) Study of NPs optical properties. e) Immobilization of NPs into the shell of polymer capsules for drug delivery applications. f) Probing the remote drug activation inside cells and nanothermometry.

being demonstrated as unique carriers for safe and efficient delivery of biologically active compounds such as gene materials,[15] macromolecules,[16] proteins,[17] drugs.[18] In the previous works, various plasmonic NPs were employed as nanoheaters to reduce laser intensity threshold for the capsules opening, while their additional functionalization by thermally sensitive nanomaterials was performed for all-optical local nanothermometry.[19]

In this work, we incorporate optically resonant dielectric NPs into polymer capsules for all-optical remote drug release with simultaneous nanothermometry upon laser irradiation. In order to achieve high optical field enhancement in the NPs and their efficient heating, we employ biocompatible iron oxide (α-Fe_2O_3) NPs[20] instead of previously used dielectric ones,[4,8,10] owing to their high refractive index ($n \approx 2.7$–3.2) and moderate losses ($k \approx 0.02$–0.2) in red and near-infrared (NIR) ranges.[21] This phase of iron oxide has very pronounced and easily recognizable multipeak Raman response in broad range of wavenumbers (200–1400 cm^{-1}[22]), making it much more convenient for temperature-induced peak shift registration as compared to the silicon possessing only one Raman-active phonon mode.[13] The use of such NPs allows for direct measurement of the capsules rupturing temperature with the accuracy no worse than 40 K, corresponding to a characteristic Raman linewidth. Also, the NPs decrease the rupture threshold intensity down to 4.0×10^4 W $cm^{-}2$. Finally, the developed microcapsules modified with α-Fe_2O_3 NPs are used to deliver antitumor drug vincristine (VCR) into two primary cell types: i) carcinoma cells (CCs) as an example of malignant tumor, and ii) human mesenchymal stem cells (hMSCs) as a model of healthy cells. Our findings show that the optically resonant α-Fe_2O_3 NPs have high potential to be a versatile platform in order to fabricate multifunctional drug carriers possessing tumor-specific drug release.

2. Results and Discussion

The main concept of this study is depicted in **Figure 1**, where we present the theoretical and experimental stages of designing a multifunctional drug carrier that simultaneously allows for external drug release triggering and local temperature detection. As shown in Figure 1a, the used biocompatible α-Fe_2O_3 NPs should possess high enough refractive index and moderate losses, as well as demonstrate thermally sensitive Raman lines. Also, to predict the optimal NP size for efficient optimal heating, the electromagnetic simulations should be performed (Figure 1a). After the theoretical calculations, synthesized (Figure 1b) and characterized (Figure 1c) NPs can be experimentally tested for optical heating and Raman thermometry (Figure 1d). The fully characterized iron oxide NPs can be then used to modify the wall of polymer capsules, which are widely used to deliver cargo

into cells (Figure 1e). The efficient optical heating of the NPs allows for remote low-intensity release of cargo inside cells (Figure 1f). In the following sections, we discuss each step in more details.

Theoretical background. General model for heating of a spherical nanoparticle comprised of an arbitrary material (metals or dielectrics) by continuous laser illumination in a homogeneous medium was developed elsewhere.[11,23,24] We combined it with a simple analytical solution for light absorption by the nanoparticle from the Mie theory.[25] The Mie theory deals with a single spherical NP in homogeneous medium, yielding general understanding regarding which optical modes can be excited and what their optical response is. For instance, scattering (σ_{sca}), extinction (σ_{ext}), and absorption (σ_{abs}) cross-sections can be derived from following equations:

$$\sigma_{sca} = \frac{W_{sca}}{I_i} = \frac{2\pi}{k^2}\sum_{n=1}^{\infty}(2n+1)(|a_n|^2 + |b_n|^2) \quad (1)$$

$$\sigma_{ext} = \frac{W_{ext}}{I_i} = \frac{2\pi}{k^2}\sum_{n=1}^{\infty}(2n+1)Re(a_n + b_n) \quad (2)$$

$$\sigma_{abs} = \sigma_{ext} - \sigma_{sca} \quad (3)$$

where a_n and b_n are the Mie-coefficients for electric and magnetic types of modes, respectively. As a result, the solution of a thermal diffusion equation in a steady-state regime with a heat source defined by the light intensity (I) and the NP absorption cross-section (σ_{abs}) gives the following equation for temperature increase inside the NP[24]:

$$\delta T_{NP} = \frac{I\sigma_{abs}}{4\pi\kappa_2 R} \quad (4)$$

where κ_2 is the thermal conductivity of the surrounding medium, which is significantly smaller than that of the NP; and R is the NP radius. The details of derivation of this formula and calculations of the absorption cross-section can be found in the Supporting Information. It is worth noting that this consideration is only suitable for structures with thermal conductivity several orders higher than that of surrounding homogeneous media.

Since the concept of NP-induced enhancement and localization of optical heating[26] is attractive for the most of bio- or chemical applications, it is vital to study their resonant properties in water ($n = 1.33$), because such studies are taken in aqueous medium. The theoretical calculations on various NPs optical heating in water are summarized in **Figure 2**. Based on Equations (1)—(4) we carried out a comparative analysis for optical heating in the visible and NIR ranges of three spherical NPs: gold,[27] silicon,[28] iron oxide (Fe_2O_3),[29] while their thermal constants are taken from ref. [30].

It is clearly seen from Figure 2a that gold nanospheres are efficient light-to-heat converters at their localized surface plasmon resonance wavelength (around $\lambda \sim 500$–600 nm) at all sizes, as reported previously.[26] On the other hand, a silicon nanosphere, as shown in Figure 2b, supports a variety of Mie modes (electric and magnetic ones[2]), which allow to use c-Si NPs as light-to-heat converters even in the red region of visible light spectra.[11] However, their performance worsens at the wavelengths larger than $\lambda \approx 800$ nm. In its turn, α-Fe_2O_3 NPs combine benefits of both gold and silicon by providing the broad absorption band in the visible at $\lambda < 600$ nm wavelengths and support Mie modes in NIR as well (Figure 2c). Additionally, a comparison of performances between α-Fe_2O_3, c-Si and Au nanospheres is presented in Figure 2c,d, where one can clearly see that the α-Fe_2O_3 NP outperforms the Au NPs even at the plasmon resonance wavelength in water $\lambda \approx 530$ nm. Moreover, the α-Fe_2O_3 NP absorbs light better than Si NPs at all wavelengths of interest ($\lambda = 400$-1000 nm). The origin of such outstanding performance of Fe_2O_3 is based on the optimized combination of real and imaginary parts of its dielectric function. Indeed, radiative and non-radiative losses of any resonators have to be balanced to achieve the highest optical heating.[11]

Besides high efficiency of light-to-heat conversion, it is crucial to obtain a pronounced Raman signal for local optical temperature measurements. This concept of far-field optical temperature detection at nanoscale is based on thermo-sensitive Raman response due to anharmonic effects in light scattering on optical phonons.[31] **Figure 3**a shows that α-Fe_2O_3 has very intensive and rich Raman spectrum with clearly distinguishable Stokes lines.

As a result, in this part we revealed that α-Fe_2O_3 is one of the most prospective materials for all-optical heating and nanothermometry. Namely, it fulfills the following requirements: i) relatively simple and cost-efficient fabrication; ii) active optical phonons for thermo-sensitive optical response (Raman scattering); iii) high-refractive index in order to support Mie resonances in nanostructures in the visible and NIR for enhanced heating and reduced signal collection (dwell) time.

Nanoparticles fabrication and structural characterization. α-Fe_2O_3 NPs were prepared via solvothermal method.[33] The characterization by scanning electron microscopy (SEM) found NPs with diameter (D) between 300 and 800 nm (Figure S3, Supporting Information). This is further confirmed by transmission electron microscopy (TEM), which also shows a second population of NPs with diameters in the range of 5–20 nm (Figure S5, Supporting Information). Despite the fact that larger α-Fe_2O_3 NPs do not possess a perfect spherical shape, the aspect ratio remains sufficiently low to maintain the quasi-spherical approach reasonable for theoretical calculations, since the factor of facets for resonant dielectric NPs is almost negligible as shown in previous works.[8,10]

X-ray photoelectron spectroscopy (XPS) results confirm that NPs are composed of iron oxide (Figure 3b). However, the peaks in the obtained spectra correspond to both +II and +III oxidation states (i.e. α-Fe_2O_3 and Fe_3O_4, respectively). The challenge to determine composition and crystallogaphic strucutre of NPs arises due to the fact that two phases share either the same stoichiometry (α-Fe_2O_3 hematite, and γ-Fe_2O_3 maghemite) or structural similarities (γ-Fe_2O_3 maghemite and γ-Fe_3O_4 magnetite).[34] However, α-Fe_2O_3 and Fe_3O_4 can be additionally differentiated by electron energy loss spectroscopy (EELS).[35] In the case of the large NPs shown in Figure 3c, the experimental EELS spectrum shows the typical features of α-Fe_2O_3, which are a double peak in the O K-edge and a shoulder in the Fe $L_{2,3}$ edge Figure 3e. Knowing the stoichimetry, selected area is used to determine the structure of the same NP. The diffraction pattern shown in Figure 3d revealed that such NPs have high crystallinity and interplanar distances match very well with the diffraction

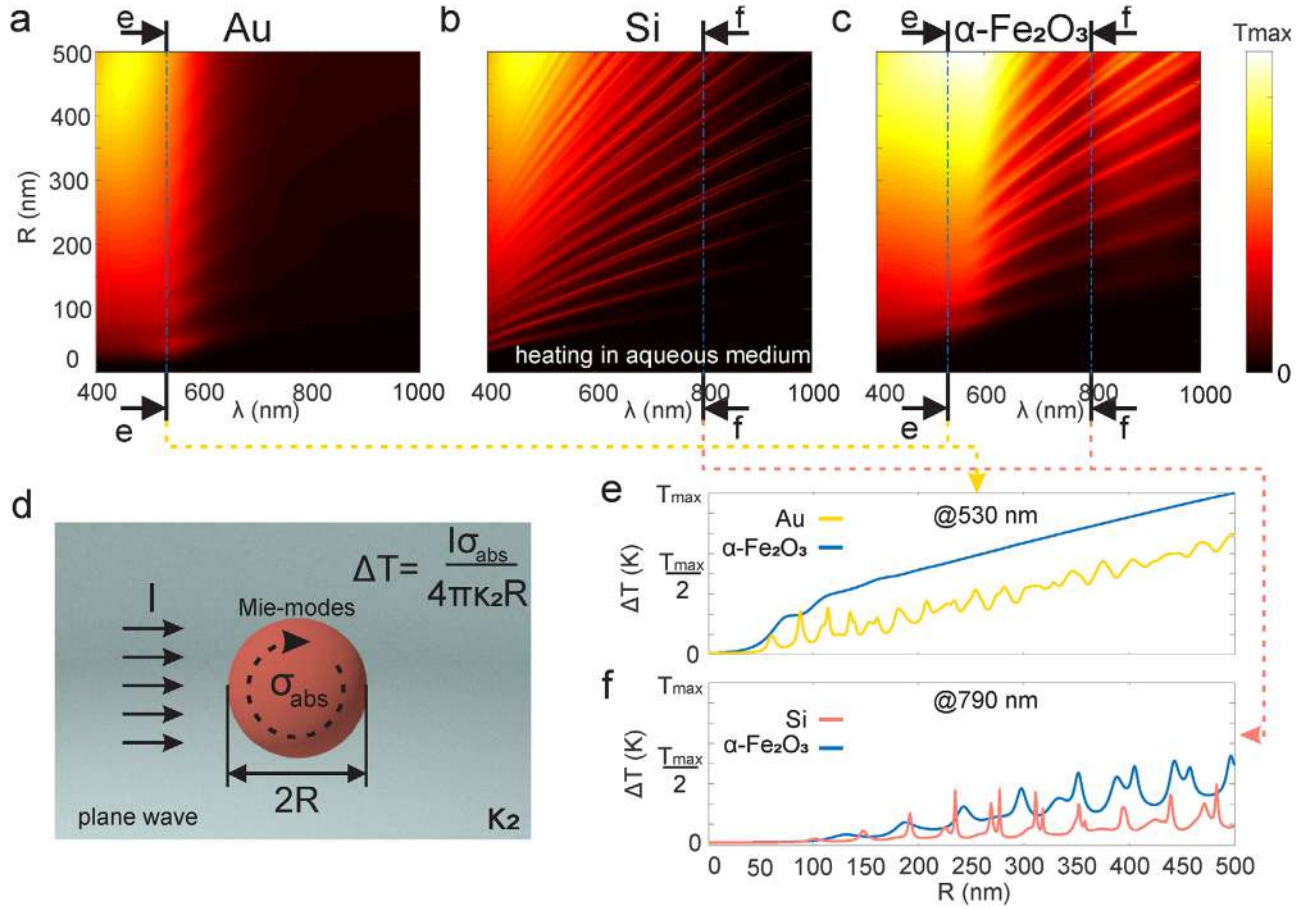

Figure 2. Theoretical modeling of NPs optical heating. Calculated maps for optical heating of a) Au, b) Si and c) α-Fe_2O_3 spherical NPs in water using Equations (1)–(4). The colorbar is temperature increase in arbitrary units. d) Schematic of optical heating theoretical model. Incident plane-wave excites resonant optical modes of a sphere (Mie-theory) in homogeneous surrounding medium with thermal conductivity κ_2. e,f) 1D plots for the dependence of ΔT on NP radius R extracted from (a) and (b) for fixed excitation wavelengths: $\lambda = 530$ nm for Au (e) and $\lambda = 790$ nm for Si (f), compared with heating of α-Fe_2O_3 NPs taken from (c).

pattern of α-Fe_2O_3 in [010] zone axis (Figure S6, Supporting Information). Characterization of smaller particles was carried out by following the same procedure. Unlike in the case of larger NPs, EELS spectra as well as diffraction pattern correspond to Fe_3O_4 magnetite (Figure S7, Supporting Information). This explains the detection of both oxidation states on the XPS spectra. The presence of both oxides is not necessarily an issue for this study, since Fe_3O_4 shows only limited optical heating for particle radius below 50 nm (Figure S1, Supporting Information). Moreover, since there is a correlation between size and crystallographic phase, the smaller NPs can be easily removed during the centrifugation process (e.g., during capsule synthesis).

As it has been mentioned, α-Fe_2O_3 NPs can serve not only as a nanoscale heater, but also simultaneously as multi-purpose nanothermometer[22] with high melting point ($T \approx 1850$ K[36]) as compared to gold ($T \approx 1250$ K[37]) and silicon ($T \approx 1600$ K[38]). Thus, Figure 3a depicts not only phase and bond fingerprint of fabricated structure, but also can serve as temperature sensor, because of thermally dependent Raman response. For instance, A_1 band (vibration of Fe–O bond[22,39]) scattering demonstrate spectral blue-shift, as it is shown in the inset.[32] For higher precision of the temperature measurements, we average the temperature between 225, 290, and 400 cm^{-1} Raman Stokes lines according to previous works.[22]

Optical characterization of resonant α-Fe_2O_3 NPs. In order to study resonant optical properties of fabricated single α-Fe_2O_3 NPs, dark-field (DF) spectroscopy technique was applied (**Figure 4**a,b, for more details see Supporting Information). It is worth noticing that DF spectra serves not only as a tool for characterization of the far-field optical properties and description of the excited optical modes in NPs, but also for the verification of the NPs sizes obtained by SEM or TEM. In order to carry out the "optical size" verification, the full-wave numerical simulations in the commercial software COMSOL Multiphysics was employed. As shown in Figure 4b, the numerical and experimental results are in a good qualitative agreement, even though the fabricated NPs are not perfectly spherical according to Figure 3c,f. The modeling also reveals the local optical field enhancement up to two times within NP and up to six times outside NP (see insets in Figure 4b).

The DF spectrum shows that the chosen NP (340 nm diameter particle) provides resonant elastic scattering around the

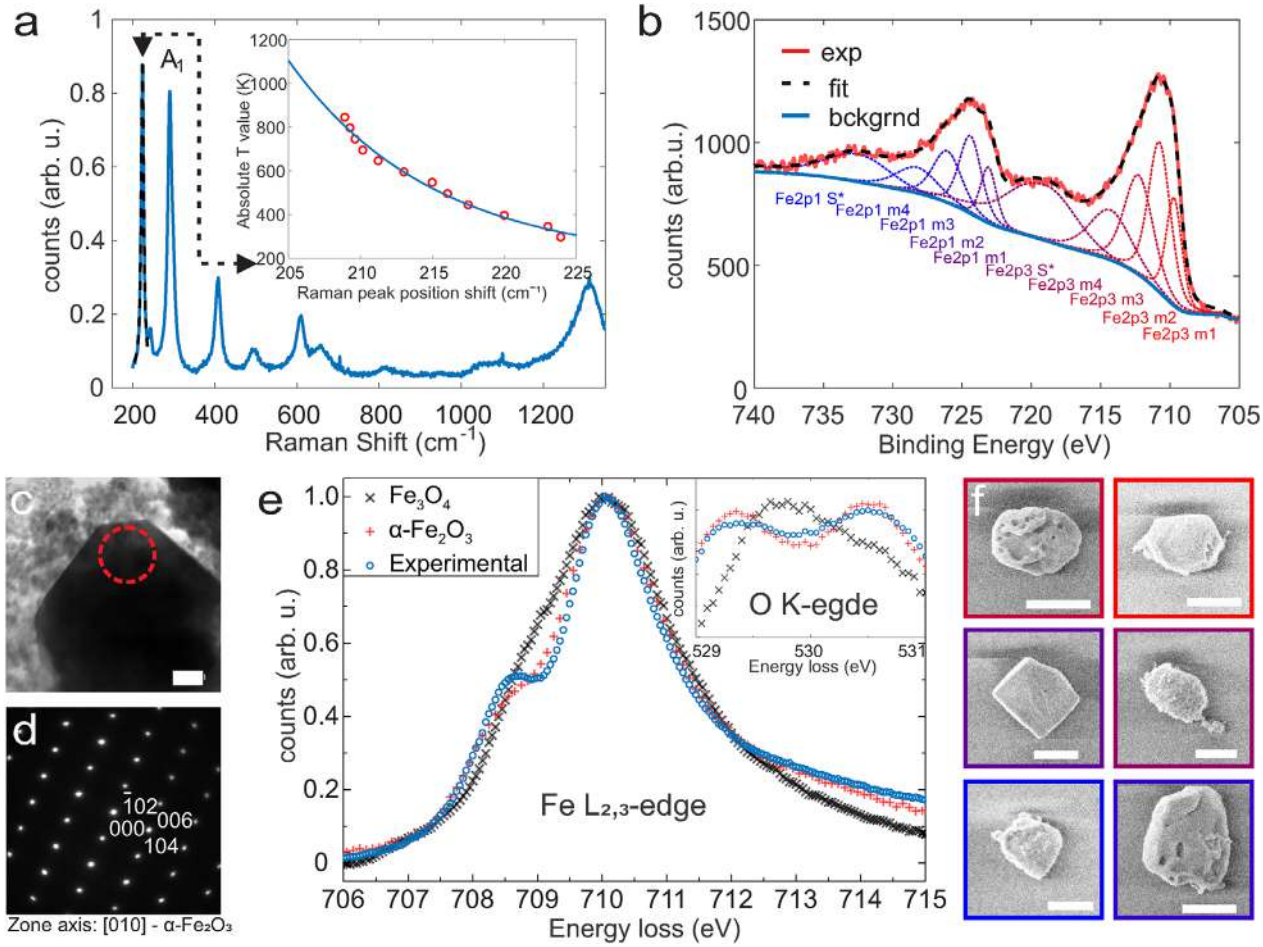

Figure 3. α-Fe_2O_3 NPs characterization. a) Stokes Raman scattering from fabricated α-Fe_2O_3 NPs. Inset illustrates evolution of A_1 band position with increase in temperature (adopted from ref. [32]) b) X-ray photoelectron spectroscopy of fabricated structures. Captions under curves correspond to specific response of Fe atoms. c) TEM image of the iron oxide NPs. Scale bar is 50 nm. Dashed region corresponds to the area of consideration for d) electron diffraction patterns. e) Electron Energy Loss Spectroscopy (EELS) for the same NPs of α-Fe_2O_3. f) Typical shapes, sizes, and morphologies of fabricated α-Fe_2O_3 NPs carried out by means of scanning electron microscopy (scale bar is 400 nm).

emission wavelength of He-Ne laser ($\lambda = 632.8$ nm) used for Raman experiments in this work. This results in the local field enhancement and NP's heating observed as a spectral shift of characteristic Raman-active modes (Figure 4c; Figure S10, Supporting Information). As it has been mentioned, the spectral shift of the Raman Stokes line between "cold" and "hot" regimes can be back-converted into temperature increase. By the term "cold" Raman scattering regime from either bulk material response, or low pump intensity response from single iron oxide nanoparticle is considered, whereas the "hot" regime stands for enhanced absorption regime with high (> 2 mW/μm^2) pump intensity, which results in spectral blue-shift of the Raman response. It is clearly seen that for such high heating temperatures, only a number of Raman lines remain pronounced (i.e., initial 225 cm^{-1}), unlike 600 and 1320 cm^{-1} ones.

Figure 4d depicts both theoretical and experimental optical heating results for NP with radius $R \approx 170$ nm at 632.8 nm wavelength with intensity $I_0 = 2.4$ mW/μm^2. According to SEM images, α-Fe_2O_3 NPs are not perfectly spherical, thus the thermal contact area determination remains only one fitting parameter for our numerical calculations. In this regard, blue dashed line corresponds to dipped by diameter over 5 (R/2.5) nanometers into SiO_2 substrate and red dashed line is the case of a slight physical contact (20 nm into substrate). The experimental values are mostly located within the region bordered by two calculated lines; however, larger particles are in little less match with the theoretical predictions. We believe that this might happen due to shape inhomogeneity. Indeed, any roughness reduces quality factor of the dielectric microresonator,[40] whereas the heating efficiency is a linear function of quality factor.[11]

Polymer capsules with resonant α-Fe_2O_3 NPs. After proving the ability of both heating and thermometry by single iron oxide NPs (Figure 1d), we implemented them into drug carriers, so-called polymer capsules, to probe remote drug activation in vitro and simultaneous nanothermometry (Figure 1e). It is worth noting that various carriers composed of different materials like silica,[41] liposomes,[42] as well as rare earth,[43] and plasmonic NPs[44] were employed for external triggering to release bioactive molecules upon laser irradiation. However, polymer capsules have an obvious advantage over reported delivery

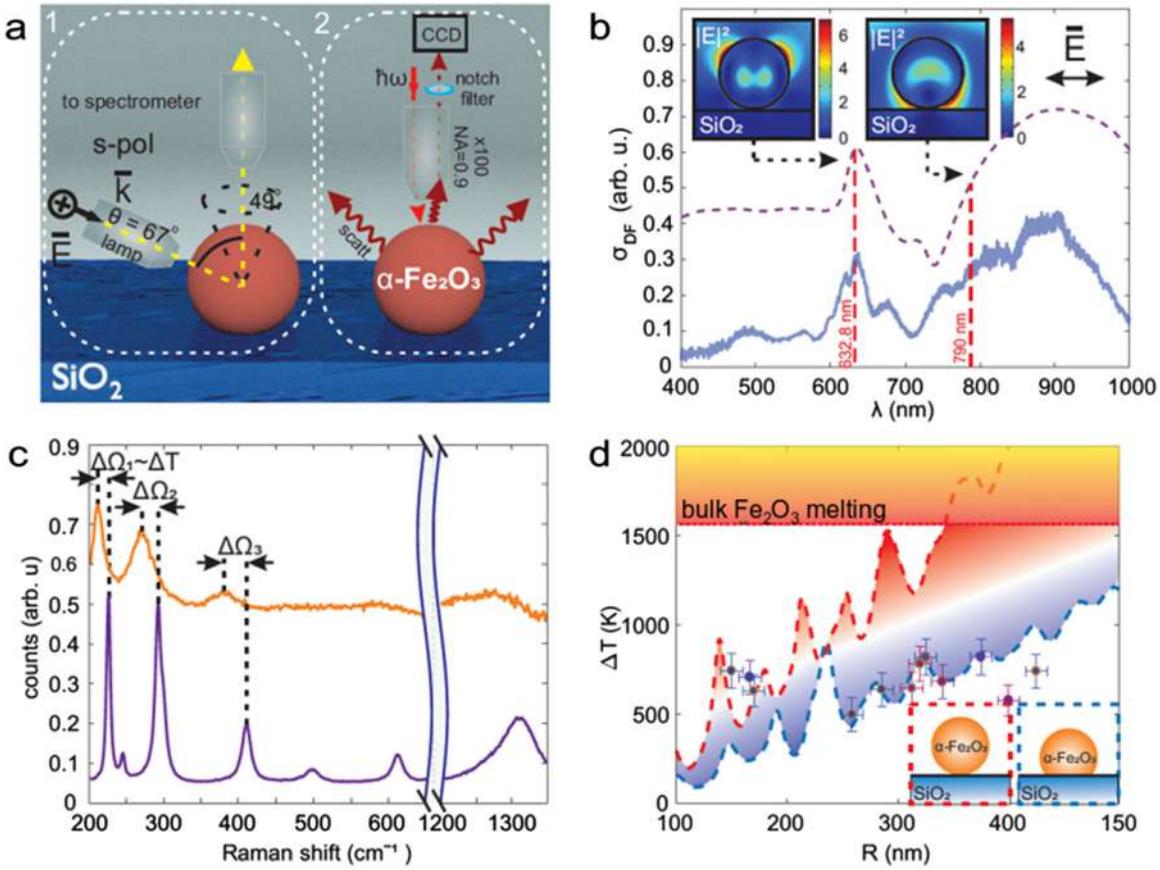

Figure 4. Optical heating of α-Fe_2O_3 NPs. a) Schematic of (1) dark-field (DF) elastic scattering spectroscopy and (2) Stokes-Raman spectroscopy experimental setups. b) Dark-field scattering spectra of a single α-Fe_2O_3 NP (radius R = 170 nm): experimental (solid blue) and numerically calculated (dashed purple). Insets depict calculated electric field distribution at corresponding wavelengths (632.8 nm and 790 nm) corresponding to the wavelengths of laser sources for the optical heating experiments. c) Stokes range of Raman scattering from single the α-Fe_2O_3 NP from (b) at two intensities 0.6 mW/μm^2 ("cold regime", purple line) and 2.4 mW/μm^2 ("hot regime", orange line). d) Experimental (dots) and theoretical (dashed lines) dependencies of optical heating of a single α-Fe_2O_3 NP upon irradiation by CW-laser with intensity 2.4 mW/μm^2 at wavelength 632.8 nm. Blue dashed and red dashed lines correspond to theoretical calculations with different thermal contact areas between the nanoparticle and SiO_2 substrate, as shown in the insets, where a nanosphere is dipped by R/2.5 and 0 nm into the substrate, respectively).

systems, such as increased drug-loading capacity, protective features of capsule wall, low cytotoxicity, high stability in the biological fluids, and efficient uptake by various cell types.[16,45] Polymer capsules modified with α-Fe_2O_3 NPs were prepared with layer-by-layer method.[16,46] The size range of synthesized capsules was around 4.38 – 5.21 μm, as determined by SEM and confocal laser scanning microscopy (CLSM) analysis (inset of **Figure 5a**; Figure S8a,b, Supporting Information). It can be seen that α-Fe_2O_3 NPs were not aggregated after attachment to the capsules wall (Figure S8, Supporting Information).

CLSM was used to verify the loading with dextran conjugated with AlexaFluor 647 (AF647) into the cavity of the capsules (Figure S8b, Supporting Information). SEM images demonstrated successful dissolution of $CaCO_3$ core-template, since the polymer capsules were in collapsed form under vacuum (Figure S8a, Supporting Information). The attachment of α-Fe_2O_3 NPs onto the capsules wall (spots onto the capsules wall) can be clearly seen in SEM, dark field (DF) and CLSM images highlighted with the white arrows (Figure S8a–c, Supporting Information). The statistical data for the number of attached α-Fe_2O_3 NPs onto the capsules wall are shown in Figure 5a. Successful loading of commercially available antitumor drug VCR into the capsules cavity could be detected with indirect method via measuring absorption spectra of the drug. According to the measured calibration curve shown in Figure S4, Supporting Information and measured supernatant after the formation of the $CaCO_3$ core-particles, amount of encapsulated VCR was 0.65×10^{-12} g/cap. It was assumed that after the core dissolution, the amount of VCR, which diffused through the capsule wall, is negligibly low.

In order to determine the temperature of the capsules rupture upon laser illumination, we employed the developed Raman nanothermometry with the resonant α-Fe_2O_3 NPs incorporated into the capsule walls. We measured Raman spectra of different capsules up to the signal disappearance as an indicator of the capsule's destruction. According to the measurements from a set of capsules with incorporated NPs placed as a droplet between two cover glasses, the mean temperature of their rupture is around 170 °C (Figure 5b). The fact of capsule damage was confirmed by bright-field optical microscopy (Figure 5c). The average

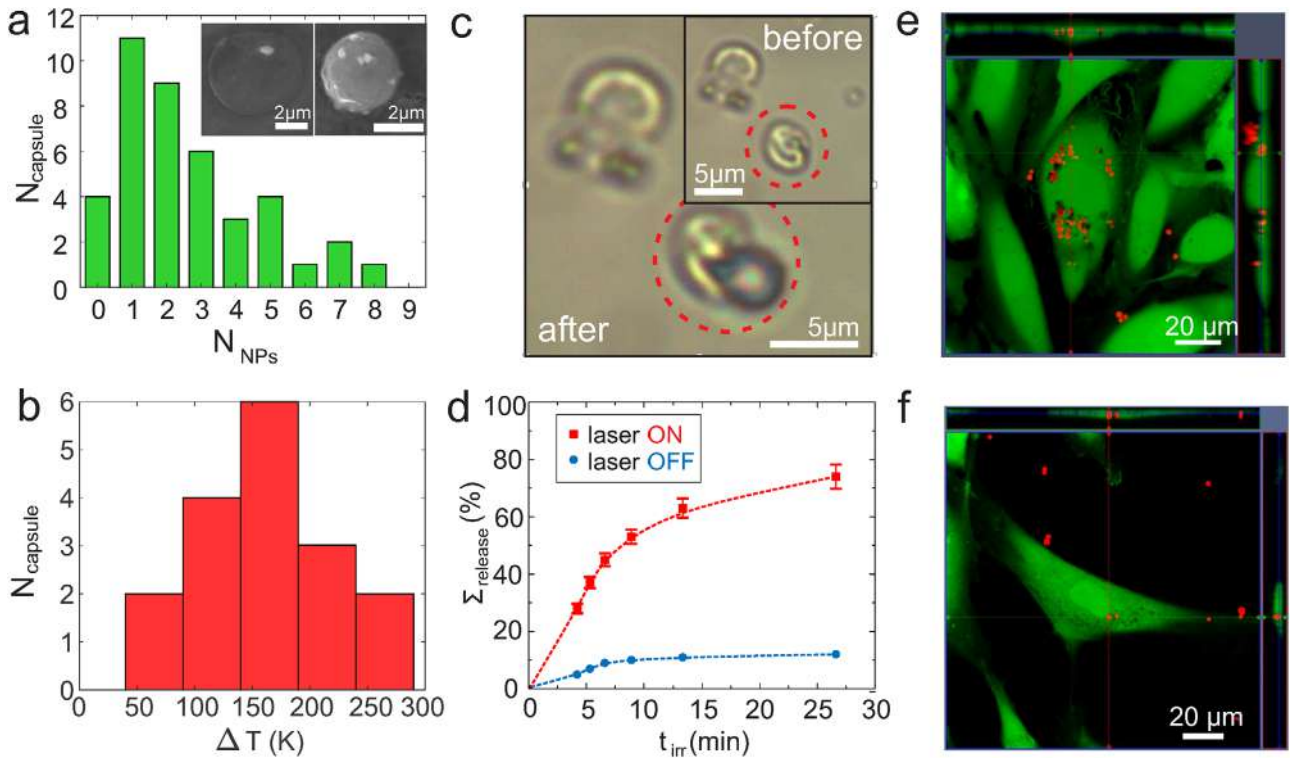

Figure 5. **α-Fe_2O_3 NPs in polymer capsule**. a) Number of α-Fe_2O_3 NPs embedded into capsules walls according to SEM images. Inset: SEM images of fabricated capsule with embedded α-Fe_2O_3 NPs into walls. Scale bar is 2 μm. b) Optical thermal destruction temperature distribution according to Raman experiments. Experiments were performed on empty capsules. c) Bright field images of capsule before (inset) and after laser irradiation. d) Percentage of released antitumor drug VCR from polymer capsules irradiated during different time periods (red curve) and without irradiation (blue curve). e) Orthogonal view from different planes (x/y, x/z or y/z) of the confocal microscope images used to analyze the particle uptake. Example corresponds to hMSCs with internalized capsules. Cells were staied with calcein AM (shown in green) and capsules were labeled with AF647 (shown in red). f) Orthogonal view from different planes (x/y, x/z or y/z) of the CLSM images used to analyze the capsules uptake. Example corresponds to CCs with internalized capsules. Cells were tagged with calcein AM (shown in green) and capsules were labelled with AF647 (shown in red).

Table 1. Comparison of the proposed resonant α-Fe_2O_3 NPs with previously published design for enhanced optical heating and simultaneous nanothermometry.

Approach	Capsule damage intensity, wavelength	Thermometry method	Temperature resolution	Ref
Gold NPs with CNT	9.6×10^4 W cm^{-2}, λ=532 nm	Raman: Stokes/Anti-Stokes ratio	5–40 K	[19]
α-Fe_2O_3 NPs	$4.0\pm1.0\times10^4$ W cm^{-2}, λ=633 nm	Raman: Stokes spectral shift	40 K	This work

intensity of He–Ne laser radiation (λ=632.8 nm) required to achieve this threshold temperature is around 4×10^4 W cm^{-2}. The value of temperature is comparable with that reported elsewhere,[19] while the applied intensity is more than two times lower, because of high efficiency of light-to-heat conversion of α-Fe_2O_3 NPs, as shown in Figure 2. It is worth noting that efficiency of drug delivery using capsules might be influenced by the number of embedded NPs into the capsule wall owing to higher probability of capsule rupture upon laser irradiation. The comparison of main characteristics of the proposed method with published before is given in **Table 1**. To confirm that permeability of polymer capsules changes after laser irradiation and delivered cargo can be successfully released, polymer capsules modified with α-Fe_2O_3 NPs were loaded with commercially available antitumor drug VCR and the defined area containing capsules was irradiated with near infrared laser for different periods of time. As it can be seen in Figure 5d, with the increasing time of irradiation within the area containing capsules, the amount of released drug increases. However, the capsules that were not irradiated also showed slight drug release, which can be explained by leakage of the cargo through the porous capsules walls.

The obtained capsule heating temperature (170 °C) is sufficient to change the permeability of polymer capsules, since the glass transition temperature of PAH is around 85 °C[47] and PSS is around 152 °C.[48] The photodecomposition of polymer capsules can lead to the release of loaded molecules into the surroundings. In comparison to the previous work,[19] to achieve temperature 170 °C less laser power density is required

($4.0\pm1.0\times10^4$ W cm^{-2}), which is in favor of the biomedical laser application, since such laser power densities do not induce phototoxicity of cells. Indeed, no phototoxicity was observed even at intensity 3.8×10^5 W cm^{-2} as shown in ref. [49]. Moreover, according to Equation (S30), Supporting Information, at such high temperature, biological objects decay by more than 10 times on a scale of several microns around the locally heated NP, being safe for the irradiated living cell containing an internalized capsule modified with the α-Fe_2O_3 NPs.

Cell uptake and association of polymer capsules modified with α-Fe_2O_3 NPs. It is worth mentioning that cell experiments were performed on relevant cell models: i) clear cell renal cell carcinoma cells (CCs), and ii) human mesenchymal stem cells (hMSCs), which were derived from patients who signed a voluntary consent. Numerous studies suggest that cell lines poorly represent the diversity, heterogeneity, and drug-resistant tumors occurring in patients.[50] The derivation and short–term culture of primary cells from solid tumors have, thus, gained significant importance in personalized cancer therapy. CCs are sensitive to VCR at high dosages but not sensitive to the concentrations of this drug used in clinics.[51] hMSCs were used in this study as a model of healthy cells.

In order to verify whether micrometric polymer capsules modified with α-Fe_2O_3 NPs can be internalized with CCs and hMSCs, CLSM measurements were performed. For this, after incubation with different amount of polymer capsules loaded with AF647, cells were stained with calcein AM and the co-localization of the red fluorescently labeled capsules within the cellular compartments was visualized with *z*-stack images as shown in Figure 5e,f. An indicator for intracellular localization of capsules was red fluorescence signal coming from AF647 labeled capsules surrounded with green fluorescence signal coming from stained living cell with calcein AM. Figure S16, Supporting Information, shows 3D reconstruction of cells incubated with capsules. These results are in agreement with previous studies, where it was shown that even micrometric sized non-targeted polymer capsules can be efficiently internalized with stem cells[18] and carcinoma cells.[16] Note that multiple endocytotic pathways are responsible for micrometric capsules internalization.[52]

In order to quantify the association of AF647-labeled capsules at different capsule concentrations with CCs and hMSCs, fluorescence flow cytometry was used. Here, the amount of red fluorescence originating from each analyzed cell was derived and quantified to reveal the relative amount of capsules associated with cells. It is worth mentioning that apart from autofluorescence, cells do not contribute to the red fluorescence signal (Figure S14, Supporting Information). According to the obtained data, it is clearly seen that the amount of capsules associated with cells increases with the number of added capsules per cell. This is valid for both the cell lines. However, it is also seen that the capsules were associated with CCs in a higher rate than with hMSCs (Figure S15, Supporting Information). These results are in agreement with previous works.[53] As it has been discussed above, multiple internalization pathways are involved in micrometric sized capsules internalization. Internalization of capsules depends on the metabolism of the cells, which defines their ability to internalize the capsules. Metabolism of carcinoma cells is known to be enhanced[54] and distorted, which explains the higher uptake rate of capsules by CCs than by hMSCs.

In vitro laser-triggered release of antitumor drug vincristine (VCR). To demonstrate remote photoinduced activation of drug, α-Fe_2O_3 NPs modified polymer capsules loaded with VCR were added to the CCs and hMSCs at different amounts. Next day, cells were washed three times with cell culture medium in order to remove residual capsules, and then irradiated with NIR (λ=790 nm) in the defined area (**Figure 6**; Figure S11p). NIR laser irradiation was used for the experiments with cells, since this wavelength lies in the "tissue window," and it is optimal for penetration of light into tissue.[55] Similar wavelengths are often used in the biology and medicine for therapy.[56]

During the NIR laser irradiation at "CW-like" regime (repetition rate 80 MHz) with an average power of 250 mW, laser beam randomly hits the capsules inside the scanning area (for details, see Section S3h, Supporting Information). After the irradiation of the capsules with the NIR light, the α-Fe_2O_3 NPs exhibit strong absorption supported by Mie modes, which results in light-to-heat energy conversion followed by the NPs temperature increase and, subsequently, in the rupture of capsules, as shown in Figure 6a–c. In other words, the interaction between the laser beam and α-Fe_2O_3 NPs embedded into the capsules wall leads to the thermally induced deformation/disintegration of the polymer capsules with the change in their permeability, as observed in Figure 5c. It worth noting that the heating of α-Fe_2O_3 NPs by a single femtosecond laser pulse with the used energy (3 nJ) is not enough for the capsules rupture, indicating multipulse character of the photoinduced drug release, as also confirmed by calculations in Figure S2, Supporting Information.

In the control experiments, the cells without capsules were irradiated with NIR laser at the same conditions, as well as the cells without and with capsules (added at different amounts) were not irradiated with NIR laser. After irradiation, LIVE/DEAD viability assay was performed, where the cells alive were stained in green and nuclei of dead cells were stained in red. According to the obtained data, the used power density of laser irradiation was not toxic for CCs and hMSCs (Figure 6a,b). As expected, laser irradiation of CCs with internalized/associated capsules resulted in higher toxicity, due to the release of antitumor drug VCR in intra- and extracellular environment. As it can be seen in Figure 6d, this toxicity of CCs is dependent on the amount of added capsules per cell. The possible explanation for this can be that the probability to hit the capsule added at the rate of 50 capsules per cell is higher and, thus, higher amounts of drugs were released from the capsules associated with cells, which resulted in higher toxicity. This assumption is confirmed by the performed release study where different amounts of VCR loaded capsules modified with iron oxide NPs were irradiated under the same conditions but without cells Figure S13, Supporting Information. The obtained results demonstrate that higher amount of added capsules results in a higher rate of released drugs after laser irradiation keeping the irradiation time constant. Interestingly, hMSCs showed significantly higher survival rate compared to CCs at the same added amount of capsules. The reason for this could be the higher uptake of tumor cells, what results in higher amount of antitumor drug inside cells. Moreover, hMSCs are resistant to the number of antitumor drugs, what can be a reason of higher survival rate of hMSCs compared to CCs.[57]

Capsules added to both the cell models, which were not irradiated with NIR laser, were slightly toxic at higher concentrations

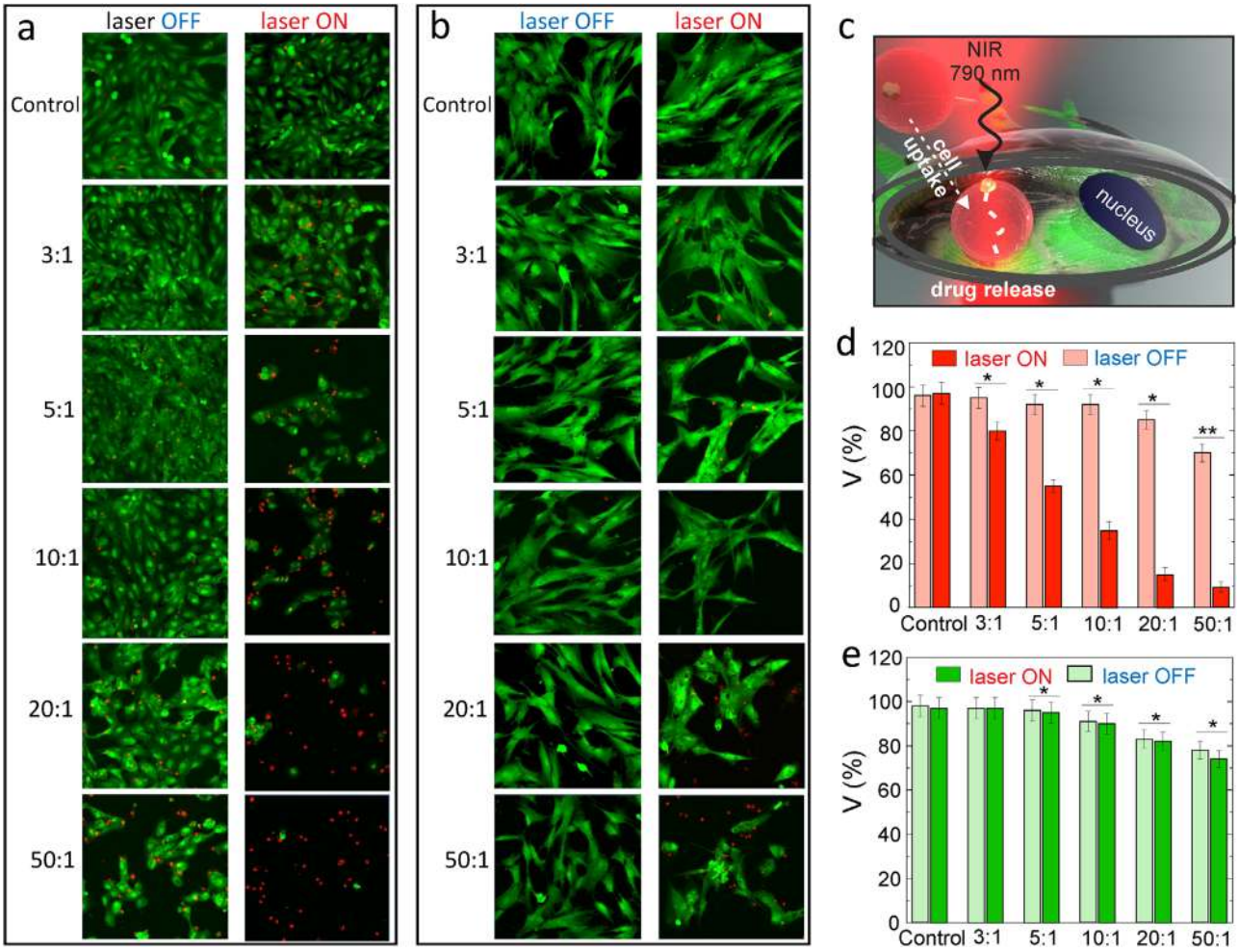

Figure 6. α-Fe_2O_3 **NPs in capsules for remote drug delivery upon laser irradiation**. a) CLSM images of CCs incubated with different amounts of polymer capsules modified withα-Fe_2O_3 NPs and loaded with antitumor drug VCR for 24 h. CCs were not irradiated with NIR laser (right column) and CCs were irradiated with laser (left column). Living cells were stained with calcein AM (green) and dead cells with propidium iodide (red). b) CLSM images of hMSCs incubated with different amounts of polymer capsules modified with α-Fe_2O_3 NPs and loaded with antitumor drug VCR for 24 h. hMSCs were not irradiated with NIR laser (right column) and hMSCs were irradiated with laser (left column). Living cells were stained with calcein AM (green) and dead cells with propidium iodide (red). The scale bar for (a,b) is 50 μm. c) Schematic illustration of experimental setup: cross-section of a cell with internalized capsule inside. Capsule is irradiated with NIR 790 nm laser. d) CCs viability after incubation with polymer capsules modified with α-Fe_2O_3 NPs and loaded with antitumor drug VCR for 24 h before (red) and after (pink) irradiation with NIR laser. e) hMSCs viability after incubation with polymer capsules modified with α-Fe_2O_3 NPs and loaded with antitumor drug VCR for 24 h before (green) and after (bright green) irradiation with NIR laser. The results are presented as the average value ± standard deviation (* represents $p < 0.05$ and ** represents $p < 0.005$).

(86% for 20 caps/cell, 70% for 50 caps/cell for CCs and 84% for 20 caps/cell, 78% for 50 caps/cell for hMSCs). This can be explained by leakage of drugs through the capsules wall during the internalization process. Indeed, during the internalization process mechanical deformation of polymer capsules can occur, which can result in the leakage of drug loaded into the capsules.[14] According to the recent study, mechanical forces can vary between cell types, and it was shown that capsules internalized within carcinoma cells are exposed to higher mechanical forces during the internalization process in carcinoma cells than in other tested cell types resulting in a higher rate of capsule degradation,[58] which can lead to a higher drug release rate inside cells. Moreover, it has been shown that capsules added at the rate of more than 20 capsules per cell are toxic[59] to the cells resulting in reduced cell density in Figure 6b. Thereby, the revealed data confirm that α-Fe_2O_3 NPs can be effectively used as heat mediators for remote activation of drugs inside cells.

3. Conclusion

To summarize, we have proposed a novel "all-in-one" concept for controllable drug release in living cells based on nonplasmonic optically resonant nanoparticles which allowed for lowering the drug release irradiation threshold and local thermometry. It has been proven both theoretically and experimentally that α-Fe_2O_3 NPs larger than 100 nm have several advantages in terms of light-to-heat energy conversion comparing to

conventional materials, such as noble metals and silicon: i) α-Fe_2O_3 NPs demonstrate broader and stronger electromagnetic radiation absorption in the visible and near-IR ranges; ii) do not require strict fulfilling of Mie-resonant conditions to achieve similar heating temperatures; iii) support number of thermally sensitive Raman lines in the range of 200–1400 cm^{-1}, which is more convenient for nanothermometry and might be useful for tracing additional molecular events in real time. Additionally, the developed α-Fe_2O_3 NPs make it possible to avoid complicated functionalization steps with plasmonic NPs enhancing optical absorption.[60] The simplicity of α-Fe_2O_3 NPs synthesis and its biocompatibility make this material suitable for biomedical applications. Taken together, we believe that such iron oxide based nanostructures pave the way towards optically controlled noninvasive intracellular drug release.

Supporting Information

Supporting Information is available from the Wiley Online Library or from the author.

Acknowledgements

Part of this work related to the synthesis of nano- and micromaterials, as well as their characterization was supported by the Russian Science Foundation, grant No. 19-75-00039 (M.V.Z.). The biological experiments concerning cells interaction with capsules were supported by the Russian Science Foundation, No. 19-75-10010 (A.S.T.). The part of this work related to optical experiments and their simulations were supported by the Russian Science Foundation, grant No. 18-79-00338 (G.P.Z.). Visualization of real-time capsules rupture was done with support of National Key Research and Development Program of China (2017YFE0100200). G.Z. thanks Dr. Soslan Khubezhov for XPS experiments, Dr. Mikhail Zhukov and Filipp Komissarenko for SEM investigations and Dr. Mihail Petrov for valuable discussion. A.N. acknowledges the Government of the Russian Federation through the ITMO Fellowship and Professorship program. A.N. and J.G. are grateful to the French Ministry of Higher Education and Research for support through "Programme Hubert Curien–Kolmogorov".

Conflict of Interest

The authors declare no conflict of interest.

Keywords

dielectric nanophotonics, drug delivery, Mie-resonances, optical heating

Received: March 7, 2019
Revised: December 11, 2019
Published online:

[1] I. Staude, J. Schilling, *Nat. Photonics* **2017**, *11*, 274.
[2] A. I. Kuznetsov, A. E. Miroshnichenko, M. L. Brongersma, Y. S. Kivshar, B. Luk'yanchuk, *Science* **2016**, *354*, aag2472.
[3] A. B. Evlyukhin, S. M. Novikov, U. Zywietz, R. L. Eriksen, C. Reinhardt, S. I. Bozhevolnyi, B. N. Chichkov, *Nano Lett.* **2012**, *12*, 3749.
[4] A. Tittl, A. Leitis, M. Liu, F. Yesilkoy, D. Y. Choi, D. N. Neshev, Y. S. Kivshar, H. Altug, *Science* **2018**, *360*, 1105.
[5] G. Grinblat, Y. Li, M. P. Nielsen, R. F. Oulton, S. A. Maier, *Nano Lett.* **2016**, *16*, 4635.
[6] S. Liu, M. B. Sinclair, S. Saravi, G. A. Keeler, Y. Yang, J. Reno, G. M. Peake, F. Setzpfandt, I. Staude, T. Pertsch, *Nano Lett.* **2016**, *16*, 5426.
[7] J. Cambiasso, G. Grinblat, Y. Li, A. Rakovich, E. Cortés, S. A. Maier, *Nano Lett.* **2017**, *17*, 1219.
[8] F. Timpu, A. Sergeyev, N. R. Hendricks, R. Grange, *ACS Photonics* **2016**, *4*, 76.
[9] R. E. Noskov, I. I. Shishkin, H. Barhom, P. Ginzburg, *Nanoscale* **2018**, *10*, 21031.
[10] E. Tiguntseva, G. P. Zograf, F. E. Komissarenko, D. A. Zuev, A. A. Zakhidov, S. V. Makarov, Y. S. Kivshar, *Nano Lett.* **2018**, *18*, 1185.
[11] G. P. Zograf, M. I. Petrov, D. A. Zuev, P. A. Dmitriev, V. A. Milichko, S. V. Makarov, P. A. Belov, *Nano Lett.* **2017**, *17*, 2945.
[12] P. A. Dmitriev, D. G. Baranov, V. A. Milichko, S. V. Makarov, I. S. Mukhin, A. K. Samusev, A. E. Krasnok, P. A. Belov, Y. S. Kivshar, *Nanoscale* **2016**, *8*, 9721.
[13] V. A. Milichko, D. A. Zuev, D. G. Baranov, G. P. Zograf, K. Volodina, A. A. Krasilin, I. S. Mukhin, P. A. Dmitriev, V. V. Vinogradov, *Laser Photonics Rev.* **2018**, *12*, 1700227.
[14] K. Kantner, J. Rejman, K. V. Kraft, M. G. Soliman, M. V. Zyuzin, A. Escudero, P. del Pino, W. J. Parak, *Chem. - Eur. J.* **2018**, *24*, 2098.
[15] A. Ott, X. Yu, R. Hartmann, J. Rejman, A. Schütz, M. Ochs, W. J. Parak, S. Carregal-Romero, *Chem. Mater.* **2015**, *27*, 1929.
[16] M. V. Zyuzin, P. Díez, M. Goldsmith, S. Carregal-Romero, C. Teodosio, J. Rejman, N. Feliu, A. Escudero, M. J. Almendral, U. Linne, W. Parak, *Bioconjugate Chem.* **2017**, *28*, 556.
[17] C. S. Karamitros, A. M. Yashchenok, H. Möhwald, A. G. Skirtach, M. Konrad, *Biomacromolecules* **2013**, *14*, 4398.
[18] A. S. Timin, A. R. Muslimov, M. V. Zyuzin, O. O. Peltek, T. E. Karpov, I. S. Sergeev, A. I. Dotsenko, A. A. Goncharenko, N. D. Yolshin, A. Sinelnik, *ACS Appl. Mater. Interfaces* **2018**, *10*, 34849.
[19] A. Yashchenok, A. Masic, D. Gorin, O. Inozemtseva, B. S. Shim, N. Kotov, A. Skirtach, H. Möhwald, *Small* **2015**, *11*, 1320.
[20] S. Laurent, D. Forge, M. Port, A. Roch, C. Robic, L. Vander Elst, R. N. Muller, *Chem. Rev.* **2008**, *108*, 2064.
[21] A. A. Akl, *Appl. Surf. Sci.* **2004**, *233*, 307.
[22] J. E. Maslar, W. S. Hurst, W. Bowers, J. H. Hendricks, M. Aquino, *J. Electrochem. Soc.* **2000**, *147*, 2532.
[23] A. G. Skirtach, C. Dejugnat, D. Braun, A. S. Susha, A. L. Rogach, W. J. Parak, H. Möhwald, G. B. Sukhorukov, *Nano Lett.* **2005**, *5*, 1371.
[24] G. Baffou, R. Quidant, F. J. García de Abajo, *ACS Nano* **2010**, *4*, 709.
[25] C. F. Bohren, D. R. Huffman, *Absorption and Scattering of Light by Small Particles*, John Wiley & Sons, Hoboken, NJ, USA**2008**.
[26] G. Baffou, R. Quidant, *Laser Photonics Rev.* **2013**, *7*, 171.
[27] P. B. Johnson, R. W. Christy, *Phys. Rev. B* **1972**, *6*, 4370.
[28] D. E. Aspnes, A. Studna, *Phys. Rev. B* **1983**, *27*, 985.
[29] M. R. Querry, *Optical Constants*, Technical Report, Missouri University, Kansas City **1985**.
[30] J. G. Speight, *Lange's Handbook of Chemistry*, McGraw-Hill, New York **2005**.
[31] M. Balkanski, R. Wallis, E. Haro, *Phys. Rev. B* **1983**, *28*, 1928.
[32] D. Rout, K. S. Moon, S. J. L. Kang, *J. Raman Spectrosc.* **2009**, *40*, 618.
[33] S. Mitra, S. Das, K. Mandal, S. Chaudhuri, *Nanotechnology* **2007**, *18*, 275608.
[34] S. Y. Chen, A. Gloter, A. Zobelli, L. Wang, C. H. Chen, C. Colliex, *Phys. Rev. B* **2009**, *79*, 104103.
[35] P. Ewels, T. Sikora, V. Serin, C. P. Ewels, L. Lajaunie, *Microsc. Microanal.* **2016**, *22*, 717.
[36] B. Zhao, Y. Wang, H. Guo, J. Wang, Y. He, Z. Jiao, M. Wu, *Mater. Sci.-Pol.* **2007**, *25*, 1143.
[37] K. Dick, T. Dhanasekaran, Z. Zhang, D. Meisel, *J. Am. Chem. Soc.* **2002**, *124*, 2312.

[38] R. Hull, *Properties of Crystalline Silicon*, INSPEC, London**1999**.
[39] I. Chamritski, G. Burns, *J. Phys. Chem. B* **2005**, *109*, 4965.
[40] M. Borselli, T. J. Johnson, O. Painter, *Opt. Express* **2005**, *13*, 1515.
[41] J. Liu, C. Detrembleur, M. C. De Pauw-Gillet, S. Mornet, C. Jérôme, E. Duguet, *Small* **2015**, *11*, 2323.
[42] D. Luo, K. A. Carter, A. Razi, J. Geng, S. Shao, D. Giraldo, U. Sunar, J. Ortega, J. F. Lovell, *Biomaterials* **2016**, *75*, 193.
[43] A. Bagheri, H. Arandiyan, C. Boyer, M. Lim, *Adv. Sci.* **2016**, *3*, 1500437.
[44] A. M. Goodman, N. J. Hogan, S. Gottheim, C. Li, S. E. Clare, N. J. Halas, *ACS Nano* **2016**, *11*, 171.
[45] A. S. Timin, D. J. Gould, G. B. Sukhorukov, *Expert Opin. Drug Delivery* **2017**, *4*, 583.
[46] S. Z. Hussain, M. V. Zyuzin, I. Hussain, W. J. Parak, S. Carregal-Romero, *RSC Adv.* **2016**, *6*, 81569.
[47] H. C. Zhao, X. T. Wu, W. W. Tian, S. T. Ren, *Adv. Mater. Res.* **2011**, *150*, 1480.
[48] Y. Niidome, A. Hori, T. Sato, S. Yamada, *Chem. Lett.* **2000**, *29*, 310.
[49] S. Carregal-Romero, M. Ochs, P. Rivera-Gil, C. Ganas, A. M. Pavlov, G. B. Sukhorukov, W. J. Parak, *J. Controlled Release* **2012**, *159*, 120.
[50] B. B. S. Zhou, H. Zhang, M. Damelin, K. G. Geles, J. C. Grindley, P. B. Dirks, *Nat. Rev. Drug Discovery* **2009**, *8*, 806.
[51] J. Hartmann, C. Bokemeyer, *Anticancer Res.* **1999**, *19*, 1541.
[52] L. Kastl, D. Sasse, V. Wulf, R. Hartmann, J. Mircheski, C. Ranke, S. Carregal-Romero, J. A. Martínez-López, R. Fernández-Chacón, W. J. Parak, *ACS Nano* **2013**, *7*, 6605.
[53] C. K. Huang, C. L. Lo, H. H. Chen, G. H. Hsiue, *Adv. Funct. Mater.* **2007**, *17*, 2291.
[54] Y. Zhang, C. Y. Ang, M. Li, S. Y. Tan, Q. Qu, Z. Luo, Y. Zhao, *ACS Appl. Mater. Interfaces* **2015**, *7*, 18179.
[55] J. F. Hainfeld, M. J. O'Connor, P. Lin, L. Qian, D. N. Slatkin, H. M. Smilowitz, *PloS One* **2014**, *9*, e88414.
[56] S. He, J. Song, J. Qu, Z. Cheng, *Chem. Soc. Rev.* **2018**, *47*, 4258.
[57] B. C. Bellagamba, B. R. R. d. Abreu, I. Grivicich, C. F. Markarian, M. Camassola, N. B. Nardi, R. R. Dihl, *Genet. Mol. Biol.* **2016**, *39*, 129.
[58] X. Chen, J. Cui, H. Sun, M. Müllner, Y. Yan, K. F. Noi, Y. Ping, F. Caruso, *Nanoscale* **2016**, *8*, 11924.
[59] K. V. Lepik, A. R. Muslimov, A. S. Timin, V. S. Sergeev, D. S. Romanyuk, I. S. Moiseev, E. V. Popova, I. L. Radchenko, A. D. Vilesov, O. V. Galibin, *Adv. Healthcare Mater.* **2016**, *5*, 3182.
[60] G. A. Sotiriou, F. Starsich, A. Dasargyri, M. C. Wurnig, F. Krumeich, A. Boss, J. C. Leroux, S. E. Pratsinis, *Adv. Funct. Mater.* **2014**, *24*, 2818.

ISSN 0021-3640, JETP Letters, 2018, Vol. 107, No. 11, pp. 699–704. © Pleiades Publishing, Inc., 2018.
Original Russian Text © G.P. Zograf, Y.F. Yu, K.V. Baryshnikova, A.I. Kuznetsov, S.V. Makarov, 2018, published in Pis'ma v Zhurnal Eksperimental'noi i Teoreticheskoi Fizjki, 2018, Vol. 107, No. 11, pp. 732–738.

CONDENSED MATTER

Local Crystallization of a Resonant Amorphous Silicon Nanoparticle for the Implementation of Optical Nanothermometry

G. P. Zograf[a], Y. F. Yu[b], K. V. Baryshnikova[a], A. I. Kuznetsov[b, c], and S. V. Makarov[a, *]

[a] *National Research University of Information Technologies, Mechanics, and Optics, St. Petersburg, 197101 Russia*
[b] *Data Storage Institute, A*STAR (Agency for Science, Technology and Research), Singapore, 138634 Singapore*
[c] *Institute of Materials Research and Engineering, A*STAR (Agency for Science, Technology and Research), Singapore, 138634 Singapore*
**e-mail: s.makarov@metalab.ifmo.ru*

Received April 19, 2018

Local optical heating and Raman nanothermometry based on resonant silicon particles provide a new promising platform for a number of key nanophotonics applications associated with thermally induced processes at the nano- and microscale. In this work, the crystallization of amorphous silicon nanodisks with optical resonances caused by local optical heating has been studied. The crystallization process is controlled by Raman microspectroscopy. The crystallization temperature of a single nanodisk of about 900 K has been determined under the action of a strongly focused cw laser beam. As a result, an annealed resonant silicon nanoparticle has allowed controlled and reversible heating in the temperature range of 300–1000 K with the possibility of mapping the heating region with submicron spatial resolution.

DOI: 10.1134/S0021364018110140

1. INTRODUCTION

In recent years, a new field of nanophotonics associated with optical resonances in dielectric particles with a high refractive index [1] has been successfully applied to light control problems on a nanoscale [2–4], ultrafast modulation of an optical signal [5–7], and optical harmonic generation [8, 9], as well as for the creation of ultrathin optical holograms [10] and many other applications [11–13]. Indeed, owing to the presence of a magnetic response, low dissipative losses in the infrared range, and the possibility of a wide tuning of all excited resonances, silicon particles of a simple shape (e.g., spherical particles) [14, 15] have a number of advantages in comparison with analogs based on resonant metallic nanostructures [16]. Another notable feature of silicon is the presence of low but gradually increasing optical losses in the visible range, which makes it possible, on one hand, to excite high-Q Mie resonances [17, 18] and, on the other hand, to ensure effective absorption of light by coordinating radiative and nonradiative losses in the nanoparticle [19]. This allows efficient optical heating of silicon nanoparticles with the possibility of the simultaneous measurement of the local temperature using temperature-sensitive phonon modes [20]. This concept of the use of crystalline silicon nanoparticles as a nanosized source of heat, providing the possibility of direct nanothermometry, was successfully applied for the local diagnostics of thermally induced processes [21], as well as for high-precision laser nanofabrication [22].

The main condition for nanothermometry based on the thermosensitive Raman response of silicon nanoparticles is the need to use a crystalline phase, since the amorphous one has an extremely unpronounced phonon spectrum unusable for thermometry. This imposes serious limitations on the methods of manufacturing such nanostructures, since a standard and relatively inexpensive technique for manufacturing amorphous nanostructures from hydrogenated silicon (α-Si:H) becomes unsuitable, and the production of crystalline nanoparticles based on the "*silicon-on-insulator*" platform leads to an unwanted background Raman signal from the silicon substrate. The preparation of crystalline nanoparticles on sapphire (the "*silicon-on-sapphire*" technology) also has a number of shortcomings: high cost; a relatively high refractive index of sapphire ($n = 1.77$), which reduces the Q-factor of the silicon nanoparticle; and a high thermal conductivity of sapphire 40 times higher than that for glass, which hinders the localization of optical heating.

In this work, a new approach is developed to perform optical nanothermometry based on resonant silicon nanoparticles in the crystalline phase on a quartz substrate. This approach is based on the method of strong local optical heating up to the phase transition temperature, which is controlled in real time by

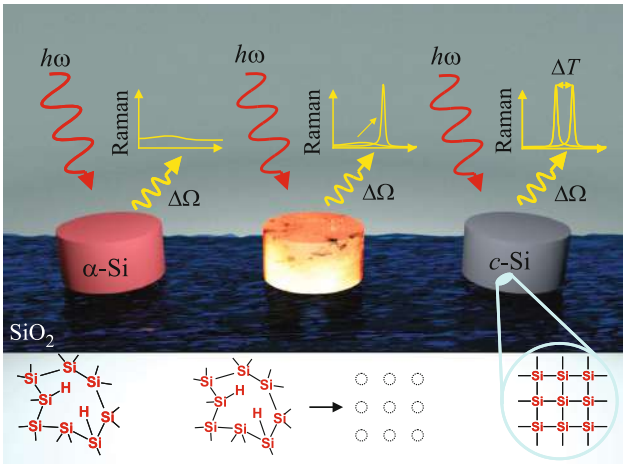

Fig. 1. (Color online) Schematic of controlled annealing of an amorphous disk irradiated by intense light by means of confocal Raman spectroscopy. The insets schematically show (left) the Raman spectrum of the initial amorphous nanodisk, (middle) the spectra "before" and "after" annealing of the nanodisk, and (right) the reversible Raman spectrum shift of the annealed nanodisk during its optical heating.

Raman microspectroscopy. This concept is schematically presented in Fig. 1.

2. RESULTS AND DISCUSSION

We study α-Si: H nanodisks on a quartz substrate. The amorphous nanodisks with diameters D = 300–450 nm and height h = 165 nm were prepared by nanolithographic techniques used earlier [23] (for a detailed description see Section 3). The insets of Figs. 2c and 4c show the images of the prepared single amorphous silicon nanodisks located on the quartz substrate. The images were obtained on a Carl Zeiss Neon 40 scanning electron microscope (SEM).

The choice of the material and sizes of nanodisks is due to the need to excite resonant optical modes in the visible spectral region for achieving the most efficient optical heating and thermometry. Figure 2a shows the numerical calculation of the extinction, scattering, and absorption cross sections for a single amorphous silicon nanodisk (with the dispersion of the permittivity of amorphous silicon obtained in ellipsometry experiments [23, 24]) with a height of 165 nm and a diameter of 330 nm on a glass substrate (see Section 3). It can be seen in Fig. 2c that this disk demonstrates resonance absorption at a wavelength near 632.8 nm corresponding to the wavelength of the HeNe pump laser in the Raman thermometry setup. Figure 2b makes it possible to estimate the contributions from each optical mode to the total scattering cross section [25]. As a result, the resonance state at a wavelength of 632.8 nm corresponds to the interference of two contributions, electric dipole (ED) and magnetic dipole (MD). This is confirmed by the distributions of the electric and magnetic fields depicted in Fig. 2d. It should be noted that, together with the resonance absorption, intense heating of the disk is possible. Indeed, as was shown in [26], the increase in the temperature of the nanoparticle is proportional to the power absorbed in it:

$$P_{\text{abs}} = \frac{1}{2}\text{Re}\int_V \mathbf{J}^*(\mathbf{r})\mathbf{E}(\mathbf{r})dV, \qquad (1)$$

where $\mathbf{J}(\mathbf{r})$ is the current density, $\mathbf{E}(\mathbf{r})$ is the electric field inside the material, and the integration is carried out over the volume of the nanoparticle V. It follows from this expression that the higher the electromagnetic field in the structure, the greater the energy absorbed. The heating itself is due to ohmic losses, which are determined by the electrical conductivity σ, since $\mathbf{J} = \sigma\mathbf{E}$. The imaginary part of the dielectric constant determines the conductivity as $\sigma = \epsilon_0\omega\text{Im}(\epsilon)$, where ϵ_0 and ω are the permittivity of free space and the frequency of the incident light, respectively.

Figure 3a shows the experimentally recorded crystallization process of a silicon nanodisk with a size of 330 nm under the effect of a HeNe laser with a working wavelength of 632.8 nm. First, Raman scattering was excited in the so-called "cold" mode in an amorphous disk at relatively low pump powers (0.06 MW/cm^2), in which the temperature of the nanodisk remained almost unchanged. The red curve corresponds to the unpronounced Raman scattering from amorphous silicon with a maximum at 480 cm^{-1}, which is well described in [27]. Then, a single disk was subjected to a more intense exposure of the HeNe laser (0.39 MW/cm^2), which initiated the crystallization process. It was observed experimentally that the spectral position of Raman scattering from a single nanodisk undergoing a phase transition corresponded to a temperature of about 600–800°C. Such temperatures fit the modern view on the crystallization process of amorphous silicon [28] and are comparable with those previously obtained with similar pumping powers but for spherical nanoparticles [19]. It is noteworthy that the resulting annealed resonant nanoparticle begins to exhibit a pronounced temperature-sensitive dependence of the phonon mode at 520 cm^{-1}, which is described by the expression

$$\Omega(T) = \Omega_0 + A\left(1 + \frac{2}{e^x - 1}\right) + B\left(1 + \frac{3}{e^y - 1} + \frac{3}{(e^y - 1)^2}\right), \qquad (2)$$

where Ω_0 = 528 cm^{-1}, A = –2.96 cm^{-1}, B = –0.174 cm^{-1}, $x = \hbar\Omega_0/2kT$, and $y = \hbar\Omega_0/3kT$ for crystalline silicon [20].

Figure 3b shows the temperature dependence of the spectral position of the Raman scattering signal for silicon obtained from Eq. (2) and allows one to

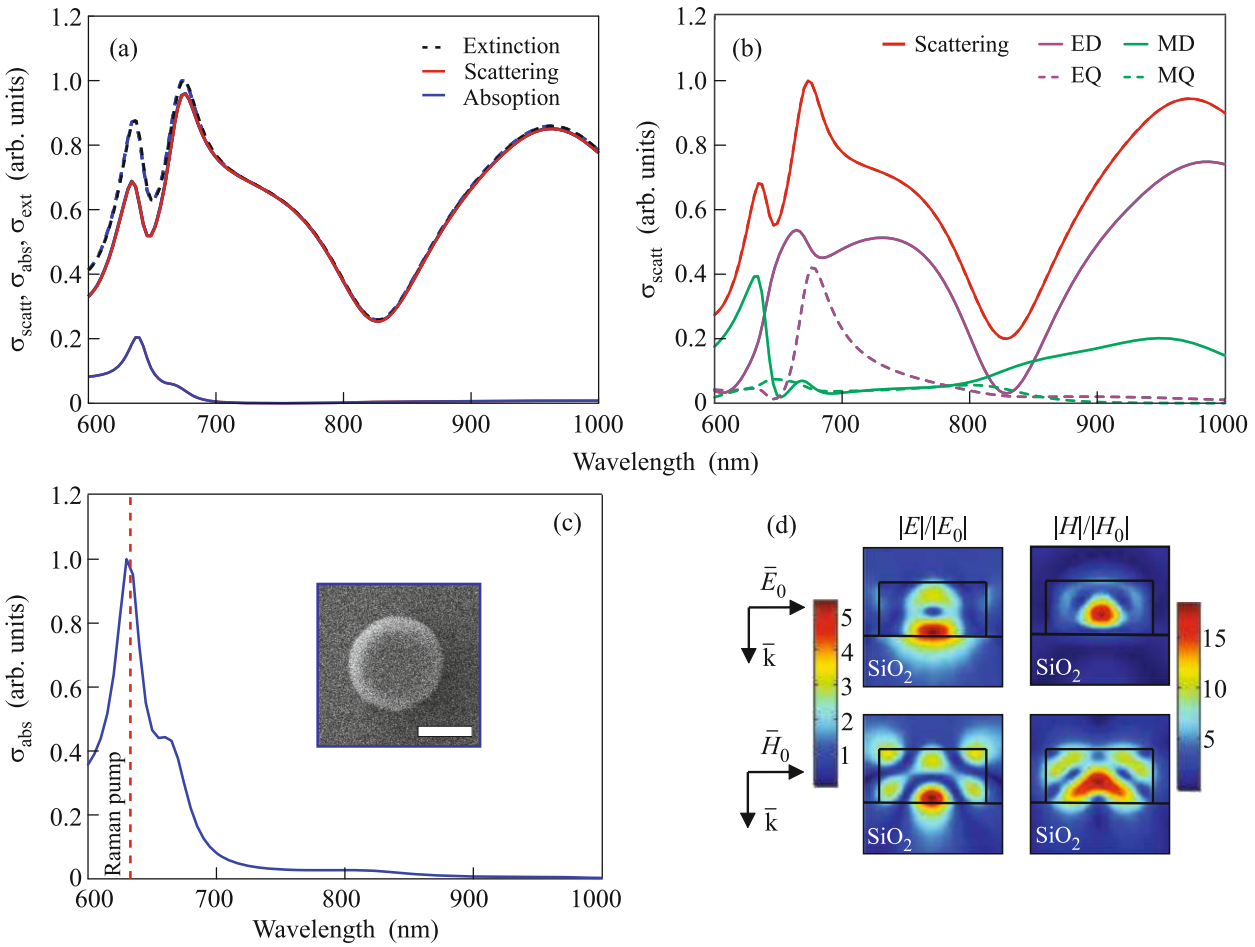

Fig. 2. (Color online) (a) Calculation of (black dashed line) extinction, (red line) scattering, and (blue line) absorption cross sections of a single silicon amorphous nanodisk 165 nm in height and 330 nm in diameter (see Section 3). (b) Decomposition of excited optical resonance modes in the scattering cross section of a single nanodisk [25]. (c) Absorption spectrum of a single amorphous disk with a diameter of 330 nm on a quartz substrate under normal irradiation by the excitation wave numerically calculated with the commercial COMSOL Multiphysics software package (see Section 3). The inset shows the SEM image of a single disk with a diameter of 330 nm on a quartz substrate (the scale corresponds to 200 nm). (d) Calculated distributions of the normalized electric and magnetic fields at the absorption resonance corresponding to a wavelength of 632.8 nm of the HeNe pump laser.

directly relate the Raman line shift to the temperature of the material. The experimental dependence of the Raman scattering signal for a single nanodisk at different values of the pump intensity is shown in Fig. 3c. The spectra obtained have the following features characteristic of polycrystalline silicon structures [28]: first, an asymmetric shape that is noticeably manifested at higher temperatures of the disk; second, the characteristic FWHMs of the Raman peaks exceed 10 cm^{-1} even at low intensities, while this value for monocrystalline silicon does not exceed 5 cm^{-1}.

Figure 3d shows a two-dimensional map of Raman thermometry and optical heating of a single annealed nanodisk with a size of 330 nm (for details of the experiment, see Section 3). The spectra obtained for each position are described by a single Lorentz contour. As a result, this approximation allows direct mapping of the local temperature distribution in the region of a silicon nanoparticle with a high spatial resolution, and the accuracy of the temperature measurement is determined only by the width of the pump laser line and the spectrometer grating. In our case, this accuracy is about several degrees Celsius in the temperature range up to the melting point.

It is noteworthy that the proposed approach for the crystallization of nanoparticles differs significantly from that used in [29], where laser-printed nanoparticles were used as nanoparticles in the initial amorphous phase. In this state, silicon has a high concentration of defects in the form of dangling bonds. In this regard, its optical properties are significantly different from the properties of single-crystal silicon; in particular, defects lead to high losses in the visible part of the spectrum. On the contrary, in hydrogenated silicon, hydrogen atoms close the dangling bonds, forming an optical gap, which is relatively "pure" from impurity

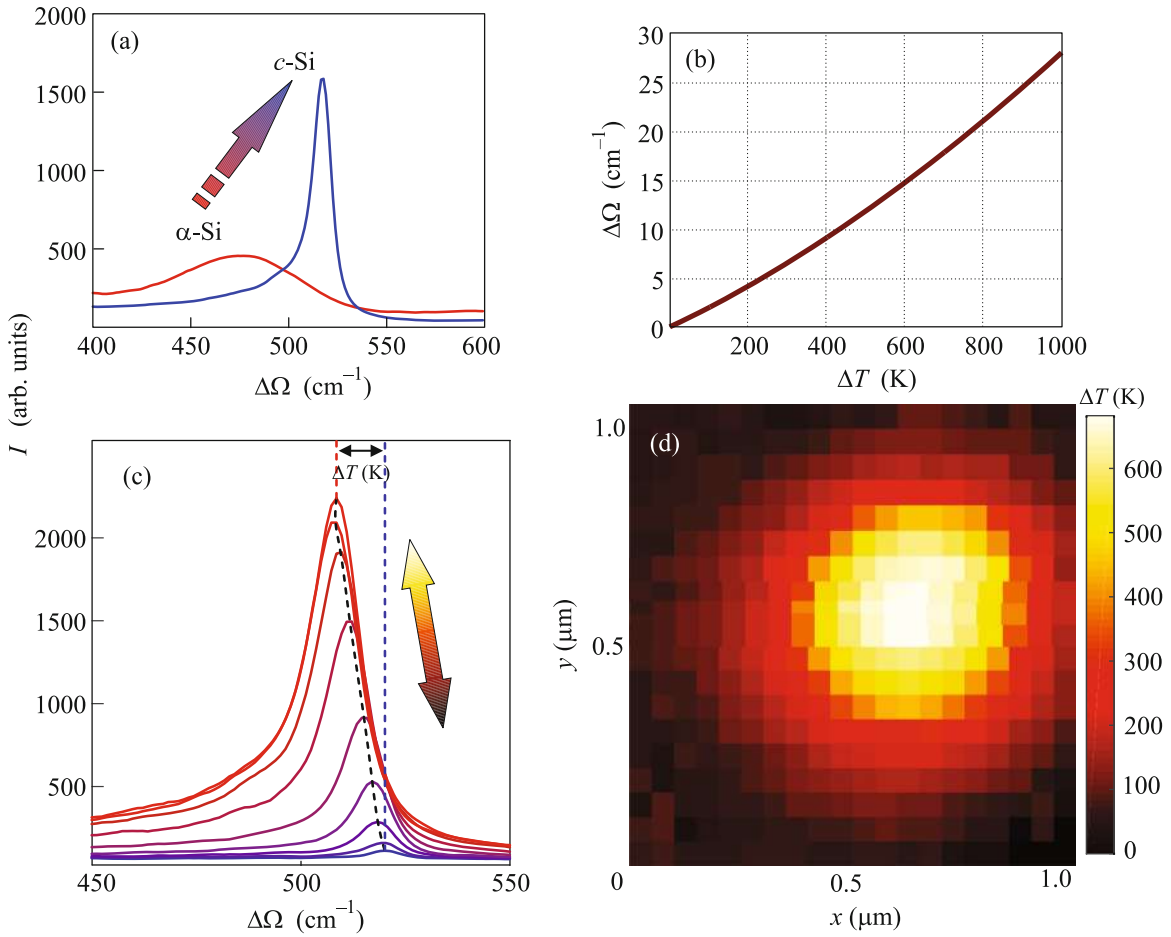

Fig. 3. (Color online) (a) Measured Raman spectra of an amorphous silicon nanodisk before and after laser annealing. (b) Spectral line shift corresponding to the optical phonon of crystalline silicon versus the temperature of the material according to Eq. (2). (c) Experimental Raman spectra measured in an annealed silicon nanodisk at various intensities of the incident light. (d) Experimental map of the optical heating of an annealed silicon nanodisk with a diameter of 330 nm at an intensity of the HeNe laser radiation of 0.24 MW/cm^2.

levels with a width of about 2 eV, reducing losses in the wavelength region >600 nm to the level of crystalline silicon. In confirmation of this, the shape of the scattering spectra obtained in dark-field microspectroscopy experiments hardly changes, as shown in Figs. 4b and 4c (see details in Section 3). These results are also confirmed by theoretical calculations with the COMSOL Multiphysics program (see details in Section 3). After annealing, the disks also retain their geometric shape, which is confirmed by the SEM images in the inset of Fig. 4c.

3. METHODS

Fabrication of nanoparticles. To fabricate cylindrical nanoparticles studied in this work, the amorphous silicon film 165 nm thick was first deposited on a quartz substrate, using the chemical vapor deposition method (Plasmalab System 380, Oxford Instruments). Electron beam lithography (Elionix, 100 kV) was carried out using hydrogen silsesquioxane (Dow Corning, XR-1541-006) as a resist. The non-irradiated portion of hydrogen silsesquioxane was removed with tetramethylammonium hydroxide (25%). The sample was then etched (Plasmalab System 100, Oxford) to prepare silicon nanodisk arrays on the quartz substrate.

Dark-field spectroscopy. To measure the scattering spectra, we apply a dark-field scheme, where one lens (10×, NA = 0.26, Mitutoyo Plan Apo NIR) is used for lighting a sample with a white light source (halogen lamp HL-2000) at an angle of incidence of 65°–67° (see Fig. 4a). The second lens (50×, NA = 0.42 Mitutoyo Plan Apo NIR) placed perpendicularly to the surface of the sample is used to collect the scattering signal. The scattered signal is analyzed by a confocal system with a spectrometer (HORIBA LabRam HR) and a charge-coupled device (CCD) (Andor DU 420A-OE 325) equipped with a 150 lines/mm diffraction grating. The position of the nanoparticles is controlled by an additional CCD camera (Canon 400 D).

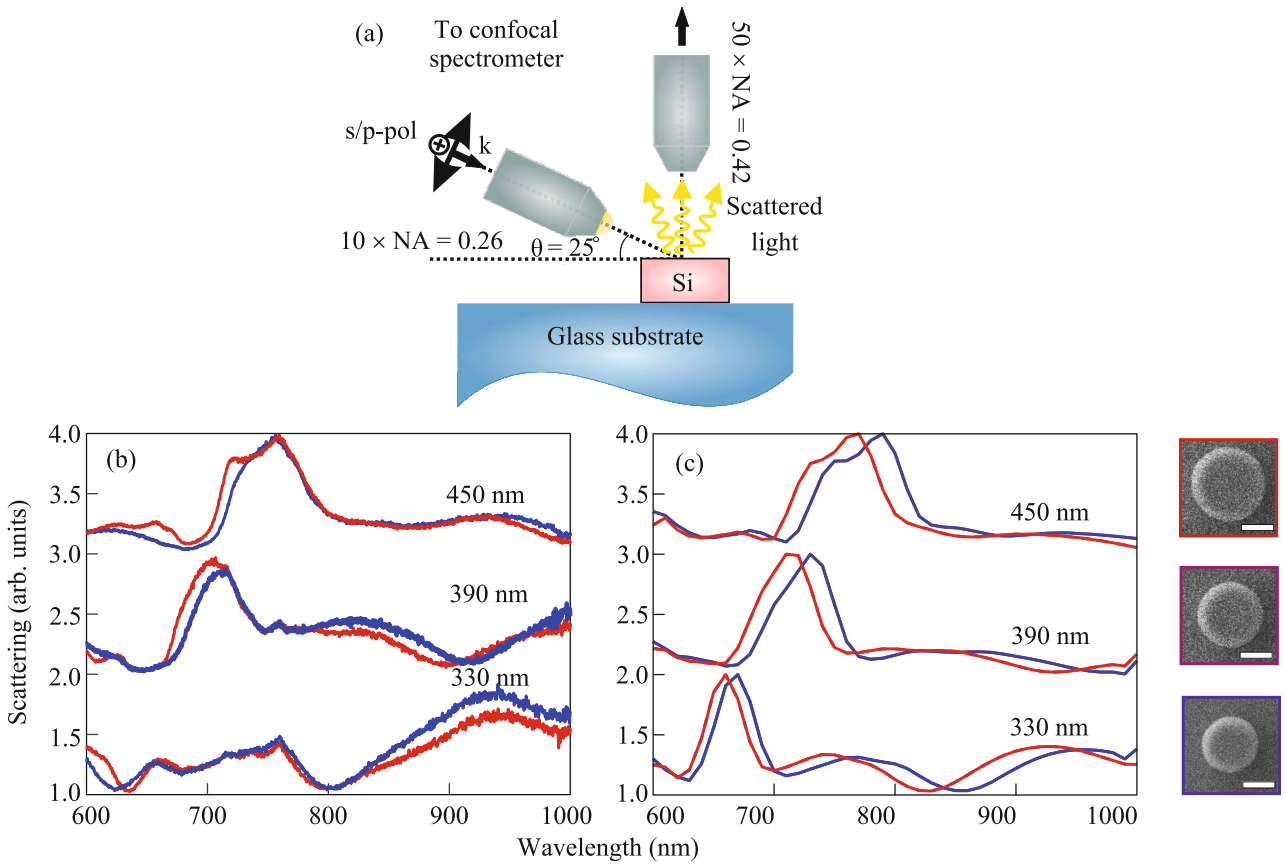

Fig. 4. (Color online) (a) Schematic of the geometry of the experiment using dark-field optical spectroscopy (for a detailed description, see Section 3). (b) Measured and (c) calculated scattering cross sections of single (blue) amorphous and (red) crystalline nanodisks with the diameters indicated near each pair of curves. The insets on the right of panel (c) show SEM images of single disks with the corresponding diameters after optical annealing.

Raman spectroscopy. Raman spectra were measured using the same recording system (HORIBA LabRam HR) with a 600 lines/mm grating and a HeNe laser at 632.8 nm as an optical heating source focused in a spot about 1 μm in size at a level of $1/e$ through a microscope lens (100×, NA = 0.9 Mitutoyo Plan Apo HR) on the surface of the sample. The lens is used to excite and collect the Raman signal. A nanoparticle sample was placed on a piezoelectric table (AISTNT) providing a positioning accuracy of 10 nm during the two-dimensional mapping and measurement of nanoparticle spectra. The HeNe laser is chosen for Raman thermometry because of its high stability and narrow spectral width, which gives a high accuracy of temperature measurements [19]. The range of laser power was varied with neutral filters in the range of 0.1–8 mW.

Theoretical model. The theoretical description of the scattering spectra of silicon nanoparticles on a quartz substrate, as well as the estimate of the optical heating values, was carried out with the commercial software package COMSOL Multiphysics. The created models reproduced the geometry of experimental studies. In particular, for the study of dark-field scattering spectra, the excitation was performed at a grazing angle (angle of incidence was 65°–67°), and the scattered signal, as well as in the experiment, was collected in the numerical aperture NA = 0.42. Dispersions of the permittivities for amorphous and crystalline silicon were taken from [23, 24] and [30], respectively. The lower hemisphere plays the role of a glass substrate, while the upper hemisphere acts as an air medium.

The decomposition of optical resonance modes in single nanodisks was calculated using the method described in [25].

4. CONCLUSIONS

To summarize, it has been shown that the proposed approach allows the local controlled crystallization of resonant silicon nanoparticles, improving their thermometric characteristics without significant change in their permittivity. The results obtained make it possible to locally change the phase of silicon nanoresonators, which not only improves the phonon spectrum

but also drastically changes some optical properties of this material associated with the crystalline phase of the material, which is important for the problems of second harmonic generation [9] and broadband photoluminescence [31]. This opens up new opportunities for recording optical information. The implemented nanothermometry and controlled local heating can also be applied in photocatalysis, hyperthermia of cancer cells, targeted drug delivery, and nanofabrication.

We are grateful to Filipp Komissarenko for assistance in scanning electron microscopy and to Ramon Paniagua-Domínguez for the development of the method of the decomposition of optical modes. Experimental studies and fabrication of nanostructures were supported by the Russian Foundation for Basic Research (project nos. 16-02-00684 and 16-29-05317) and by the A*STAR SERC Pharos program (Singapore, project no. 1527300025). The theoretical description was supported by the Russian Science Foundation (project no. 17-72-10230).

REFERENCES

1. A. I. Kuznetsov, A. E. Miroshnichenko, M. L. Brongersma, Y. S. Kivshar, and B. Luk'yanchuk, Science **354** (6314), aag2472 (2016).
2. Y. H. Fu, A. I. Kuznetsov, A. E. Miroshnichenko, Y. F. Yu, and B. Luk'yanchuk, Nat. Commun. **4**, 1527 (2013).
3. I. S. Sinev, A. A. Bogdanov, F. E. Komissarenko, K. S. Frizyuk, M. I. Petrov, I. S. Mukhin, S. V. Makarov, A. K. Samusev, A. V. Lavrinenko, and I. V. Iorsh, Laser Photon. Rev. **11**, 1700168 (2017).
4. A. B. Evlyukhin and S. I. Bozhevolnyi, JETP Lett. **83**, 653 (2006).
5. S. V. Makarov, S. I. Kudryashov, I. S. Mukhin, A. Mozharov, V. A. Milichko, A. E. Krasnok, and P. E. Belov, Nano Lett. **15**, 6187 (2015).
6. M. R. Shcherbakov, P. P. Vabishchevich, A. S. Shorokhov, K. E. Chong, D. Choi, I. Staude, A. E. Miroshnichenko, D. Neshev, A. A. Fedyanin, and Y. S. Kivshar, Nano Lett. **15**, 6985 (2015).
7. S. V. Makarov, A. S. Zalogina, M. Tajik, D. A. Zuev, M. V. Rybin, A. A. Kuchmizhak, S. Juodkazis, and Y. S. Kivshar, Laser Photon. Rev. **11**, 1700108 (2017).
8. M. R. Shcherbakov, D. N. Neshev, B. Hopkins, A. S. Shorokhov, I. Staude, E. V. Melik-Gaykazyan, M. Decker, A. A. Ezhov, A. E. Miroshnichenko, I. Brener, A. A. Fedyanin, and Y. S. Kivshar, Nano Lett. **14**, 6488 (2014).
9. S. V. Makarov, M. I. Petrov, U. Zywietz, V. A. Milichko, D. A. Zuev, N. Lopanitsyna, A. Kuksin, I. A. Mukhin, G. P. Zograf, E. Ubyivovk, D. Smirnova, S. Starikov, B. N. Chichkov, and Y. S. Kivshar, Nano Lett. **17**, 3047 (2017).
10. L. Wang, S. Kruk, H. Tang, T. Li, I. Kravchenko, D. N. Neshev, and Y. S. Kivshar, Optica **3**, 1504 (2016).
11. M. I. Tribelsky, J. Geffrin, A. Litman, C. Eyraud, and F. Moreno, Sci. Rep. **5**, 12288 (2015).
12. J. Proust, F. Bedu, B. Gallas, I. Ozerov, and N. Bonod, ACS Nano **10**, 7761 (2016).
13. O. Yavas, M. Svedendahl, P. Dobosz, V. Sanz, and R. Quidant, Nano Lett. **17**, 4421 (2017).
14. A. B. Evlyukhin, C. Reinhardt, A. Seidel, B. S. Luk'yanchuk, and B. N. Chichkov, Phys. Rev. B **82**, 045404 (2010).
15. A. García-Etxarri, R. Gómez-Medina, L. S. Froufe-Pérez, C. López, L. Chantada, F. Scheffold, J. Aizpurua, M. Nieto-Vesperinas, and J. J. Sáenz, Opt. Express **19**, 4815 (2011).
16. S. A. Maier, *Plasmonics: Fundamentals and Applications* (Springer, New York, 2007), p. 224.
17. A. I. Kuznetsov, A. E. Miroshnichenko, Y. H. Fu, J. Zhang, and B. Luk'yanchuk, Sci. Rep. **2**, 492 (2012).
18. A. B. Evlyukhin, S. M. Novikov, U. Zywietz, R. L. Eriksen, C. Reinhardt, S. I. Bozhevolnyi, and B. N. Chichkov, Nano Lett. **12**, 3749 (2012).
19. G. P. Zograf, M. I. Petrov, D. A. Zuev, P. A. Dmitriev, V. A. Milichko, S. V. Makarov, and P. A. Belov, Nano Lett. **17**, 2945 (2017).
20. M. Balkanski, R. F. Wallis, and E. Haro, Phys. Rev. B **28**, 1928 (1983).
21. V. A. Milichko, D. A. Zuev, D. G. Baranov, G. P. Zograf, K. Volodina, A. A. Krasilin, I. S. Mukhin, P. A. Dmitriev, V. V. Vinogradov, S. V. Makarov, and P. A. Belov, Laser Photon. Rev. **12** (1) (2018).
22. M. Aouassa, E. Mitsai, S. Syubaev, D. Pavlov, A. Zhizhchenko, I. Jadli, L. Hassayoun, G. Zograf, S. Makarov, and A. Kuchmizhak, Appl. Phys. Lett. **111**, 243103 (2017).
23. A. P. Slobozhanyuk, A. N. Poddubny, I. S. Sinev, A. K. Samusev, Y. F. Yu, A. I. Kuznetsov, A. E. Miroshnichenko, and Y. S. Kivshar, Laser Photon. Rev. **10**, 656 (2016).
24. R. M. Bakker, D. Permyakov, Y. F. Yu, D. Markovich, R. Paniagua-Domínguez, L. Gonzaga, A. K. Samusev, Y. S. Kivshar, B. S. Luk'yanchuk, and A. I. Kuznetsov, Nano Lett. **15**, 2137 (2015).
25. R. Paniagua-Domínguez, Y. F. Yu, A. E. Miroshnichenko, L. A. Krivitsky, Y. H. Fu, V. Valuckas, L. Gonzaga, Y. T. Toh, A. Y. S. Kay, B. Luk'yanchuk, and A. I. Kuznetsov, Nat. Commun. **7**, 10362 (2016).
26. G. Baffou and R. Quidant, Laser Photon. Rev. **7**, 171 (2013).
27. Z. Iqbal and S. Veprek, J. Phys. C: Solid State Phys. **15**, 377 (1982).
28. M. K. Hatalis and D. W. Greve, J. Appl. Phys. **63**, 2260 (1988).
29. U. Zywietz, A. B. Evlyukhin, C. Reinhardt, and B. N. Chichkov, Nat. Commun. **5**, 3402 (2014).
30. D. E. Aspnes and A. A. Studna, Phys. Rev. B **27**, 985 (1983).
31. S. V. Makarov, I. S. Sinev, V. A. Milichko, F. E. Komissarenko, D. A. Zuev, E. V. Ushakova, I. S. Mukhin, Y. F. Yu, A. I. Kuznetsov, P. A. Belov, I. V. Iorsh, A. N. Poddubny, A. K. Samusev, and Yu. S. Kivshar, Nano Lett. **18**, 535 (2018).

Translated by L. Mosina

NANO LETTERS

pubs.acs.org/NanoLett Letter

Stimulated Raman Scattering from Mie-Resonant Subwavelength Nanoparticles

George P. Zograf, Daniil Ryabov, Viktoria Rutckaia, Pavel Voroshilov, Pavel Tonkaev, Dmitry V. Permyakov, Yuri Kivshar,* and Sergey V. Makarov*

Cite This: *Nano Lett.* 2020, 20, 5786−5791 Read Online

ACCESS | Metrics & More | Article Recommendations | Supporting Information

ABSTRACT: Resonant dielectric structures have emerged recently as a new platform for subwavelength nonplasmonic photonics. It was suggested and demonstrated that magnetic and electric Mie resonances can enhance substantially many effects at the nanoscale including spontaneous Raman scattering. Here, we demonstrate stimulated Raman scattering (SRS) for isolated crystalline silicon (c-Si) nanoparticles and observe experimentally a transition from spontaneous to stimulated scattering manifested in a nonlinear growth of the signal intensity above a certain pump threshold. At the Mie resonance, the light gets confined into a low volume of the resonant mode with enhanced electromagnetic fields inside the c-Si nanoparticle due to its high refractive index, which leads to an overall strong SRS signal at low pump intensities. Our finding paves the way for the development of efficient Raman nanolasers for multifunctional photonic metadevices.

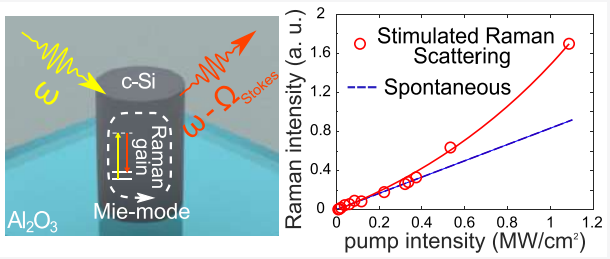

KEYWORDS: *Stimulated Raman scattering, Mie resonances, crystalline silicon, nanoparticles, nonlinear nanophotonics, multipolar mode expansion*

Raman scattering is a powerful tool for analyzing both plasmonic[1,2] and dielectric[3−5] optical structures. Semiconductors, which are often considered as relevant materials for all-dielectric photonics, have a strong inherent Raman response due to their crystalline lattice structure. In particular, crystalline silicon (c-Si) has a sharp Raman line around 520 cm^{-1}, caused by the interaction of light with optical phonons. A few years ago, it was demonstrated experimentally[6] that this Raman response can be enhanced resonantly through the excitation of magnetic dipole Mie modes in dielectric nanostructures.

Spontaneous Raman scattering enhanced by the electric and magnetic Mie resonances of subwavelength particles[6,7] was suggested for sensing,[5] nanothermometry,[8,9] and controllable drug delivery.[10] However, spontaneous Raman scattering remains a relatively weak effect as compared with luminescence observed in resonant dielectric nanostructures.[11−13] A transition from spontaneous to stimulated Raman emission[14] empowered by Mie resonances is expected to enhance the scattering efficiency in subwavelength photonics.

High-quality factor (high-*Q* factor) Raman microlasers were first demonstrated for micrometer-size liquid droplets[15,16] and silica microspheres.[17] To shrink the resonator dimensions, one needs to employ semiconductors, and a Raman gain of about 10^5 times higher than that for silica has been demonstrated for silicon resonators.[18−20] Stimulated Raman scattering (SRS) was achieved in cavity-enhanced nanowires longer than 1 μm,[21,22] with the pump intensities larger than 10 kW/cm^2, which were accompanied by strong overheating.

In this Letter, we observe experimentally, for the first time to our knowledge, SRS from isolated subwavelength c-Si nanoparticles empowered by multipolar Mie resonances. We optimize the parameters of both nanoparticles and a substrate to achieve enhanced stimulated emission without overheating. This approach provides an additional degree of freedom for achieving the highest Raman scattering yield from fully subwavelength all-dielectric nanoscale structures, and it may be employed for useful functionalities such as sensing and nanothermometry.

RESULTS

Sample Fabrication and Characterization. Our samples are made from a silicon-on-sapphire wafer with a thickness of the c-Si film of 600 nm. The nanoparticles are nanodisk shapes (or nanopillars; see Figure 1a) with diameters of 200−1000 nm, and they are fabricated by electron-beam lithography (for details, see Methods below). Distance between isolated

Received: April 16, 2020
Revised: June 23, 2020
Published: June 24, 2020

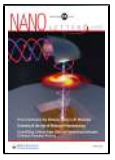

https://dx.doi.org/10.1021/acs.nanolett.0c01646
Nano Lett. 2020, 20, 5786−5791

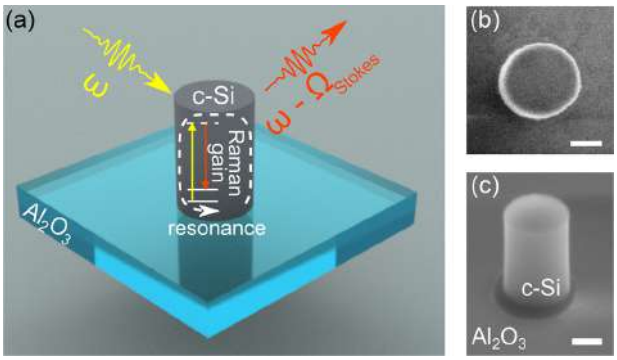

Figure 1. Mie-resonant c-Si nanoparticle on a substrate for SRS experiments. (a) Schematic view of a Si nanoparticle excited with a laser light. (b,c) Top and side SEM images of a c-Si nanoparticle fabricated on a sapphire substrate. Scale bars are 200 nm.

nanoparticles is 50 μm (all additional details are given in Supporting Information), and this removes any effect of neighboring particles in confocal optical measurements. Figure 1b,c shows the scanning electron microscopy (SEM) images of typical nanoparticles used in the experiment.

Optical Mie-type resonances in nanoparticles can be characterized experimentally by dark-field spectroscopy, when white light is illuminated on an isolated nanoparticle under an oblique incidence, and the scattered signal is collected by an objective, which is then sent to a spectrometer and a charge-coupled device (CCD) camera (for details, see Methods; the optical setup is shown in Supporting Information). Experimental dark-field spectra are shown in Figure 2a, and they should be compared with numerically simulated white-light scattering spectra of Figure 2b (see Methods for details of calculations). These results reveal the excitation of Mie resonances that can be characterized by applying the multipole mode decomposition, as shown in Figure 2c (see also Supporting Information).

As is known, *spontaneous* Raman scattering was demonstrated to be a very useful tool in the study of optical modes because it involves the emission from bulk nanoparticles.[6,8,23] A strongly enhanced Raman scattering signal corresponds to an efficient energy coupling to the nanoparticle modes. In order to select the subwavelength nanoparticle with the strongest Raman scattering signal, we carry out confocal Raman scattering measurements from individual c-Si nanoparticles (for details, see Methods) and obtain the size dependence of the signal excited at a pump wavelength of 633 nm, as summarized in Figure 3a. The beam radius of focused light is estimated to be around $r \approx 0.5$ μm. Remarkably, the

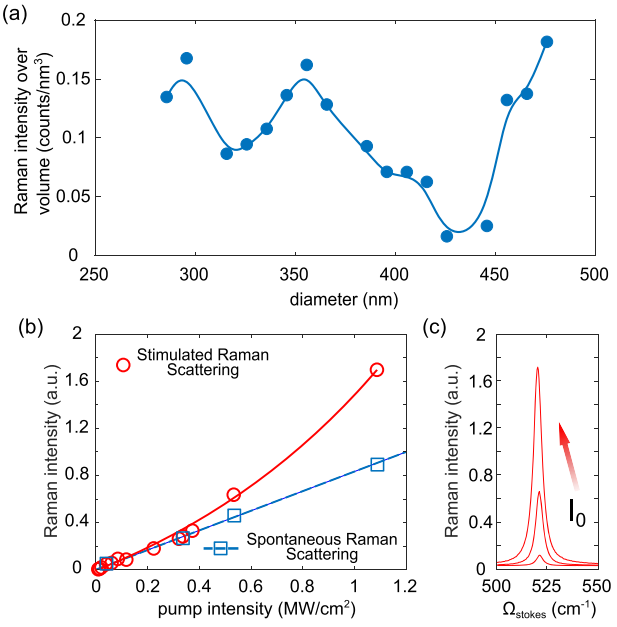

Figure 3. Experimental Raman scattering from c-Si nanoparticles. (a) Raman scattering intensity for varying diameters of nanoparticles measured at 0.22 MW/cm^2 intensity at a pump wavelength of 633 nm. (b) Experimental Raman scattering intensities at different pumps for the resonant 475 nm nanoparticle (red circles) and nonresonant 445 nm nanoparticle (blue squares). The red line corresponds to an exponential fitting based on eq 2. (c) SRS spectra for the 475 nm nanoparticle at the following pump intensities: 0.1, 0.55, and 1.1 MW/cm^2. An arrow shows the growth of the pump intensity.

sapphire substrate with thermal conductivity almost 50 times higher than that of glass provides an excellent thermal sink for the nanoparticles possessing a good thermal contact with a substrate. That is why we do not observe in experiment any overheating effects in the Raman scattering signal with an additional shift and broadening, as was reported previously for nanospheres[8] and nanowires[22] placed on a glass substrate. In our experiments at low intensity (less than 0.1 mW/μm^2), the maximum Raman scattering signal corresponds to the nanoparticle diameter of 475 nm, driven mostly by the MQ (third-order) and MD (third-order) modes, both at 654 and

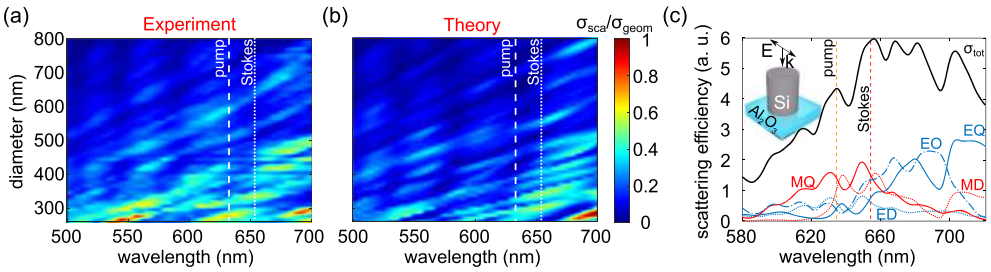

Figure 2. White-light scattering by Si nanoparticles. (a) Experimental and (b) theoretical dark-field white-light scattering (spectral range of 500−700 nm) from the Si nanoparticles with diameters of 250−800 nm and a height of 600 nm. (c) Theoretical dark-field spectrum analyzed with the modal decomposition for the 475 nm nanoparticle, corresponding to the SRS experiment. Here, ED, MD, MQ, EQ, and EO are electric dipole, magnetic dipole, magnetic quadrupole, electric quadrupole, and electric octupole, respectively.

https://dx.doi.org/10.1021/acs.nanolett.0c01646
Nano Lett. 2020, 20, 5786−5791

633 nm wavelengths, as confirmed by the multipole mode decomposition in Figure 2c.

Stimulated Raman Amplification. Figure 3b shows typical experimental dependencies of Raman scattering signal versus pump intensity. At low intensities, spontaneous Raman scattering dominates and is characterized by a linear dependence on the incident power, as was demonstrated earlier with c-Si nanoparticles.[6,8] However, at higher intensities (higher than 0.3 MW/cm^2), we observe a nonlinear growth of the Raman scattering signal for the nanodisk with a diameter of 475 nm, which is not observed for other nanodisks with diameters of 250−800 nm; see the dashed line with blue squares in Figure 3b. This sharp difference characterizes the SRS regime. The Raman spectra are shown in Figure 3c for a c-Si nanoparticle with a diameter of 475 nm and a height of 600 nm.

In the SRS regime, a stronger pump transfers a part of its energy to a weaker red-shifted Raman signal (i.e., at the Stokes wavelength or frequency) by interacting with a nonlinear medium. As a result, a weak Stokes beam can be amplified by the pump, and this process is attributed to the Raman amplification. The Raman amplification is the third-order nonlinear process described with nonlinear susceptibility, $\chi^{(3)}_{NR}(\omega_S;\omega_P, -\omega_P,\omega_S)$, or simpler $\chi^{(3)}_{NR}(\omega_S)$. The amplification can be characterized by the Raman gain of the Stokes wave:

$$g = -\frac{3\omega_S}{n_S n_P c^2 \varepsilon_0}\mathrm{Im}[\chi^{(3)}_{NR}(\omega_S)] \quad (1)$$

where ω_S is the frequency of the Stokes photons, n_S (or n_P) is the refractive index at the Stokes (or pump) frequency, c is the speed of light, and ε_0 is the permittivity of a vacuum. For Si at near-infrared frequencies, a typical gain is $g \approx 80$ cm/GW,[18,24] and it depends on crystalline properties of c-Si and the pump wavelength. For example, the Raman gain depends linearly on the Stokes frequency,[24] and its value can be several times larger than that in the visible frequency range where, however, optical losses are often higher.

When the pump photons become trapped by a resonator mode, the Raman scattering gets enhanced, and it should generate a signal that grows exponentially with the input intensity (I_P), being characterized by the gain factor:[25]

$$I_S^{NR} \sim \exp(gI_P L_S) \quad (2)$$

where I_S^{NR} is the intensity of the nonlinearly amplified Raman scattering signal at the Stokes frequency (ω_S), and the effective interaction length L_S is described as $L_S = Q_S\lambda_S/2\pi n_S$. Experimentally measured data for the nonlinear Raman scattering signal can be fitted with this exponential dependence versus incident intensity, where the transition from spontaneous scattering to the SRS amplification occurs at $I_P^{tr} \approx 0.4$ MW/cm^2, and this dependence deviates from a linear regime, thus characterizing the SRS process.

Further, the Raman lasing threshold can be achieved when the resonator round-trip gain becomes equal to its round-trip loss. Generally, the threshold power can be estimated from the equation[17,26]

$$P_{th} \approx \frac{n_S n_P}{\lambda_S \lambda_P}\frac{V_{eff}}{Q_S Q_P}\frac{\pi^2}{g}\frac{1}{B\Gamma} \quad (3)$$

where P_{th} is the incident pump power that differs from the power coupled to the resonator, n_P (or n_S) is the index of refraction at the pump (or Stokes) wavelength, V_{eff} is the effective mode volume at the Stokes wavelength, λ_P and λ_S are the pump and Stokes wavelengths, respectively, g is the nonlinear bulk Raman gain coefficient, Q_P (or Q_S) is the total Q factor for the resonant mode excited at the pump (or Stokes) wavelength, B is the coupling efficiency, and Γ is the spatial overlap factor of the modes.

Remarkably, for luminescence and lasing, the ratio V_{eff}/Q_S is directly connected with the Purcell factor, and it defines the emission efficiency.[27,28] Indeed, to initiate photoluminescence for optical photoexcitation, strong interband transitions result in high absorption at the pump wavelength suppressing optical modes in the resonator, which allows one to neglect resonant effects assuming $Q_P \sim 1$. In the SRS process, the resonant interaction at the pump wavelength becomes crucial, and as a result, the amplification depends on the term $V_{eff}/Q_S Q_P$, according to eq 3. Thus, to improve the coupling efficiency and minimize the threshold for the nonlinear Raman amplification in a resonator, the optimization of two resonances is required.

Optimization of Resonator Parameters. For the Si nanoparticles with a fixed height (600 nm) placed on a sapphire substrate (Al_2O_3), the Q factor of the Mie-type modes can be calculated numerically (see Figure 4a) in order to define

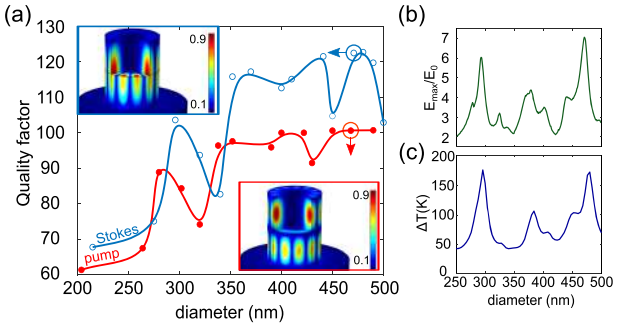

Figure 4. Numerical study of resonant properties of nanoparticles. (a) Quality factor of the eigenmodes of Si disks with 600 nm height for the wavelength 633 nm corresponding to the pump wavelength of the HeNe laser (filled red circles) and for the Raman Stokes emission wavelength (hollow blue circles). Insets show the normalized electric field magnitude distribution of the eigenmodes for the nanoparticle supporting stimulated Raman emission at pump and Stokes wavelengths. Color bar scales are of normalized units. Solid lines are built for the ease of perception. (b) Numerical calculation of the field enhancement inside a single nanoparticle excited by a plane wave at 633 nm for varying diameters. (c) Numerical calculation of optical heating of a single nanoparticle with varying diameters.

the best parameters for experiment. The numerical study is performed with COMSOL software (for more details, see Methods). According to eq 3, the optimal SRS conditions correspond to the case when the pump wavelength, λ_P = 633 nm, and Stokes wavelength, λ_S = 654 nm, match the eigenmodes of the nanoparticle. Figure 4a shows that this requirement can be fulfilled for a number of diameters. Remarkably, the values of the Q factor are generally higher for the Stokes wavelength because of lower material losses of c-Si in this spectral range as compared with the pump wavelength.

Although some of the eigenmodes have larger Q factors, they are difficult to excite due to the symmetry constrains. The field distribution for an eigenmode is shown in Figure 4a, revealing its complex character. Figure 4b shows the local field enhancement for the excitation by a linear polarized plane wave, providing the important information that a plane wave

https://dx.doi.org/10.1021/acs.nanolett.0c01646
Nano Lett. 2020, 20, 5786−5791

with the linear polarization can excite efficiently the nanoparticle with diameter D = 475 nm, where both the maximum field enhancement (corresponding to calculated coupling efficiency B = 2.41; see section S5 of Supporting Information) and high-Q factors ($Q_P \approx 100$ and $Q_S \approx 120$) can be achieved. Experimental measurements of the Raman intensity confirm that the Raman scattering signal takes a maximum value at D = 475 nm (see Figure 3a). Finally, a spatial overlapping between pump and Stokes modes is an important parameter which affects the efficiency of SRS, according to eq 3. Our numerical calculations give the value $\Gamma \approx 0.784$ (see section S5 of Supporting Information).

This analysis allows estimating a threshold for Raman lasing from eq 3 to understand better the observed phenomena. Namely, we use the Raman gain coefficient of c-Si as 76 cm/GW from ref 18 and the following parameters: λ_P = 633 nm, λ_S = 654 nm, $n_S \approx n_P \approx 3.8$ from ref 29 and $V_{eff} = 0.108V$, where V is the nanoparticle volume (for details of numerical calculations, see section S5 of Supporting Information). For the threshold, we obtain $P_{th}^{calc} \approx 250$ mW, being 2 orders of magnitude higher than the experimental value $P_{exp}^{tr} = I_P^{tr}\pi r^2 \approx 3$ mW. Along with the absence of spectral narrowing of the Raman peak,[30] this means that we do not achieve the lasing threshold but instead demonstrate nonlinear amplification of the Raman scattering via stimulated emission mechanism.

Reduction of Thermal Overheating. Finally, we discuss the Mie-empowered thermal effects because c-Si has nonvanishing optical losses ($\alpha \approx 3.9 \times 10^4$ cm^{-1} from ref 29) at the pump wavelength λ_P = 633 nm. As shown previously,[8,9,22] strong heating of Si nanoparticles can be achieved at critical coupling and low thermal conductivity of the substrate. For example, a spherical Si nanoparticle placed on a glass substrate can be heated to 600 K under conditions similar to those in our study.[8] Such a strong overheating reduces and broadens the Raman peak. In our design, we employ sapphire as the substrate material with much higher thermal conductivity (~40 Wm^{-1} K^{-1}) as compared to that of silica glass (~1 Wm^{-1} K^{-1}). Moreover, a tight contact of the nanoparticle with the substrate is better for a thermal sink than that for spherical nanoparticles[8,9] or nanowires.[22] Figure 4c shows the calculated average temperature of the nanoparticles with a height of 600 nm and different diameters. Even though the heating maximum is achieved at D = 475 nm, it shows a weaker effect on optical properties of c-Si nanoparticles. However, this estimate suggests that the intensity of 1.1 MW/cm^2 is close to the limiting value due to overheating.

In summary, we have reported the first observation of the stimulated Raman scattering from subwavelength crystalline silicon nanoparticles enhanced by Mie-type resonances. We have revealed the importance of critical optimization of the Q factors of nanoparticles and thermal conductivity of a substrate to achieve a strong optical response and avoid overheating at higher intensities. We believe that our finding will be useful for advanced applications of resonant dielectric nanophotonics for nanoscale thermometry and biosensing, and we envision further studies of the stimulated Raman scattering in various nanophotonic designs.[31−33]

METHODS

Fabrication of Samples. A set of single-crystal silicon nanoparticles (nanopillars and nanodisks) with different diameters placed on sapphire (Al_2O_3) substrates are fabricated by using a top-down technique. An epitaxial structure is grown by molecular beam epitaxy at 600 °C using the Stranski−Krastanov growth mode. A set of isolated nanoparticle resonators with diameters variable with a 10 nm step in diameters is created on the grown epitaxial structure by applying focused gallium ion beam milling using a FEI Versa 3D dual beam system. Ion current adjustment down to 1.5 pA allows nearly vertical side walls of the nanoparticles to be maintained.

Optical Characterization. The experimental optical elastic scattering properties of the nanoparticles were studied by means of a dark-field optical scattering technique. The setup consists of an infinity-corrected objective (10×, NA = 0.26, Mitutoyo Plan Apo NIR) that is used for illumination with a white-light source (HL-2000 halogen lamp) of the sample under a 67° angle to the substrate normal. The second objective (50×, NA = 0.42 Mitutoyo Plan Apo NIR) placed perpendicularly on top of the sample substrate is applied for acquiring the scattering signal. The scattered signal is analyzed by a confocal system with a spectrometer (HORIBA LabRam HR) and cooled CCD camera (Andor DU 420A-OE 325) equipped with a 150 g/mm diffraction grating. The position of the nanoparticles is controlled by an additional CCD camera.

Raman Scattering Measurements. The experimental studies of Raman scattering are performed with the confocal spectrometer (HORIBA LabRam HR) and confocal setup with 1800 g/mm diffractional grating allowing higher spectral resolution. The excitation source of a 632.8 nm HeNe continuous wave laser is focused through the optical microscope lens (100×, NA = 0.9 Mitutoyo Plan Apo HR) perpendicular to the sample substrate. The same objective is used for both excitation and collection of the Raman scattering signal. The employed laser system provides desired stability in both output intensity and laser spectral bandwidth of less than 0.002 nm (0.05 cm^{-1}), allowing precise Raman scattering measurements. The reflected signal is subsequently passed through a 632.8 nm notch-filter in order to get rid of elastic scattering from the nanoparticles samples. A set of optical filters is used for varying the incident laser intensity on the nanoparticle samples.

Numerical Simulations. For numerical simulations of the dark-field scattering, we employ the cylindrical symmetry of the problem to reduce it from fully three-dimensional to a two-dimensional electromagnetic problem. In the experimental setup, the incident TM-polarized plane wave (in-plane E-vector) excites the nanoparticle propagating at the angle of 67° to normal. This plane wave is expanded into a series of the azimuthal harmonics $\sim e^{im\varphi}$ to calculate their contribution to the total scattering cross section. We estimate the number of harmonics that have significant contributions to the total scattering by comparing the partial cross sections with the results of the lower orders to include a finite number of them into the calculation. The commercial software COMSOL Multiphysics is used to model the computational domain size around 6 times larger than the size of a nanoparticle (this parameter is estimated from the computed dependence of the solution convergence from the size of the outer area). Physical domains include the cylindrical silicon nanoparticle (a rectangle in the plane projection), a sapphire substrate, and air. To avoid reflections from the outer boundaries, the computational domain is surrounded by a perfectly matched layer. The scattered radiation is collected in a solid angle with the angular opening of 49°. Then, at the top of the model, the line segment is selected where we calculate the radiation flow.

https://dx.doi.org/10.1021/acs.nanolett.0c01646
Nano Lett. 2020, 20, 5786−5791

In the eigenmode calculations, we employ a three-dimensional model that is important not only for the evaluation of the Q factor of the eigenmodes but also for the estimation of the field distribution inside the nanoparticle and the type of its symmetry. We employ the commercial numerical software COMSOL to study a cylindrical particle, its substrate, and the air surrounded by the cylindrical perfectly matched layer. The size of the computational domain depends on the nanoparticle diameter, and it is approximately 5−6 diameters. The study of the eigenmodes is conducted using the eigenfrequency module around the frequency corresponding to the incident wavelength. Analyzing the shift of the field distribution with the growth of the nanoparticle diameter, it is possible to estimate the configurations for which the eigenmode wavelength coincides with the initial one and select the nanoparticle with the best Q factors.

Optical Heating. Calculations of optical heating are conducted by using numerical commercial software COMSOL Multiphysics. Fully three-dimensional problem for the electromagnetic wave propagation and heat transfer in solids is solved using the multiphysics solution. The computational domain consists of an outer sphere (radius 2 μm) placed on a sapphire hemisphere. Further computational steps are the same as described in ref 8.

Multipolar Mode Decomposition. The multipole mode decomposition of the radiation is performed by applying the approach described previously.[34,35] The basic multipole moments are evaluated by integrating numerically the total electric field inside the nanoparticle induced by a normally incident plane wave. Scattering power is decomposed up to the octupole terms, and higher-order terms are neglected. Further details can be found in Supporting Information.

■ ASSOCIATED CONTENT

Supporting Information

The Supporting Information is available free of charge at https://pubs.acs.org/doi/10.1021/acs.nanolett.0c01646.

Sample description; details of multipole mode decomposition for silicon nanoparticles with and without a substrate; description of the setups for dark-field and Raman scattering measurements; details of connection between Raman spectral shift and local temperature of the nanoparticles; Raman scattering spectra for nanoparticles with diameters 300 and 350 nm; calculations of optical properties (effective mode volume, coupling efficiency, modes overlapping, and field components) for the nanoparticle with 475 nm diameter at pump and Stokes wavelengths (PDF)

■ AUTHOR INFORMATION

Corresponding Authors

Yuri Kivshar − *Department of Physics and Engineering, ITMO University, St. Petersburg 197101, Russia; Nonlinear Physics Centre, Australian National University, Canberra, ACT 2601, Australia;* orcid.org/0000-0002-3410-812X; Email: yuri.kivshar@anu.edu.au

Sergey V. Makarov − *Department of Physics and Engineering, ITMO University, St. Petersburg 197101, Russia;* orcid.org/0000-0002-9257-6183; Email: s.makarov@metalab.ifmo.ru

Authors

George P. Zograf − *Department of Physics and Engineering, ITMO University, St. Petersburg 197101, Russia*

Daniil Ryabov − *Department of Physics and Engineering, ITMO University, St. Petersburg 197101, Russia*

Viktoria Rutckaia − *Center for Innovation Competence SiLi-Nano, Martin-Luther-University Halle-Wittenberg, 06120 Halle, Germany;* orcid.org/0000-0001-8890-1775

Pavel Voroshilov − *Department of Physics and Engineering, ITMO University, St. Petersburg 197101, Russia;* orcid.org/0000-0002-4039-4513

Pavel Tonkaev − *Department of Physics and Engineering, ITMO University, St. Petersburg 197101, Russia*

Dmitry V. Permyakov − *Department of Physics and Engineering, ITMO University, St. Petersburg 197101, Russia;* orcid.org/0000-0003-2708-9140

Complete contact information is available at: https://pubs.acs.org/10.1021/acs.nanolett.0c01646

Notes

The authors declare no competing financial interest.

■ ACKNOWLEDGMENTS

This work was supported by the Ministry of Education and Science of the Russian Federation (Project 14.Y26.31.0010), Russian Foundation for Basic Research (Project 18-32-20205), the Australian Research Council (Grant No. DP200101168), and the Strategic Fund of the Australian National University. The authors are indebted to Filipp Komissarenko for the SEM images of nanoparticles, as well as Andrey Bogdanov and Kirill Koshelev for a help with numerical calculations. They also thank Anton Samusev, Dmitry Zuev, and Pavel Belov for fruitful discussions.

■ REFERENCES

(1) Kneipp, K.; Moskovits, M.; Kneipp, H. *Surface-Enhanced Raman Scattering: Physics and Applications*; Springer Science & Business Media, 2006; Vol. *103*.

(2) Ding, S.-Y.; Yi, J.; Li, J.-F.; Ren, B.; Wu, D.-Y.; Panneerselvam, R.; Tian, Z.-Q. Nanostructure-based plasmon-enhanced Raman spectroscopy for surface analysis of materials. *Nature Reviews Materials* **2016**, *1*, 16021.

(3) Rodriguez, I.; Shi, L.; Lu, X.; Korgel, B. A.; Alvarez-Puebla, R.; Meseguer, F. Silicon nanoparticles as Raman scattering enhancers. *Nanoscale* **2014**, *6*, 5666−5670.

(4) Caldarola, M.; Albella, P.; Cortés, E.; Rahmani, M.; Roschuk, T.; Grinblat, G.; Oulton, R. F.; Bragas, A. V.; Maier, S. A. Non-plasmonic nanoantennas for surface enhanced spectroscopies with ultra-low heat conversion. *Nat. Commun.* **2015**, *6*, 7915.

(5) Alessandri, I.; Lombardi, J. R. Enhanced Raman scattering with dielectrics. *Chem. Rev.* **2016**, *116*, 14921−14981.

(6) Dmitriev, P. A.; Baranov, D. G.; Milichko, V. A.; Makarov, S. V.; Mukhin, I. S.; Samusev, A. K.; Krasnok, A. E.; Belov, P. A.; Kivshar, Y. S. Resonant Raman scattering from silicon nanoparticles enhanced by magnetic response. *Nanoscale* **2016**, *8*, 9721−9726.

(7) Frizyuk, K.; Hasan, M.; Krasnok, A.; Alú, A.; Petrov, M. Enhancement of Raman scattering in dielectric nanostructures with electric and magnetic Mie resonances. *Phys. Rev. B: Condens. Matter Mater. Phys.* **2018**, *97*, 085414.

(8) Zograf, G. P.; Petrov, M. I.; Zuev, D. A.; Dmitriev, P. A.; Milichko, V. A.; Makarov, S. V.; Belov, P. A. Resonant non-plasmonic nanoparticles for efficient temperature-feedback optical heating. *Nano Lett.* **2017**, *17*, 2945−2952.

(9) Milichko, V. A.; Zuev, D. A.; Baranov, D. G.; Zograf, G. P.; Volodina, K.; Krasilin, A. A.; Mukhin, I. S.; Dmitriev, P. A.;

Vinogradov, V. V.; Makarov, S. V.; et al. Metal-dielectric nanocavity for real-time tracing molecular events with temperature feedback. *Laser & Photonics Reviews* **2018**, *12*, 1700227.
(10) Zograf, G. P.; Timin, A. S.; Muslimov, A. R.; Shishkin, I. I.; Nominé, A.; Ghanbaja, J.; Ghosh, P.; Li, Q.; Zyuzin, M. V.; Makarov, S. V. All-optical nanoscale heating and thermometry with resonant dielectric nanoparticles for controllable drug release in living cells. *Laser Photonics Rev.* **2020**, *14*, 1900082.
(11) Rutckaia, V.; Heyroth, F.; Novikov, A.; Shaleev, M.; Petrov, M.; Schilling, J. Quantum dot emission driven by Mie resonances in silicon nanostructures. *Nano Lett.* **2017**, *17*, 6886−6892.
(12) Zhang, C.; Xu, Y.; Liu, J.; Li, J.; Xiang, J.; Li, H.; Li, J.; Dai, Q.; Lan, S.; Miroshnichenko, A. E. Lighting up silicon nanoparticles with Mie resonances. *Nat. Commun.* **2018**, *9*, 2964.
(13) Tiguntseva, E.; Zograf, G.; Komissarenko, F.; Zuev, D.; Zakhidov, A.; Makarov, S.; Kivshar, Y. S. Light-emitting halide perovskite nanoantennas. *Nano Lett.* **2018**, *18*, 1185−1190.
(14) Prince, R. C.; Frontiera, R. R.; Potma, E. O. Stimulated Raman scattering: from bulk to nano. *Chem. Rev.* **2017**, *117*, 5070−5094.
(15) Qian, S.-X.; Chang, R. K. Multiorder Stokes emission from micrometer-size droplets. *Phys. Rev. Lett.* **1986**, *56*, 926.
(16) Lin, H.-B.; Huston, A.; Eversole, J. D.; Campillo, A. J. Double-resonance stimulated Raman scattering in micrometer-sized droplets. *J. Opt. Soc. Am. B* **1990**, *7*, 2079−2089.
(17) Spillane, S.; Kippenberg, T.; Vahala, K. Ultralow-threshold Raman laser using a spherical dielectric microcavity. *Nature* **2002**, *415*, 621−623.
(18) Claps, R.; Dimitropoulos, D.; Han, Y.; Jalali, B. Observation of Raman emission in silicon waveguides at 1.54 μm. *Opt. Express* **2002**, *10*, 1305−1313.
(19) Claps, R.; Dimitropoulos, D.; Raghunathan, V.; Han, Y.; Jalali, B. Observation of stimulated Raman amplification in silicon waveguides. *Opt. Express* **2003**, *11*, 1731−1739.
(20) Yang, X.; Wong, C. W. Design of photonic band gap nanocavities for stimulated Raman amplification and lasing in monolithic silicon. *Opt. Express* **2005**, *13*, 4723−4730.
(21) Wu, J.; Gupta, A. K.; Gutierrez, H. R.; Eklund, P. C. Cavity-enhanced stimulated Raman scattering from short GaP nanowires. *Nano Lett.* **2009**, *9*, 3252−3257.
(22) Agarwal, D.; Ren, M.-L.; Berger, J. S.; Yoo, J.; Pan, A.; Agarwal, R. Nanocavity-enhanced giant stimulated Raman scattering in Si nanowires in the visible light region. *Nano Lett.* **2019**, *19*, 1204−1209.
(23) Baryshnikova, K. V.; Frizyuk, K.; Zograf, G.; Makarov, S.; Baranov, M. A.; Zuev, D.; Milichko, V. A.; Mukhin, I.; Petrov, M.; Evlyukhin, A. Revealing low-radiative modes of nanoresonators with internal Raman scattering. *JETP Lett.* **2019**, *110*, 25−30.
(24) Hon, N. K.; Soref, R.; Jalali, B. The third-order nonlinear optical coefficients of Si, Ge, and Si_{1-x} Ge_x in the mid-wave and long-wave infrared. *J. Appl. Phys.* **2011**, *110*, 9.
(25) Hopkins, R. J.; Symes, R.; Sayer, R. M.; Reid, J. P. Determination of the size and composition of multicomponent ethanol/water droplets by cavity-enhanced Raman scattering. *Chem. Phys. Lett.* **2003**, *380*, 665−672.
(26) Grudinin, I. S.; Maleki, L. Ultralow-threshold Raman lasing with CaF2 resonators. *Opt. Lett.* **2007**, *32*, 166−168.
(27) Suhr, T.; Gregersen, N.; Yvind, K.; Mørk, J. Modulation response of nanoLEDs and nanolasers exploiting Purcell enhanced spontaneous emission. *Opt. Express* **2010**, *18*, 11230−11241.
(28) Khurgin, J. B.; Sun, G. Comparative analysis of spasers, vertical-cavity surface-emitting lasers and surface-plasmon-emitting diodes. *Nat. Photonics* **2014**, *8*, 468.
(29) Aspnes, D. E.; Studna, A. Dielectric functions and optical parameters of Si, Ge, GaP, GaAs, GaSb, InP, InAs, and InSb from 1.5 to 6.0 ev. *Phys. Rev. B: Condens. Matter Mater. Phys.* **1983**, *27*, 985.
(30) Rong, H.; Liu, A.; Jones, R.; Cohen, O.; Hak, D.; Nicolaescu, R.; Fang, A.; Paniccia, M. An all-silicon Raman laser. *Nature* **2005**, *433*, 292−294.
(31) Ha, S. T.; Fu, Y. H.; Emani, N. K.; Pan, Z.; Bakker, R. M.; Paniagua-Domínguez, R.; Kuznetsov, A. I. Directional lasing in resonant semiconductor nanoantenna arrays. *Nat. Nanotechnol.* **2018**, *13*, 1042−1047.
(32) Koshelev, K.; Kruk, S.; Melik-Gaykazyan, E.; Choi, J.-H.; Bogdanov, A.; Park, H.-G.; Kivshar, Y. Subwavelength dielectric resonators for nonlinear nanophotonics. *Science* **2020**, *367*, 288−292.
(33) Tiguntseva, E.; Koshelev, K.; Furasova, A.; Tonkaev, P.; Mikhailovskii, V.; Ushakova, E. V.; Baranov, D. G.; Shegai, T.; Zakhidov, A. A.; Kivshar, Y.; Makarov, S. V. Room-Temperature Lasing from Mie-Resonant Non-Plasmonic Nanoparticles. *ACS Nano* **2020**, DOI: 10.1021/acsnano.0c01468.
(34) Alaee, R.; Rockstuhl, C.; Fernandez-Corbaton, I. An electromagnetic multipole expansion beyond the long-wavelength approximation. *Opt. Commun.* **2018**, *407*, 17−21.
(35) Evlyukhin, A. B.; Chichkov, B. N. Multipole decompositions for directional light scattering. *Phys. Rev. B: Condens. Matter Mater. Phys.* **2019**, *100*, 125415.

https://dx.doi.org/10.1021/acs.nanolett.0c01646
Nano Lett. 2020, 20, 5786−5791